Synthesis of CdSe Nanoparticles: Tuning of Optical Properties and Potential Application

By

Avinash Singh

CHEM01201304034

Bhabha Atomic Research Centre, Mumbai-400085

A thesis submitted to the

Board of Studies in Chemical Sciences
In partial fulfillment of requirements

for the Degree of

DOCTOR OF PHILOSOPHY

of

HOMI BHABHA NATIONAL INSTITUTE

June, 2018

Homi Bhabha National Institute

Recommendations of the Viva Voce Committee

As members of the Viva Voce Committee, we certify that we have read the dissertation prepared by **Avinash Singh** entitled **"Synthesis of CdSe Nanoparticles: Tuning of Optical Properties and Potential Application"** and recommend that it may be accepted as fulfilling the thesis requirement for the award of Degree of Doctor of Philosophy.

Chairman – Prof. H. Pal		**Date:** 28/09/2018
Guide / Convener – Prof. M. C. Rath		**Date:** 28/09/2018
Examiner – Prof. Abhijit Saha		**Date:** 28/09/2018
Member 1- Prof. S. Adhikari		**Date:** 28/09/2018
Member 2- Prof. V. Sudarsan	Sudarsan. V	**Date:** 28/09/2018
Member 2- Prof. Y. K. Bhardwaj		**Date:** 28/09/2018

Final approval and acceptance of this thesis is contingent upon the candidate's submission of the final copies of the thesis to HBNI.

I/We hereby certify that I/we have read this thesis prepared under my/our direction and recommend that it may be accepted as fulfilling the thesis requirement.

Date:

Place: HBNI, Mumbai

Dr. M. C. Rath

(Guide)

STATEMENT BY AUTHOR

This dissertation has been submitted in partial fulfillment of requirements for an advanced degree at Homi Bhabha National Institute (HBNI) and is deposited in the Library to be made available to borrowers under rules of the HBNI.

Brief quotations from this dissertation are allowable without special permission, provided that accurate acknowledgement of source is made. Requests for permission for extended quotation from or reproduction of this manuscript in whole or in part may be granted by the Competent Authority of HBNI when in his or her judgment the proposed use of the material is in the interests of scholarship. In all other instances, however, permission must be obtained from the author.

Avinash Singh

Avinash Singh

DECLARATION

I, hereby declare that the investigation presented in the thesis has been carried out by me. The work is original and has not been submitted earlier as a whole or in part for a degree / diploma at this or any other Institution / University.

Avinash Singh

Avinash Singh

List of Publications arising from the thesis

Journals

1. "An Insight into the optical properties of CdSe Quantum Dots During Their Growth in Bovine Serum Albumin Solution." **Avinash Singh**, M. Ahmed, Apurav Guleria, A.K. Singh, S. Adhikari and M.C. Rath, *J. Lumin.* **2016**, 179, 122–131 (doi:http:10.1016/j.jlumin.2016.05. 058).
2. "Saccharide Capped CdSe Quantum Dots Grown via Electron Beam Irradiation." **Avinash Singh**, Apurav Guleria, Amit Kunwar, Suman Neogy and M.C. Rath, *Mat. Chem. Phys.* **2017**, 199, 609-615 (doi:10.1016/j.matchemphys. 2017.07.062).
3. "L-Cysteine Capped CdSe Quantum Dots Synthesized by Photo-chemical Route." **Avinash Singh**, Amit Kunwar and M.C. Rath, *J. Nanosci. Nanotechnol.* **2018**, 18, 3419–3426 (doi:10.1166/jnn.2018. 14687).
4. "Facile and green synthesis of 1-thioglycerol capped CdSe quantum dots in aqueous solution." **Avinash Singh**, V. S. Tripathi, S. Neogy, and M.C. Rath, *Mat. Chem. Phys.* **2018,** 214, 320-329 (doi.org/10.1016/j.matchemphys. 2018.04.116).
5. "Dynamics of Radiolytic Formation of CdSe Quantum Dots in Aqueous Solution Containing Different Alcohols: A Pulse Radiolysis Study" **Avinash Singh** and M. C. Rath, *Radiat. Phys. Chem.* **2018**, 152, 49-55 (doi: 10.1016/j.radphyschem.2018.07.013).
6. "Rapid One Pot Photochemical Synthesis of Starch capped CdSe Quantum Dots in Aqueous Solution and their Fluorimetric Determination of Cu(II), Hg (II) and Cr (VI)." **Avinash Singh**, Apurav Guleria, Suman Neogy and M.C. Rath, (*Arab. J. Chem.* Accepted).

Conferences

Oral Presentation

1. Research Scholars Meet (RSM) FEB 9-10, 2018, Jaihind College, Mumbai University, Mumbai.
2. "Green synthesis of starch capped CdSe quantum dots in aqueous solution." **Avinash Singh** and M.C. Rath, ICN-3I, DEC 6-8, 2017, IIT Roorkee, Roorkee.
3. "Photochemical Induced Synthesis of L-Cysteine capped CdSe Quantum Dots." **Avinash Singh** and M.C. Rath, ICSMC, NOV 26-28, 2015, University of Mumbai, Mumbai.

Poster Presentation

4. "Saccharide capped CdSe quantum dots grown *via* electron beam irradiation." **Avinash Singh** and M.C. Rath, TSRP-2018, JAN 3-7, 2018, BARC, Mumbai **(Best poster award)**.
5. DAE-BRNS 4th National Workshop on Materials Chemistry (Energy and Bio-Material) NWMC-2017 (ENBIO-MAT), DEC 15-16, 2017, University of Mumbai, Mumbai.
6. "Green synthesis of selenium nanoparticles in aqueous solution under ambient conditions." **Avinash Singh**, Apurav Guleria and M.C. Rath, SSCB-2017, NOV 9-11, 2017, BARC, Mumbai **(Best poster award)**.
7. "Photochemical synthesis of starch capped CdSe nanoparticles in aqueous solution." **Avinash Singh,** S. Neogy and M.C. Rath, NSRP-2017, MAR 2-4, 2017, Manipal University, Manipal.
8. "Electron beam induced synthesis of CdSe quantum dots in aqueous solutions containing different alcohols." **Avinash Singh** and M.C. Rath TSRP- 2016, JAN 5-9, 2016, BARC, Mumbai.

9. "An insight into the optical properties of bovine serum albumin assisted growth of CdSe quantum dots in aqueous solution." **Avinash Singh**, M. Ahmed, A. Guleria, A.K. Singh, S. Adhikari and M.C. Rath, TSRP- 2016, JAN 5-9, 2016, BARC, Mumbai.
10. "Facile green synthesis of thioglycerol capped CdSe quantum dots in aqueous solution" **Avinash Singh**, S. Neogy and M.C. Rath, ISMC-2016, DEC 6-10, 2016 BARC, Mumbai.
11. "Photochemical and radiation chemical reduction of toxic metal ions." **Avinash Singh,** Sangeeta Keny, M.C. Rath and D. B. Naik, NSRP-2015, MAR 9-11, 2015 IIT-Kanpur.

Others Publication

1. "Rapid one-pot facile synthesis of Se nanoparticles at ambient condition: Role of starch in their phase transformation from crystalline to amorphous with reduced toxicity." **Avinash Singh**, Apurav Guleria, Amit Kunwar, Suman Neogy and M.C. Rath (Communicated *Mater. Res. Exp.*).

Avinash Singh
Avinash Singh

DEDICATIONS

To my respected teachers, beloved parents, sisters and friends……

ACKNOWLEDGEMENTS

I would like to take this opportunity to thank one and all who are directly or indirectly involved in the successful accomplishment of the thesis.

First and foremost, I would like to begin by expressing my heartfelt and sincere gratitude to my guide Dr. M. C. Rath for his constant supervision, encouragement and motivation. His deep knowledge of subject, out of box thinking, enthusiastic temperament, scientific endeavor and rational thinking helped me immensely throughout the work. I am grateful to him for sharing his knowledge and scientific understanding during the fruitful discussions with me throughout the work.

I feel privileged to acknowledge Dr. P.D. Naik, Associate Director, Chemistry group and Head, Radiation and Photochemistry Division for his bountiful patronage and inspiration.

I would like to express my sincere regards to Dr. D. B. Naik for his knowledge sharing, constructive conversation and valuable suggestions.

My sincere and deep acknowledge to Dr. Apurav Guleria for his persistent support, encouragement, stimulating discussions and precious guidance. His scientific temperament, precise and balanced approach to deal with the difficulties during experiments which have substantially helped me in my research work.

I extend my regards to Sirisha Majji for scientific discussion and knowledge sharing.

My special thanks to my friends D. Srinivas, Dr. Monali Kawade and Dr. Ankur Saha for their moral support, cooperative attitude and cheerful ambience. I am grateful to my flat mates Jayanta Da, Raman, Shaukat, Mrinal, Poojan and Utpal for sharing several joyful moments and funs which will be remain with me throughout my life. I greatly value all my friends in BARC for their friendship and having deep faith in me.

I sincerely thank to Dr. V. S. Tripathi, Dr. Sangeeta Keny and K. K. Bairwa for their support and valuable suggestions. I gratefully acknowledge Dr. Amit Kunwar for his help in carrying out cytotoxicity studies. His wide and in depth knowledge helped me enormously to develop understanding of the subject.

I am grateful to all the members of RPCD for their cooperative and caring attitude. I am obliged for their highly motivated and research orientated approach which provided me wonderful atmosphere to work and motivated me a lot.

I express my deep regards to the LINAC staff of RPCD (Shri S. A. Nadkarni, Smt. M. A. Toley, Shri S. J. Shinde and Shri B. B. Chaudhari) for their immense help in carrying out irradiation and pulse radiolysis experiments.

I am deeply grateful to Dr. Suman Neogy, Dr. S. N. Achary and Amit Kanjilal to provide me the TEM, SEM, XRD and FTIR facilities.

My sincere acknowledge and deep respect to the distinguished members of the doctoral committee, Dr. H. Pal (chairman), Dr. D. K. Palit (former chairman), Dr. S. Adhikari (member), Dr. V. Sudarsan (member) and Dr. Y. K. Bhardwaj (member) for their critical reviews and suggestions during the annual reviews and pre-synopsis presentation.

I will always be in debt to my teachers whose contribution in my life is invaluable and my current position without them is unimaginable. I express my deep regards to them all.

I owe a lot to my uncle, aunty and cousins for providing me homely environment and taking care of me. Finally, I owe whole-hearted gratitude to my parents for their constant faith, encouragement and love and for becoming my source of inspiration. I am obliged to my sisters and brother-in-law for their insistent support, care and love. Their blessings and compliments helped me a lot for this achievement.

June, 2018

Avinash Singh

Avinash Singh

RPCD, BARC, Mumbai

CONTENTS

Synopsis **1-9**

Abbreviations **10-11**

List of Figures **12-24**

List of Schemes **25**

List of Tables **26-30**

CHAPTER 1 **31-72**

INTRODUCTION 32

1.1 Nanoscience and Nanotechnology 33
1.2 Nanomaterials and their classification 34
1.3 Semiconductor Nanomaterials 35
1.4 Quantum Confinement in semiconductor nanocrystals 36
1.4.1 Confinement in one direction (quantum well) 38
1.4.2 Confinement in two directions (quantum wire) 39
1.4.3 Confinement in three directions (quantum dot) 39
1.5 Electronic Structure of QDs 41
1.6 Photophysical properties of QDs 44
1.6.1 Absorption and photoluminescence 44
1.6.2 Photoluminescence (Pl) lifetime of QDs 47
1.7 Classification of QDs 47
1.7.1 Core QDs 47
1.7.2 Core-Shell QDs 48
1.7.3 Alloyed QDs 48
1.8 Application of Nanomaterials/QDs 49
1.8.1 LEDs (Light Emitting Devices) 50
1.8.2 Photovoltaics 50
1.8.3 Photodetectors 51
1.8.4 Sensors 51
1.8.5 Photocatalyst 51
1.8.6 Bio-imaging 52

1.8.7 FRET based studies 52
1.9 Cytotoxicity of QDs 52
1.10 Synthesis of Nanomaterials 53
1.10.1 Physical method (top down approach) 54
1.10.2 Chemical method (bottom up approach) 55
1.11 Significance of synthesis of quantum dots in aqueous solution 58
1.12 Photochemical synthesis 59
1.13 Radiation chemical synthesis 61
1.13.1 Radiation Chemistry and Radiolysis of Water 61
1.13.2 Radiation Chemistry as a tool to synthesize semiconductor nanoparticles and quantum dots 64
1.14 Room temperature synthesis 65
1.15 Kinetics and Thermodynamics of Growth of Nanoparticles 66
1.16 Overview and scope of the thesis 69

CHAPTER 2 **73-102**
EXPERIMENTAL TECHNIQUES 73
2.1. Introduction 74
2.2 Radiation Chemical Synthesis 74
2.2.1 Pulse radiolysis and its principle 75
2.2.2 Linear Electron Accelerator (LINAC) 77
2.2.3 Kinetic spectrophotometer 79
2.2.4 Transient absorption measurement 80
2.2.5 Pulse radiolysis dosimetry 81
2.2.6 Kinetic treatment and experiment data handling 82
2.3 Photochemical Synthesis 84
2.3.1 Rayonet Photo reactor 85
2.4 X Ray Diffraction 86
2.5 Transmission electron microscopy (TEM) 88
2.6 Scanning electron microscopy (SEM) 90
2.7 Steady state UV-vis absorption measurement 92
2.8 Steady state photoluminescence measurements 93
2.9 Photoluminescence lifetime measurements 95
2.10 Fourier transform infrared (FTIR) spectroscopy 98

2.11 Raman spectroscopy 100

CHAPTER 3 **103-136**

PHOTOCHEMICAL SYNTHESIS OF CdSe NANOPARTICLES 103

3.1 Introduction 104

3.2 Experimental 106

3.2.1 Materials 106

3.3 Synthesis 106

3.3.1 Synthesis of L-Cysteine capped CdSe QDs 106

3.3.2 Synthesis of starch capped CdSe QDs 108

3.4 Characterization 108

3.5 MTT assay 110

3.6 Results and Discussion 110

3.6.1 L-Cysteine capped CdSe QDs 110

3.6.1.1 Characterization of L-Cysteine capped CdSe QDs 112

3.6.1.2 UV-visible absorption studies 116

3.6.1.3 Photoluminescence studies 117

3.6.1.4 In vitro toxicity study of CdSe QDs 119

3.6.2 Starch capped CdSe QDs 121

3.6.2.1 Synthesis of starch capped CdSe QDs 121

3.6.2.2 Characterization of starch capped CdSe QDs 125

3.6.2.3 Effect of temperature and pH on the Pl properties of thiourea functionalized CdSe QDs 128

3.6.2.4 Metal ion sensing studies 130

3.6.2.4.1 Selectivity 130

3.6.2.4.2 Pl quenching by Cu^{2+}, Cr^{6+} or Hg^{2+} ions 130

3.6.2.4.3 Pl quenching mechanism 133

3.6.2.4.4 Interference effect of Pb^{2+}, $Cd^{2+}$and Fe^{3+} ions 135

3.7 Summary and Conclusion 136

CHAPTER 4 **137-172**

RADIATION CHEMICAL SYNTHESIS OF CdSe NANOPARTICLES 138

4.1 Introduction 138

4.2 Saccharide capped CdSe QDs grown *via* electron beam irradiation 138

4.2.1 Experimental 139
4.2.1.1 Synthesis of CdSe QDs 139
4.2.1.2 Characterization 140
4.2.1.3 Pulse Radiolysis Study 140
4.2.1.4 *In vitro* toxicity studies of CdSe QDs 141
4.2.2 Results and discussion 141
4.2.2.1 XRD and TEM studies 142
4.2.2.2 FTIR studies 145
4.2.2.3. Optical absorption studies 146
4.2.2.4. Photoluminescence studies 148
4.2.2.5. Pulse radiolysis studies 151
4.2.2.6. Cytotoxicity studies 153
4.3 Dynamics of radiolytic formation of CdSe QDs in aqueous solution containing different alcohols: a pulse radiolysis study 155
4.3.1 Experimental 155
4.3.1.1 Chemicals 155
4.3.1.2 Pulse Radiolysis 156
4.3.1.3 Characterization 156
4.3.2 Results and discussion 157
4.3.2.1 Synthesis of CdSe QDs 157
4.3.2.2 Characterization of CdSe QDs 161
4.3.2.3. Photoluminescence of CdSe QDs 163
4.3.2.4. Pulse radiolysis studies 164
4.4 Conclusion 170

CHAPTER 5 **173-230**
ROOM TEMPERATURE SYNTHESIS OF CdSe NANOPARTICLES 174
5.1 Introduction 174
5.2 Facile and green synthesis of 1-thioglycerol capped CdSe QDs in aqueous solution 176
5.2.1 Experimental section 176
5.2.1.1. Materials 176
5.2.1.2 Synthesis 176
5.2.1.3 Materials characterization 177

5.2.1.4. Pulse radiolysis 178
5.2.1.5. Cyclic voltammetry 178
5.2.3 Results and discussion 179
5.2.3.1. Synthesis and characterization 179
5.2.3.2 Optical properties 187
5.2.3.2.1 UV-visible absorption studies 187
5.2.3.2.2 Photoluminescence studies 190
5.2.3.3 Reduction Potential studies 195
5.2.3.3.1 Pulse radiolysis studies 195
5.2.3.3.2 Cyclic voltammetric studies 197
5.2.3.4. Reaction mechanism 202
5.3 An insight into the optical properties of CdSe QDs during their growth in bovine serum albumin solution 204
5.3.1 Experimental details 204
5.3.1.1 Materials 204
5.3.1.2 Synthesis of CdSe nanoparticles 204
5.3.1.3. Characterization 205
5.3.1.4. Stopped-flow measurements 206
5.3.2 Results and Discussion 206
5.3.2.1. UV-visible absorption studies 208
5.3.2.2 Room temperature fluorescence studies 210
5.3.2.2.1 Steady-state fluorescence 210
5.3.2.2.2 Time-resolved fluorescence 220
5.3.2.3 FRET analysis and growth of CdSe QDs 224
5.4 Conclusion 229

CHAPTER 6 **231-240**
SUMMARY AND OUTLOOK 232
6.1 Summary 232
6.2 Future perspectives 239

References 241-255

SYNOPSIS

Semiconductor nanoparticles are very important materials as they have tremendous applications in various fields like- photovoltaics, light emitting devices, lasers, photocatalysis, sensors, bio-imaging, photo thermal and photodynamic therapy, etc [1-3]. CdS, CdSe, CdTe, PbSe, SnSe, InP, HgTe, etc. are the examples of such semiconductor nanomaterials which are used for different applications. The physical, optical and other properties of these semiconductor nanomaterials very much depends upon the type of capping agents used and the method of synthesis along with the materials of semiconductor [4]. In general, there are two approach of synthesis of nanomaterials i.e. (i) Top down and (ii) Bottom up approach. Semiconductor nanomaterials are predominantly synthesized using the Bottom up approach [5]. There are several methods in Bottom up approach which have been used to synthesized these nanomaterials like- high temperature organometallic route, microwave assisted, electrochemical route, hydrothermal/solvothermal route, photochemical, radiation chemical and normal chemical route. To adopt a proper synthesis route is still a challenge for researchers after many years and the common goal to achieve is (i) No use of external reducing agents, (ii) the reaction should occur at ambient condition i.e. normal temperature and pressure, (iii) no involvement of stringent laboratory conditions, (iv) minimal requirement of precursors, (v) the product should be of good quality (vi) the method should be facile and (vii) the product should be less cytotoxic [6]. In this regard, radiation induced synthesis of nanomaterials is very crucial as this method offers many advantages over the others [7].

In the present thesis work, we focus mainly on the synthesis, characterization and tuning of the optical and other properties of CdSe quantum dots (QDs) using high energy radiation, UV radiation and normal chemical route in aqueous solution at ambient conditions. The mechanism of synthesis has been studied using transient absorption spectroscopy and cyclic voltammetry (CV). We have used different capping agents mainly biomolecules like-saccharides and L-

Cysteine for the capping/surface passivation of these QDs. Finally, to explore the application of these QDs, we have used them in sensing of different heavy metal ions.

CHAPTER 1: Introduction

This chapter explains briefly about the nanoscience and nanotechnology and its applications, nanomaterials and their classifications, various methods of synthesis (top down and bottom up) and their advantages and disadvantages, kinetics and thermodynamics of growth of nanoparticles. In the methods of synthesis, we have elaborated the basics of radiation and photochemical processes involved along with radiolysis of water and the advantages of these two methods. Further, we have explained about the semiconductor nanoparticles, their electronic structure, quantum confinement behaviour, photophysical properties, cytotoxicity, classification and applications in different areas. We have also highlighted the role of the medium in the synthesis of these nanoparticles.

CHAPTER 2: Experimental techniques

In this chapter, the principles of pulse radiolysis, parts of Linear Accelerator (LINAC) which is used as radiation source and the kinetics processes involved and their interpretation have been explained thoroughly. A brief of Rayonet Photoreactor (source of UV photon) have been discussed. The basic principles of operation along with outlines of all the instruments used for the characterization of the nanoparticles such as- X-ray diffraction (XRD), Transmission electron microscope (TEM) and Scanning electron microscope (SEM) has been presented. Fundamentals of the techniques involved in the optical studies of QDs like UV-vis absorption spectrophotometer, steady state spectrofluorometer, Time correlated single photon counting (TCSPC), Raman and FTIR spectrometer has also been discussed in this chapter.

CHAPTER 3: Photochemical synthesis of CdSe nanoparticles.

Photochemical method of synthesis of nanoparticles offers many advantages over the other methods like, there is no use of additional reducing agents, no requirement of stringent laboratory conditions like inert atmosphere and high temperature, etc [8]. In this chapter, we have synthesized CdSe QDs using different capping agent i. e. - (i) L-cysteine and (ii) starch separately, by using UV irradiation in the aqueous solution containing cadmium sulphate, sodium selenosulfate, acetone and 2-propanol. No external reducing agents were added to the solution, as the radicals generated *in situ* upon photoirradiation i.e. 2-hydroxy-2-propyl radicals, $(CH_3)_2C^{\bullet}OH$ [9] could reduce the precursor ions for the synthesis of these QDs. This method is highly facile, rapid and one-pot approach for the synthesis of water soluble QDs. In this chapter we have synthesized (i) L-cysteine and (ii) starch capped CdSe QDs by using UV irradiation in the aqueous solution containing cadmium sulphate, sodium selenosulfate, acetone and 2-propanol.

These QDs were characterized by various techniques such as UV-Vis absorption, XRD, Raman, FTIR, TEM and SEM measurements. The presence of strong quantum confinement effects could be realized from their very small size i.e., ~ 3 nm as revealed by TEM studies with both the capping agents. Besides, these QDs were found to exhibit broad photoluminescence (PL) in the longer wavelength region with FWHM~170 nm. The PL intensity as well as the charge carrier lifetime values could be conveniently tuned by simply varying the Cd to Se precursor ratio during the synthesis in both the L-Cysteine and starch capped CdSe QDs. The charge carrier life time was found to be longer in the case of L-Cysteine capped QDs (~57 ns) as compared to starch capped (~38 ns). The cytotoxicity of capped QDs as well as bare CdSe QDs was monitored with both the capping agent and L-Cysteine capped CdSe QDs were found to be more biocompatible. Furthermore, a relatively novel approach has been adopted to extract the starch capped CdSe QDs from the colloidal solution by freezing it to $0^{o}C$ followed by de-

freezing to room temperature. The extracted QDs were functionalized with thiourea in order to increase the PL quantum yield and the stability of the QDs. The PL intensity of functionalized CdSe QDs was found to be maximum at room temperature and pH~7. The as functionalized QDs were also investigated for their applicability in sensing of heavy metal ions. Interestingly, the QDs displayed highly selective PL quenching in the presence of Cu^{2+}, Cr^{6+} and Hg^{2+} metal ions. The limits of detection for these metal ions were in the micro molar range. The quenching rate constant was found of the order of 10^{14} $M^{-1}s^{-1}$.

CHAPTER 4: Radiation chemical synthesis of CdSe nanoparticles.

This chapter consists of two sections. In section (i) CdSe QDs were synthesized in aqueous solutions using equimolar cadmium sulfate and sodium selenosulfate in aqueous solutions through 7 MeV electron beam irradiation in a linear electron accelerator, LINAC in the presence of different saccharides, such as fructose, glucose, sucrose and starch. These QDs were characterized by XRD, TEM and FTIR spectroscopy. The as grown CdSe QDs in colloidal solution were fairly stable under ambient conditions and exhibit room temperature excitonic absorption and broad PL (FWHM~160 nm). The charge carrier life time was also found to vary in different saccharide from 15 ns (fructose) to 32 ns (starch). From these studies it is found that the starch capped CdSe quantum dots were more stable as well as exhibit higher PL as compared to other saccharide capped quantum dots. The mechanism of the formation of these quantum dots was investigated by the pulse radiolysis studies and it was found that the synthesis involved transient intermediate species with absorption maximum at 500 nm. The glucose capped CdSe quantum dots were found to be more biocompatible as compared to the uncapped as well capped with other saccharides. It is expected that these quantum dots could find importance in the biological applications.

In section (ii) the dynamics of formation of cadmium selenide, CdSe QDs in aqueous solution containing equimolar ammoniated cadmium sulphate, $Cd(NH_3)_4SO_4$ and sodium selenosulphate, Na_2SeSO_3 as starting materials have been investigated in presence of different aliphatic alcohols by electron pulse radiolysis coupled with kinetic spectrometry. The formation of the CdSe QDs was found to proceed via formation of short lived transient intermediate species at around 500 nm in presence of these alcohols, which are formed upon the reaction of the different secondary alcohols produced with the cadmium and selenium precursors under N_2O saturated condition. These different transient intermediates have different formation and decay rate constants. The growth rate constant for the formation of transient species formed by reaction between $Cd^{\bullet+}$ and $Se^{\bullet-}$ were found to be of 10^8 $M^{-1}s^{-1}$ order, which is lower than in the case of reaction involved e^-_{aq}. These QDs were characterized by XRD and TEM. The excitonic absorption peak was found to vary from 536 nm to 436 nm from methanol to ethanol.

CHAPTER 5: Room temperature synthesis of CdSe nanoparticles.

This chapter broadly consists of two sections. Section (i) deals with the facile and green synthesis of 1-thioglycerol capped CdSe QDs. In summary, we have investigated the optical properties of the CdSe quantum dots synthesized in the presence of 1-thioglycerol in aqueous solution through a facile and green route. It was observed that 1-thioglycerol plays a dual role as a catalyst in the synthesis of the CdSe quantum dots and a perfect capping agent. These QDs were characterized by TEM, SEM, XRD, Raman and FTIR spectroscopy. The as grown quantum dots were found exhibit sharp excitonic absorption peaks at around 420 nm, which is very unusual in the case of the CdSe quantum dots synthesized at room temperature and ambient conditions. The excitonic absorption peak position could be nicely tuned by varying the stoichiometric compositions of the precursors, i.e. ammoniated cadmium sulphate and

sodium selenosulphate. However, these quantum dots exhibit a very broad PL with a large stokes shift at room temperature, which is rather in contrast to those are synthesized at high temperature using TOPO and TOP with a sharp excitonic absorption as well as sharp band gap emission with very less stokes shift [10]. The PL lifetime values were found to increase with the increase in the emission wavelength indicating a longer lifetime for the deep trap states as compared to the shallow trap states. The lifetime values were longer in the case of Cd: Se ratio as 0.5:0.5 and these values decrease from 11 ns to 6 ns with a variation in this stoichiometry. This indicates an increased contribution of the non-radiative deactivation of the photo excited carriers upon deviation in the perfect stoichiometric composition in the CdSe quantum dots synthesized in the presence of 1-thioglycerol in aqueous solution. The reaction mechanism for the synthesis of QDs was studied using Cyclic Voltammetry (CV). From the CV studies it is found that the S-atom of 1-thioglycerol seems to facilitate oxidation of Se^{2-} to Se^{-} and eventually catalyze the synthesis of QDs. Thus, CdSe QDs with sharp excitonic absorption can be synthesized by a facile root at room temperature using 1-thioglycerol which acts as both capping as well as reducing agent.

Section (ii) deals with the study of the insights into the optical properties of CdSe QDs grown in Bovine serum albumin (BSA) [11]. BSA assisted synthesis of CdSe QDs exhibits remarkable changes in the optical properties of the QDs as well as BSA during their growth. The growth of these QDs was investigated by recording the UV–visible absorption spectra and room temperature steady state PL at different time intervals after the mixing of the precursors. The growth of these QDs was associated with a quenching of the PL from BSA. The PL from these QDs was found to be associated with several features:(1) a gradual red-shift in its peak position, (2) increase in intensity with an isoemissive point up to few minutes from the time of mixing of the two precursors, and (3) subsequent decrease in intensity reaching a minimum value, which remains almost unchanged thereafter. The decrease and increase in the PL from

BSA and CdSe QDs, respectively have been explained on the basis of Forster resonance energy transfer (FRET) as well as the simultaneous growth of these QDs. In the present situation, BSA acts as a donor and CdSe QD acts as an acceptor. From these studies, it clear that the CdSe QDs are formed in the close proximity to the BSA molecules so that FRET could occur and the tertiary structure of BSA provides a suitable environment so that these QDs do not undergo any substantial agglomeration leading to their precipitation. This study is expected to provide an understanding the kinetics of growth of nanoparticles through their time-dependent optical properties.

CHAPTER 6: Summery and outlook

To summarize, the present thesis work reveals that CdSe QDs of very small size (3-4 nm) can be effectively synthesized at ambient conditions without requirement of stringent laboratory conditions and high temperature and pressure by just by using high energy electron beam, UV radiation and at room temperature chemical route using 1-thioglycerol. The optical properties and the cytotoxicity of these QDs depend upon the precursor ratio and the capping agent used. Saccharides like-glucose, fructose, sucrose, starch and protein like L-Cysteine have been used as capping agents. Out of various capping agents, L-Cysteine capped CdSe was found to have more biocompatibility. Also the PL life time value of L-Cysteine capped CdSe is more as compared to saccharide and thioglycerol capped CdSe QDs. Optical properties wise starch capped CdSe QDs were better. Further, the starch capped CdSe QDs can be extracted by first freezing its colloidal solution followed by defreezing at room temperature. The as obtained QDs can be further functionalized with different molecules like – thiourea to improve its optical properties. The as functionalized QDs can be useful in the sensing of different heavy metal ions. The reaction mechanism and the transient intermediate species involved in the synthesis of CdSe quantum dots were studied by pulse radiolysis and cyclic voltammetry. Out

of various methods used in the synthesis of CdSe QDs photochemical method to synthesize starch capped QDs would be useful and its surface functionalization with thiourea yields higher PL which could be used in various applications like- metal ion sensing etc. These methods of synthesis can also be successfully employed to synthesize different quantum dots like, SnSe, CuSe, CdTe, etc.

References

1. D. Bera, L. Qian, T. Tseng, P.H. Holloway, Quantum dots and their multimodal applications: A Review, *Materials* 3 (2010) 2266-2345.
2. C.T Matea, T. Mocan, F. Tabaran, T. Pop, O. Mosteanu, C. Puia, C. Iancu, L. Mocan, Quantum dots in imaging, drug delivery and sensor applications, *Int. J. Nanomed.* 2 (2017) 5421-5431.
3. I.V. Martynenko, A.P. Litvin, F. Purcell-Milton, A.V. Baranov, A. V. Fedorov, Y. K. Gunko, *J. Mater. Chem. B*, 5 (2017) 6701-6727.
4. S.M, Farkhani, A. Valizadeh, Review: three synthesis methods of CdX (X = Se, S or Te) quantum dots, *IET Nanobiotechnol.* 8 (2014), 59-76.
5. C. Dhand, N. Dwivedi, X.J. Loh, A. N. J. Ying, N.K. Verma, R.W. Beuerman, R. Lakshminarayanan, S. Ramakrishna, *RSC Adv.*, 5 (2015) 105003-105037.
6. M.Z. Hu, T. Zhu, Semiconductor nanocrystal quantum dot synthesis approaches towards large-scale, industrial production for energy applications, *Nanoscale Res. Let.* 10 (2015) 469-483.
7. C. Dispenza, N. Grimaldi, M.A. Sabatino, I.L. Soroka, M. Jonsson, Radiation-engineered functional nanoparticles in aqueous systems, *J. Nanosci. Nanotechnol.* 15 (2015) 3445–3467.

8. M. Sakamoto, M. Fujistuka, T. Majima, Light as a construction tool of metal nanoparticles: synthesis and mechanism, *J. Photochem. Photobiol. C: Photochem. Rev.* 10 (2009) 33–56.
9. P.R. Levstein, H.V. Willigen, Fourier transform-electron paramagnetic resonance study of the photochemical reaction of acetone with 2-propanol, *J. Chem. Phys.* 95 (1991) 900-908.
10. C.B. Murray, D.J. Norris, M.G. Bawendi, Synthesis and characterization of nearly monodisperse CdE (E = sulfur, selenium, tellurium) semiconductor nanocrystallites, *J. Am. Chem. Soc.*115 (1993) 8706-8715.
11. M. Ahmed, A. Guleria, M.C. Rath, A. K. Singh, S. Adhikari, S. K. Sarkar, Facile and green synthesis of CdSe quantum dots in protein matrix: tuning of morphology and optical properties, *Nanosci. Nanotechnol.* 14 (2014) 5730–5742.

Abbreviations

Abs	absorbance
ADC	analog to digital converter
a.u.	arbitrary unit
BSA	bovine serum albumin
CB	conduction band
CFD	constant fraction discriminator
Cm-153	Cumarin 153
CNT	classical nucleation theory
CV	cyclic voltammetry
DLS	dynamic light scattering
DNA	deoxyribonucleic acid
FRET	fluorescence resonance energy transfer
FTIR	Fourier transform infrared spectroscopy
FWHM	full width at half maximum
HRTEM	high resolution transmission electron microscopy
HSAB	hard soft acid base
IR	infrared
LED	light-emitting diode
LINAC	linear electron accelerator
MCA	multichannel analyzer
MTT	3-(4,5-dimethylthiazol-2-yl)-2,5-diphenyltetrazolium bromide
NC	nanocrystal
nm	nanometer
ns	nanosecond

Pl	photoluminescence (fluorescence)
PMT	photomultiplier tube
QDs	quantum dots
RF	radio frequency
SAED	selected area electron diffraction
SEM	scanning electron microscope
SDPG	sequential delay pulse generator
TAC	time to amplitude converter
TCSPC	time correlated single photon counting
TEM	transmission electron microscopy
TGA	thioglycolic acid
TG	thioglycerol
TOP	trioctyl phosphine
TOPO	trioctyl phophine oxide
UV-Vis	ultraviolet-visible
VB	valence band
XRD	X-ray diffraction
ZB	zinc blende

LIST OF FIGURES

Figure 1.1 **32**

Size of nanomaterials in comparison to the other objects (from nano to meter scale).

Figure 1.2 **33**

Lycurgus Cup (a) in absence and (b) in presence of light.

Figure 1.3 **35**

Classification of Nanomaterials based on their dimension and morphology.

Figure 1.4 **37**

(a) band structure of direct and indirect band gap semiconductor in the bulk state and (b) band structure of direct band gap semiconductor nanocrystals showing the discreteness of the band: quantum confinement effect.

Figure 1.5 **37**

Wannier-Mott and Frenkel exciton in the lattice.

Figure 1.6 **39**

Quantum confinement in various nanostructures.

Figure 1.7 **40**

Schematic Representation of quantum confinement effect, decrease in band gap due to increase in size, absorption and Pl spectra of different size QDs and colloidal solution of different coloured (size) QDs.

Figure 1.8 **44**

Change in band gap with radius of QDs and theoretical variation of the band gap with radius of the QDs for different semiconductor materials using equation (1.2).

Figure 1.9 **45**

Schematic diagram illustrating the electronic density of states depending on dimensionality.

Figure 1.10 **46**

Representation of photo physics of semiconductor both bulk and quantum confined- (a) and (b) corresponds to bulk system, (c) corresponds to quantum confined system, (d) absorption and emission spectra of bulk, (e) absorption spectra of quantum confined system with increase in size and (f) absorption and different emission channel in quantum dots.

Figure 1.11 **47**

Different types of QDs- (a) Core QDs (MX), (b) Core-shell QDs (MXPQ), (c) alloyed QDs (MLX) and (d) Core QDs surface passivated with ligands.

Figure 1.12 **49**

Application of nanomaterials in diverse arena.

Figure 1.13 **54**

Scheme for top down and bottom up approach and various methods of synthesis.

Figure 1.14 **60**

Scheme for the processes involved in photochemical method.

Figure 1.15 **60**

Schematic representation for the photochemical formation of 2-hydroxy-2-propyl radicals.

Figure 1.16 **62**

Scheme for the process involved in (a) radiation chemical methods and (b) radiolysis of water.

Figure 1.17 **63**

Reaction scheme for radiolysis of water and products formed at different time scale.

Figure 1.18 **65**

Schematic representation for room temperature chemical method of synthesis of nanoparticles.

Figure 1.19 **68**

Free energy diagram for nucleation explaining the existence of "critical nucleus''.

Figure 1.20 **69**

LaMer model of growth of nanoparticles.

Figure 2.1 **75**

Schematic representation of radiolytic synthesis of nanoparticles; reaction mixture- (a) before irradiation, (b) after irradiation.

Figure 2.2 **76**

Schematic diagram of Pulse Radiolysis Set Up.

Figure 2.3 **78**

Schematic diagram of linear electron accelerator.

Figure 2.4 **85**

Rayonet Photoreactor (inset lamp of 300 nm output light).

Figure 2.5 **87**

Diagrammatic representation of diffraction of X ray from the plane of the crystal.

Figure 2.6 **89**

Layout of optical components of a Transmission Electron Microscope.

Figure 2.7 **92**

Layout of optical components of a Scanning Electron Microscope.

Figure 2.8 **96**

Layout of a TCSPC set up.

Figure 3.1 **113**

(a) XRD pattern and (b) Raman Spectra of CdSe QDs synthesized with the precursors 1 mM each and L-cysteine 0.3 mM upon UV photo-irradiation.

Figure 3.2 **114**

TEM image of CdSe QDs synthesized with the precursors (a) 1 mM each (b) 1 mM and 0.5 mM of Cd and Se respectively and L-cysteine 0.3 mM upon UV photo-irradiation, Inset: Histogram plot showing the particle size distribution.

Figure 3.3 **114**

FTIR spectra of a) L-Cysteine and b) L-cysteine capped CdSe QDs.

Figure 3.4 **117**

UV-vis absorption spectra of CdSe QDs synthesized with the precursors (a) 1 mM each (b) 1 mM and 0.5 mM of Cd and Se respectively and L-cysteine 0.3 mM each upon UV photo-irradiation at different time intervals.

Figure 3.5 **118**

(i) Room temperature steady-state Pl spectra of CdSe QDs synthesized with different concentrations of the precursors, a) 1,1; b) 1, 0.5; c) 1.25,0.5; and d) 1.5,0.5 mM; (ii) Time resolved Pl decay profiles of CdSe QDs for concentrations of the precursors.

Figure 3.6 **120**

Line graph showing the % cytotoxicity of CdSe QDs synthesized with different concentrations of the precursors and L-cysteine 0.3 mM under UV photo-irradiation, prepared under different conditions in CHO cells as determined by the MTT assay. Values are mean ± SEM (n = 4).

Figure 3.7 **121**

(a) Unirradiated reaction mixture containing Cd: Se precursors as 0.5:0.5 mM along with 0.5 mg/ml starch in the presence of 2 % (v/v) acetone and 2-propanol, (b) orange-yellow coloured colloidal solution obtained after photoirradiation with 300 nm UV lamp.

Figure 3.8 **122**

Absorption spectra of reaction mixture containing Cd and Se precursor with starch at different time of photoirradiation (inset; excitonic peak position and particle size vs. time).

Figure 3.9 **123**

(a) Steady-state Pl spectra and (b) time-resolved Pl decay profiles of CdSe QDs synthesized with different Cd: Se precursor ratios.

Figure 3.10 **124**

(a) Colloidal solution of starch; at room temperature (i), after freezing (ii), and again after attaining room temperature (iii), (b) colloidal solution of CdSe QDs capped with starch (i), after freezing (ii) and again after attaining room temperature, extracted QDs synthesized from reaction mixture with (c) 1.5:0.5, (d) 1.0:0.5 and (e)0.5:0.5 mM of Cd: Se.

Figure 3.11 **125**

(a) XRD and (b) Raman spectra of starch capped CdSe QDs synthesized with 1.0 and 0.5 mM of Cd and Se.

Figure 3.12 **126**

(a) TEM image of CdSe QDs (inset 1; particle size distribution, inset 2 FFT pattern and inset 3 HRTEM image showing inter planar distances corresponding to (111) and (200) planes, (b) SEM image showing aggregated morphology of CdSe QDs.

Figure 3.13 **127**

FTIR spectra of starch, thiourea, starch CdSe and starch CdSe with thiourea.

Figure 3.14 **127**

Absorption and photoluminescence spectra of starch capped CdSe QDs and after functionalization with thiourea.

Figure 3.15 **128**

DLS histograms of starch capped CdSe QDs a) before and b) after functionalization with thiourea.

Figure. 3.16 **129**

Temperature dependent (a) and pH dependent (b) Pl spectra of thiourea functionalized CdSe QDs.

Figure 3.17 **130**

Pl quenching of CdSe QDs in presence of different metal ions.

Figure 3.18 **131**

Pl quenching of CdSe QDs in presence of different metal ions (a) Cu^{2+}, (b) Cr^{6+} and

(c) Hg^{2+}, inset- Stern-Volmer plot.

Figure 3.19 **132**

Time-resolved Pl decay profiles of CdSe QDs in the presence of different metal ions (a) Cu^{2+}, (b) Cr^{6+} and (c) Hg^{2+}.

Figure 3.20 **133**

Absorption spectra of thiourea functionalized QDs and QDs with metal ions (Cu^{2+}, Cr^{6+} and Hg^{2+}).

Figure 3.21 **135**

Histograms showing the change in Pl of CdSe QDs in the presence of Pb^{2+}, Cd^{2+} or Fe^{3+} with Cu^{2+}, Cr^{6+} and Hg^{2+} (equal concentration and ten times higher concentration of interfering metal ions).

Figure 4.1 **142**

Camera ready pictures of as grown CdSe QDs synthesized in the presence of different saccharides via electron beam irradiation.

Figure 4.2 **143**

XRD patterns for the CdSe QDs capped with (1) Fructose, (2) Glucose, (3) Sucrose, (4) Starch.

Figure 4.3 **144**

TEM image (a) and HRTEM image (b) of fructose capped CdSe QDs.

Figure 4.4 **144**

(a) TEM image and (b) HRTEM image of glucose capped CdSe QDs**.**

Figure 4.5 **144**

(a) TEM image and (b) HRTEM image of sucrose capped CdSe QDs.

Figure 4.6 **145**

(a) TEM image (inset FFT pattern) and (b) HRTEM image of with starch capped CdSe QDs.

Figure 4.7 **146**

FTIR spectra of different saccharides and saccharides capped CdSe QDs.

Figure 4.8 **147**

Optical absorption spectra of saccharide capped CdSe QDs.

Figure 4.9 **148**

Room temperature steady-state Pl spectra of saccharide capped CdSe QDs synthesized via electron beam irradiation in aqueous solution. Insert: Normalized FL spectra of the CdSe QDs. Absorbed dose absorbed = 10 kGy. Excitation wavelength = 400 nm.

Figure 4.10 **150**

Time-resolved Pl decay profiles of saccharide capped CdSe QDs synthesized via electron beam irradiation in aqueous solution. Absorbed dose absorbed = 10 kGy. Excitation wavelength=400 nm, emission wavelength = 550 nm.

Figure 4.11 **152**

Transient absorption spectra obtained from the pulse radiolysis studies performed on the mixture of 1 mM of each precursors with different saccharides in aqueous tert butanol. Pulse width 500 ns, absorbed dose 40 Gy/pulse. Insert: Kinetic decay profile obtained at 500 nm.

Figure 4.12 **154**

Line graph showing % cytotoxicity of CdSe QDs (uncapped and capped with four different saccharides. The results are presented as mean ±SEM (n=3).

Figure 4.13 **159**

Camera ready pictures of CdSe QDs synthesized in aqueous solutions containing different alcohols (a) MeOH, (b) EtOH, (c) 2-PrOH, (d) n-PrOH, (e) n-BuOH.

Figure 4.14 **161**

Absorption spectra of CdSe QDs synthesised in the presence of different alcohols, before irradiation (a) dotted line and after irradiation (b) continuous line and their excitonic position (in nm).

Figure 4.15 **162**

XRD pattern of CdSe QDs synthesized in the presence of 2-propanol.

Figure 4.16 **163**

(a)TEM image and (b) HRTEM image of CdSe QDs synthesised in the presence of 2-PrOH (inset the lattice spacing corresponding to 220 plane).

Figure 4.17 **164**

Pl spectra of CdSe QDs synthesised in the presence of different alcohols.

Figure 4.18 **168**

Transient absorption spectra of 1.0 mM each Cd^{2+} and $SeSO_3^{2-}$ in the presence of different alcohols. (Inset: Kinetic profiles at different concentrations of precursors).

Figure 5.1 **179**

Camera ready pictures of reaction mixture containing a) Cd and Se precursors, b) Cd and Se precursor along with 1-thioglycerol.

Figure 5.2 **180**

Absorption spectra of different systems used in the synthesis of CdSe QDs.

Figure 5.3 **181**

Absorption spectra of CdSe QDs synthesized with three different concentrations of 1-thioglycerol.

Figure 5.4 **182**

XRD pattern of thioglycerol capped CdSe QDs.

Figure 5.5 **183**

Raman Spectrum of thioglycerol capped CdSe QDs.

Figure 5.6 **184**

FTIR spectra of thioglycerol and thioglycerol capped CdSe QDs.

Figure 5.7 **185**

SEM images of 1.0:0.5 mM Cd: Se QDs (a) low magnification and (b) high magnification.

Figure 5.8 **186**

SEM images of (a) 0.5:0.5 mM and (b) 0.5:1.0 mM Cd: Se quantum dots.

Figure 5.9 **186**

TEM image of CdSe QDs, inset (a) HRTEM image and (b) Particle size distribution.

Figure 5.10 **187**

TEM image of 0.5:0.5 mM Cd: Se quantum dots (inset FFT pattern and HRTEM image showing the planes of the crystal).

Figure 5.11 **188**

UV-vis absorption spectra of CdSe QDs synthesized with different Cd^{2+} and Se^{2-}ratios (Inset: Tauc plot for different Cd: Se ratios).

Figure 5.12 **189**

Band assignment of absorption spectra of CdSe QDs and schematic representation of electronic absorptions to corresponding bands**.**

Figure 5.13 **190**

Steady state Pl spectra for different Cd: Se ratio. (Inset: Normalised Pl spectra).

Figure 5.14 **192**

Multiple curve fitting of Pl spectra along with absorption spectra of 0.5:0.5 mM Cd: Se quantum dots**.**

Figure 5.15 **194**

Pl lifetime decay profiles of CdSe QDs synthesized with Cd: Se ratio 0.5:0.5 mM; monitored at 520, 560 and 600 nm emission wavelengths. The excitation wavelength at 420 nm.

Figure 5.16 **196**

Transient absorption spectra of thioglycerol cation radical obtained in the pulse radiolysis studies in the presence of azide ($N3^{\bullet-}$) radicals. Inset: Formation and decay profiles of thioglycerol cation radicals obtained in the pulse radiolysis studies in the presence of azide ($N_3^{\bullet-}$) radicals monitored at 430 nm at different TG concentrations.

Figure 5.17 **198**

Cyclic Voltammograms of 1-thioglycerol, sodium selenosulphate, sodium selenosulphate with thioglycerol, increased concentration of sodium selenosulphate with 1-thioglycerol and sodium selenosulphate with increased concentration of 1-thioglycerol (Scan Rate- 40 mV/s).

Figure 5.18 **200**

Cyclic voltammograms of sodium selenosulphate, 1-thioglycerol, sodium selenosulphate in the presence of 1-thioglycerol, glycerol and sodium selenosulphate in the presence of glycerol (at pH 11.0).

Figure 5.19 **201**

Cyclic Voltammograms of thioglycerol, cadmium sulphate, and cadmium sulphate along with thioglycerol (Scan Rate- 40 mV/sec).

Figure 5.20 **202**

Cyclic Voltammograms of cadmium sulphate with thioglycerol, sodium selenosulphate with thioglycerol and cadmium sulphate and sodium selenosulphate along with thioglycerol (Scan Rate- 40 mV/s).

Figure 5.21 **207**

TEM image of CdSe QDs synthesized from the reaction mixture 10:10.

Figure 5.22 **209**

Absorption spectra recorded at different time intervals for (a) 10:5, (b) 10:10 and (c) 10:20 reaction mixtures.

Figure 5.23 **211**

Room temperature steady-state fluorescence spectra recorded with the solution containing 0.5 mg/ml BSA only and 0.5 mg/ml BSA along with 2.5 mM $SeSO_3^{2-}$ at different time intervals: within 1 min, 5 min, 10 min and 20 min. Excitation wavelength was fixed at 290 nm.

Figure 5.24 **212**

Room temperature steady-state fluorescence spectra recorded at different time intervals for 10:10 reaction mixture. Excitation wavelength-290 nm. Inset: Fluorescence spectra shown in expanded scale for three different time intervals.

Figure 5.25 **213**

Plot of BSA fluorescence intensity at 345 nm vs time for the solution containing 0.5 mg/ml BSA and 2.5 mM $SeSO_3^{2-}$; 0.5 mg/ml BSA, 2.5 mM Cd^{2+} and 2.5 mM $SeSO_3^{2-}$.

Figure 5.26 **214**

Room temperature steady-state CdSe Pl spectra recorded at different time intervals for the 10:10 reaction mixture 1) 0, 2) 3, 3) 6, 4) 9, 5) 12, 6) 15, 7) 18, 8) 24, 9) 30, 10) 36, 11) 45, 12) 75 min. Excitation wavelength was fixed at 420 nm.

Figure 5.27 **215**

(a) Plot of room temperature BSA fluorescence intensities recorded at 345 nm vs time for the three reaction mixtures, 10:5, 10:10 and 10:20. Inset: Plot of BSA fluorescence signal vs time obtained from the stopped flow measurements for the three reaction mixtures, 10:5, 10:10 and 10:20. (b) Plot of area under the CdSe Pl spectra in the range from 450 to 750 nm vs time for the three reaction mixtures, 10:5, 10:10 and 10:20.

Figure 5.28 **218**

Room temperature steady-state CdSe Pl spectrum (black) recorded for the 10:10 reaction mixture at 30 minute. Excitation wavelength was fixed at 420 nm. Red line shows the multiple curve-fitting spectrum matching with the observed spectrum (black) and blue lines show the two fitted spectra shown with their peak positions.

Figure 5.29 **219**

Plot of CdSe Pl peak positions for as observed (λ_{obsd}^{max}, 1) and the fitted ones ($\lambda_{1\text{-}fit}^{max}$, 2 and $\lambda_{2\text{-}fit}^{max}$, 3 for the short and long wavelength peak positions respectively) vs. time for the three reaction mixtures: (a) 10:5, (b) 10:10, (c) 10:20.

Figure 5.30 **222**

Room temperature BSA fluorescence decay profiles monitored at 345 nm at different time intervals, 5, 60, 120, 300 min along with the prompt profile for the three reaction mixtures, (a) 10:5, (b) 10:10, (c) 10:20.

Figure 5.31 **223**

Plot of average lifetime (<τ>) vs time for the three reaction mixtures, 10:5, 10:10 and 10:20. Inset: (a) Plot of short lifetime, τ_1 vs time and (b) Plot of long lifetime, τ_2 vs time for these above three reaction mixtures.

Figure 5.32 **226**

Absorption spectra (of CdSe QDs) and room temperature fluorescence spectra (of BSA) at initial time intervals plotted in the same wavelength scale in order to show the overlap between them for the three reaction mixtures: (a) 10:5, (b) 10:10 and (c) 10:20.

List of Schemes

Scheme 3.1 **107**

Photochemical synthesis of L-cysteine capped CdSe quantum dots.

Scheme 3.2 **109**

Photochemical synthesis of starch capped CdSe quantum dots, extraction, functionalization and fluorimetric detection of metal ions.

Scheme 3.3 **134**

Possible bindings metal ions with thiourea attached to the surface of CdSe QDs.

Scheme 4.1 **169**

Transient species involved and their formation rate constant.

Scheme 4.2 **171**

Relative properties of different saccharide capped CdSe QDs.

Scheme 5.1 **191**

Representation of excitation and de-excitation of charge carriers in the CdSe QDs capped with 1-thioglycerol.

Scheme 5.2 **224**

Schematic representations showing the photo-excitation of BSA followed by (i) emission from BSA excited states, (ii) FRET from excited state BSA to the conduction band of CdSe QDs at the initial time, (iii) emissions from the CdSe QDs and (iv) growth of these QDs.

List of Tables

Table 1.1 **43**

Physical properties of some II-VI semiconductor.

Table 1.2 **56-58**

Comparison of various methodology used for nanomaterial synthesis.

Table 1.3 **64**

Chemical properties of the primary products of radiolysis of water.

Table 3.1 **119**

Pl lifetime values of CdSe QDs prepared with various compositions of the precursors (in mM) and L-cysteine concentration of 0.3 mM.

Table 3.2 **123**

Pl lifetime values of CdSe QDs prepared with various compositions of precursors (mM).

Table 3.3 **133**

Limit of detection (LOD) and quenching rate constant (k_q) of metal ions.

Table 4.1 **147**

Electronic band gap (E_g) and particle size (nm) of the CdSe QDs determined from the ground state absorption spectra in the presence of different saccharides.

Table 4.2 **150**

Pl lifetime values determined from the lifetime decay profiles by fitting with tri-exponential curve fitting for CdSe QDs capped with different saccharides.

Table 4.3 **152**

Decay rate constants of the transient intermediate species having absorption at 500 nm and position of absorption maximum estimated from the pulse radiolysis studies in the presence of different saccharides and polysaccharides.

Table 4.4 **157**

Rate constants of reactions of $H^{\bullet}$, $OH^{\bullet}$ radicals with alcohols [178].

Table 4.5 **159**

One-electron reduction potential (E^1) [181] values of the radicals in different solvent systems at pH 3.4 vs NHE at room temperature (25^0C).

Table 4.6 **166**

Growth and decay rate constants for $Se^{\bullet-}$ produced in the case of different alcohols.

Table 4.7 **167**

Growth and decay rate constants of the transient species formed by the reactions between $Cd^{\bullet+}$ and $SeSO_3^{2-}$ ions.

Table 4.8 **167**

Decay and growth rate constants of the transient species formed by the reactions between $Se^{\bullet-}$ and $[Cd(NH_3)_4]^{2+}$ ions.

Table 4.9 **170**

Growth and decay rate constants of the transient species formed by the reaction between $Cd^{\bullet+}$ and $Se^{\bullet-}$, along with their peak absorbance values observed in the case of different alcohols.

Table 5.1 **193**

Band gap values, particle sizes, quantum yield and zeta potentials of TG capped CdSe QDs synthesized with different stoichiometric compositions.

Table 5.2 **194**

Pl lifetime values at different emission wavelength of TG capped CdSe QDs synthesized with different stoichiometric compositions.

Table 5.3 **199**

Comparison of ratios of anodic peak currents for TG to that for Se oxidation for different concentrations of TG.

Table 5.4 **210**

Kinetic parameters determined from the excitonic absorption peak positions vs time, which was obtained from time dependent absorption spectra at different time intervals after mixing of the two precursor solutions, by fitting with first order equation, $y = y_0 + ae^{-kt}$.

Table 5.5 **216**

Kinetic parameters obtained from the fluorescence intensity of BSA at 345 nm vs time and the fluorescence (total area under the curve) of CdSe QDs vs time, which were obtained from the steady-state fluorescence measurements at different time intervals after mixing of the two precursor solutions, by fitting with first order equation, $y = y_0 + ae^{-kt}$; as well as from the stopped flow measurements in the fluorescence mode (that is mainly BSA fluorescence) by fitting with second order equation, $y = y_0 + a_1e^{-k(1)t} + a_2e^{-k(2)t}$.

Table 5.6 **220**

Pl peak positions (observed as well as fitted values) of CdSe QDs at initial time (about 0 to 5 min) and after long time duration (about 2 hrs) from the time of mixing of the two precursor solutions, in different precursor ratio conditions.

Table 5.7 **221**

First-order growth rate constants k_{g3} determined by the fitting the plots of observed and fitted values of FL peak positions of CdSe QDs against time with first order equation, $y = y_0 + ae^{-kt}$.

Table 5.8 **222**

Fluorescence lifetime values (ns) of BSA obtained at different time intervals (min) after mixing of the precursors in the case of three different precursor concentrations.

Table 5.9 **228**

FRET parameters determined for all the three reaction mixtures at different time intervals (initial period within 10 minutes, later period at about 60 minutes) from the time of mixing of the two precursor solutions.

CHAPTER 1

INTRODUCTION

1.1 Nanoscience and Nanotechnology

The prefix "*nano*" is derived from ancient Greek word "Nanos", which means "Dwarf". In modern day science, prefix "nano" means 10^{-9}. Adjoining the word "nano" with the unit of length "meter" originates the term "nanometer" which is a unit of measurement of one billionth of a meter. Materials in their bulk state possess macroscopic properties. The micron size of these materials have almost similar properties as that of bulk but when the particles assume nano dimension (Fig. 1.1), the principles of classical physics are no longer capable of describing their behaviour (structure, movement and energy). At nano dimension level, quantum mechanical principles are applied to describe their behaviour and the materials show distinctive properties to their bulk counterpart such as -(i) very high surface area, (ii) exceptional mechanical strength, (iii) unique optical properties like- size dependent absorption and emission spectra (iv) decrease in melting point etc. For example- gold nanoparticles (Au nps) have properties (mechanical, optical, electronic etc.) which are very much different (even superior) from bulk gold metals. [1].

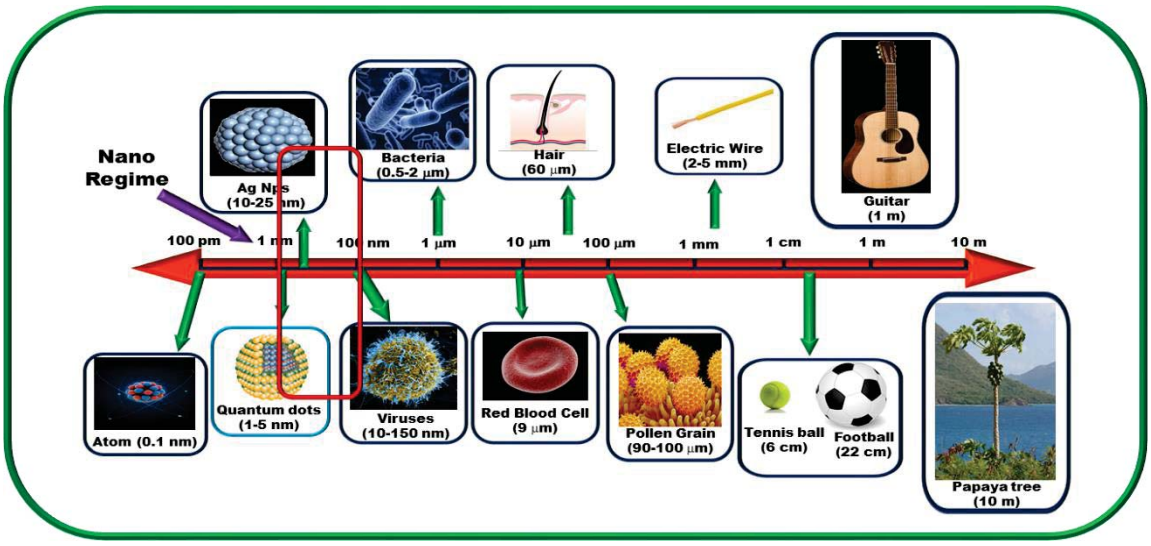

Figure 1.1 *Size of nanomaterials in comparison to other objects (from nano meter to meter scale).*

The unique properties of nanomaterials motivate the researchers to design them for desired applications. All the synthetic methodology of nanomaterials, their properties and application fall under the purview of nanoscience and nanotechnology. It is a multidisciplinary area of research in which various streams like-physics, chemistry, biology, engineering, environment science are involved. Therefore, nanotechnology and nanoscience can be defined in the following words:

"The branch of technology which deals with the design, production, characterization and application of structures, devices and systems by controlling their shape and size at nanoscale (1-100 nm)."

"Nanoscience is the study of phenomena and maneuver of materials at atomic and molecular scale, where the properties of a material differ extraordinarily from those at a larger scale."

Nanoscience is known to be in practice since very old time. One of the great examples in ancient age that shows the intelligent use of nanoparticles is the Lycurgus Cup made in 4th century A.D., which consists of gold and silver alloy nanoparticles (Fig. 1.2) and exhibits different colours in the presence or absence of light [2].

Figure 1.2. *Lycurgus Cup (a) in absence and (b) in presence of light.*

However, in the recent time, research and development in this field revolutionized after Richard P. Feynman's classical talk "*There's Plenty of Room at the Bottom*" on 29 December 1979 [3]. The term *Nanotechnology* was first coined by Eric Drexler in his book "*Engine of Creation*" in 1986 [4]. The development of unique nanoscale structures has the potential to revolutionize industry, including electronics, medicine, and consumer products. Owing to its contribution in these fields, nanoscience is a favorite area of research worldwide.

1.2. Nanomaterials and their classification

Nanomaterials are the extremely small sized (1-100 nm) objects having unusual properties which leads to several applications. These nano objects have enormous potentials to revolutionize the modern day science and technology by producing novel functionality in an object. Nanomaterials are created both by nature as well as by humans. Nature is the oldest manufacturer of nano dimensional objects. For example-(i) Lotus leaf, which is known to be water repellent has nanostructure on its surface which is inherently hydrophobic in nature, (ii) Gecko have nanostructure present on its feet which enable them to walk on any kind of surfaces at any orientation. Artificial nanomaterials can be categorized into different groups. On the basis of their shape and morphologies, nanomaterials can be categorized into the following forms: (i) nanoparticles, (ii) nano rods, (iii) nano tubes, (iv) nano films, (v) nano sheets (vi) nano ribbon, (vii) nano flowers etc (Fig. 1.3). On the basis of the constituents of the nanomaterials, they can be classified as: (i) carbon (e.g. fullerene, graphene, graphene oxide, carbon nanotubes), (ii) metal (e.g. Ag, Au nanoparticles), (iii) compound semiconductor (e.g. CdS, CdSe nanoparticles), (iv) metal-semiconductor hybrid (e.g. Ag-CdSe) and (iv) metal oxides (e.g. ZnO, TiO_2 etc).

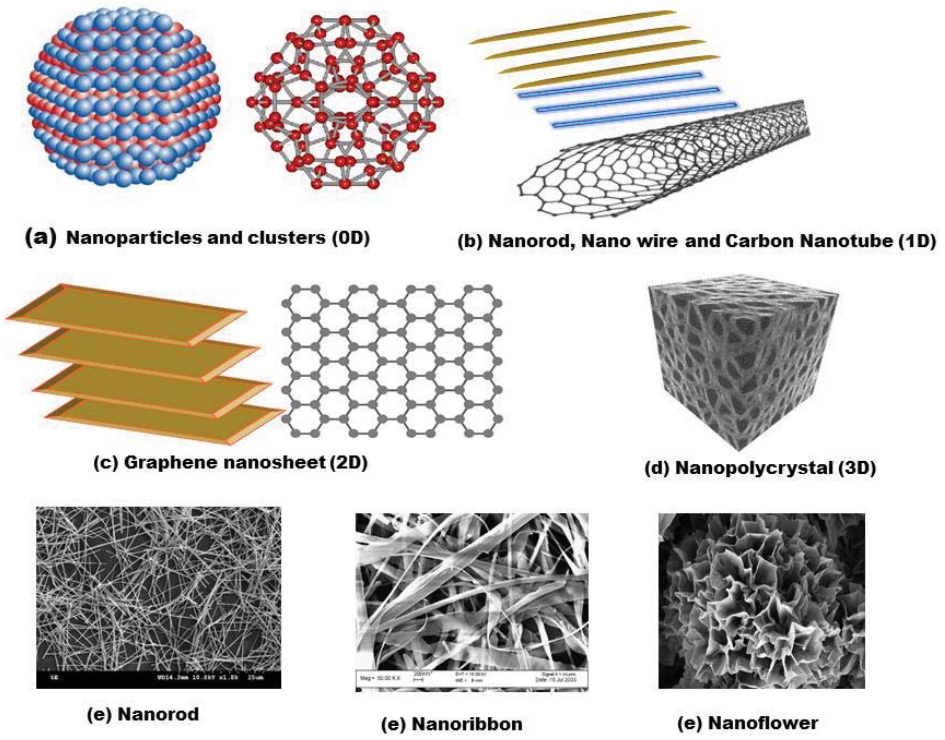

Figure 1.3 *Classification of Nanomaterials based on their dimension and different morphology*.

1.3. Semiconductor Nanomaterials

On the basis of their electrical conductivity, bulk materials can be classified into three groups- (i) conductor (electrical conductivity, $\sigma > 10^3$ S/cm), (ii) semiconductor ($10^{-8} < \sigma > 10^3$ S/cm) and (iii) insulator ($\sigma < 10^{-8}$ S/cm). These materials have valence band (lower in energy) and conduction band (higher in energy). The energy difference between the valence band (VB) and the conduction band (CB) is known as the band gap of the material. The conductivity of any material is determined by its band gap. In conductors, the valence and the conduction bands overlap because the conduction band is partially filled with electrons, while in case of insulator there is a wide gap between both bands (> 9.0 eV). Hence, a semiconductor is a material whose conductivity lies between the conductors and insulators. In semiconductors, the highest occupied energy band (valence band) is completely filled with electrons while the next band

(conduction band) is completely empty. Semiconductor nanomaterials are very fascinating because of special physico-chemical and optical properties including continuous absorption profile up to blue band edge, size and shape tunable emission with sharp emission profile and stability against photo bleaching [6]. They are used in a variety of applications like - optoelectronic devices, sensors, catalysts, cell imaging, photodynamic therapy etc. The properties of these nanomaterials depend upon the shape, size, morphology and their intrinsic structure. These properties make them superior nano materials as compare to their counterparts. They can be prepared from different combinations of elements like – Cd-Se, Cd-S, Zn-O, Zn-S, Cd-Te, Pb-Se, In-P, Ga-As etc. They are referred to as II-VI, III-V and IV-VI class of semiconductor based on the group in the periodic table from where the elements are acquired. For example- CdSe and ZnS are II-VI while InP and GaAs are III-V class semiconductors.

1.4. Quantum Confinement in semiconductor nanocrystals

In the bulk semiconductor crystals, the band gap between the valence band and the conduction band is not wide. Thus it is possible to excite the electrons from the valence band to the conduction band with some amount of energy. The overall behaviour of the bulk material changes when the dimensions of the material are reduced to the nanoscale. In such case, the charge carriers get confined in the lattice points leading to change in the band structure and the energy level becomes discrete (Fig 1.4 b) in nature. In the case of direct band gap semiconductors, the band energy minimum of the CB and band energy maximum of the VB lie in the same k value (k=0). In the case of indirect band gap semiconductors, the minimum of the CB is shifted and hence the formation of charge carriers depends on light absorption followed by the absorption of a phonon.

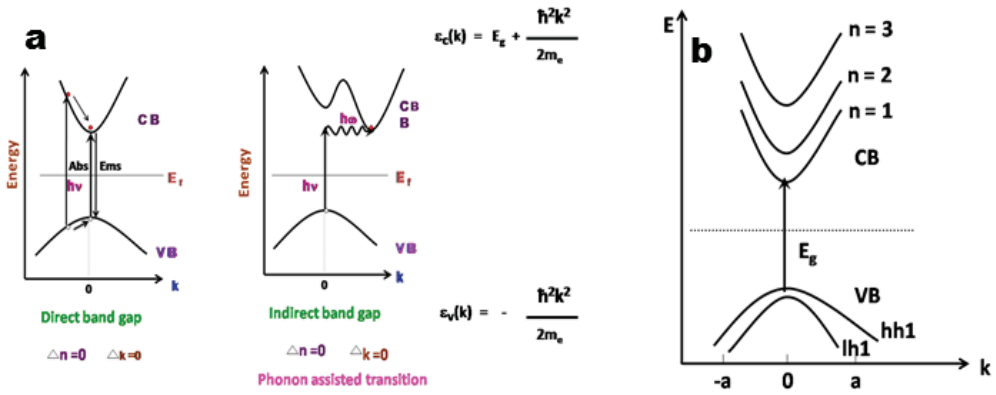

Figure 1.4 *(a) Band structure of direct and indirect band gap semiconductor in the bulk state and (b) band structure of direct band gap semiconductor nanocrystals showing the discreteness of the band: quantum confinement effect.*

The charge carriers (electron (e) and hole (h)) which are generated upon photoexcitation, feel coulombic attraction because of opposite charge and thus form a hydrogen atom like structure which is called "*exciton*" [7]. Depending on the nature of the materials in which these charge carriers are generated, the excitons are of two types- (i) Wannier- Mott exciton (in semiconductors) and (ii) Frankel exciton (in insulators). The semiconductor materials have large dielectric constant. Hence, the electric field screening reduces the coulombic interaction between the charge carriers which results in Wannier- Mott exciton (Fig. 1.5) with radius larger than the lattice spacing.

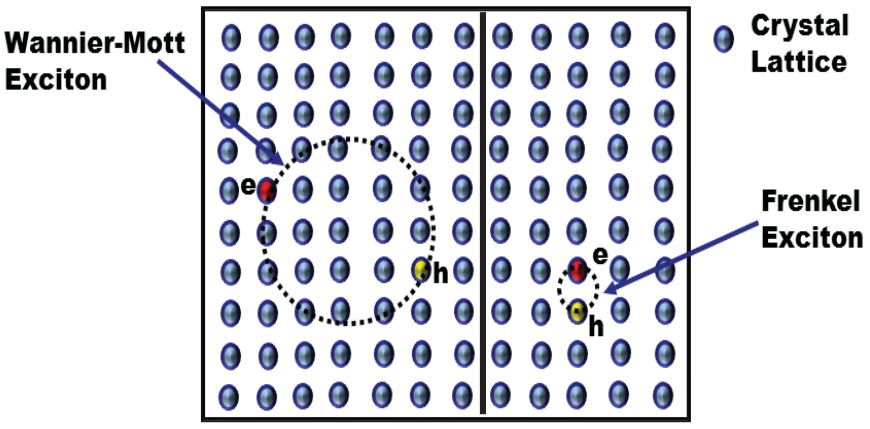

Figure 1.5 *Wannier-Mott and Frenkel exciton in the lattice.*

On the other hand, in materials of small dielectric constant, the coulombic interaction between the charge carrier is strong and the size of the exciton tends to be small and the order of the size of unit cell. These excitons are called Frenkel excitons. The charge carriers in the reduced dimensional nano system behaves like the *particle in a box.* Such effect is called *quantum confinement effect*. On the basis of de-Broglie equation, we can state that the quantum confinement effect arises when the size of the nanostructure is below or equal to the de-Broglie wavelength of the charge carriers.

$$\lambda_{de-Broglie} = \frac{h}{mv} = \frac{h}{\sqrt{2mE}} \qquad (1.1)$$

where, m = effective mass of charge carriers, E = thermal energy in one direction kT. There are three dimensions (x, y and z) along which the confinement can occur. The quantum confinement in all the three dimensions is shown in Fig. 1.6.

1.4.1. Confinement in one direction (quantum well)

In a quantum well structure, the quantum confinement occurs only in one dimension (x axis) where the charge carriers are free to move in two dimensions (y-z plane) and hence called as 2D nanomaterials (see Fig. 1.6). When a lower band semiconductor thin film is sandwiched between two higher band semiconductor thin films, this becomes a quantum well structure. For example, a quantum well is formed when a thin film of gallium arsenide (Eg = 1.4 eV) is sandwiched between two layers of aluminium arsenide (Eg = 2.1 eV). Another example is when a thin film of CdSe (Eg = 1.7 eV) is sandwiched between two thin films of ZnSe (Eg = 2.7 eV). These structures can be nicely grown by molecular beam epitaxy (MBE) or chemical vapour deposition with control of layer thickness in the form of monolayer. Quantum wells are used in transistor, laser diodes and IR detectors, all-optical switches, etc.

1.4.2. Confinement in two directions (quantum wire)

A semiconductor nanostructure in which the quantum confinement occurs in two dimensions (x and y axes) is called as *quantum wire*. In such nanomaterials, the charge carriers are free to move only in one dimension (i.e. z axis) and hence called as 1D nanomaterials too (see Fig. 1.6). Carbon nanotubes are example of quantum wire. These are used in energy storage devices, transistors and sensors.

1.4.3. Confinement in three directions (quantum dot)

A semiconductor nanostructure in which the quantum confinement occurs in all three dimensions (x, y and z axes) i.e. where the charge carriers are confined in all the three dimensions, is called as *quantum dot* (Fig 1.6). Sometimes these are also called as 0D nanomaterials in the literature.

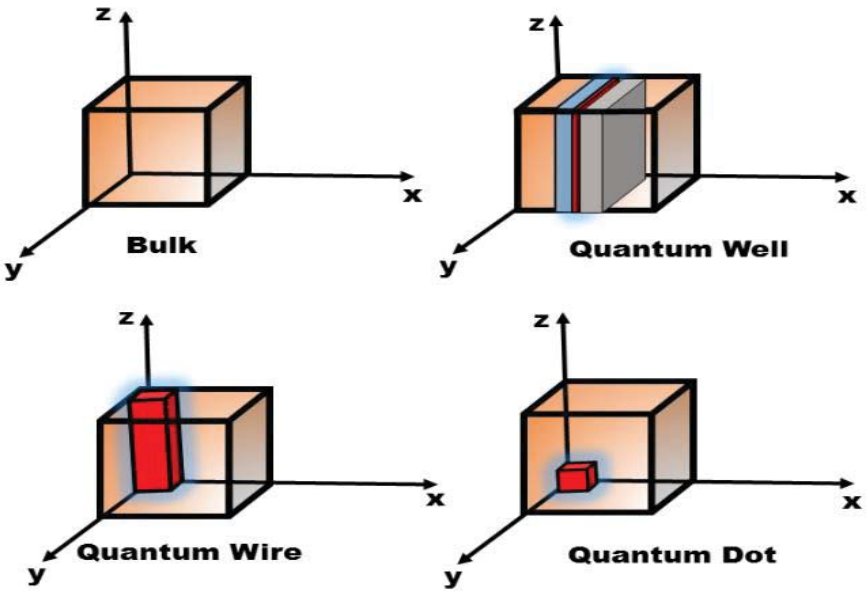

Figure 1.6 *Quantum confinement in various nanostructures.*

The history of semiconductor nanocrystals was started back around thirty years ago when Russian solid state physicist Alexey Ekimov discovered the CdS QDs in glass matrix in mid 1980s while working in Vasilov State Optical Institute in Russia [8]. After this pioneered

discovery, Louis E. Brus for the first time synthesized the CdS QDs in colloidal solution [9,10]. Colloidal synthesis of QDs further inspired the systematic study and progress in the science and technology of QDs. Working in AT &T Bell lab, Louis E. Brus discovered a relation between the particle size and the band gap of the semiconductor nanoparticles using particle in a box approximation to the wave function of the bulk semiconductor [10]. It was Mark Reed who first coined the term "QDs" in his paper in 1988 which was actually sounds more pleasurable than "zero dimensional semiconductor" [11]. After Brus, another important milestone came in the history of semiconductor QDs when in 1993 Murray, Norris and Bawendi described a hot injection method to synthesize mono dispersed high quality QDs [12]. These researchers started extracting the possibilities of QDs in several applications. The size range of QDs is 2-20 nm but strictly speaking according to some literature it should be below 10 nm [13]. However, the exact size of the QDs also depends upon the material used to synthesize them. QDs exhibit very unique properties which are in between the bulk semiconductor and discrete molecules.

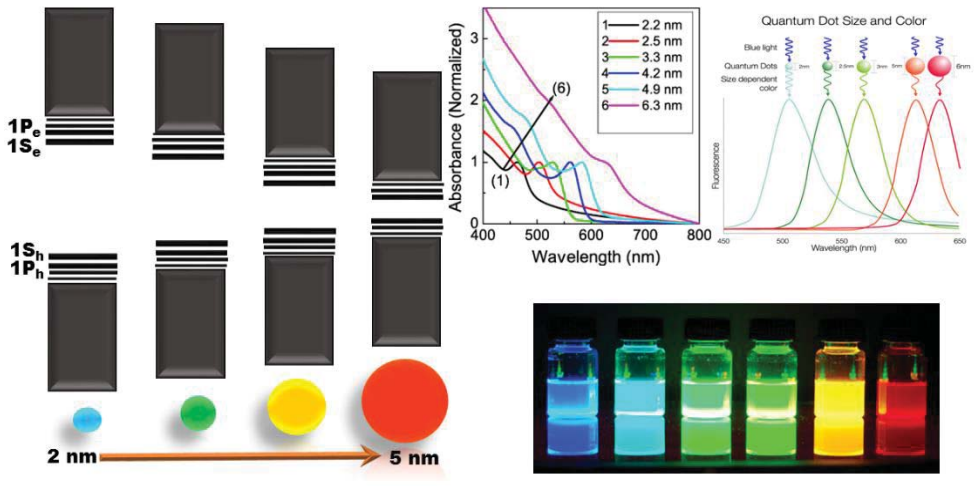

Figure 1.7 *Schematic Representation of quantum confinement effect, decrease in band gap due to increase in size, absorption and fluorescence spectra of different size QDs and colloidal solution of different colored (size) QDs.*

Due to very small size of QDs, the electrons are confined in very small region (quantum box). When the radii of the QDs are smaller than the Bohr excitonic radius (the average distance between the electron (in conduction band)- hole (in the valence band) pair) there is quantization of energy levels (Fig. 1.7).

The phenomena of quantum confinement effect in semiconductor nanocrystals provide the band gap tunability by changing the shape and size of the nanocrystals [14, 15]. This yields the fascinating optoelectronic properties to the semiconductor QDs. The recent decades have been devoted to extensive research activities involved in synthesis and applications of QDs.

1.5. Electronic Structure of QDs

QDs possess unique photo physical properties which directly depend upon the band gap and hence on the size of the QD. In last two decades, various researchers have put lots of efforts to synthesize QDs of different sizes and shapes having different band gaps and observed their photo physical properties [14-18]. As already mentioned, in the bulk semiconductor materials the valence band and conduction band are separated by a forbidden gap which is called energy band gap (E_g). By photoexcitation process, a photon having energy, $h\nu \geq E_g$ transfer an electron from the VB to the CB and create a hole in the VB. Due to coulombic attraction, these electron and hole can't move independently and form an electron-hole pair (Exciton) [7]. Decrease in particle size eventually leads to a condition in which the crystal dimension becomes smaller than the exciton radius. In such a case, QDs accept higher kinetic energy which leads to the augmentation of the gap and confinement of the energy levels in discrete values. This phenomenon is termed as "*quantum confinement*" [11]. Due to decrease in diameter the continuous band structure becomes discrete levels structure (Fig. 1.7).

The correlation between the radius of the particle and the band gap energy (E_g) for semiconductor nanocrystals was proposed by Brus [10] using the spherical particle approximation as:

$$E_g = \mathrm{E}_\mathrm{g}^{\mathrm{bulk}} + \frac{\hbar^2\pi^2}{2r^2}\left(\frac{1}{m_e^* + m_h^*}\right) - \frac{1.8\mathrm{e}^2}{4\pi\varepsilon\varepsilon_0}\frac{1}{\mathrm{r}} \qquad (1.2)$$

We can also write,

$$E_g = \mathrm{E}_\mathrm{g}^{\mathrm{bulk}} + \frac{h^2}{8r^2}\left(\frac{1}{m_e^* + m_h^*}\right) - \frac{1.8\mathrm{e}^2}{4\pi\varepsilon\varepsilon_0}\frac{1}{\mathrm{r}} \qquad (1.3)$$

Where, $\mathrm{E}_\mathrm{g}^{\mathrm{bulk}}$ corresponds to the band gap energy of the bulk crystal, the second term corresponds to the quantum confinement calculated following the hypothesis of spherical potentials in which electron and hole of effective masses m_e^* and m_h^* respectively are confined. $\hbar$ is the reduced Planck's constant (Planck's constant h/2π, h=6.62607x10^{-34} Js). The third term is for the coulombic interaction between the electron and the hole, ε is the dielectric constant of the material relative to the dielectric constant of the vacuum (ε_0 = 8.854x10^{-12} F/m). Bohr radius of an exciton (r_B) is the physical distance that separate an electron-hole pair. This distance depends upon the materials of the semiconductor and hence varies for various semiconductors. The Bohr radius r_B can be calculated by applying the Bohr hydrogen atom model to the semiconductor nanocrystals [19a].

$$r_B = \frac{\hbar^2\varepsilon}{e^2}\left(\frac{1}{\mathrm{m}_\mathrm{e}^*} + \frac{1}{\mathrm{m}_\mathrm{h}^*}\right) \qquad (1.4)$$

The broadness of the band can be given by –

$$\Delta E_{g\,(\mathrm{QDs})} = \frac{h^2}{8r^2}\left(\frac{1}{m_e^* + m_h^*}\right) - \frac{1.8\mathrm{e}^2}{4\pi\varepsilon\varepsilon_0}\frac{1}{\mathrm{r}} \qquad (1.5)$$

The modified form of equation 1.2 can be written is

$$E_{g(QD)} = E_{g(bulk)} + \frac{\alpha}{d^2} \quad (1.6)$$

where α is a constant and has a value of 3.7 eV-nm^2 for CdSe. d is the particle size. $E_{g(bulk)}$ is 1.74 eV for CdSe and $E_{g(QD)}$ can be obtained from Tauc plot [19b]. Equation 1.6 is known as modified Brus equation. The other equation which is widely used for the calculation of particle size is Peng equation. For CdSe nanocrystals it can be given as follows:

$$d= (1.6122\times10^{-9})\lambda^4-(2.6575\times10^{-6})\lambda^3+(1.6242\times10^{-3})\lambda^2-(0.4277)\lambda+(41.57) \quad (1.7)$$

In equation (1.7), d (nm) is the size of a given nanocrystal sample, and λ (nm) is the wavelength of the first excitonic absorption peak [19c]. Various parameters for the bulk II-VI semiconductor materials at room temperature has been listed in table 1.1 [20].

Table 1.1 Physical properties of some II-VI semiconductor.

Material	Crystal Structure	Eg (eV) (bulk) at 300 K	m_e^*	m_h^*	e_r	r_B (nm)
ZnO	Wurtzite	3.4	0.26	0.60	8.2	2.4
ZnS	Zinc Blende	3.6	0.28	0.61	8.9	2.5
ZnSe	Zinc Blende	2.6	0.16	0.75	8.7	3.6
CdS	Wurtzite	2.4	0.20	0.70	8.8	3.0
CdSe	Wurtzite	1.7	0.12	0.45	9.5	5.4
CdTe	Zinc Blende	1.5	0.10	0.40	7.2	4.8

Choosing suitable combination of semiconductor materials, the band gap energy of semiconductor QDs can be tuned from UV to the NIR. Theoretical band gap Eg (eV) and corresponding wavelength (nm) of different semiconductor material is shown in Fig. 1.8 [20].

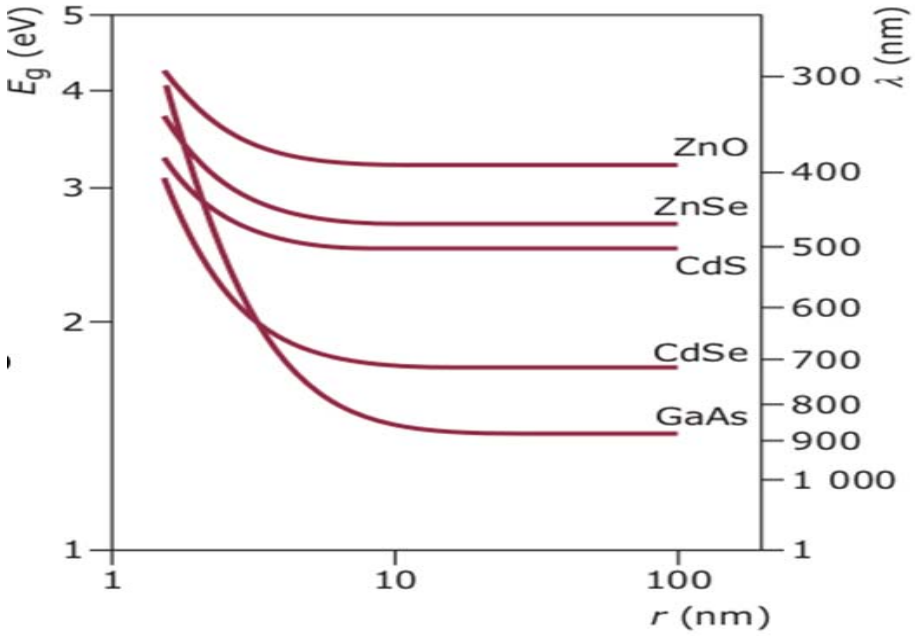

Figure 1.8 *Change in band gap with radius of QDs and theoretical variation of the band gap with radius of the QDs for different semiconductor materials using equation (1.2).*

1.6. Photophysical properties of QDs

1.6.1. Absorption and photoluminescence

As we have mentioned earlier that an important feature of semiconductor is the band gap, which separates the valence band and conduction band. When a semiconductor is exposed to light an electron is promoted from the valence band to the conduction band leaving behind a hole in the valence band. When these two charge carriers (electron and hole) recombine or the electron comes back to the valence band radiatively, it emits light. The wavelength of absorbed and emitted light is determined by the band gap width of the semiconductor. In a bulk

semiconductor, the density of states of the valence and the conduction band is essentially continuous (density of states of a system is defined as the no. states per interval of energy at each level available to be occupied). In a strongly confined system (i.e. in QDs), the three dimensional confinement modifies the Hamiltonian, a potential that determine the location of electron and hole in the system. This forced spatial overlap results in a discrete density of states [21] (Fig. 1.9).

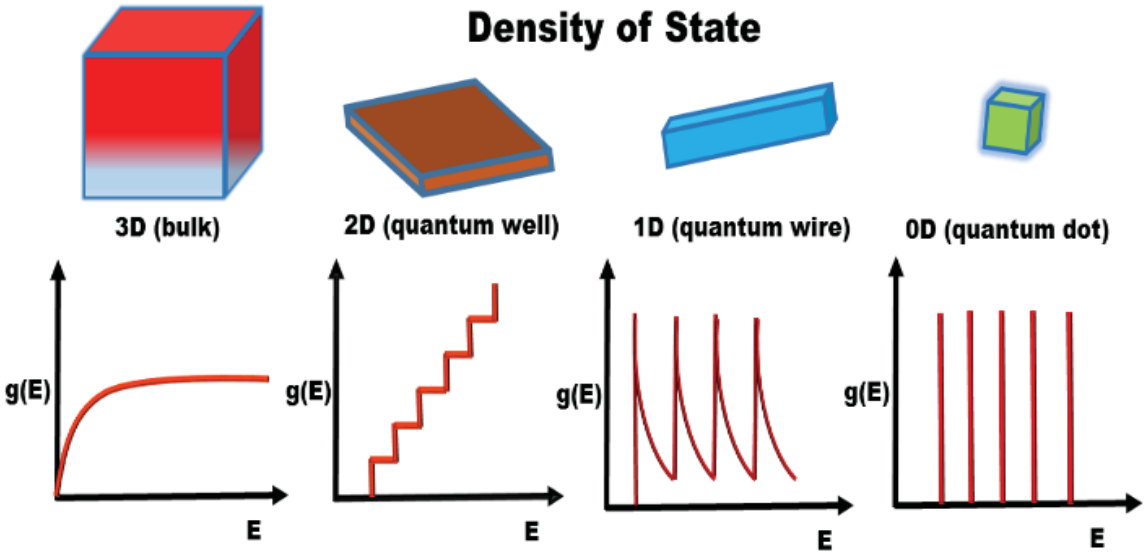

Figure 1.9 *Schematic diagram illustrating the electronic density of states depending on dimensionality.*

The position of these states and therefore the absorption spectrum depends upon the spatial confinement of exciton, which is determine by the dimension of the nanocrystal. This confinement can be described using the particle in a box model [22]. The energy level of the quantum confined semiconductor nanocrystal can be defined using two schemes. One is modelled like a bulk system in which electron and hole are separate as shown in Figure 1.10a & b. The other one is mapped onto the different states of exciton (ground-g, exciton-e, bi exciton-b, tri exciton-t) (Fig. 1.10c). The absorption spectrum of a textbook bulk semiconductor shown in Fig. 1.10d is continuous except a step-function-like increase in the

absorption cross section at the band gap energy. But in a strongly confined semiconductor system, the confinement changes the continuous energy band of bulk semiconductor into discrete exciton energy levels. These exciton energy levels produce peaks in the absorption spectrum as shown in Fig. 1.10e. The absorption of light primarily populates the exciton states. After the excitation, the excited state may decay radiatively or non-radiatively. A portion of excitons relaxes via radiatively which is called photoluminescence (Pl). The portion of adsorbed light which is reemitted as Pl in strongly confined nanocrystals depends strongly on the nature of surface (surface trap state) and intrinsic crystal structure and its imperfection (deep trap state) as shown in Fig. 1.10f [23-28].

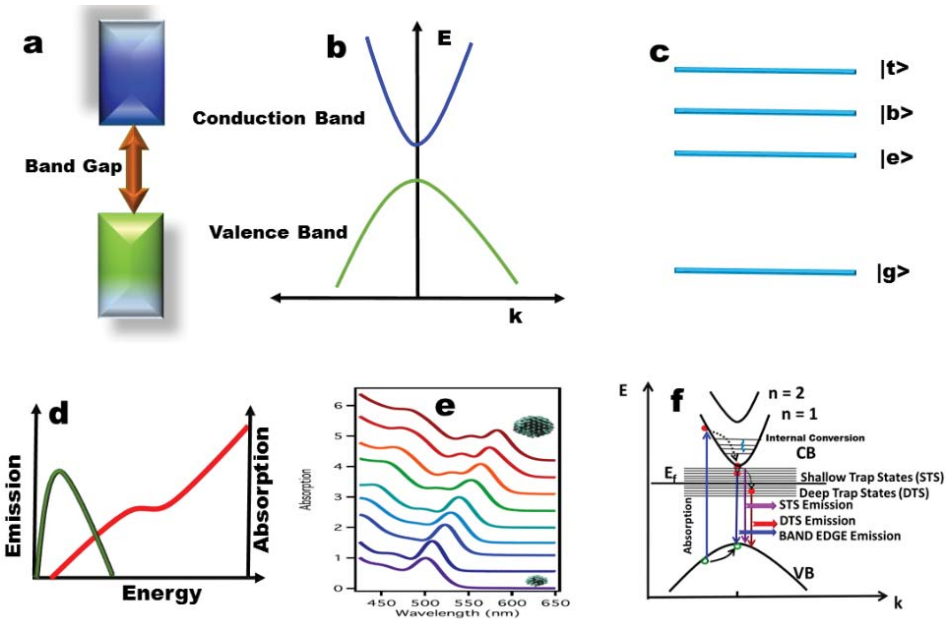

Figure 1.10 *Representation of photo physics of semiconductor both bulk and quantum confined- (a) and (b) corresponds to bulk system, (c) corresponds to quantum confined system, (d) absorption and emission spectra of bulk, (e) absorption spectra of quantum confined system with increase in size and (f) absorption and different emission channel in QDs.*

A nanocrystal has a large percentage of atoms on its surface and atoms at the surface are part of incomplete unit cell resulting in dangling bonds. Some of these surface atoms bind with the organic ligands which suspend the nanoparticles in the solution. However, not all the

surface atom bind which results in the trapping of electron or hole on the surface atoms after photoexcitation. This trapping of the excited charge carriers mainly serves to quench the Pl. So, by surface passivation of QDs with suitable ligands supress the trapping of charge carriers and enhances the radiative recombination of electron and holes resulting in increase in the Pl quantum yield [25]. However, not all the surface state leads to trapping of charge carriers but some of them promotes the electron and hole to recombine with lower energy, resulting in the broadening of emission spectrum.

1.6.2. Photoluminescence (Pl) lifetime of QDs

Compared to the conventional organic dye which have a Pl lifetime of 1-10 ns, QDs have comparatively longer lifetime typically from 10-100 of nanoseconds. One major difference between the dye and the QDs is the decay kinetics. Dyes are known to follow typical mono exponential decay kinetics while QDs follow the complicated bi or multi exponential decay kinetics depending upon the size, surface, wavelength and time [27]. The presence of the surface and deep trap states hinders the relaxation of excited charge carriers resulting in the increase of Pl life time of QDs [28].

1.7. Classification of QDs

On the basis of constituent materials, QDs can be can be classified as follows:

1.7.1. Core QDs

QDs of single component materials with uniform internal composition are classified under core QDs (Fig. 1.11a). Examples of these types of QDs are the chalcogenides of different metals

like CdS, CdSe, ZnSe, CdTe etc. The physical and electronic properties of these QDs depends upon the constituent metal and chalcogens and can be tuned by tuning the size of the QDs.

1.7.2. Core-Shell QDs

The QDs consists of exterior coating (shell) on the surface of the core QDs by another QD of wider band gap (Fig. 1.11b) are called as core-shell QDs (CSQDs) or core-shell semiconducting nanocrystals (CSSNCs). Coating of core QDs with shell of higher band gap improves its Pl quantum yield by passivating the non-radiative recombination surface sites. The photo physical properties of core-shell QDs depends upon the materials and the thickness of the shell along with the materials and size of the core. For example- QDs with CdSe in core and ZnSe in shell available in Sigma Aldrich brand have Pl quantum yield of around 80 %.

1.7.3. Alloyed QDs

Alloyed QDs are synthesized by alloying two or more semiconductors with different band gap energies (Fig. 1.11c). Alloyed QDs exhibit different properties not only from the bulk form but also from their parent semiconductors. In this way, the alloyed QDs possess unique and additional compositional characteristics due to quantum confinement effect that can be tuned by changing the size and composition of the alloyed QDs.

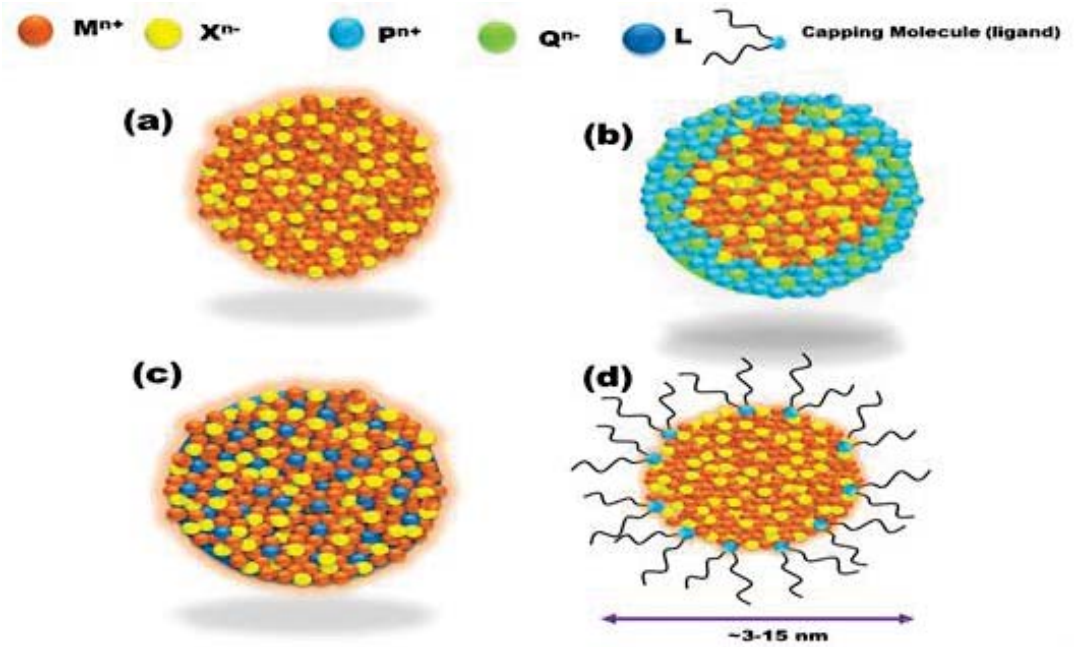

Figure 1.11 *Different types of QDs- (a) Core QDs (MX), (b) Core-shell QDs (MXPQ), (c) alloyed QDs (MLX) and (d) Core QDs surface passivated with ligands.*

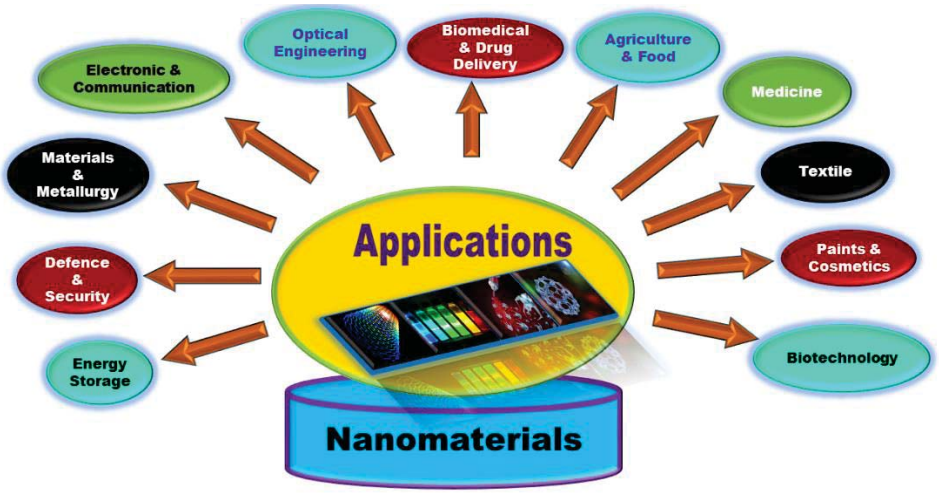

Figure 1.12 *Applications of nanomaterials in diverse arena.*

1.8. Applications of Nanomaterials/QDs

Nanomaterials possess unique advantageous chemical, physical and mechanical properties. The broad absorption spectra with high absorption coefficient, narrow emission

with high quantum yield, resist to photo bleaching, emission throughout the ultraviolet to infrared wavelength with band gap tunability are the remarkable properties of QDs which make it potential candidate to be used in various fields (Fig. 1.12).

QDs are extensively used in the following areas.

1.8.1. LEDs (Light Emitting Devices)

After conventional LEDs and organic LEDs (OLED), QDs LEDs (QLED) are widely used nowadays. The introduction of QDLED marks critical step in reducing the cost of LED production and improved colour reproduction. The advantage of QDs in using as LEDs is the emission colour which can be tuned by changing the QD size and the narrow emission profile provides spectral purity [29]. In addition to that QLEDs can also be made thin, compact and flexible. QLEDs are available in different colour like yellow, red, blue, green and white [30-32].

1.8.2. Photovoltaics

The simple synthesis procedure, sensitivity to diffused light, tunable absorption and emission spectrum and high absorption cross section of QDs enable it to be used as light harvesting material in photovoltaic [33]. The ability of multi exciton generation (MEG) of QDs is very crucial for enhancing the efficiency of solar cell. QDs are used in different generation solar cell like QDs only solar cell, QDs in hybrid solar cell and QDs with nanowire in solar cell to successively increase the efficiency of the solar cell [34].

1.8.3. Photodetectors

The size tunable electronic structure of QDs drive the unique opportunity for the infrared detection. For application requiring light absorption and emission in near-IR region, semiconductor QDs with narrow band gap like- PbS, PbSe and HgTe etc. are very useful because their band gap can be precisely tuned from visible spectral region to 3500 nm region [35,36].

1.8.4. Sensors

The quantum confinement and large surface to volume (S/V) ratio make QDs suitable sensor with very low limit of detection. QDs have been used as chemical sensor for different chemical species like - Ammonia, hydrazine, hydroxyl amine and for different heavy and toxic metal ions [37, 38]. QDs offers rapid, efficient, cost effective, simple and selective sensing of analytes as compare to other methods [37].

1.8.5. Photocatalyst

QDs are very important in photocatalysis and used in light driven splitting of water into hydrogen and oxygen [39, 40]. Hydrogen generation is the need of hour to fulfill the energy demand of exponentially growing population. In photocatalysis, electron-hole pair formed upon photoexcitation in QDs accelerate the redox processes in the surrounding. The photocatalytic activity of QDs depends upon its size and degree of quantum confinement because the band gap, which depends upon the size of the QDs determine the stored chemical energy in the excited state of the QDs [41]. The capping molecules or ligand interfere the catalysis by slowing down the electron transfer process.

1.8.6. Bio-imaging

One of the most important application of QDs is in imaging of biological systems. The prerequisites for the imaging of biological system is – aqueous dispersibility, non-cytotoxicity, photo stability, large stokes-shift, narrow emission, high emission quantum yield (QY) and long life time (hundreds of nanosecond) [42]. QDs capped with biomolecules reduces the cytotoxicity. These properties of QDs offer high resolution three dimensional images. The real time tracking of molecules and cells for longer time period is also possible because of its extraordinary photo stability [43]. Peptides, DNA, antibodies and small molecule as ligand can be used to target QDs to specific protein or cell [43].

1.8.7. FRET based studies

FRET (Forster Resonance Energy Transfer) based processes with QDs are very important because it gives significant information about the environment around the QDs and the size of the molecules. QDs based FRET is the key to probe specific biological processes [44]. Compared with conventional FRET, quantum dot mediated FRET is advantageous because of their unique photophysical properties such as size tunable, narrow emission spectra but broad excitation spectra, strong signal intensity, high photo stability, and good biocompatibility [44]. Large extinction coefficient and spectral purity make QDs eligible to act as superior fluorophore. The broad absorption and narrow emission of QDs make them a suitable donor with organic dye as acceptor [45].

1.9. Cytotoxicity of QDs

Although, QDs offer potentially invaluable application, they also possess risk to human life and environment. QDs are inherently cytotoxic in nature which is the intrinsic properties

of the size and surface chemistry of QDs [46]. Apart from that oxidation, photolysis, the environment and mechanical instability of QDs are also the determining factors of cytotoxicity of QDs [47, 48]. The inherent cytotoxicity of QDs limits their use in biomedical applications. QDs in even very low concentration can exert toxic effect on microorganism leading to DNA damage and protein degradation. In CdSe QDs both Cd and Se are known to induce the generation of reactive oxygen species (ROS) causing apoptosis [49-51]. Nevertheless, by stabilizing the core of a QD with a shell such as ZnS and with a capping agent on the surface of QD can reduce or completely suppress its cytotoxicity. Systematic assessment of cytotoxicity caused by QDs is of critical importance for use of these QDs in biological applications. Various researches have studied the QDs cytotoxicity in details. It has been shown that surface oxidation of QDs led to the formation of reduced Cd on the QD surface and liberate free Cd ions, which causes the cell death [49]. Shiohara et al. have revealed that the cytotoxicity is caused by the functional group of surface capping molecules (-NH_2, -COOH) along with the inorganic core of QDs [52]. Parak et al. have demonstrated that in addition to the release of Cd^{2+}, ions from the surface of the QDs, precipitation of QDs on the cell surface also causes damage to the cells [53]. They further proposed that QDs ingested by the cell causes more cytotoxic effect than QDs only present in the surrounding of the cell. These studies are very useful to understand the mechanism and assessment of cytotoxicity of QDs.

1.10. Synthesis of Nanomaterials

The common goal of scientific community is to explore all the possibilities to synthesize nanomaterials with unique physical, chemical, mechanical and optical properties. There are various methods used for the synthesis of the nanomaterials. In general, it can be divided into three groups- (i) physical methods, (ii) chemical methods and (iii) bio-assisted methods (Fig. 1.13). Broadly, these nanomaterials can be synthesized by adopting two approach.

(i) Top down approach- size reduction from bulk material (Physical methods).

(ii) Bottom up Approach- material synthesis from atomic level (Chemical & Biological method).

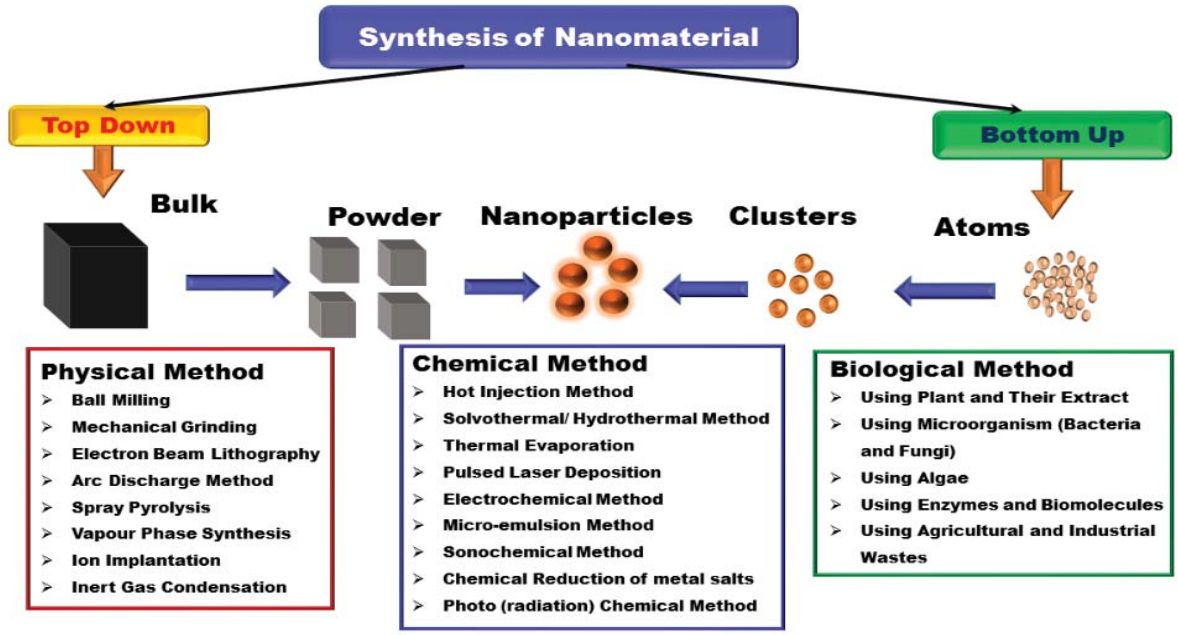

Figure 1.13 *Scheme for top down and bottom up approach and various methods of synthesis.*

1.10.1. Physical method (top down approach)

It typically includes solid state processing of materials. This route is based on the principle to make the bulk material smaller (of nm size) by breaking up larger particles using physical processes like-grinding, crushing or ball milling. This method has certain shortcomings like- huge amount of energy is required in synthesis and difficult to achieve very small and homogeneous particle size [54]. The biggest problem with this method is the imperfection of surface structure which has significant impact on the physical properties and chemistry of the nanomaterials. Examples of top down approach are- high energy ball milling, lithography, gas condensation, severe plastic deformation etc [54].

1.10.2. Chemical method (bottom up approach)

Bottom up approach involve buildup of materials from bottom i.e. from atom-by-atom, molecule-by-molecule or cluster-by-cluster. This method offers uniform size distribution and better size and shape control. It mainly covers the chemical and biological synthesis. This method offers precise control of the reactions to inhibit further particle growth [54]. Synthesis of nanoparticles of desired particle size, shape, morphology, purity and quality employing environmental friendly and economic processes has always been a challenge for the scientists and researchers [55]. The choice of synthesis technique can be lynchpin in determining efficiency and cost effectiveness of the material. Bottom up approach mainly involve vapor phase fabrication and liquid phase fabrication. There are several synthesis techniques involved liquid phase fabrication. Here we restrict our discussion to Chemical synthesis of nanomaterials involved the bottom up approach in liquid phase. These synthesis techniques can be described as follows:

(i) Hot injection method

(ii) Solvothermal/Hydrothermal method

(iii) Thermal evaporation method

(iv) Pulsed laser deposition.

(v) Template assisted electrochemical deposition.

(vi) Room temperature chemical method.

(vii) Photochemical method.

(viii) Radiation chemical method.

The above mentioned methods are generally used to synthesize nanomaterials. These methods have their own advantages and disadvantages which are explained in table 1.2. Except normal

chemical method, photochemical and radiation chemical methods of synthesis of nanomaterials, all the other methods involve high temperature, high pressure or vacuum and harmful chemicals. Also, these methods require specific laboratory arrangement.

In this thesis, we have adopted the photochemical, radiation chemical and room temperature chemical reduction method to synthesize CdSe QDs and studied its optical and electronic properties and the mechanism of synthesis involved. A brief description of the above these three methods is mentioned below.

Table 1.2 Comparison of various methodology used for nanomaterial synthesis**.**

Synthesis Methodology	***Experimental Requirement***	***Pros***	***Cons***
Hot Injection [56]	➢ High temperature ➢ Inert atmosphere ➢ Specific chemicals	➢ Instant nucleation ➢ Narrow size distribution ➢ Good control on particle size ➢ High temperature so good quality of crystal	➢ Expensive and poisonous chemicals ➢ Difficult to scale up
Solvothermal/ Hydrothermal [57]	➢ Autoclave ➢ High temperature ➢ High pressure ➢ Black Box	➢ One step process ➢ Minimize energy consumption ➢ Closed systems, low environmental impact ➢ Products with much higher homogeneity ➢ Better control over product ➢ Versatile method	➢ Need of Expensive Autoclave ➢ Safety issue during the reaction ➢ Impossible to observe reaction process ➢ Involvement of high temperature and high pressure
Pulsed Laser Deposition [58]	➢ High Power Laser set up ➢ High Vacuum and high temperature ➢ Ar or Ne for inert atmosphere	➢ Capable of high deposition rate ➢ Film of variable thickness can be deposited	➢ High temperature ➢ Low quality of materials deposited ➢ Not a versatile method

	➢ Special laboratory with proper cooling system	➢ Better stoichiometric control	
Thermal Evaporation [59]	➢ Very high temperature ➢ Inert gas atmosphere ➢ Special Laboratory consists of gas delivery system, reactor chamber, energy source, exhaust system etc.	➢ Can be used for wide range of materials ➢ Better control in thickness and morphology ➢ Versatile ➢ High purity objects are possible ➢ More environment friendly	➢ High capital cost ➢ Appropriate cooling system ➢ Slow and time consuming process and difficult to scale up
Template Assisted Electro-deposition [60]	➢ Electrochemical cell ➢ Substance to prepare templates	➢ Low cost and easy to fabricate ➢ Versatile technique to synthesize nanomaterials of desired morphology	➢ Preparation of template is cumbersome ➢ Properties of nanomaterial is highly influenced by the surface characteristics of the electrode surface
Chemical Reduction [61]	➢ Normal temperature and pressure ➢ Suitable reducing agent e.g. $NaBH_4$, citric acid etc.	➢ Involvement of ambient conditions ➢ No specific laboratory is required ➢ Less energy consumption	➢ No control over size and morphology of nanoparticles ➢ Involvement of harmful reducing agents
Photochemical [62]	➢ ➢ Light source (UV, visible or IR) ➢ Normal temperature and pressure	➢ Less energy consumption ➢ Minimal use of potentially harmful chemicals ➢ No need of specific instrument ➢ Requirement of ambient reaction conditions ➢ Large scale production is possible ➢ Environment friendly ➢ Low concentration of precursor is required	➢ No control over size and morphology of nanoparticles
		➢ Low energy consumption	➢ Specific radiation source ➢ Radiation handling

Radiation Chemical [63]	➢ Radiation source like- γ rays, electron beam etc.	➢ Minimal use of potentially harmful chemicals ➢ Large scale production is possible ➢ Less time consuming ➢ Parallel Sterilization ➢ No harmful by product ➢ Synthesis at normal temperature and pressure ➢ Low precursor concentration is required	➢ Chances of radiation Exposure

1.11. Significance of synthesis of QDs in aqueous solution

The non-aqueous approach of synthesis of QDs, also called as TOP/TOPO capped or hot injection method was developed initially by Bawendi and co-workers in 1990s [12, 64]. This method is very effective for synthesizing good quality QDs with high QY. It is a non aqueous method involving organic solvents and high temperature which yields good quality of nanocrystals. But these non-aqueous QDs have several limitations like - these QDs are not ecofriendly, cost-effective and can't be used in biological applications without ligand exchange to make the QDs water dispersible [65]. On the contrary, aqueous based QDs have many advantages such as - (i) they are more environmentally benign, (ii) cost effective, (iii) excellent biocompatibility, (iv) potentially better scalability etc [66]. Along with all these attributes, aqueous based QDs can be specifically tailored for many applications by functionalize its surface easily. Better water solubility of these QDs brighten its chance to use in biological systems for bio imaging and bio labelling [67]. The aqueous compatibility of various biomolecules like- DNA, nucleic acids, proteins, amino acids enable them to be used in bio functionalization of the QDs for diverse applications in the field of biology and medicine [68, 69]. The versatile surface chemistry of aqueous based QDs brings new insights into its optical

properties and applications [66]. In optoelectronic applications like- photovoltaics, light emitting diodes, photocatalysis, photodetectors etc. the long chain of organic capping molecules hinder the charge separation and its transfer. So in all these fields, aqueous based semiconductor QDs have very important role to play. In terms of the formation mechanism involved, the aqueous based QDs have more complicated reaction mechanism because of more complex redox environment in aqueous solution (presence of H^+ and OH^- ions) [66]. So, fundamentals of synthesizing QDs in aqueous solution, understanding the mechanism of synthesis, characterization and application is very important study.

1.12. Photochemical synthesis

It is highly selective, energy efficient, rapid, facile and single step synthesis procedure [70]. This method does not require any external reducing chemicals and energy in the form of heat. Hence, the photochemical method offers a green alternative route of nanoparticle synthesis. In this method, a light sensitive molecule/ system in the form of solute is irradiated with light of suitable wavelength undergoes higher excited state and form transient radicals (Fig. 1.14) [71, 72]. These radicals are highly reducing in nature and reduces the precursor molecules which eventually form nanostructures. For example - photochemical generation of isopropyl radical ($(CH_3)_2C^{\bullet}OH$) in a reaction mixture of acetone and isopropanol upon photoirradiation with 300 nm light which is highly reducing in nature having $E^0 = -1.5$ V *vs.* NHE. $(CH_3)_2C^{\bullet}OH$ are generated when triplet excited state of acetone extract one H atom from the secondary carbon of isopropanol (Fig. 1.15) [73]. This method has been used by various researchers to synthesize metal and semiconductor nanoparticles and QDs of different size and shape [74-78].

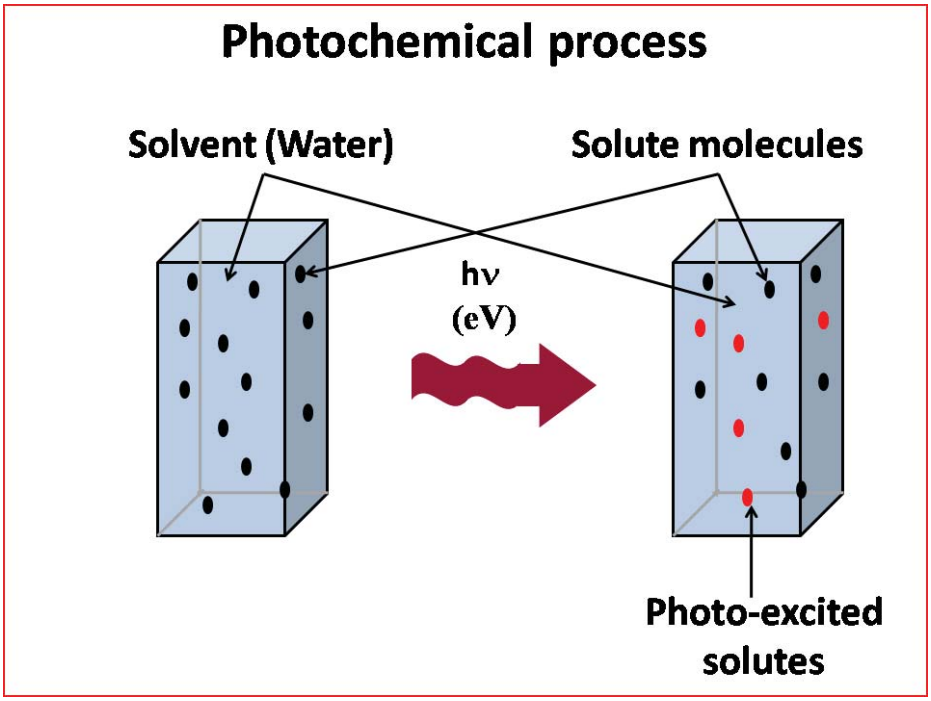

Figure 1.14 *Scheme for the processes involved in photochemical method.*

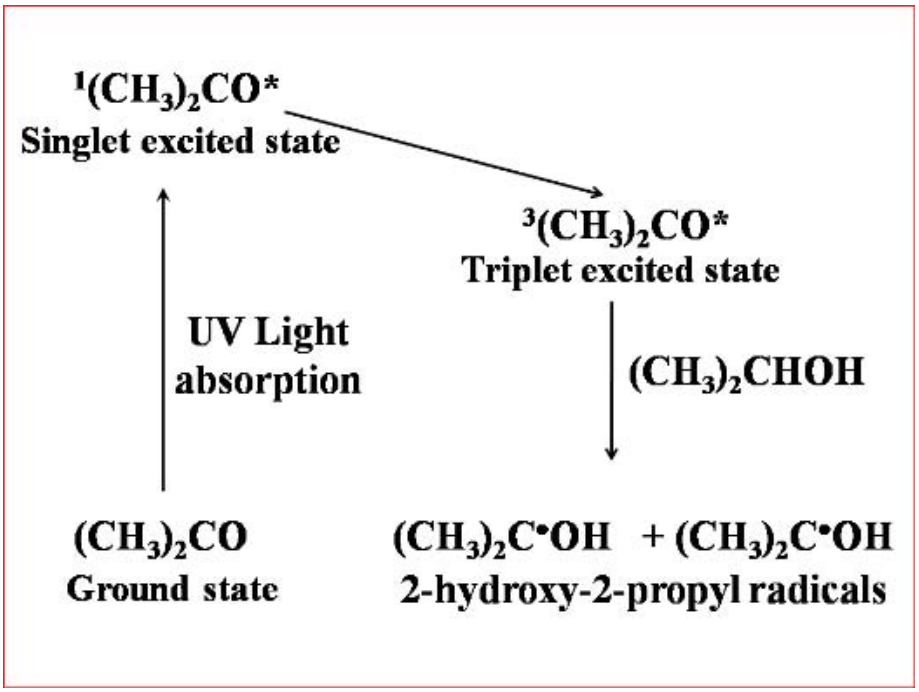

Figure 1.15 *Schematic representation for the photochemical formation of 2-hydroxy-2-propyl radicals.*

1.13. Radiation chemical synthesis

The use of ionizing radiation from particle accelerator and radioisotopes to synthesize nanoparticles has many advantages like- (i) minimal energy consumption, (ii) rapid, (iii) less use of harmful chemicals, (iv) simple production scheme, (v) *in situ* sterilization if required. (vi) low concentration of precursor is required etc. [79]. Radiation induced synthesis can be carried out in aqueous solution which minimizes the use of organic solvents and hence the tedious separation, purification and characterization processes can be avoided. In addition to these advantages, controllable and flexible irradiation process parameters, provide extra edge to this method.

1.13.1. Radiation Chemistry and Radiolysis of Water

Radiation chemistry involves the study of interaction of particles or electromagnetic radiation with sufficient energy with a system which upon absorption of particles or radiation causes multiple ionizations. The absorption of ionizing radiation in a given material depends upon the type of radiation and its energy. The heavy charged particles exhibit stronger interaction with matter than the light charged particles. For photons, the interaction is even weaker than the light charged particles. The important difference between the charged particles and photons is that; particles of given energy has a given penetration depth in a given material while the absorption of photon follows an exponential function (Lambert Beer's law) and the penetration depth cannot be strictly defined. The penetration depth is one of the important parameter in radiation chemistry. A large penetration depth is required for the radiation processing of the bulk materials while for the surface modification of the materials small penetration depth is sufficient. The radiation energy absorbed per unit mass in a system is termed as absorbed dose and its SI unit is Gy (1 Gy=1 J/kg). The absorbed dose per unit time is referred to as the dose rate. Both the absorbed dose and dose rate are important parameter in radiation chemistry. For

charged particles and photons, energy is mainly transferred to the electrons of absorbing material and so the stopping power of a material is directly proportional to its electron density. To summarize, the absorption of ionizing radiation results in excitation and ionization of the material.

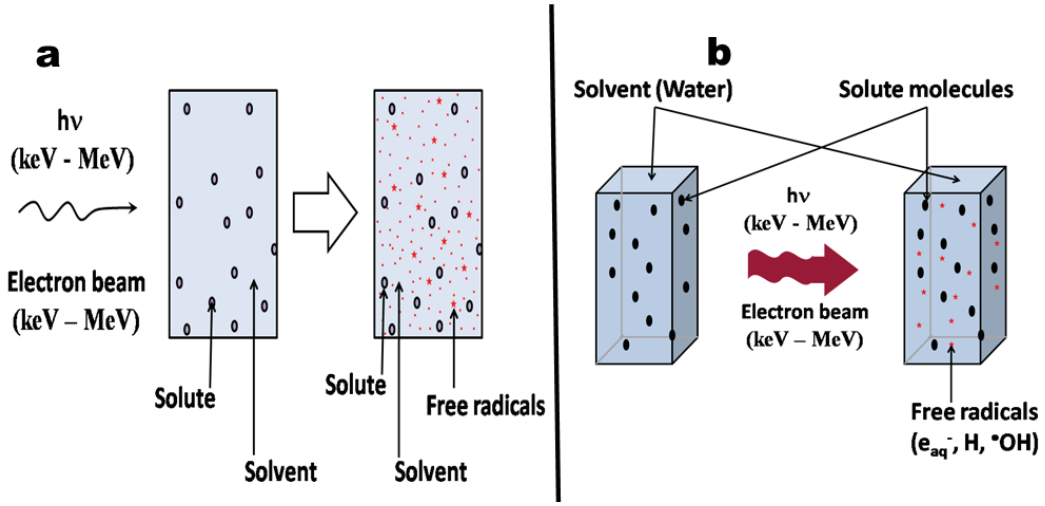

Figure 1.16 *Scheme for the process involved in (a) radiation chemical methods and (b) radiolysis of water.*

Radiation induced changes illustrated by the chemical are quantified by the term radiation chemical yield (G-value). The G-value is defined as "The number of moles of given species produced or consumed upon absorption of 1 J of radiation energy (molJ^{-1})" [79]. Earlier, number of molecules per 100 eV of radiation energy absorbed was frequently used. The radiation chemistry primarily starts from the radiolysis of water because the concentration of water molecules is higher than any other species so, the radiation predominantly interacts with the water molecules. As a result of this interaction, within femtosecond time scale the ionization and excitation of water molecule takes place followed by rapid fragmentation in form of homolysis and deprotonation. The fragments are free radicals that recombine to yield more stable molecular products. The concentration of molecular products depends upon the

type of radiation e.g.- heavier charged particles like proton and alpha particles have short penetration depth and deposit their energy in small volume (spur) resulting in higher number of excitation and ionization in small volume which increases the recombination probability of radicals and hence yield of molecular products. In contrast, gamma radiation and electron beam produces lower amount of recombination products and large number of radicals and ions. The ionization and excitation processes at various time scale and primary products of radiolysis of water by electron beam or γ rays are shown in Fig. 1.17.

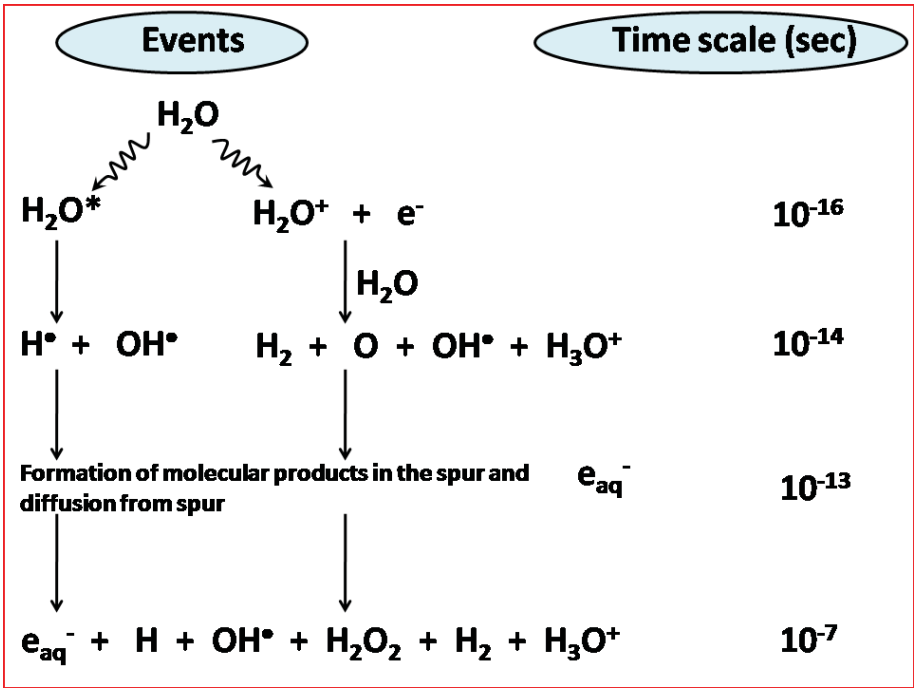

Figure 1.17 *Reaction scheme for radiolysis of water and products formed at different time scale.*

Out of these primary products, $OH^{\bullet}$, $H^{\bullet}$ and $e^{-}_{aq.}$, $OH^{\bullet}$ are oxidizing whereas, $H^{\bullet}$ and $e^{-}_{aq.}$ are reducing in nature (table 1.3) [80]. So, selectively redox conditions can be controlled by adding suitable solute which acts as radical quenchers. For example- $OH^{\bullet}$ is quenched by adding tert-butanol to the reaction mixture [81]. Tert-butanol reacts with $OH^{\bullet}$ according to following reaction.

$OH^{\bullet} + (CH_3)_3COH \longrightarrow (CH_3)_2CH_2{}^{\bullet}OH + H_2O$ $(k=6x10^8\ M^{-1}s^{-1})$ (1.8)

Similarly, to convert the aqueous medium purely oxidizing, the medium is saturated with N_2O. N_2O rapidly reacts with $e^-_{aq.}$ as follows:

$e^-_{aq} + N_2O \longrightarrow N_2 + OH^{\bullet} + OH^-$ $(k= 9.1x10^9\ M^{-1}s^{-1})$ (1.9)

In this way, the yield of $OH^{\bullet}$ get doubled in the solution and a purely oxidizing condition is achieved [83].

Table 1.3 Chemical properties of the primary products of radiolysis of water [82].

Properties	e^-_{aq}	$H^{\bullet}$	$OH^{\bullet}$
Absorption Maximum (nm)	720	<200	~225
Extinction Coefficient	19000 (720)	1620 (188)	540 (188)
Charge	-1	0	0
Radiation Chemical Yield (μMJ^{-1}) pH 7	0.264	0.055	0.273
Standard Reduction Potential	-2.8	-2.1	1.77

1.13.2. Radiation Chemistry as a tool to synthesize semiconductor nanoparticles and QDs

Semiconductor nanoparticles and QDs can be synthesized by several methods in aqueous medium. The advantage and disadvantage of these methods have been discussed in earlier section of this chapter. The standard process involved in the synthesis is to reduce the precursors of metals to lower oxidation states which reacts with the counter ions to give the corresponding nanoparticles. The radicals produced upon the radiolysis of water are strong

reducing agents so they can easily reduce the precursors to form nanoparticles. The shape, size, morphology and hence the properties of these QDs can be tunned by modifying the dose as well as dose rate [83]. Radiation induced synthesis provide a green, facile and rapid alternative to synhtesize nanoparticles in aqueous solution.

1.14. Room temperature synthesis

Room temperature synthesis method is a soft chemical route that does not require organometallic precursors or any complicated instrumentations [84]. This method requires a complexing agents like- ammonia, ethylene diamine etc. for the slow release of precursor molecule, reducing agents like- sodium borohydride, citric acid, ascorbic acid, L-cysteine, thioglycolic acid etc. for the initiation of the reaction and a capping/surface passivating agent to control and truncate the growth of the nanocrystal [85] (Fig. 1.18).

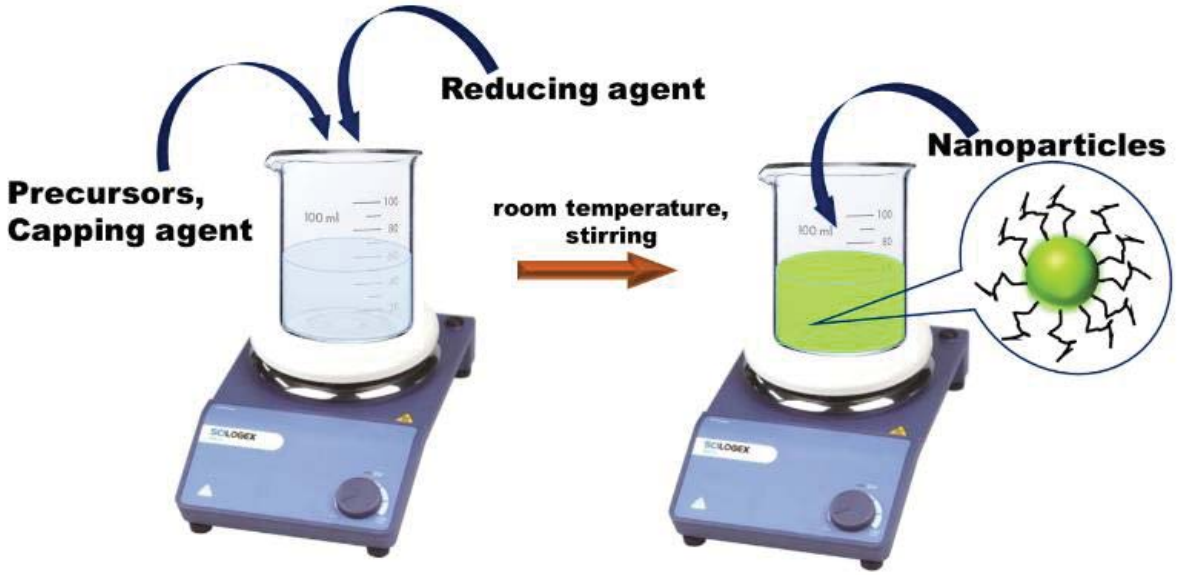

Figure 1.18 *Schematic representation for room temperature chemical method of synthesis of nanoparticles.*

This method is very facile, one-pot and rapid method for the synthesis of nanomaterials. In the radiation chemical and photochemical synthesis, very low concentration of the precursor is required whereas, in the room temperature chemical reduction method, relatively higher concentration of precursors is required. The shape and size of the nanomaterials can be controlled by controlling the concentration of precursors and concentration and rate of addition of reducing agents [86]. This method of synthesis has certain drawbacks like- sometimes the reducing agents used are expensive and toxic, need of extra capping agents and mediocre quality of the product etc. All these drawbacks can be vanquished by using suitable capping and reducing agent.

1.15. Kinetics and Thermodynamics of Growth of Nanoparticles

Kinetics of growth of nanoparticles can be explained by classical nucleation theory (CNT) [87]. CNT is the most common model to understand the formation of new thermodynamic phase such as solid or liquid. Nucleation is a process where the nuclei act as a template for the growth of the crystal. First, primary nucleation occurs without presence of any crystalline matter [88]. The primary nucleation is followed by secondary nucleation which can be homogeneous or heterogeneous nucleation. Homogeneous nucleation occurs when nuclei form uniformly throughout the parent phase, while heterogeneous nucleation forms at structural inhomogeneity. The process of homogeneous nucleation can be understood thermodynamically by looking at the total free energy of the nanoparticles which will be the sum of the surface free energy and the bulk free energy. For a spherical particle of radius r and surface energy γ and the free energy of the bulk crystal ΔG_v, the total free energy ΔG is given by equation (1.10) [89].

$$\Delta G = 4\pi r^2 \gamma + \frac{4}{3}\pi r^3 \Delta G_v \qquad (1.10)$$

The crystal free energy ΔG_v, itself depends upon temperature T, Boltzmann's constant k_B, the supersaturation of the solution S and its molar volume, v. ΔG_v is defined as:

$$\Delta G_v = -k_B T \frac{\ln S}{v} \tag{1.11}$$

The surface free energy always being positive and the crystal free energy always being negative so it is possible to find a maximum free energy which a nucleus will pass through to form a stable nucleus. By differentiating ΔG with respect to r and setting it to zero, i.e. dΔG/dr=0, we get critical free energy (equation 1.12).

$$\Delta G_{crit} = \frac{4}{3}\pi r_{crit}^2 = \Delta G_{crit}^{homo} \tag{1.12}$$

The critical radius r_{crit} is defined as

$$r_{crit} = \frac{2\gamma}{\Delta G_v} = \frac{2\gamma v}{k_B T \ln S} \tag{1.13}$$

This critical radius corresponds to the minimum size of the particle that can be sustained without redissloving in solution. In terms of free energy, there is a critical free energy corresponds to the critical radius (Fig. 1.19), which is required to attain stable particle in the solution [90].

The rate of nucleation of N particles during time t, is a very crucial parameter to control the shape, size and the properties of nanoparticles [91]. It can be described by an Arrhenius type equation given as:

$$\frac{dN}{dT} = A\exp\left(\frac{-\Delta G_{crit}}{k_B T}\right) \tag{1.14}$$

$$\frac{dN}{dT} = A\exp\left(\frac{16\pi\gamma^3 v^2}{3k_B^3 T^3 (\ln S)^2}\right) \tag{1.15}$$

From equation (1.11), three variables i. e.- supersaturation (S), temperature (T) and the surface free energy (γ) can be varied to control the rate of nucleation and hence the shape and size of the particles.

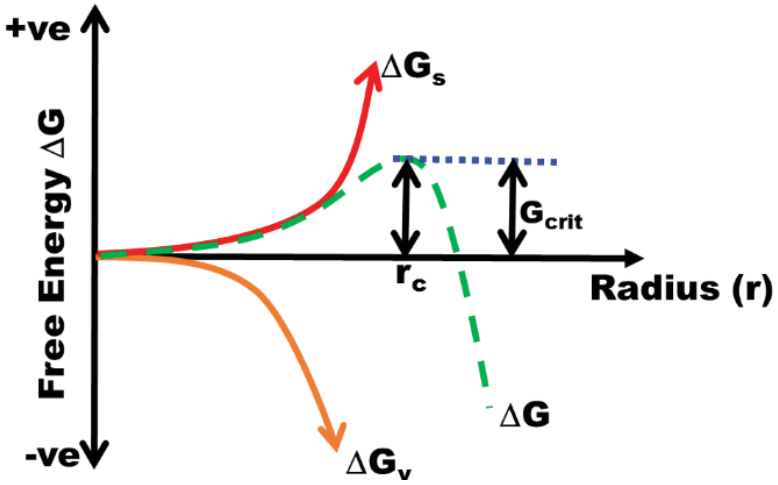

Figure 1.19 *Free energy diagram for nucleation explaining the existence of "critical nucleus''.*

The growth of the nanoparticles can be explained by LaMer model [92]. The LaMer model proposed that there is two-step process for growth of nanoparticles. The first one is nucleation and the second one is crystal growth. The process of nucleation and growth can be divided into three parts- (i) A rapid increase in the concentration of free monomer in the solute ion, (ii) The monomer undergoes "abrupt nucleation" which reduces the concentration of monomer in the solution, after this process no further nucleation takes place because of the low concentration of monomer after this point of time, (iii) Following nucleation, growth occurs under the controlled diffusion of monomers in the solution. These three stages of growth have been shown in Fig. 1.20, where the concentration of monomer is schematically plotted as a function of time. Due to the high solubility and surface energy of the smaller particles within the solution, they get redissolve and in turn allow the larger particles to grow even more. This process is termed as Ostwald Ripening [93].

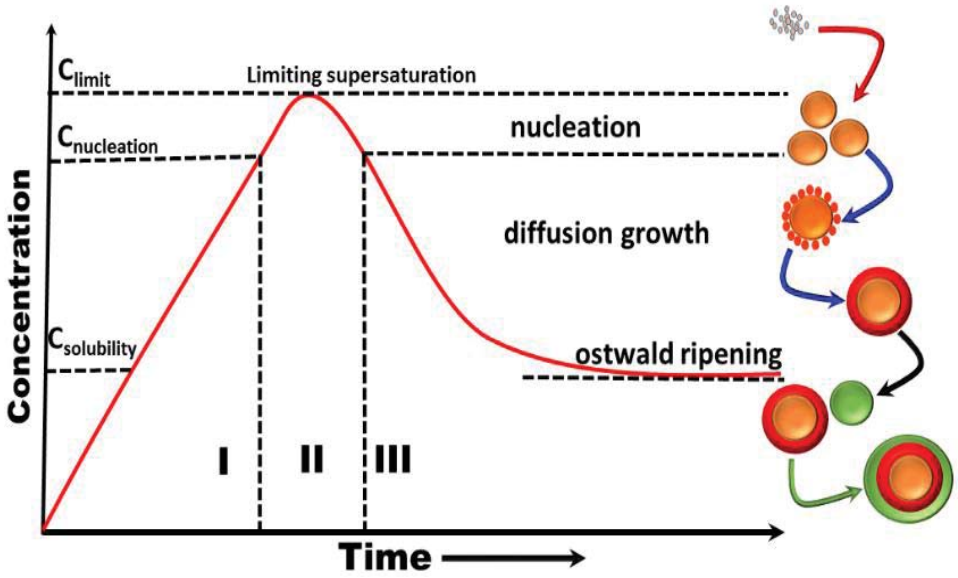

Figure 1.20 *LaMer model of growth of nanoparticles.*

1.16. Overview and scope of the thesis

The aim of this thesis is to synthesize CdSe QDs using radiation chemical, photochemical and room temperature chemical method. Further aim is to understand the processes and mechanism involved in the synthesis of these QDs capped with different molecules and to characterize and study the physical and optical properties of the synthesized QDs. Subsequently, explore possible application of these QDs in fluorimetric detection of heavy metal ions, study their fluorescence quenching mechanism.

In this thesis, we have demonstrated the synthesis of CdSe QDs in aqueous solution using photochemical, radiation chemical and green chemical synthesis at ambient conditions without using high temperature, high pressure and hazardous reducing agents. Various biocompatible molecules; e.g.- proteins like- L-cysteine, bovine serum albumin (BSA), saccharides like- fructose, glucose, sucrose, starch; and 1-thioglcerol has been used as surface passivating/ capping agent.

This thesis consists of six chapters. Chapter 1 and 2 are introductory while chapter 3, 4 and 5 contains the main part i.e. results and discussions of the thesis. In chapter 6, the overview of the thesis as well as future perspectives have been discussed.

In chapter 1, we have explained briefly about nanoscience and nanotechnology and its applications, nanomaterials and its classifications, various methods of synthesis of nanoparticles and their advantages and disadvantages, kinetics and thermodynamics of growth of nanoparticles. Further, we have explained about the semiconductor nanoparticles, their electronic structure, quantum confinement behaviour, photophysical properties, cytotoxicity, classification and applications in different areas. In the method of synthesis, we have elaborated the basics of radiation and photochemical processes and radiolysis of water and the advantages and disadvantages of these two methods and discussed in brief about the room temperature synthesis of nanomaterials. **In chapter 2,** we have discussed about the basics and working principles of different instrumentations involved in the synthesis and characterization of nanoparticles. The principles of pulse radiolysis, LINAC which is used as radiation source, Rayonet photo reactor which is used as UV source for the synthesis of nanoparticles has been discussed thoroughly. The basic principle and outline of the instruments used in characterization like-XRD, Raman, TEM, SEM, FTIR, UV-vis absorption spectrophotometer, steady state spectrofluorometer, Time Correlated Single Photon Counting (TCSPC) etc. has been also described in this chapter. **Chapter 3** is devoted for photochemical synthesis of CdSe QDs. In this chapter, we have discussed about the synthesis, optical properties and characterisation of CdSe QDs capped with L-Cysteine and starch, separately. The cytotoxicity of the L-cysteine capped QDs has also been studied. The starch capped QDs has been extracted from the colloidal solution and functionalised with thiourea. We have also study the application of the thiourea functionalized CdSe QDs in the fluorimetric detection of heavy metal ions. **In chapter 4,** radiation chemical synthesis of CdSe QDs has been discussed. CdSe QDs has been

synthesized using the *in situ* generated e^-_{aq} upon radiolysis of water as reducing agent in the presence of different saccharides like- fructose, glucose, sucrose and starch as the capping agent. The reaction mechanism of synthesis optical properties of the as synthesized QDs and their cytotoxicity has been studied. In different set of work, CdSe QDs has been synthesized using a series of secondary alcohol radicals as reducing agent. The dynamics of the reaction involved were studied using the pulse radiolysis technique. The optical properties of the QDs synthesized by these different alcohol radicals have also been studied. **Chapter 5** is dedicated for the room temperature chemical synthesis of CdSe QDs. In this chapter we have described about the green synthesis of CdSe QDs using BSA and 1-thioglycerol separately. Both the BSA and 1-thioglycerol acted as capping and catalysing agent in the synthesis. The optical properties of the BSA and 1-thioglycerol capped CdSe QDs have been studied. The decrease and increase in the Pl. intensity of BSA and CdSe QDs has been discussed on the basis of FRET theory. The reaction mechanism involved in the synthesis of 1-thioglycerol capped CdSe QDs has been studied using cyclic voltammetry. Finally, in **chapter 6**, the whole work has been summarised and the overview has been given. Future perspectives have also been discussed in this chapter.

CHAPTER 2
EXPERIMENTAL TECHNIQUES

2.1. Introduction

In the previous chapter we have discussed about the nanomaterials, semiconductor nanoparticles, quantum confinement in semiconductor nanoparticles, their electronic and optical properties, cytotoxicity and different applications of these semiconductor nanomaterials. The above mentioned properties as well as the applications of the semiconductor nanoparticles depends a lot on various characteristics such as their size, shape, morphology, composition, crystal structure, the surface passivating molecules and the approach of synthesis. So meticulous characterization of nanomaterials is very crucial. In this thesis, we have used three methods to synthesize CdSe QDs i.e.- radiation chemical, photochemical and room temperature chemical reduction method.

Apart from these instruments involved in the synthesis of nanoparticles, several techniques have been used for the characterization of these nanoparticles i.e.- Optical absorption, Fluorescence, Fluorescence life time, XRD, TEM, SEM, FTIR, Raman, DLS, Zeta potential etc. Therefore, in this chapter a brief overview of the instruments involved in the synthesis and characterization of the nanoparticles has been discussed.

2.2. Radiation chemical synthesis

The radiation chemical method of synthesis involved the generation of transient intermediate species, which are very reactive having short life time. Identification and characterization of such species is very crucial as it gives us insights of the physical phenomena involved in the synthesis of the nanoparticles. For the same purpose a very sophisticated instrument and technique is involved. The other radiation source involved is Cobalt-60 (Co-60) γ-rays which is also a very potent radiation source. In this thesis, for the radiation chemical synthesis of CdSe QDs we have used 7 MeV electron beam as radiation which was obtained from 7 MeV LINAC (linear electron accelerator). For synthesis, the reaction mixture was irradiated repetitively for

certain dose while for the reaction mechanistic studies pulse radiolysis was done. The colour of the reaction mixture changes after irradiation which indicates the accomplishment of the synthesis (Fig 2.1).

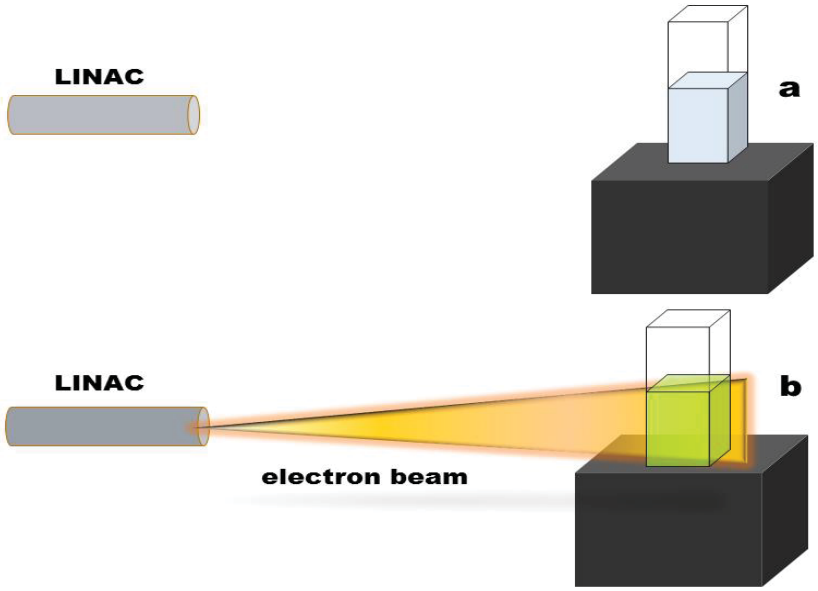

Figure 2.1 *Schematic representation of radiolytic synthesis of nanoparticles; reaction mixture- (a) before irradiation, (b) after irradiation.*

All the instrumentation and principles involved in the radiation chemical synthesis has been explained in the following sections.

2.2.1 Pulse radiolysis and its principle

In pulse radiolysis, the system under investigation is irradiated with intense pulse of radiation (electron) causing perturbation in the system by the production of primary radicals which causes radiolysis of the solvent molecules. These radicals generated after the radiolysis interact with the molecules under investigation to produce different transient/intermediate species. The resulting transient intermediate species are monitored online using various suitable physical techniques like- optical absorption, emission, conductivity, electron spin resonance etc [94-96]. Typically, the electron pulse width should be shorter than the life time of the transient

involved in a chemical reaction with sufficient energy to produce sufficient concentration of transient species in the irradiated sample.

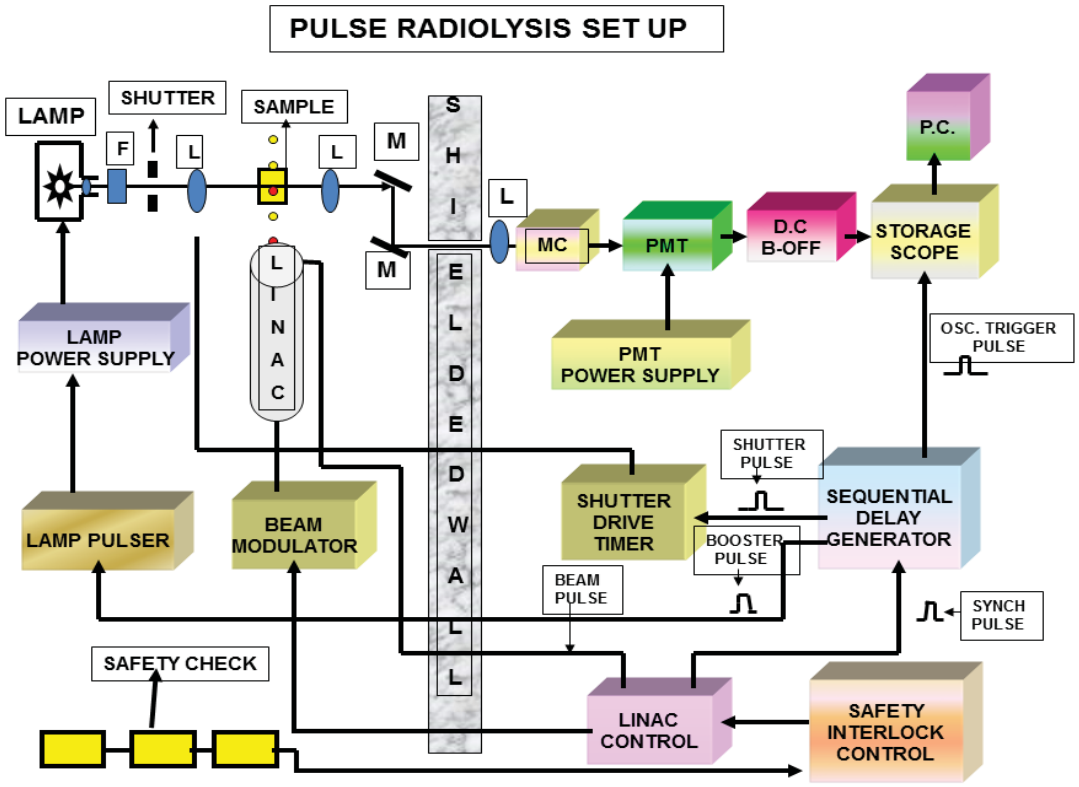

Figure 2.2 *Schematic diagram of Pulse Radiolysis Set Up.*

A schematic of pulse radiolysis set up used in our work is shown in Fig. 2.2. Herein, during the experiment the solution sample is taken in a quartz cuvette of dimension 1x1 cm and is kept at a distance of ~12 cm from the titanium electron beam window, where the beam diameter is ~1 cm. The sample solution is then irradiated with 7 MeV electron pulse beam from LINAC. Subsequently, a collimated light beam of 450 W Xenon arc lamp is used to investigate the transient change in absorbance of the solution upon irradiation. The transmitted light beam (after passing through the sample cell) is then directed to a spectrophotometer through a tunnel in the wall by making the use of fused silica lenses and mirrors coated with aluminium on the front surface. The light beam is finally focused on a monochromator, on the exit slit of which

a photomultiplier (Hamamatsu R 995) is fixed. PMT signal is then fed into a storage oscilloscope from which the traces are transferred to a computer. It is to be noticed that the accelerator, the sample cell and the monitoring Xe lamp, all are housed in a shielded cave with 1.5 meter thick concrete wall and roof. Details of LINAC facility is discussed in the following section.

2.2.2. Linear electron accelerator (LINAC)

A Linear Accelerator is a type of particle accelerator [94, 97] which greatly increased the kinetic energy of a charged particle by subjecting the charged particles to a series of oscillating electric potential along a linear beam line. The Accelerator is main component of pulse radiolysis technique and its function is to impart high energy to the electrons, which is then directed towards the sample under investigation. A brief description of the components of LINAC is as follow:

Electron Gun- A tungsten electrode is used as a source of electron in the form of a pellet. It is continuously heated by the electrons emitted from the filament (of tungsten) which is kept at -6.0 KV (DC) with respect to the cathode. The cathode potential is varied for 2 μs at an amplitude of 43 KV. As a result of this, 2 μs electron pulse of energy 43 keV is generated in the system initially. This electron pulse is focused by electromagnetic lenses to a deflector chamber before it enters to a cylindrical wave guide (Fig. 2.3).

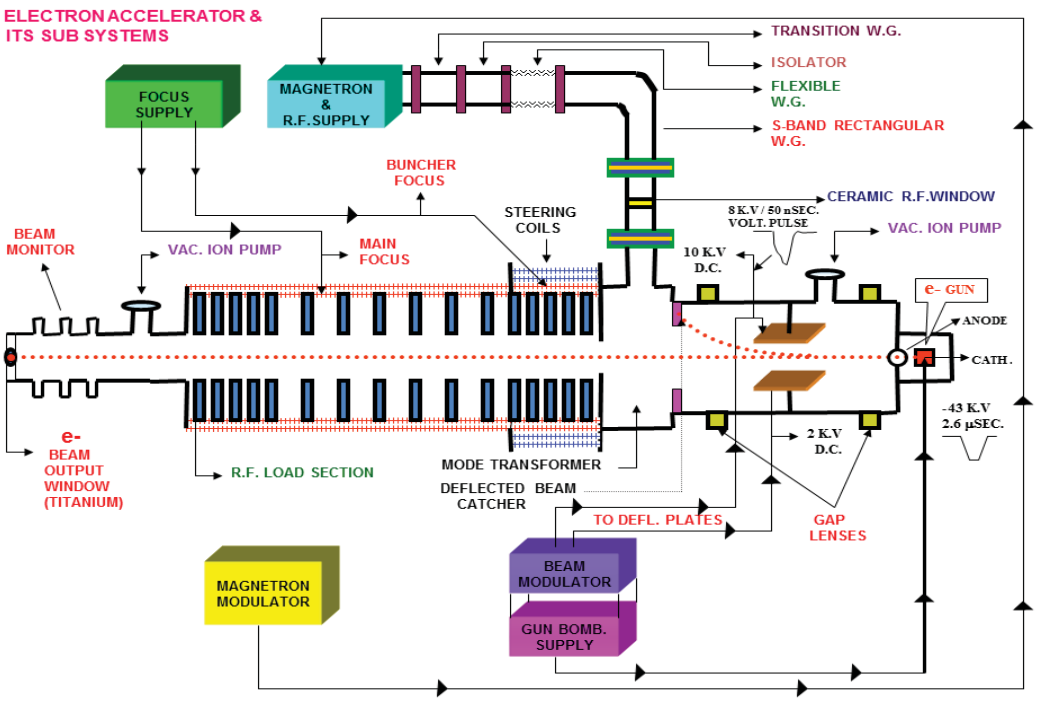

Figure 2.3 *Schematic diagram of linear electron accelerator.*

Wave Guide- A magnetron with 3 GHz frequency and 1.8 MW peak power produces a synchronous travelling R.F. (radio frequency) of 2 µs pulse width. The electrons generated in the electron gun assembly are allowed to enter into the waveguide in a phase synchronous with the RF field, wherein, the electrons are accelerated in the vacuum to a final energy of 7 MeV. A well-defined accelerated beam of electron is obtained after focusing by electromagnetic coils and comes out from the wave guide through a titanium window with mean diameter of~2 mm.

Electron pulses of various width from 5 ns to 2 µs can be obtained with the peak current ranging from 1.56 A to 70 mA by this machine. The nano second pulses are obtained by placing deflector plates between anode of the electron gun and the corrugated wave guide. The 43 KeV electrons emitted from the electron gun are deflected and collected by a beam catcher.

Working of the LINAC facility- A pulse generator, which is preset at 50 pulses per second (pps) triggers the R.F. pulses. The beam divider ratio is kept normally at 3 such that for every third R.F. pulse, one electron pulse is available for acceleration. The electron pulse is delayed

by 600 ns to synchronize it with peak portion of the RF pulse. Further, a pulse from the pulse generator of the accelerator triggers a sequential delay pulse generator (SDPG), which then sequentially activates an electromechanical shutter, a Xenon arc lamp pulse power supply (to boost the analyzing light intensity for monitoring the fast events) and an oscilloscope. Shutter, under normal working condition is kept open for 50 ms. As the oscilloscope is triggered by a pulse from the SDPG, the pre-trigger information ranging for a duration of 600 ns to 1 ms prior to the arrival of the electron pulse is used to mark the monitoring level as well as the incident light intensity (I_0). Fine adjustments in SDPG with respect to time allows the electron pulse and its effect to be recorded on the flat portion of the boosted lamp profile, during which time the output of the analyzing light remains steady. The dose imparted to the sample is varied either by defocusing the beam or by suitable adjustment of the filament to the cathode bombardment current.

2.2.3. Kinetic spectrophotometer

The time resolved studies in the current radiolysis set up have been conducted by monitoring the variations in the absorbance of sample solutions. There are various components involved in this set up. 450 watt **Xenon arc lamp** is used as the analyzing light source having white light continuum with wide effective output range i.e. from 185 to 2100 nm. To get good signal to noise (S/N) ratio the output light intensity of the lamp is very stable and can be boosted to 100 times as per experimental requirements. On the contrary commonly used continuous band light is not suitable for these purposes. An **electromechanical shutter** is used to prevent the photodecomposition of the sample as well as the fatigue of the detector during passive mode. It is placed between the sample holder and the lamp (Fig. 2.3). The shutter is synchronised in such a way that it opens prior to the boosting of analyzing light and remains open for a period over which the electron pulse arrives and the transient species generated.

A square cell (sample **cuvette**) of 1 cm X 1 cm path length is placed in its holder such that at one face it receives the electron beam and at its right angle face it receives the analyzing light beam both of which meet at the centre of the cuvette. A **monochromator** has range from 180 nm to 800 nm is used whose slit width can be continuously varied from 0.01 to 6 mm and corresponding band width of 0.1 to 19.8 nm. The analyzing light beam after passing through the sample incident upon the entrance slit of the monochromator. A **PMT** with spectral response in the working range of 200-700 nm is used for detection. The output current of the PMT is converted to voltage by a load resistor connected across its anode and ground. With a load resistor of 500 Ω, the overall rise time of detection is 75 ns. Thus, only the events of duration longer than this time period can be studied by using this detector. A **back-off device:** is used to compensate constant (-ve DC) output of the PMT (I_0) before the arrival of the electron pulse. An **oscilloscope** is used for getting the kinetic profile of the transient absorption. The PMT output is fed to the vertical amplifier of the oscilloscope. The time base of the storage scope is triggered externally by a signal (derived from the accelerator) synchronous with the electron beam pulse.

2.2.4. Transient absorption measurement

The light intensity which passes through the sample cell containing the sample, after the electron pulse irradiated can be given by the equation-

$$I = I_0.10^{(-\varepsilon cl)} \qquad (2.1)$$

where, I_0 is the intensity of transmitted light just prior to the electron pulse, c is the molar concentration of the transient species formed in the sample, ε is the molar extinction coefficient and l is the path length of the light. Because of the proportionality between the intensity of light (I) and the voltage signal (V) of the PMT, equation 2.1 can be written as-

$$V = V_0.10^{(-\varepsilon cl)} \qquad (2.2)$$

The quantity εcl is called as the optical density or absorbance (A) of the transient species at any given time, it can be expressed as-

$$A = log(V_0/V) \quad (2.3)$$

As the concentration of the transient species produced by electron pulse, depends upon time, the intensity of the transmitted and hence the voltage (V) depends on time. Hence the absorbance (A) will also depend upon time. It is the time dependence of V that is monitored with a digital oscilloscope and subsequently processed to get the other kinetic information.

2.2.5. Pulse radiolysis dosimetry

In pulse radiolysis experiments, thiocyanate dosimeter is commonly used to measure the absorbed dose per pulse. It is 0.01 molar aerated aqueous solution of potassium thiocyanate (KSCN). The hydroxyl radical ($^{\bullet}OH$) mainly react with SCN^- because the hydrogen radical ($^{\bullet}H$) and hydrated electron (e^-_{aq}) are scavenged by the dissolved oxygen in the sample solution. Reaction between $^{\bullet}OH$ and SCN^- can be shown as follow:

$$SCN^- + {}^{\bullet}OH \longrightarrow SCN^{\bullet} + {}^-OH \quad (2.4)$$

$$SCN^{\bullet} + SCN^- \longrightarrow (SCN)_2^{\bullet -} \quad (2.5)$$

The radiation dose is estimated from the absorption maxima of radical $(SCN)_2^{\bullet -}$ at 475 nm. G value and the extinction coefficient (ε) of this radical is reported to be 0.34 μMJ^{-1} and 7600 L mol^{-1} cm^{-1} respectively at 475 nm [98]. After getting the absorption, the absorbed dose can be calculated by using the following equation

$$\mathbf{D = 9.648 \times 10^6 * \Delta OD/G.\epsilon.\ell.\rho\ Gy} \quad (2.6)$$

where l and ρ are the path length of the light and density of the sample, respectively.

2.2.6. Kinetic treatment and experiment data handling

The data analysis obtained after pulse radiolysis is very important part of radiation chemical studies. In general, first order and second order kinetic behaviour is observed while complex behaviour is observed where the first and second order is less frequently occurred. For data processing, the kinetic traces are first transferred to PC and subsequently analyzed by sophisticated software packages. Different methods of data processing are explained briefly as follow:

(i) First order processes

When a reacting species A follows the first order kinetics such that

$$A \longrightarrow P \qquad (2.7)$$

The rate of reaction -dA/dt is proportional to the concentration of A

$$-dA/dt = k[A] \qquad (2.8)$$

Where k is the rate constant has a dimension of $time^{-1}$. Examples of this type of reaction are- intramolecular rearrangement reactions, rearrangement in an isolated excited state species, photochemical reactions etc. A bimolecular reaction can also show first order kinetic behaviour if concentration of one of the molecule is in large excess (pseudo unimolecular reaction):

$$A + B \longrightarrow P \qquad [B_0] >> [A_0] \qquad (2.9)$$

The rate equation of the above reaction can be written as-

$$dA/dt = k_s[A][B] = k_r[A] \qquad (2.10)$$

where k_r is pseudo first order rate constant (dimension- $time^{-1}$) and k_s is the specific second order rate constant (dimension- $(concentration \times time)^{-1}$). On integrating equation (2.10) between limit 0 to t gives:

$$\ln[A]_t - \ln[A]_0 = -k_r t \qquad (2.11)$$

$[A]_t$ and $[A]_0$ refer to the concentration at time t and at the beginning of the reaction, respectively. The observed rate constants are plotted against the concentration of reactant in excess and the slope of the plot gives the bimolecular rate constant k_s for the reaction of species A with B.

(ii) Second order processes

When in a bimolecular reaction a single molecule reacts with itself shows a second order kinetic behaviour such as:

$$A + A \longrightarrow P \qquad (2.12)$$

The corresponding rate equation for reaction 2.12 can be written as

$$-d[A]/dt = 2k[A]^2 \qquad (2.13)$$

On integrating equation 2.13 between limit 0 and t, we have

$$(\frac{1}{[A_t]}) - (\frac{1}{[A_0]}) = 2kt \qquad (2.14)$$

For [A] absorbing at the monitored wavelength, equation (2.14) can be written as:

$$\frac{1}{OD_t} - \frac{1}{OD_0} = \frac{2k}{\varepsilon l} t \qquad (2.15)$$

Where, OD_t represents the absorbance due to reactant A at any time t. The absolute rate constant 2k for this second order process can be obtained from plot of $1/OD_t$ *vs.* t. The slope of this plot is related to the rate constant by the following relation:

$$2k = \text{slope } (\varepsilon.l) \qquad (2.16)$$

(iii) Competition kinetics

For many transients formed in the pulse radiolysis experiment, the wavelength for monitoring is not in a convenient range of the spectrum, as the substrate also absorbs in the same region. In those cases, competition kinetics method is used wherein, another species is monitored

which are having suitable spectral characteristics. If $R^{\bullet}$ is the radical generated during the radiolysis, then

$$R^{\bullet} + A \longrightarrow P_A \quad (2.17)$$

$$R^{\bullet} + B \longrightarrow P_B \quad (2.18)$$

The probability that radical '$R^{\bullet}$' will react with solute 'A' will be given as $\frac{k_a[A]}{k_a[A]+k_b[B]}$ and that will react with solute 'B' will be given as $\frac{k_b[B]}{k_a[A]+k_b[B]}$. Where k_a and k_b are the rate constant for the reaction of radical '$R^{\bullet}$' reactant A and B respectively and [A] and [B] are their concentrations, respectively. The concentration of A and B can be adjusted so that the radical $R^{\bullet}$ react with ether of A and B. It is done by adjusting the reactivity (reactivity of $A=k_A x[A]$, reactivity of $B=k_B x[B]$). For $R^{\bullet}$ to react with A reactivity of A should be ten times to the reactivity of B. In terms of radiation chemical yield of the product, G_{PA} and the reacting radical, $G_{R\bullet}$

$$\frac{1}{G_{PA}} = \frac{1}{G_{R\bullet}} + \left(\frac{k_B[B]}{G_{R\bullet}\, k_A[A]}\right) \quad (2.19)$$

The plot of $\frac{1}{G_{PA}}$ *vs.* $\frac{[B]}{[A]}$ is a straight line with an intercept of $\frac{1}{G_{R\bullet}}$ and a slope $(k_B[B])/(G_{R\bullet}k_A[A])$ from which the rate constant (k_A) can be calculated.

2.3. Photochemical synthesis

The photochemical method of synthesis involved the light source. The chemical reactions are initiated by the photo chemically generated molecular/ ionic radicals which are highly reducing

in nature. These radicals are very reactive and are generated *in situ* the reaction mixture upon photo irradiation. Sun light, various lamps and photo reactors are the sources of light. For the completion of the reaction, the light source should have sufficient intensity of photons so that the concentration of the radicals generated are abundant for causing a chemical reaction. For the photochemical synthesis carried out in this thesis, we have used Rayonet Photoreactor.

2.3.1. Rayonet photo reactor

A photoreactor is an assembly of lamps of a particular wavelength of light having sufficient power and a narrow gaussian emission profile. A Rayonet Photoreactor is shown in Fig. 2.4.

Figure 2.4 *Rayonet Photoreactor (inset lamp of output light of 300 nm).*

The light source may be of different wavelengths e.g.- 260 nm, 300 nm or 360 nm etc. The light emitted by the photoreactor is absorbed by a particular molecule having the absorption profile in the region of wavelength of emitted light. This photoreactor consists of a vertical assembly of sixteen lamps. In this thesis, for photochemical experiments 300 nm lamp (shown

in the inset of Fig. 2.4) have been used. The power of each lamp was 8 watt and flux was $5x10^{15}$ photons $cm^{-2}s^{-1}$.

2.4. X ray diffraction

X radiation (X ray) is a form of electromagnetic radiation having energy in the range of 10 eV-100 keV. These radiations produce diffraction pattern on interacting with materials because their wavelength (λ) is typically same order of magnitude to that of the spacing (d) between the planes of the crystal. Due to this reason, X ray is the best suited to probe the structural arrangement of the atoms and the molecules in the wide range of materials. Further, the energetic X rays can penetrate deep into the materials and provide information about the bulk structure [99,100]. Therefore, X ray diffraction technique is the most important tool for the thumbprint characterization of the crystalline materials and to get detailed information about their crystal structure. The database maintained by the Joint Committee on Powder Diffraction Standard (JCPDS) and International Centre for Diffraction Data (ICDD) provides information on unit cell dimensions for phase identification of crystalline materials.

In the field of nanoscience, XRD is a widely used technique for detail investigation of the crystal structure of the nanomaterial. A typical XRD experimental set up requires an X ray source, the sample to be investigated and a suitable detector system to detect the diffracted X rays. The X rays are generally produced by bombarding high energy electron on a metal target in a sealed X ray tube. The most commonly used metal is Copper (Cu) because it can be kept cool easily due to its high thermal conductivity.

In crystal structure, the atoms are arranged in a particular repeating fashion. Therefore, X ray incidents on the sample undergo diffraction and form constructive or destructive interference patterns according to the interplannar spacing or distance between two planes (Fig. 2.5). When the path diffraction between two diffracted beam of X rays is equal to the integral

multiple of its wavelength, they will constructively interfere, which is called the Bragg's condition:

$$2d\sin\theta = n\lambda \qquad (2.20)$$

where n is the integer number, λ is the wavelength of incident rays, d is the interplannar distance and θ is the incident angle. Therefore, from equation (2.20), the interplannar distance and therefore lattice constant can be determined.

In an X ray diffractometer, a convergent beam strikes on the sample and the intensity of the diffracted beam is measured as a function of angle of diffraction, 2θ. The FWHM of the peak can be used to calculate the mean crystallite size in the sample by using the Scherer's equation [101]:

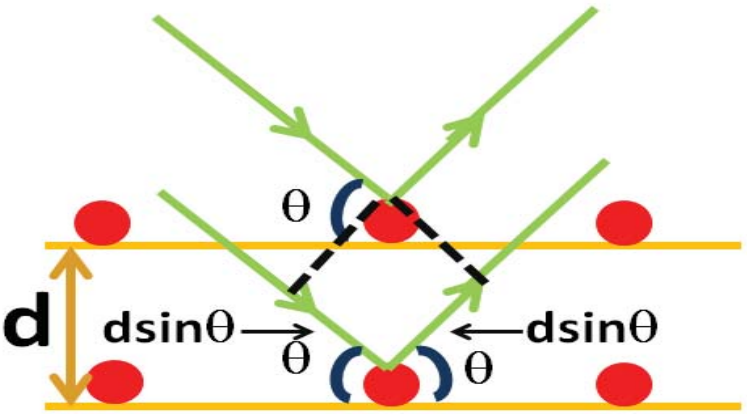

Figure 2.5 *Diagrammatic representation of diffraction of X ray from the plane of the crystal.*

$$D_{hkl} = \frac{k\lambda}{B_{hkl}\cos\theta} \qquad (2.21)$$

where, D_{hkl} is the crystallite size in the direction perpendicular to the lattice plane, hkl is the Miller indices of the planes being analyzed, K is the numerical factor frequently referred to crystallite-shape factor, λ is the wavelength of the X ray, B_{hkl} is the FWHM of the X ray

diffraction peak in radian and θ is the Bragg angle. In the absence of detailed shape information, K=0.9 is a good approximation [101].

In the present thesis work, XRD measurement were recorded on Phillips X-ray diffractometer, model PW 1710 system, using a monochromatic Cu K-α source (λ=1.54 Å).

2.5 Transmission electron microscopy (TEM)

Transmission electron microscopy (TEM) is one of the most popular and sophisticated physical technique to study and characterize nanomaterials. The area of nanomaterial research achieved new height only after the powerful TEM technique was developed few decades ago. Characterization of nanomaterials includes the determination not only of size and shape, but also of the atomic and electronic structures and other important properties. In this regards TEM technique is the most suitable one [102]. In TEM, electrons are usually generated by thermionic emission process, in which a source of electron (generally tungsten or lanthanum hexaboride, LaB_6) [103] is heated by applying high voltage. These electrons are then accelerated by applying high voltage (in the range of 100-400 kV) and focused by electromagnetic and electrostatic lenses onto the sample (Fig. 2.6). The vacuum in different parts of TEM ranges from 10^{-4} to 10^{-7} Pa. The main reason to maintain such low pressure is to increase the mean free path of the electron gas interaction. Typically, a TEM consists of three stage of lensing, which includes the condenser lenses, objective lenses and the projector lenses. The condenser lens is responsible for primary beam formation, while the objective lens focusses the beam that comes through the sample itself. The projector lens expands the beam onto the phosphor. The transmitted beam containing information about electron density, phase and periodicity is used to form an image. Since, the observed image depends not only on the amplitude of the beam, but also on the phase of the electrons.

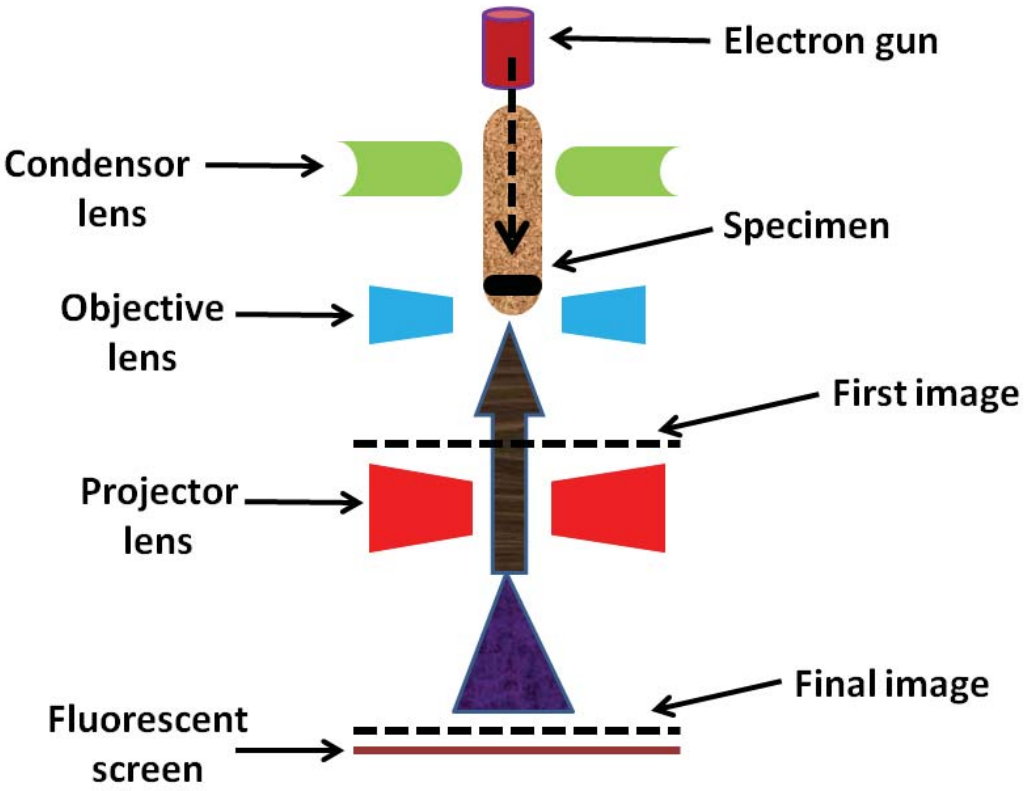

Figure 2.6 *Layout of optical components of TEM.*

Therefore, different imaging methods attempt to modify the electron waves exiting the sample in a form that is useful to obtain information with regards to the sample. Phase effects are often ignored at lower magnifications, however in case of higher resolution measurements; the images are formed by utilizing the differences in phase of electron waves, which is caused by specimen interaction [104]. With high resolution TEM (HRTEM), in addition to the size and shape of nanoparticles, information about their internal structure (i.e. lattice fringes, which are important for the analysis of crystal structure, interplannar spacing, stacking faults, and dislocations) can be determined. In addition, selective area electron diffraction (SAED) measurements can be carried out in a TEM, which provides information about whether the material is single crystal or polycrystalline. Also, the phase of the nanoparticle can be estimated from the interplannar spacing determined from the SAED pattern.

The sample preparation for TEM imaging of nanoparticles is usually carried out by putting the drops of the solution (containing nanoparticles) on a grid, while allowing the solvent to evaporate. Usual grid materials are copper, molybdenum, gold or platinum screen. Standard carbon coated copper grid of size 3.05 mm diameter with a mesh size of 200 (74 μm) was used in this thesis experiment. The TEM measurements were carried out on model no. CM200, Phillips with operating voltage range from 20-200 kV and resolution of 2.4 Å, while HRTEM images were acquired on FEI, TECNAI F-30.

2.6. Scanning electron microscopy (SEM)

Similar to TEM, scanning electron microscopy is also a very powerful tool for characterization of nanomaterials. Both the TEM and SEM technique use electron beam for imaging. However, former involved the imaging by the transmitted electron, the latter is based on the imaging by the scattered electrons [105,106]. It has been proven that along with size, the shape and morphology also influence the properties of nanomaterials. SEM provides the information about the topography and the surface morphology of the nanomaterials.

In a typical SEM, an electron beam is thermionically emitted from electron gun usually of tungsten filament cathode. Tungsten is considered to be one of the most suitable electron because of having high melting point and lowest vapor pressure of all metals, thereby allowing it to be heated for electron emission The electron beam having energy ranging from 0.2 keV to 40 keV is focused by collimating and focusing lenses to a narrow spot of the order of nanometers in diameter on the specimen surface. This beam is scanned in a rectangular raster over the specimen and the intensities of various signals created by interactions between the beam of electrons and the specimen are measured. As a result of interaction of the primary electron beam with the sample, the energy exchange results in the reflection of high-energy electrons by elastic scattering, emission of secondary electrons by inelastic scattering and the

emission of electromagnetic radiation, each of which can be detected by specialized detectors. The most common imaging mode collects low-energy (<50 eV) secondary electrons (SE) that are ejected from the k-shell of the specimen atoms by inelastic scattering interactions with beam electrons. Due to their low energy, these electrons originate within a few nanometers from the sample surface [107] and are detected by a type of scintillator-photomultiplier system. In another mode, backscattered electrons (BSE) are detected. BSE consist of high-energy electrons originating in the electron beam that are reflected or back-scattered by the specimen elastic scattering interactions. Since, heavy elements (high atomic number) backscatter electrons more strongly than light elements (low atomic number), and therefore appear brighter in the image and used to detect contrast between areas with different chemical compositions. The X-rays are produced by inelastic collisions of the incident electrons with the electrons in the discrete orbitals (shells) of atoms in the sample. As the excited electrons return to lower energy states, they yield X rays that are of a fixed wavelength (that is related to the difference in energy levels of electrons in different shells for a given element). Thus, characteristic X-rays are produced for each element in the sample. And, this forms the basis of energy dispersive X-ray spectroscopy (EDS) and has been widely employed for determining the composition of the samples. A basic layout of a SEM is shown in Fig. 2.7. A crucial aspect of SEM sample characterization is that the sample must dissipate charge. For conducting materials on a conductive substrate, this requirement is easily met. However, a thin layer of conducting material such as carbon, gold, or some other metal/alloy is coated on the electrically insulating samples.

Surface and morphological characterization of nanoparticles synthesized in the present thesis work was carried out on JEOL JSM-T330 SEM.

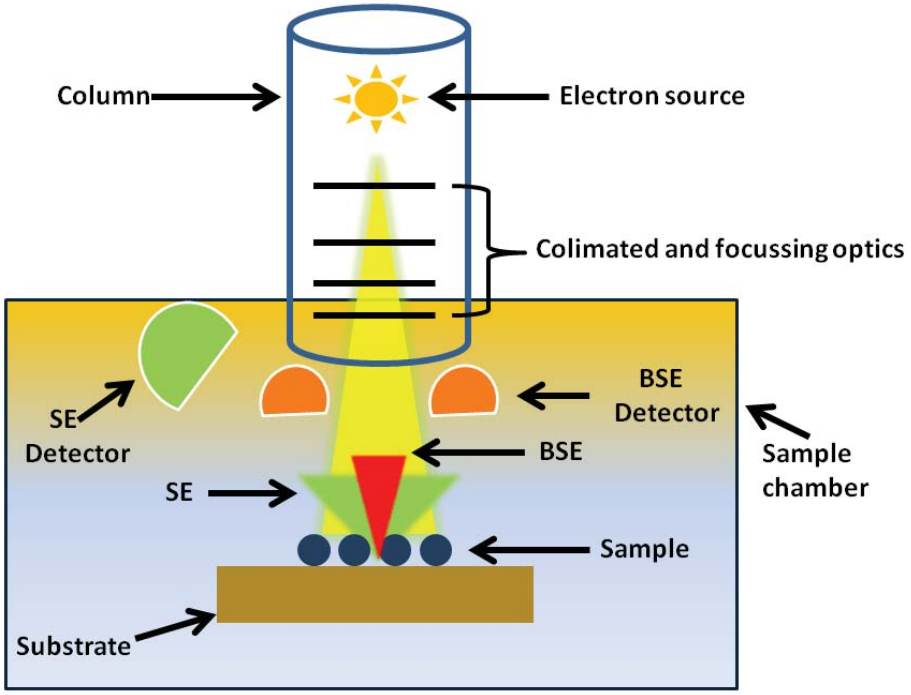

Fig. 2.7 *Layout of optical components of a Scanning Electron Microscope.*

The preparation of samples for SEM analysis were carried out by putting a drop of solution containing nanoparticles on a Silicon wafer, and subsequently allowing the solvent to evaporate.

2.7. Steady state UV-vis absorption measurement

Steady state UV-vis absorption spectroscopy also known as electronic spectroscopy as it involved the electronic energy level transition in a compound/ molecule is used for quantitative measurement of absorption or transmission of UV-vis light by a sample as a function of wavelength. The working principle of the spectrophotometer is based on the Beer- Lambert's law which states that the absorbance of a solution is directly proportional to the concentration of the absorbing species in the solution and the path length [108, 109].

$$A = \log\left(\frac{I_0}{I}\right) = \varepsilon c l \qquad (2.22)$$

where A is the absorbance (a unit less quantity), I_0 is intensity of incident light, I is the intensity of transmitted light, *l* is path length of the sample and ε is the molar extinction coefficient or molar absorptivity of the sample. The sample solution is generally taken in a quartz cell. The basic parts of a spectrophotometer are a light source, a holder for the sample, a diffraction grating in a monochromator or a prism to separate the different wavelengths of light, and a detector. A spectrophotometer can be either single beam or double beam. In a single beam instrument, all of the light passes through the sample cell. I_0 must be measured by removing the sample. In a double-beam instrument, the light is split into two beams before it reaches the sample. One beam is used as the reference; the other beam passes through the sample. The reference beam intensity is taken as 100% Transmission (or 0 Absorbance), and the measurement displayed is the ratio of the two beam intensities. Ground state optical absorption measurements were carried out on a JASCO V 650 UV-Visible spectrophotometer. It is a double-beam spectrophotometer with a PMT detector. Typical wavelength range is 190-900 nm. The light sources used in this instrument are Deuterium lamp (range: 190 to 350 nm) and a Halogen lamp (range: 330 to 900 nm).

2.8. Steady state photoluminescence measurements

Photoluminescence spectroscopy is contactless, non-destructive, popular technique for characterization of electronic and optical properties of molecules and semiconductors. Light is directed onto a sample, where it is absorbed and imparts excess energy into the material in a process called *photo-excitation*. The photo excited molecule dissipates its excess energy by different photophysical processes. One way this excess energy can be dissipated by the sample is through the emission of light, or *luminescence*. In the case of photo-excitation, this luminescence is called *photoluminescence*. The luminescence process involves- (i) fluorescence (no change in spin state) and (ii) phosphorescence (change in spin state) [108,109,

110]. The other way to dissipate the excess energy is radiation less relaxation which involves- (i) internal conversion or vibrational relaxation with no change in spin state, (ii) intersystem crossing –relaxation with change in spin states). The energy of the emitted light (Pl) is equivalent to the energy difference between the excited state energy level and the ground state energy level. Observation of Pl at certain energy can be viewed as an indication that the excitation event had populated an excited state associated with this transition energy. Fluorescence and phosphorescence are forms of Pl and observed at lower energy than absorption [109]. Pl measurements were carried out using a spectrofluorometer. In a typical fluorescence (emission) measurement, the excitation wavelength is fixed and the detection wavelength region is specified, while in a fluorescence excitation measurement, the detection wavelength is fixed and the excitation wavelength is varied across a region of interest. The light from an excitation source passes through a filter or monochromator, and strikes the sample. A proportion of the incident light is absorbed by the molecules in the sample and some of them fluoresces back. The fluorescent light is emitted in all directions. Some of this fluorescent light passes through a second filter or monochromator and reaches a detector, which is usually placed at 90° to the incident light beam to minimize the risk of transmitted or reflected incident light reaching the detector. In the present thesis work, steady-state fluorescence measurements (excitation spectra or emission spectra) were carried out using a Hitachi model F-4500 fluorescence spectrometer. The instrument uses a xenon lamp (150 W; continuous) as an excitation source and R-928F (Hamamatsu) PMT as the photodetector. Sample is taken in a quartz cuvette of dimensions 1 cm × 1 cm and the fluorescence is collected and measured in a perpendicular direction with respect to the direction of the excitation beam. The wavelength range covered in the present instrument is 220 to 800 nm, while the resolution is 1 nm.

The Pl quantum efficiency or quantum yield of a sample solution was determined based on the comparative method by using equation (2.23) [109]:

$$\phi_S = \phi_R * \frac{A_S}{A_R} * \frac{OD_R}{OD_S} * (\frac{n_S}{n_R})^2 \quad (2.23)$$

where, 'ϕ_S' and 'ϕ_R' are the quantum yields of sample and reference, respectively, 'A' is the integrated Pl intensity, 'OD' is the optical density, and 'n' is the refractive index. The excitation wavelength was chosen on the basis, where the OD values of both the sample and the reference matched with each other.

2.9. Photoluminescence lifetime measurements

Absorption of an appropriate photon energy follows a chain of photophysical events, such as internal conversion or vibrational relaxation (loss of energy in the absence of light emission), fluorescence, intersystem crossing (from singlet state to a triplet state), and phosphorescence [107, 109, 110]. Each of these processes occurs with a certain probability, characterized by decay rate constants (k) and the average length of time (τ) for the set of molecules to decay from one state to another can be expressed as: $\tau = 1/k$. This average length of time is called the mean lifetime or simply lifetime. The lifetime of photophysical processes vary significantly from tens of femtoseconds for internal conversion to nanoseconds for fluorescence and microseconds or seconds for phosphorescence [109]. Moreover, fluorescence lifetime can be sensitive to a great variety of internal factors defined by the fluorophore structure and external factors that include temperature, polarity, and the presence of fluorescence quenchers. Therefore, fluorescence (or Pl) lifetime measurements are essential to obtain information regarding the kinetics and dynamics of various photophysical processes as well as their mechanism involved in the deactivation of the excited fluorophores. The versatility of the

fluorescence lifetime method allows its application in diverse areas of study, including materials science, aeronautics, agriculture, forensics, biology and medicine.

At present, most of the time-domain measurements in the nanosecond to picosecond time scales are performed using time-correlated single-photon counting technique (TCSPC). The working principle of TCSPC is described as follows. Basically, it is a technique with well defined (Poisson) statistics, and is not affected by the changes in source intensity [108, 111]. It makes use of a pulsed excitation source such as a laser or a flash lamp, which excites the sample, while the detection system monitors the time difference between the excitation pulse and the first fluorescence photon from the sample. However, for TCSPC, the conditions are adjusted in such a way that less than one photon is detected per laser pulse [108]. In fact, the detection rate is typically 1 photon per 100 excitation pulses. The layout of a typical TCSPC set up is shown in Fig. 2.8.

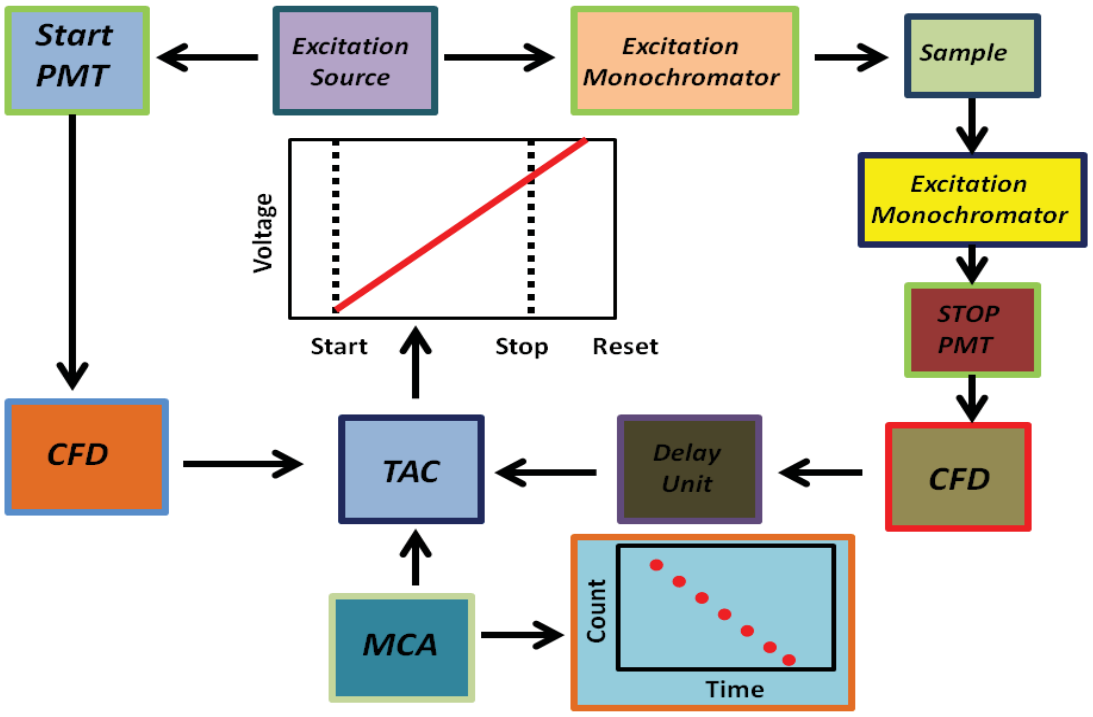

Figure 2.8 *Layout of a TCSPC set up*

The experiment starts with the excitation pulse, one part of which is used to excite the sample kept in the sample chamber and the other part of the light pulse is directed to a start PMT. The signal at the start PMT generates a START pulse and is then routed through a constant function discriminator (CFD), which accurately measures the arrival time of the pulse. This signal is passed to a time-to-amplitude converter (TAC), which generates a voltage ramp that increases linearly with time on the nanosecond time scale. This voltage level is then fed to the input of a Multichannel Analyzer (MCA) through an Analog-to-Digital Converter (ADC). The ADC generates a numerical value proportional to the height of the TAC output pulse and thus selects the corresponding memory address (channel) in the MCA, where a single count is added up. The above cycle (from the triggering of the pulsed excitation light source to the data storage in the MCA) is repeated for a large number of times and such events are binned to form a histogram of counts versus channel number (time). During experiment, the data collection rate is kept very low i.e. <0.02 photons/excitation pulse. The histogram represents the decay of the excited state convoluted with the instrument response function. Pl lifetime measurements were carried out by using a TCSPC instrument (model: IBH, UK). Both diode laser and LED are used as excitation source. The instrument response function (IRF) of the setup was measured by collecting the scattered light from a TiO_2 suspension in water. An emission polarizer is used before collection optics and Pl decay profile is recorded at magic angle (54.7°) polarization with respect to excitation light (source as diode laser). The fluorescence collected at the magic angle is free from any anisotropy components and represents the actual total fluorescence intensity decay. The as obtained decay curves were analyzed and fitted by using a non-linear least square analysis supported by instrument fitting program of IBH DAS 6.2 software:

$$I(t) = \sum_{i=1}^{n} \alpha_i e^{-t/\tau_i} \qquad (2.24)$$

where, I (t) is the time-dependent emission intensity, τ_i are the decay times and 'α_i' represent the amplitudes of the components at t = 0, and n is the number of decay times. The goodness

of the fit was judged by the reduced χ^2 value, which should be close to 1 and weighted residuals should be randomly distributed about the zero line for the whole range of the data channels used in the decay analysis.

2.10. Fourier transform infrared (FTIR) spectroscopy

The infrared spectroscopy (IR spectroscopy) involves the interaction of electromagnetic radiation of IR range (10 cm^{-1} to 10,000 cm^{-1}) with the sample. Some of the radiation is absorbed by the sample and some are transmitted. The absorbed IR radiation causes the vibrational and rotational changes in the molecule. The absorbed and transmitted IR radiation produce a spectrum which is fingerprint of the molecule of the sample. This fingerprint is unique for each and every molecular structure and no two unique molecules can produce same infrared spectrum. This concept makes infrared spectroscopy very advantageous for structural analysis [112,113]. However, the fundamental requirement for a molecule to have IR activity is that the IR radiation absorbed by the molecule must cause a net change in the dipole moment of the molecule during vibration.

Nowadays, Fourier Transform Infrared Spectroscopy (FTIR) technique is widely used to record the IR spectra of a sample. The frequency used in the FTIR spectrum are the inverse of the wavelength (wave no.) with unit of cm^{-1}. The original IR instruments were of dispersive type where one wavelength at a time passes through the sample which was a time consuming process in recording the whole spectra and also the signal to noise ratio was very poor. On the contrary, in FTIR signals corresponding to all the frequencies are collected simultaneously, improving both the speed as well as signal to noise ratio. This is also known as “Fellgett’s advantage” or “Multiplex advantage” [114]. The other method is called “Jacquinot’s advantage”, which refers to the higher optical throughput obtained in FTIR and leads to better signal to noise ratio. Essentially, an optical device called as interferometer is used in FTIR

which produces a unique signal called as interferogram. This signal consists of all the frequency and can be measured very quickly. This measured interferogram cannot be interpreted directly and is accomplished by a well-known mathematical technique called Fourier Transformation (equation 2.25).

$$f(v) = \int_{-\infty}^{+\infty} f(t) e^{-2\pi i v t} dt \qquad (2.25)$$

where, t is the time and ν is the frequency.

In this thesis work, the FTIR spectra of the samples were recorded in an IR Affinity-1 spectrometer with a resolution of 1 cm^{-1}. Attenuated total reflectance (ATR) based sampling technique was used in recording the spectra. ATR mode in FTIR is based on measuring the changes that occur in totally internally reflected IR beam when it comes into the contact of the sample. An IR beam is directed onto an optically dense crystal (diamond in the present work) with a high refractive index at a certain angle. The internal reflection forms an evanescent wave, which extends beyond the surface of the crystal into the sample held in contact with the crystal. The penetration depth into the sample is typically between 0.5 to 5 μm, with the exact value being determined by the wavelength of light, the angle of incidence and the indices of refraction for the ATR crystal and the medium being probed [115,116]. In regions of the IR spectrum, where the sample absorbs energy, the evanescent wave will be attenuated or altered. The attenuated energy from each evanescent wave is passed back to the IR beam, which then exits the opposite end of the crystal and is passed to the detector in the IR spectrometer. The system then generates an infrared spectrum. There must be good contact between the sample and the crystal surface for reliable measurements.

2.11. Raman spectroscopy

Along with XRD, Raman spectroscopy is very important tool to characterize the crystal structure of the nanomaterials. When a sample is irradiated with intense monochromatic light source (usually a laser) major portion of the light is scattered by the sample with the same wavelength as that of the wavelength of the incident light. This scattering process is known as Rayleigh scattering. However, a small portion of the incoming light (nearly one photon out of millions of photon) is scattered at the wavelength which is shifted from the wavelength of incident light. This shift is either towards the higher frequency (Anti Stokes) or towards the lower frequency (Stokes) with respect to the excitation frequency and is called as. Raman Scattering Effect [117-119]. Raman scattering is an example of inelastic scattering because of the energy and momentum transfer between the photon and the molecules of the material. On the contrary, Rayleigh scattering is an example of elastic scattering as the energy of the scattered photon is same as that of the incident photon. The fundamental requirement for the Raman effect to be observed the net change in the bond polarizability associated with the vibration must be non-zero. The dipole moment P, induced in a molecule by an external electric field E associated with the photon, is proportional to the electric field as shown in equation 2.26.

$$P = \alpha E \tag{2.26}$$

The proportionality constant, α is the polarizability of the molecule and is the characteristics of the molecule. It is the measure of the ease with which the electron cloud of the molecule can be distorted. The induced dipole emits or scatters light at the frequency of the incident light. Raman scattering occurs only when a molecular vibration results into a net change in the polarizability of the molecule. It can be expressed as

$$\frac{d\alpha}{dQ} \neq 0 \tag{2.27}$$

where Q is the normal co-ordinates of the vibration.

In a centrosymmetric molecule the vibrational modes which are Raman active will be silent in the IR and vice versa. This principle is called as *Mutual Exclusion Principle*. Typically, strong Raman scattering molecules have moieties with distributed electron clouds, such as carbon-carbon double bonds. These π-electron cloud of the double bond can easily be distorted in an external electric field. On the contrary, bending and stretching of bonds changes the distribution of electron density around the bond substantially causing a large change in the induced dipole moment [120]. In this thesis work, Raman spectral studies were carried out using a micro-Raman spectrometer (STR-300, SEKI Technotron, Japan). A fiber coupled 532 nm CW diode pumped solid state laser (DPSS, gem532, Laser Quantum) having an excitation power of approximately 50 mW at the source was initially passed through a band pass filter (532 nm), and directed on the sample *via* microscope (Make: Olympus). The Raman scattered light was collected by the same objective lens and passed through a fibre coupled to a 300 mm focal length imaging spectrograph (Action series SP2300i, 1200 groove/mm) and was detected by a thermo-electric cooled (-75°C) charge coupled device (CCD) detector (Pixis 256 CCD camera, Princeton Instruments). The spectrograph was calibrated using the 520.5 cm^{-1} line from silicon wafer. For recording the Raman spectra, samples (liquid as well as solid) were taken on a glass slide and used for carrying out the Raman spectral studies.

CHAPTER 3
PHOTOCHEMICAL SYNTHESIS OF CdSe NANOPARTICLES

3.1. Introduction

Radiation induced synthesis of nanoparticles is a subject of attention because of its several advantages over the other methods which has already been discussed in chapter one. Radiation involves both high energy and low energy. Synthesis of nanoparticles using radiation can be broadly categorized into two type- (i) Photochemical method which involves relatively lower energy (~eV). In photochemical method the source of energy used are mainly UV-vis light. Radiation chemical method involves high energy (~keV-MeV) and the source of energy are e^- beam, H^+ beam, γ rays etc. Due to different in energy, the mode of interaction of these low and high energy radiation with the matter is different which has already been discussed in chapter one. The ultimate outcome is generation of radicals *via* different mechanism.

The Photochemical method of synthesis of metal and semiconductor nanomaterials/Quantum Dots (QDs) is propitious in comparison to the other methods like- organometallic, solvothermal/hydrothermal, pyrolysis methods etc. The photochemical method offers many advantages like -it is a facile, rapid, one-pot route. Moreover, no external hazardous reducing agents are involved [121] and reactions occur without involvement of stringent laboratory conditions. Besides, elementary instrumentation is involved in this methods. All these advantages make photochemical method economical and viable and motivate the researchers to adopt this methodology to synthesize nanoparticles. Various researchers have followed this method for synthesis of both the metal and the semiconductor nanoparticles [122-125]. McGilvray et al. have synthesized gold nanoparticles using UV photoreactor [126]. Zhu et al. have synthesized PbSe nanoparticles using high pressure indium lamp (λ = 420 - 450 nm) [127].

Semiconductor nanoparticles/QDs are inherently toxic in nature because of involvement of various heavy metals like- Cd, Pb, Sn etc [128]. For their use in bio-application it is mandatory to reduce their toxicity. Using biomolecules as capping/ surface passivating agents is well

stablished approach to reduce the toxicity of nanoparticles. Various biomolecules like- protein, DNA, nucleic acids, saccharides have been used as capping agents to minimize the toxicity of nanoparticles/QDs [129-132]. Photochemical method to synthesize semiconductor QDs using various biomolecules as capping agent and study their properties systematically is still to be investigated. Further use of the as synthesized QDs in various applications like metal ion sensing is also very much significant and relatively unexplored. The aim of this chapter is systematic and in depth study of photochemical synthesis and properties of CdSe QDs using different biomolecules as capping agents. Further to explore application of the as synthesized QDs in fluorimetric detection of metal ions.

This chapter has two sections, 3.2 and 3.3, in which we have described the synthesis of CdSe QDs capped with (i) L-Cysteine and (ii) starch respectively, using photochemical route in aqueous solutions containing very low concentrations of the precursors and the capping agent along with acetone and 2-propanol each 2 % (v/v). Rayonet photoreactor having 300 nm lamp has been used as light source. The synthesis of CdSe QDs was initiated by the reducing agent 1-hydroxy-2-propyl radicals, $(CH_3)_2C•OH$ which are produced upon UV photoexcitation of acetone in the presence of 2-propanol. These QDs were found to have tunable Pl, which strongly depends on the composition of the precursors. The as synthesized QDs were characterized by XRD, Raman, FTIR, SEM, TEM etc. Optical properties of as synthesized QDs were studied by UV-vis absorption spectrophotometer, Steady state spectrofluorometer and time resolved single photon counting (TCSPC). The L-Cysteine capped QDs also show a reduction in the cytotoxicity as compared to the bare ones. The starch capped CdSe QDs were further functionalized with thiourea in order to improve its Photoluminescence (Pl) intensity. The thiourea functionalized QDs were used in sensing of Cu^{2+}, Cr^{6+} and Hg^{2+} metal ions.

3.2. Experimental

3.2.1. Materials

High purity chemicals $CdSO_4$, Na_2SO_3, Se powder, 2-propanol, acetone, 3-[4,5-dimethylthialzol-2-yl]-2,5-diphenyltetrazolium bromide (MTT), L-cysteine and starch were used without further purification. Ammoniated cadmium sulfate, $Cd(NH_3)_4SO_4$ was used as cadmium precursor and freshly prepared sodium selenosulfate, Na_2SeSO_3 was used as selenium precursor. Sodium selenosulfate was synthesized by following the reported literature; typically, a mixture of 5 g of Na_2SO_3 and 0.5 g of Se powder was refluxed at 70^0 C for 7 hours to obtain a clear transparent solution, which contains Na_2SeSO_3 (250 mM) and unreacted Na_2SO_3 [133]. It is to be noted here that the excess Na_2SO_3 present in the solution neither take part nor hinder the reactions during the formation of CdSe QDs [134]. $Zn(SO_4).7H_2O$, $HgCl_2$, Hg_2Cl_2, $NiSO_4.6H_2O$, $MnSO_4.7H_2O$, $CoSO_4.7H_2O$, $CrCl_3$, K_2CrO_4, $CuCl_2$, $FeCl_3$, $PbCl_2$ salts were used in the metal ion sensing experiments. Nanopure water obtained from Millipore water purifying system (resistivity > 18 megaohm cm) was used for preparation of the solutions.

3.3. Synthesis

3.3.1. Synthesis of L-Cysteine capped CdSe QDs

Reaction mixtures with different concentrations of ammoniated cadmium sulfate, ($[Cd(NH_3)_4]SO_4$), sodium selenosulfate (Na_2SeSO_3) and L-cysteine were prepared in aqueous solutions containing acetone and 2-propanol each 2 % (v/v) for the synthesis of CdSe QDs. Typically, a 10 ml solution containing 2 mM ammoniated cadmium sulfate, 0.6 mM L-Cysteine, 0.2 ml 2-propanol and 0.2 ml acetone was prepared named as the Cd solution. Similarly, another 10 ml solution containing 2 mM sodium selenosulfate, 0.2 ml 2-propanol and 0.2 ml acetone was prepared named as Se solution. Finally, 5 ml of Cd solution and 5 ml Se solution were added in a round quartz cell and sealed with a rubber septum. This solution

was named as 1, 1 reaction mixture. Similarly, other reaction mixtures were prepared by just varying the concentrations of ammoniated cadmium sulfate and sodium selenosulfate, without changing the concentrations of L-Cysteine, 2-propanol and acetone. Final concentrations of the precursors, i.e. $[Cd(NH_3)_4]^{2+}$ and $SeSO_3^{2-}$ in different reaction mixtures were; (i) 0.5, 1; (ii) 1, 1; (iii) 1, 0.5; (iv) 1.25, 0.5; (v) 1.5, 0.5 mM, respectively. The concentration of the capping agent L-cysteine was 0.3 mM in all these cases. In these five set of reaction mixtures, we have studied the effect of different compositions of the precursors on the optical properties (mainly steady-state and time-resolved photoluminescence) of the CdSe QDs. We have also studied the cytotoxicity effect of these QDs synthesized from the reaction mixtures of 1, 1 mM and 1, 0.5 mM only. The reaction mixtures were purged with high purity N_2 or Ar gas for about 5 minutes just before photo-irradiation. Photo-irradiation experiments were carried out in a Rayonet photoreactor equipped with sixteen UV lamps with spectral peak at 300 nm. The individual reaction mixture was continuously irradiated for about 1 hour and then taken for further characterizations like FTIR, Raman spectroscopy, XRD and TEM. In order to record the absorption spectra of the QDs at different time intervals, the reaction mixture could not be continuously photo irradiated. A schematic representation is shown below.

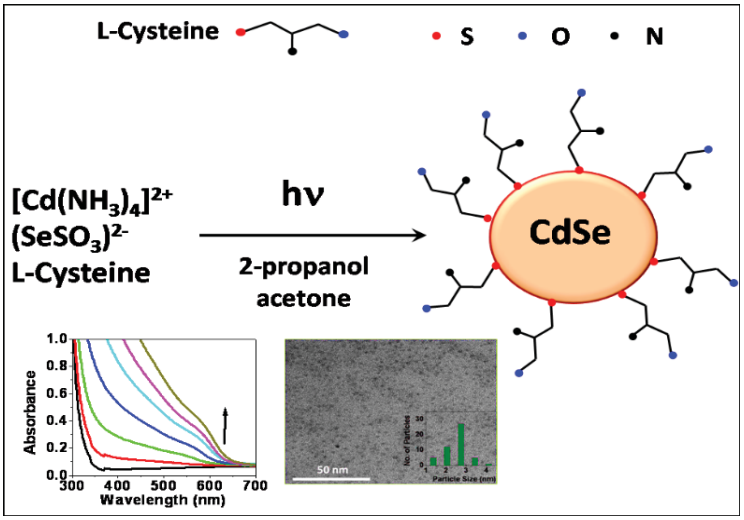

Scheme 3.1 *Photochemical synthesis of L-cysteine capped CdSe quantum dots.*

3.3.2. Synthesis of starch capped CdSe QDs

5 mg/mL of potato starch solution was prepared by taking the required amount of potato starch in 25 mL of water and heated to 60ºC for 20 minutes. The initial turbid solution of starch became clear after heating. This process is termed as gelatinization of starch [135]. Reaction mixture with different amount of $CdSO_4$ and Na_2SeSO_3 were taken in 10 mL flask containing 0.5 mg/mL of starch solution. 2 % v/v of acetone and 2-propanol were added to it. The reaction mixtures were purged with high purity N_2 or Ar gas for about 5 minutes just before photo-irradiation and photo irradiated in a quartz cell sealed with rubber septum, inside a Rayonet Photoreacter equipped with sixteen 300 nm UV lamps. The concentrations of $CdSO_4$and Na_2SeSO_3 were different in the case of different stoichiometric ratios, (i) 0.5:0.5 mM, (ii) 0.5:1.0 mM, (iii) 1.0:0.5 mM, (iv) 1.5:0.5 mM and (v) 2.0:0.5 mM. QDs extracted from the colloidal solution synthesized with 1.5:0.5 mM of precursors were functionalized with thiourea by taking 20 mg of QDs with 10 mM of thiourea in 10 ml water and refluxing it at 85^0 C for 7 hours. Metal ion sensing experiments were performed by diluting ten times the stock solution of the as functionalized QDs followed by addition of 10 mM of different metal ions. Interference study was performed by adding 0.1 mM of Cu^{2+}, 1.0 mM of Cr^{6+} and 2.0 mM of Hg^{2+} along with equal and ten times higher concentration of interfering metal ions (Scheme 3.2).

3.4. Characterization

UV-visible absorption spectra of the reaction mixtures were recorded using a spectrophotometer with a model no. JASCO V650 and a quartz cell with 10 mm optical path length. Room temperature steady-state photoluminescence (Pl) spectra of the QDs were recorded using a spectrofluorometer with a model no. Hitachi F-450. Pl lifetime measurements

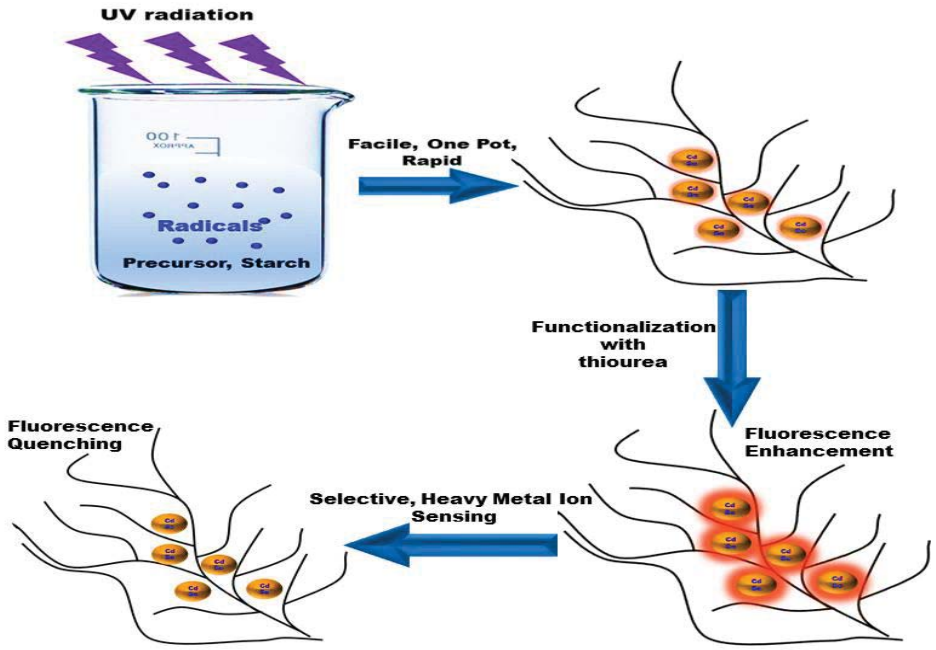

Scheme 3.2 *Photochemical synthesis of starch capped CdSe quantum dots, extraction, functionalization and fluorimetric detection of metal ions.*

were carried out using a time-resolved spectrofluorometer using time-correlated single photon counting (TCSPC) principle with a model no. Horiba Jobin Yvon IBH 400. X-ray diffraction (XRD) measurements of CdSe QDs were carried out by using a Panalytic (model-X-Pert pro) instrument using Cu K-α source. Transmission electron microscopy (TEM) images were recorded using the instrument Libra 120 keV from Carl Zeiss. Samples for TEM measurements were prepared by putting a drop of the as prepared colloidal solution on thin carbon coated copper grid and consecutively allowing the solvent to evaporate. SEM images were recorded using JEOL JSM-T330 SEM instrument. Fourier transform infrared (FTIR) spectra were recorded with the sample put on a KBr pallet using a SHIMADZU IR-Affinity-1 FTIR instrument in diamond ATR mode. Raman spectral studies were carried out on Seki's STR300 Raman spectrometer equipped with a single monochromator (Princeton instruments) and a peltier cooled charge coupled device (CCD). A fiber coupled diode-pumped solid-state laser

(DPSSL) source was used as an excitation source with a wavelength of 532 nm. The spectral and spatial resolution of the Raman system was nearly 3 cm^{-1} and 5 cm^{-1}, respectively.

3.5. MTT assay

The *in vitro* cytotoxicity of CdSe QDs was assessed by a standard (MTT) assay in Chinese Hamster Ovary epithelial (CHO) cells. Firstly, cells suspended in complete medium (RPMI containing 10% fetal calf serum) were seeded in 96-well plate at (5 x 10^3) cells per well and cultured for 12 hours at 37 ºC and 5 % CO_2. The stock solution of CdSe QDs were prepared in phosphate buffered saline (pH 7.4) and added to the cells in culture to attain the desired final concentration raging from (0-10 μg/mL). The cells were cultured for 48 h with the compounds and following this MTT (5 mg/mL) was added to each well, and incubated for another 4 hrs. Finally, sodium dodecyl sulphate (SDS, 10 % in 0.01 N HCl/well) was added, and the optical density at 550 nm for each well was recorded. The percentage (%) cytotoxicity was calculated from the decrease in absorbance of treated samples as compared to that of control by using the following equation

$$\% \text{ cytotoxicity} = 100 - ((OD@570\text{ nm}_{sample}/OD@570\text{ nm}_{control}) \times 100) \quad (3.1)$$

3.6. Results and Discussion

3.6.1. L-Cysteine capped CdSe QDs

Aqueous solution containing $[Cd(NH_3)_4]^{2+}$ and $SeSO_3^{2-}$ (1 mM each) along with acetone and 2-propanol (2 % (v/v) each) was found to undergo a change from transparent colourless to orange colour upon photo-irradiation with UV light for a few minutes. However, this colloidal solution was found to settle down after a few minutes from the post irradiation time. This clearly indicates that the particles are not stabilized to maintain a uniform colloidal solution. Furthermore, it was found that the settled down particles get decomposed with time if the

reaction mixture was not de-aerated. However, these settled down particles were reasonably stable if the reaction mixture was de-aerated with either nitrogen or argon. In order to prohibit the agglomeration leading to the settling down of the as grown colloidal particles, we have added a bio-molecule, L-cysteine in the above reaction mixture, which is expected to act as a capping agent for the particles L-cysteine is also known to act as a reducing agent and hence its concentration was optimized at 0.3 mM which did not induce the formation of CdSe without any photo-irradiation. It was observed that following UV photo-irradiation a clear orange coloured solution was obtained, which did not settle down even after a few days. On the contrary, there was no change in the colour of the reaction mixture under dark condition for several days. This indicates that change in the colour of the solution from colourless to orange colour is certainly associated with the formation of a new species and such process is only initiated by the UV light. It is known that UV light photo excites acetone and the photo excited acetone (triplet state) abstracts one H atom from the nearby 2-propanol to form two 1-hydroxy-2-propyl radicals, $(CH_3)_2C^{\bullet}OH$) in the solution. These radicals are reducing (E^1 = -2.1 V *vs* NHE at pH 12) in nature [136]. It is previously reported that the formation of orange coloured CdSe nanoparticles could take place in aqueous solutions containing even less than 1 mM $[Cd(NH_3)_4]^{2+}$ and $SeSO_3^{2-}$ through the reactions of these precursors with a strongly reducing agent, hydrated electron (e_{aq}^-) which is generated upon water radiolysis [137]. This hydrated electron reduces $[Cd(NH_3)_4]^{2+}$ to $Cd^{\bullet+}$ and releases $Se^{\bullet-}$ from $SeSO_3^{2-}$ and subsequently these two radical ions react to form CdSe [134]. Therefore, it is here expected that these reducing radicals could also initiate such processes leading to the formation of CdSe nanoparticles. An initial guess from appearance of the orange colour of the photolysed reaction mixture indicates that the products could be CdSe nanoparticles. However, for the confirmation regarding the products obtained, we have carried out various characterization measurements.

3.6.1.1. Characterization of L-Cysteine capped CdSe QDs

The orange coloured colloidal particles in the photolysed solution were precipitated and recovered by repeated centrifugation followed by washing with nanopure water. The solid powder was dried under IR lamp. These products were analyzed by XRD measurements. One representative XRD pattern for the product obtained from the reaction mixture containing the precursors 1 mM each is shown in Fig. 3.1a. It has three peaks with 2θ values at 25.4°, 42.5° and 50.3° corresponding to (1 1 1), (2 2 0) and (3 1 1) lattice planes which matches the standard ICDD no.19-191 and confirms the cubic phase of CdSe nanocrystallites with typical zinc blende structure [138]. The broadening of peaks confirms the formation of nanocrystalline CdSe structure. Similar XRD patterns were also obtained for the products from other reaction mixtures. The effective lattice strain and the crystallite size of these CdSe nanoparticles were determined by the modified Scherrer formula [139].

$$\frac{\beta\cos\theta}{\lambda} = \frac{1}{\varepsilon} + \frac{\eta\sin\theta}{\lambda} \qquad (3.2)$$

where, β is the FWHM of the peak, θ half of 2θ value corresponding to the peak, λ is the wavelength of the X-ray (Cu-Kα), i.e. 1.5406 Å, ε is the crystallite size and η is the effective strain in the lattice. From the plot of βcosθ/λ *vs* sinθ/λ the value of the crystallite size was found to be 2.3 nm and the effective strain was -0.13. As the crystallite size obtained in this study is less than the exciton Bohr radius of CdSe (i.e. 5.6 nm), these nanoparticles are written as QDs throughout the text. Room temperature Raman spectra of as synthesized CdSe QDs (synthesized with the precursors 1 mM each) as shown in Fig. 3.1 b comprises of fundamental longitudinal optical phonon peak (LO) at 205 cm^{-1} along with its overtone (2LO) peak at 411 cm^{-1}. There is a red shift (down shift) from its position in the bulk CdSe of 210-213 cm^{-1} [140].

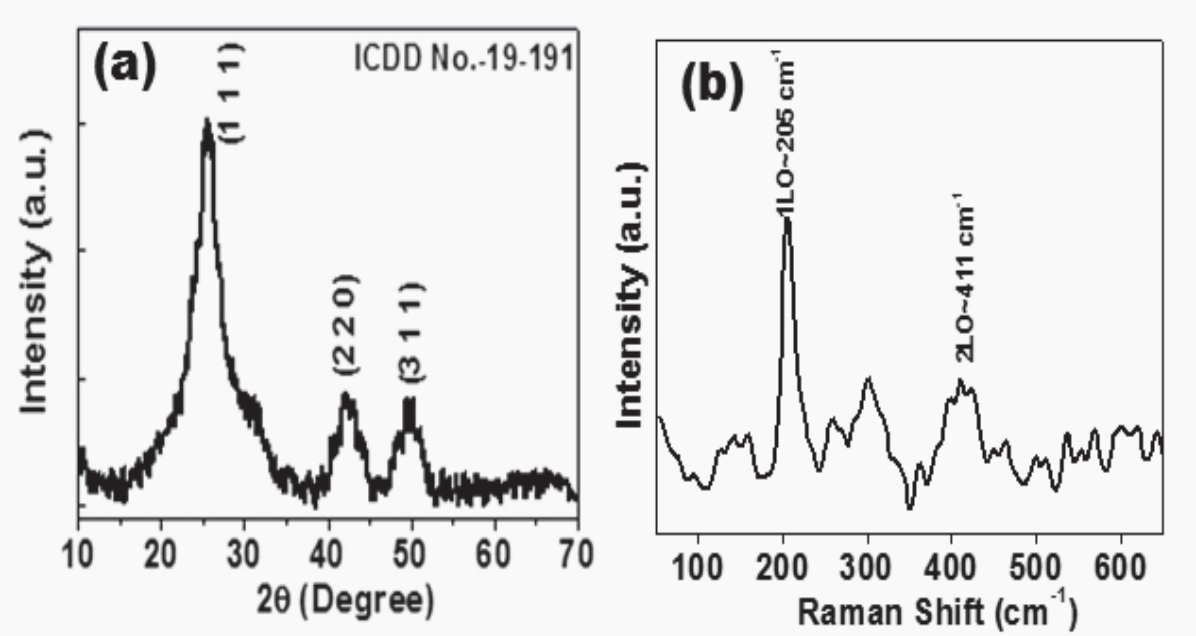

Figure 3.1 *(a) XRD pattern and (b) Raman Spectra of CdSe QDs synthesized with the precursors 1 mM each and L-cysteine 0.3 mM upon UV photo-irradiation.*

CdSe QDs were analyzed by TEM measurements. TEM images obtained for the CdSe QDs synthesized from the reaction mixture containing the Cd and Se precursors 1.0 mM each and for 1.0 and 0.5 mM are shown in Fig. 3.2 a and b respectively. It is observed that the particles are spherical in nature having a narrow size distribution of with maximum in the range 2 - 6 nm (shown in the inset of Fig. 3.2). This result matches well with that obtained in the case of XRD measurements. FTIR spectra of both L-cysteine and L-cysteine capped CdSe QDs (synthesized with the precursors 1 mM each) are shown in Fig. 3.3. L-Cysteine has potentially three binding sites i.e. – thiol, amino and carboxylate groups. In the free L-Cysteine the presence of strong bands at 1595 cm^{-1} and 1400 cm^{-1} are due to NH_2 asymmetric bending and COO^- symmetric stretching band confirms the zwitter ionic form of L-Cysteine. The broad band at 3200-2700 cm^{-1} corresponds to NH_3^+ symmetric vibration and at 1130 cm^{-1} corresponds to NH_3^+ rocking mode. Bands at 1480 and 1380 cm^{-1} correspond to $–COO^-$ asymmetric and symmetric bands.

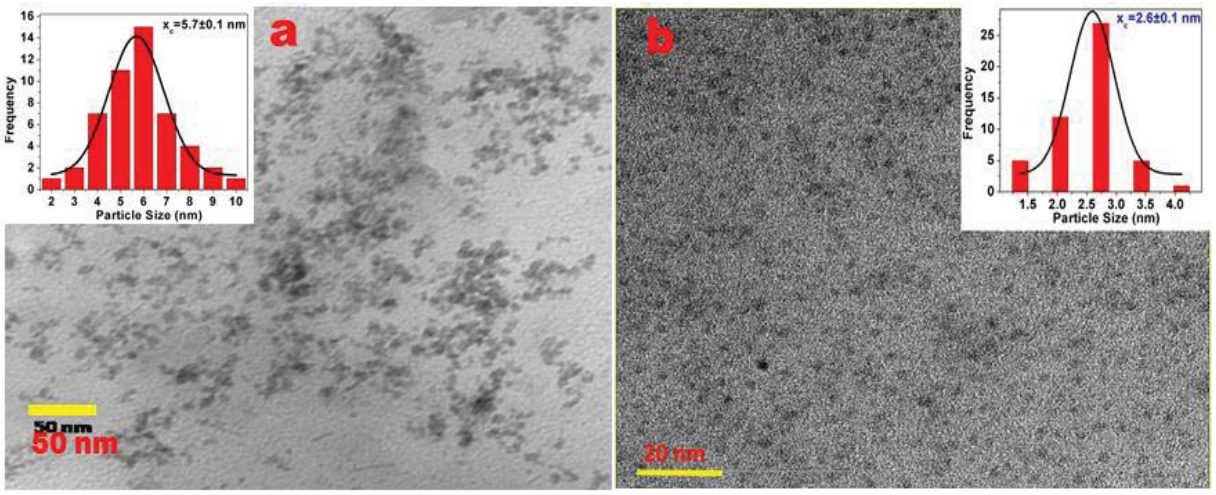

Figure 3.2 *TEM image of CdSe QDs synthesized with the precursors (a) 1 mM each (b) 1 mM and 0.5 mM of Cd and Se respectively and L-cysteine 0.3 mM upon UV photo-irradiation, Inset: Histogram plot showing the particle size distribution.*

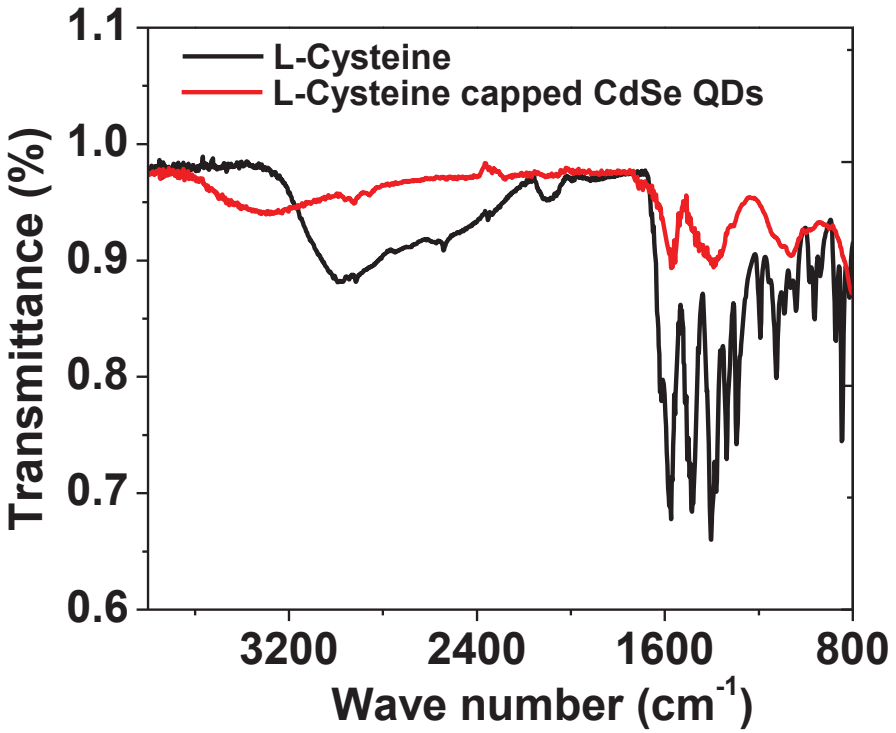

Figure 3.3 *FTIR spectra of a) L-Cysteine and b) L-cysteine capped CdSe QDs.*

The S-H stretching and bending frequencies of vibrations were observed at around 2500 cm^{-1} and 960 cm^{-1} respectively. In the FTIR spectra of CdSe capped by L-Cysteine these bands for

–SH are absent. This arises because of the cleavage of the S-H bond and the formation of new Cd-S bond [141]. This observation provides a clear evidence of surface bonding of L-cysteine with the CdSe QDs. The broad band in the region of 2200 - 3200 cm^{-1} obtained in the case of L-cysteine is found to be red shifted to 2700 - 3600 cm^{-1} in the case of L-cysteine capped CdSe QDs. This is due to the N-H and N-H-O stretching which may arise because of H-bonding in the alkaline pH of the reaction mixture. The sharp peaks in the region of 1040 - 1580 cm^{-1} in the case of L-cysteine became weaker and get merged at three broad peaks in the case of L-cysteine capped CdSe, which is probably due to the change in pH and change in the dipole moment when L-cysteine binds with the metal surface with high electron density [142, 143]. It can also be seen that the characteristic frequency at 1400 cm^{-1} and 1580 cm^{-1}, which corresponds to COO^- symmetric stretch and NH_2 asymmetric bending mode [144], respectively are present in both the spectra. This observation confirms the capping of the CdSe QDs surface is occurring by L-cysteine *via* the thiol group. Similar observations were found in the case of CdSe QDs synthesized with other reaction mixtures. All these studies clearly confirmed that L-cysteine capped CdSe QDs are formed in the aqueous solution containing 2 % (v/v) acetone and 2-propanol from the precursors $[Cd(NH_3)_4]^{2+}$ and $SeSO_3^{2-}$ 1 mM each in the presence of 0.3 mM L-cysteine. CdSe QDs synthesized from other reaction mixtures also exhibit similar results confirming the capping of L-cysteine with these QDs.

Based on these observations, it can be mentioned that 1-hydroxy-2-propyl radicals, $(CH_3)_2C^{\bullet}OH$ reduce $[Cd(NH_3)_4]^{2+}$ to form $Cd^{\bullet+}$ and reacts with $SeSO_3^{2-}$ to give $Se^{\bullet-}$. $Cd^{\bullet+}$ and $Se^{\bullet-}$ react to form CdSe, which finally undergoes nucleation and growth to form CdSe QDs. L-Cysteine in the present case acts as capping agent as its concentration is very low. The surface of these QDs gets passivated by the L-cysteine molecules present in the solution, which prevent them from getting agglomerated. The reaction mechanism proposed is as follows.

$$(CH_3)_2C^{\bullet}OH + [Cd(NH_3)_4]^{2+} \longrightarrow Cd^{\bullet+} + (CH_3)_2CO + H^+ \quad (3.3)$$

$$SeSO_3^{2-} + (CH_3)_2C^{\bullet}OH \longrightarrow Se^{\bullet-} + SO_3^{2-} + (CH_3)_2CO + H^+ \quad (3.4)$$

$$Cd^{\bullet+} + Se^{\bullet-} \longrightarrow CdSe \dashrightarrow (CdSe)_n \quad (3.5)$$

It is to be noted here that the H^+ ions generated in the above reactions, gets neutralized by the ammonia present in the solution. L-Cysteine molecules get involved in the surface binding with these QDs through the SH group. Therefore, the as grown QDs do not get precipitated out from the solution.

3.6.1.2. UV-visible absorption studies

UV-vis absorption spectra of the reaction mixtures containing different concentrations of the precursors and L-cysteine were recorded at different time of UV photo-irradiation. Figure 3.4 shows the absorption spectra recorded at different time of photo-irradiation for the solution containing (a)1 mM each precursors (Cd:Se = 1:1) , (b) 1 and 0.5 mM of Cd and Se respectively and 0.3 mM L-cysteine along with 2 % (v/v) acetone and 2-propanol. It is observed from this figure that there is an increase in the absorbance value with time of photo-irradiation. This clearly confirms that there is a growth of CdSe QDs during the photo-irradiation with time. The particle size of these QDs was calculated by using the empirical formula given Peng and coworkers [145]. The estimated values of the particle sizes were found to be within 3 to 4 nm, which match well with those obtained from the XRD and TEM measurements. It was observed that the formation of CdSe QDs with 1.0 mM and 0.5 mM of Cd and Se precursors respectively was complete within 10 minutes, whereas in the case of reaction mixture containing 1 mM each precursors and 0.3 mM L-cysteine the formation is not complete even up to 1 hour.

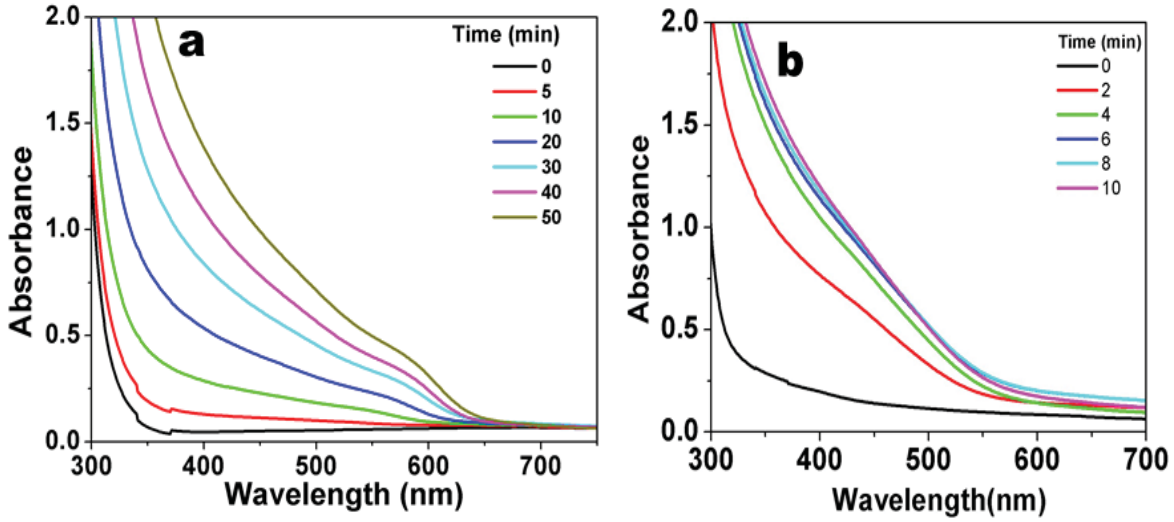

Figure 3.4 *UV-vis absorption spectra of CdSe QDs synthesized with the precursors (a) 1 mM each (b) 1 mM and 0.5 mM of Cd and Se respectively and L-cysteine 0.3 mM each upon UV photo-irradiation at different time intervals.*

In the case of reaction mixture containing 0.5 mM $[Cd(NH_3)_4]^{2+}$, 1 mM $SeSO_3^{2-}$ (Cd:Se = 1:2), 0.3 mM L-cysteine along with acetone and 2-propanol each 2 % (v/v), it was observed that the formation of CdSe QDs was complete even at an earlier time of photo-irradiation. However, the QDs in this case were not stable and underwent agglomeration to form bigger particles in the solution. It was thus clear that for a higher Cd:Se ratio of 2:1, CdSe QDs are better capped with L-cysteine leading to a higher stability of the QDs. However, for a lower Cd:Se ratio of 1:2, the QDs are weakly capped with L-cysteine and thus the QDs could easily get agglomerated to form bigger particles. The possible explanation of these observations is that L-cysteine has stronger affinity towards Cd compared to Se and it binds to the surface Cd atoms as evidenced from the FTIR studies mentioned in the previous section.

3.6.1.3. Photoluminescence studies

Steady state photoluminescence (Pl) spectra of the fully grown CdSe QDs were recorded at room temperature with an excitation wavelength 400 nm (shown in Fig. 3.5 (i)). The CdSe QDs

studied here were grown with various reaction mixtures containing different concentrations of precursors $[Cd(NH_3)_4]^{2+}$ and $SeSO_3^{2-}$ as (a) 1 mM each (Cd:Se = 1:1), (b) 1 and 0.5 mM (Cd:Se = 2:1), (c) 1.25 and 0.5 mM (Cd:Se = 2.5:1) and (d) 1.5 and 0.5 mM (Cd:Se = 3:1) with 0.3 mM L-cysteine. It is observed that the Pl spectra are very broad having emission from 480 to 750 nm with the emission maximum at 580 nm and FWHM of 170 nm. The emission intensity was found to increase with the increase in the Cd:Se ratio in the reaction mixture. This is probably due to the decrease in the surface trap states in the CdSe QDs with an increase in the Cd content which arises because of better surface passivation by L-cysteine with Cd.

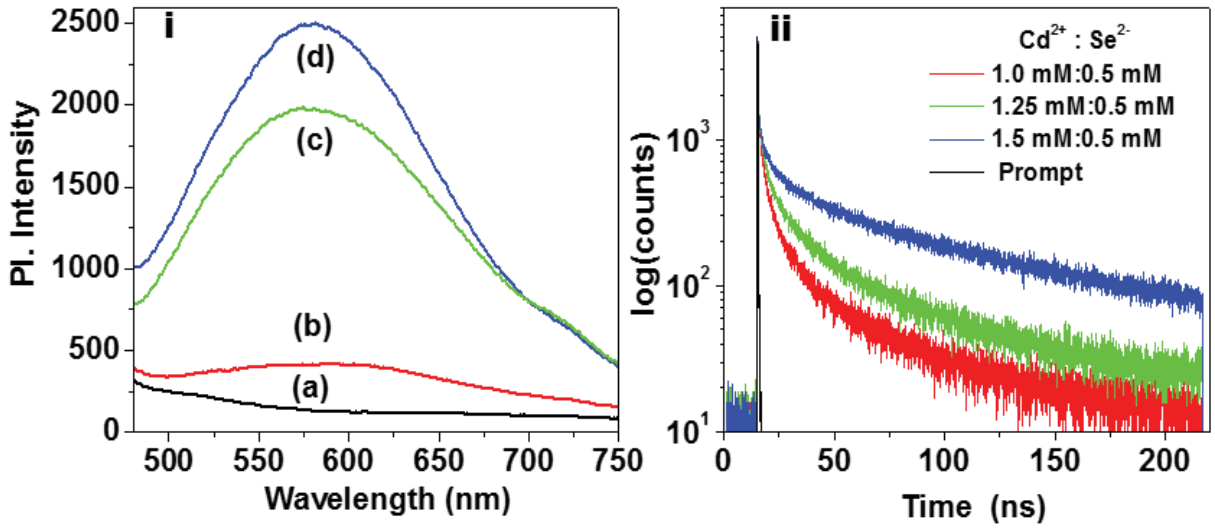

Figure 3.5 (i) *Room temperature steady-state Pl spectra of CdSe QDs synthesized with different concentrations of the precursors, a) 1,1; b) 1, 0.5; c) 1.25,0.5; and d) 1.5,0.5 mM; (ii) Time resolved Pl decay profiles of CdSe QDs for concentrations of the precursors.*

Time resolved Pl measurements were carried out by using a time correlated single photon counting (TCSPC) instrument to find out the Pl lifetime of the CdSe QDs synthesized in the reaction mixtures as mentioned above (Fig. 3.5 (ii)). The samples were excited by a diode laser of output wavelength of 405 nm with an IRF of less than 100 ps and Pl was monitored at 580 nm. The instrument response function (IRF) of the setup was measured by collecting the

scattered light at 405 nm from a TiO_2 suspension in water. The Pl decay profiles of these CdSe QDs were of multi-exponential behaviour and fitted with tri-exponential fitting function to obtain a χ^2 value close to 1. The average lifetime values $<\tau>$ were calculated using the eq. (3.6) below.

$$<\tau> = \frac{a_1\tau_1 + a_2\tau_2 + a_3\tau_3}{a_1 + a_2 + a_3} \quad (3.6)$$

It was observed that the average lifetime value of the CdSe QDs increases with the increase in the Cd content in the reaction mixture as 2:1 < 2.5:1 < 3:1 (see Table 3.1).

Table 3.1 Pl lifetime values of CdSe QDs prepared with various compositions of the precursors (in mM) and L-cysteine concentration of 0.3 mM.

Cd, Se	τ_1 (ns)	a_1	τ_2 (ns)	a_2	τ_3 (ns)	a_3	$<\tau>$ (ns)	χ^2
1.0, 0.5	0.37	0.130	4.46	0.345	37.02	0.525	21.0	1.256
1.25,0.5	0.33	0.080	5.19	0.260	41.59	0.660	28.8	1.248
1.5, 0.5	0.32	0.040	5.78	0.110	66.62	0.850	57.3	1.146

This could be explained as follows. In the case of higher Cd content, there is a higher degree of surface passivation by L-cysteine, which reduces the number of surface trap states. Therefore, there is a decrease in the carrier relaxation pathways by these trap states leading to an increase in the Pl lifetime value of the CdSe QDs.

3.6.1.4. *In vitro* toxicity study of CdSe QDs

The biocompatibility of above CdSe QDs prepared under different conditions was evaluated in epithelial (CHO) cells by monitoring the viability at 48 h after their addition to cells. The results

as show in Fig. 3.6 indicated that addition of uncapped QDs to cells with stoichiometry of 1:1 and 2:1 induced concentration (1-10 µg/ml) dependent cytotoxicity.

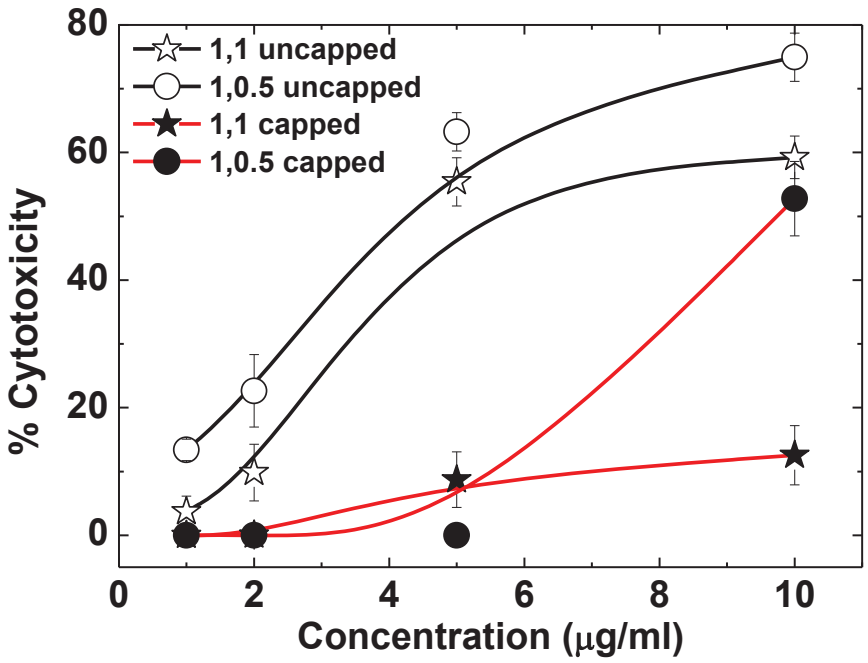

Figure 3.6 *Line graph showing the % cytotoxicity of CdSe QDs synthesized with different concentrations of the precursors and L-cysteine 0.3 mM under UV photo-irradiation, prepared under different conditions in CHO cells as determined by the MTT assay. Values are mean ± SEM (n = 4).*

The cytotoxicity of 2:1 in comparison to 1:1 was higher at each of the concentrations tested (1-10 µg/ml). The capped QDs (1:1 and 2:1) did not show any toxicity up to 5 µg/ml. At higher concentration (10 µg/ml), we could observe an increase in cytotoxicity of capped QDs, however it was significantly lower as compared to respective uncapped QDs. As the particle size for the 2:1 ratio are smaller, they are expected to have larger surface area as well as more number of Cd atom on the surface compared to the 1:1 ratio. Hence, both the concentration and surface effects will lead to increase in the cytotoxicity of 2:1 as compared to the 1:1 ratio. It is also worth to note here that the 2:1 capped QDs showed lesser cytotoxicity than the 1:1 capped.

This suggested that higher the Cd concentration better is the capping by the L-cysteine. Thus it is confirmed that capping can be used as a strategy to modulate the toxicity of synthetic CdSe QDs and convert them to biocompatible for desired biological usage.

3.6.2. Starch capped CdSe QDs

3.6.2.1. Synthesis of starch capped CdSe QDs

The reaction mixture in one of the cases was prepared by taking 0.5 mM of $CdSO_4$, 0.5 mM of Na_2SeSO_3, 0.5 mg/mL of starch solution, 2% v/v of acetone and 2% v/v of 2-propanol. After photoirradiation, the colourless solution changed to orange coloured colloidal solution (Fig. 3.7).

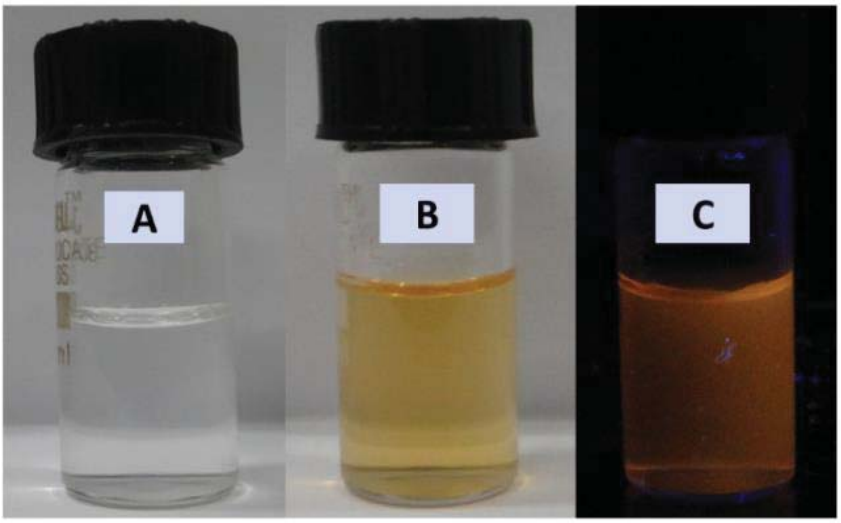

Figure 3.7 *(a) Unirradiated reaction mixture containing Cd:Se precursors as 0.5:0.5 mM along with 0.5 mg/ml starch in the presence of 2 % (v/v) acetone and 2-propanol, (b) orange-yellow coloured colloidal solution obtained after photoirradiation with 300 nm UV lamp.*

The complete reaction mechanism has already been discussed (section 3.4.1.1. equation 2-4). The growth of CdSe QDs was monitored by recording the absorption spectra at different time of irradiation. Fig. 3.8 shows the absorption spectra of a solution containing 1.5 mM of $CdSO_4$ and 0.5 mM of Na_2SeSO_3 at different time of photoirradiation. After around 10 minutes

of photoirradiation, the absorbance did not increase further indicating the synhtesis of CdSe QDs has been completed. In the absence of acetone, the colour of the reaction mixture does not change, which indicates the reaction is initiated by the excited state of acetone only. The excitonic peak position as well as particle size (calculated from Brus equation) [10] were plotted at different time of photoirradiation (insets of Fig. 3.8). The Pl spectra of as synthesized QDs (with different stoichiometric ratio of $CdSO_4$ and Na_2SeSO_3) were recorded (Fig. 3.9 a). It was found that the emission intensity increases with increase in Cd:Se ratio and was maximum for 1.5:0.5 mM. The QDs synhtesized with Cd:Se ratio 0.5:0.5 mM and 0.5:1.0 mM were found to be non photoluminescent in nature.

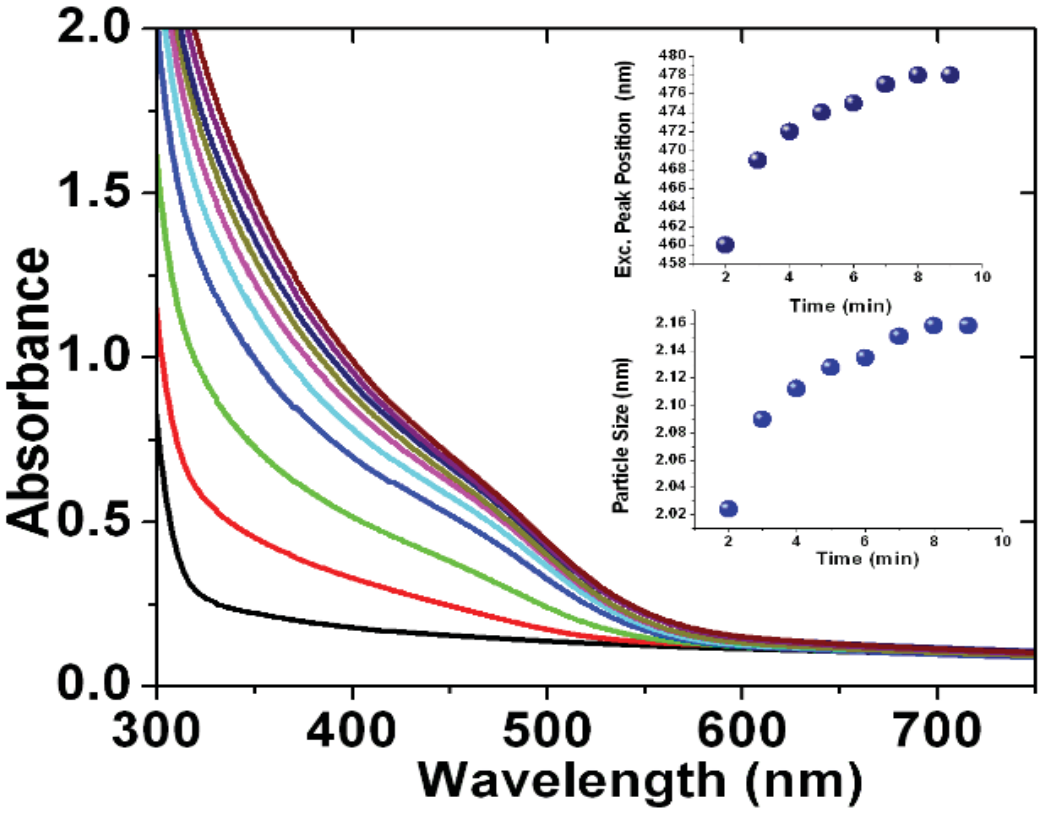

Figure 3.8 *Absorption spectra of reaction mixture containing Cd and Se precursor with starch at different time of photoirradiation (inset; excitonic peak position and particle size vs. time).*

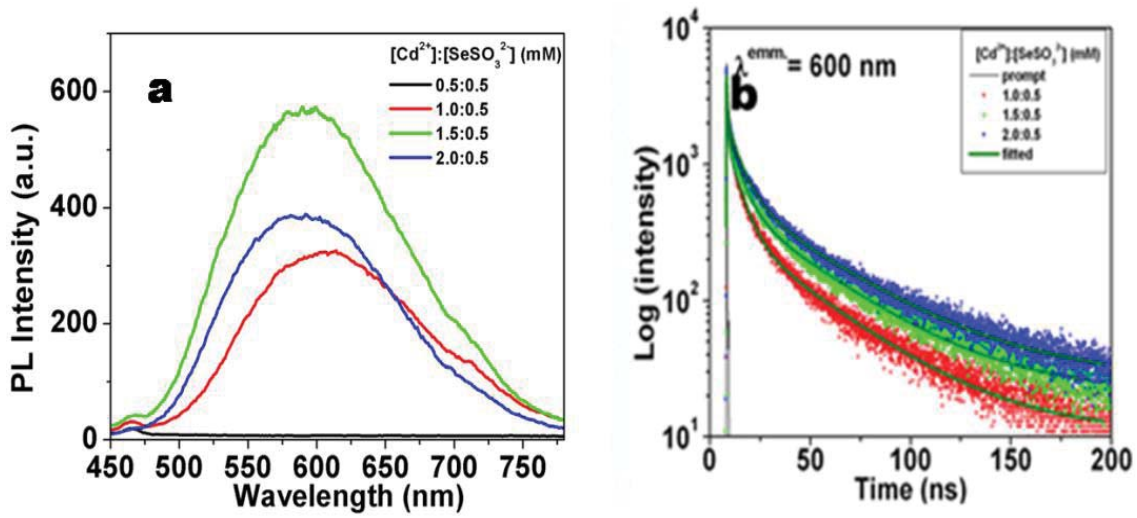

Figure 3.9 *(a) steady-state Pl spectra and (b) time-resolved Pl decay profiles of CdSe QDs synthesized with different Cd:Se precursor ratios.*

The Pl spectra were broad with emission from 500-750 nm with FWHM~150 nm. The Pl lifetimes of the CdSe QDs with Cd:Se ratio 1.0:0.5, 1.5:0.5 and 2.0:0.5 mM (Fig. 3.9 b) have two components (τ_1 and τ_2), which is expected to be originated from the band gap (τ_1) and trap states (τ_2) [146]. The band gap (τ_1) e-h pair recombine rapidly and have short life time (<10 ns), while the trap state (τ_2) e-h pair recombine slowly having lifetime larger than 30 ns.

Table 3.2 Pl lifetime values of CdSe QDs prepared with various compositions of precursors (mM).

$[Cd^{2+}]$:$[Se^{2-}]$ (mM)	lifetime (ns)				
	τ_1	A_1	τ_2	A_2	$<\tau>$
1.0:0.5	6.16	0.38	38.3	0.62	26.1
1.5:0.5	5.93	0.31	39.6	0.69	29.2
2.0:0.5	6.95	0.30	43.4	0.70	32.5

It was observed that the average lifetime value of the CdSe QDs increases with the increase in the Cd content in the reaction mixture (see Table 3.2). The QDs containing higher Cd to Se ratio get better capped by starch molecules and hence have better Pl and therefore the QDs synthesized with lower Cd:Se ratio 0.5:0.5 and 0.5:1.0 mM have very poor Pl.

The QDs were extracted by following a novel colloidal processing method developed in this study. The room temperature colloidal solution of QDs was first freezed at 0^0C and then was allowed to de-freeze to room temperature. The amylose and amylopectin residues present in starch got sedimented after freezing (Fig. 3.10 a) [147].

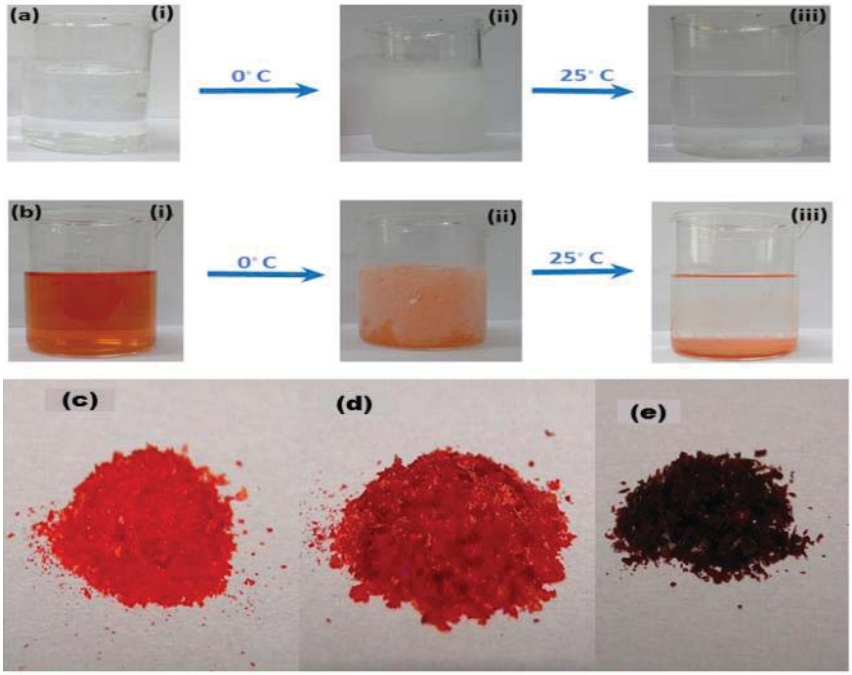

Figure 3.10 *(a) colloidal solution of starch; at room temperature (i), after freezing (ii), and again after attaining room temperature (iii), (b) colloidal solution of CdSe QDs capped with starch (i), after freezing (ii) and again after attaining room temperature, extracted QDs synthesized from reaction mixture with (c) 1.5:0.5, (d) 1.0:0.5 and (e)0.5:0.5 mM of Cd:Se.*

The colloidal solution of CdSe QDs was also found to get sedimented along with the amylose and amylopectin residues of starch in the bottom of the beaker (Fig. 3.10 b). The

sedimented starch along with QDs could be easily extracted out in the powder form (Fig. 3.10 c, d, e).

3.6.2.2. Characterization of starch capped CdSe QDs.

The XRD pattern of CdSe QDs (Fig. 3.11a) confirms cubic zinc blende crystal of CdSe [18]. The crystallite size was calculated by the Scherrer formula and was found to be around 2.0 nm. Raman spectra of the CdSe QDs (Fig. 3.11b) shows two prominent peaks at 204 and 409 cm^{-1} which corresponds to 1st and 2nd order longitudinal modes of CdSe nanocrystals [140]. TEM image of the particle is shown in Fig. 3.12a. The image showed that the particles are well dispersed and spherical in size having maximum size around 3 nm.

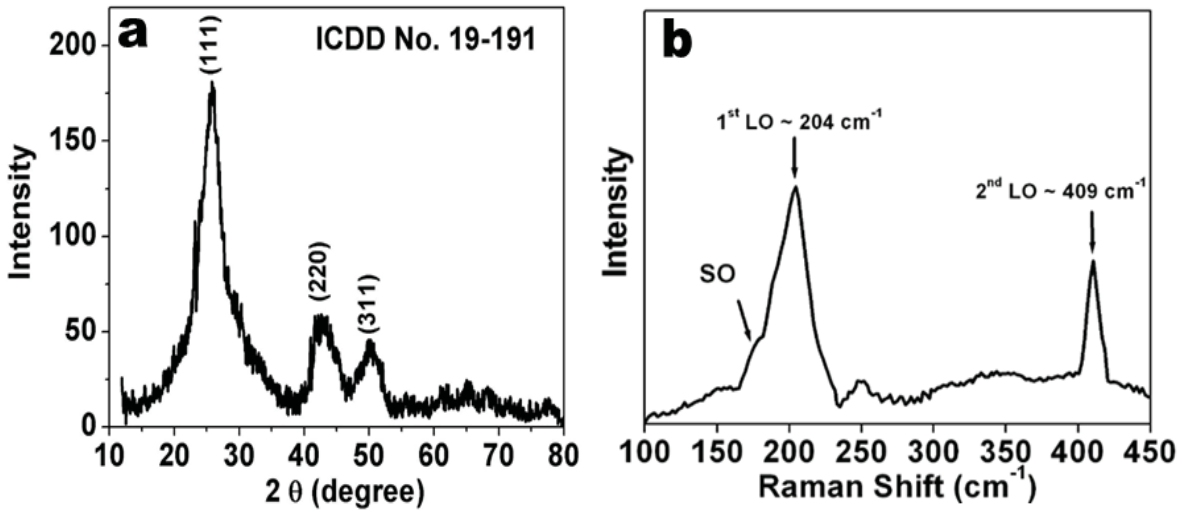

Figure 3.11 *(a) XRD and (b) Raman spectra of starch capped CdSe QDs synthesized with 1.0 and 0.5 mM of Cd and Se.*

The FFT pattern (inset Fig. 3.12a) shows the wave vector corresponding to (111) and (200) planes with 54^0 of angle between them. The HRTEM image clearly showed the (111) and (200) planes with inter planar distance of 3.5 Å and 2.9 Å respectively, which matches very well with the cubic zinc blende crystal structure of CdSe. The TEM The SEM image shows spherical

shapes of relatively bigger size, which indicates that these QDs exist in agglomerated form (Fig. 3.12b).

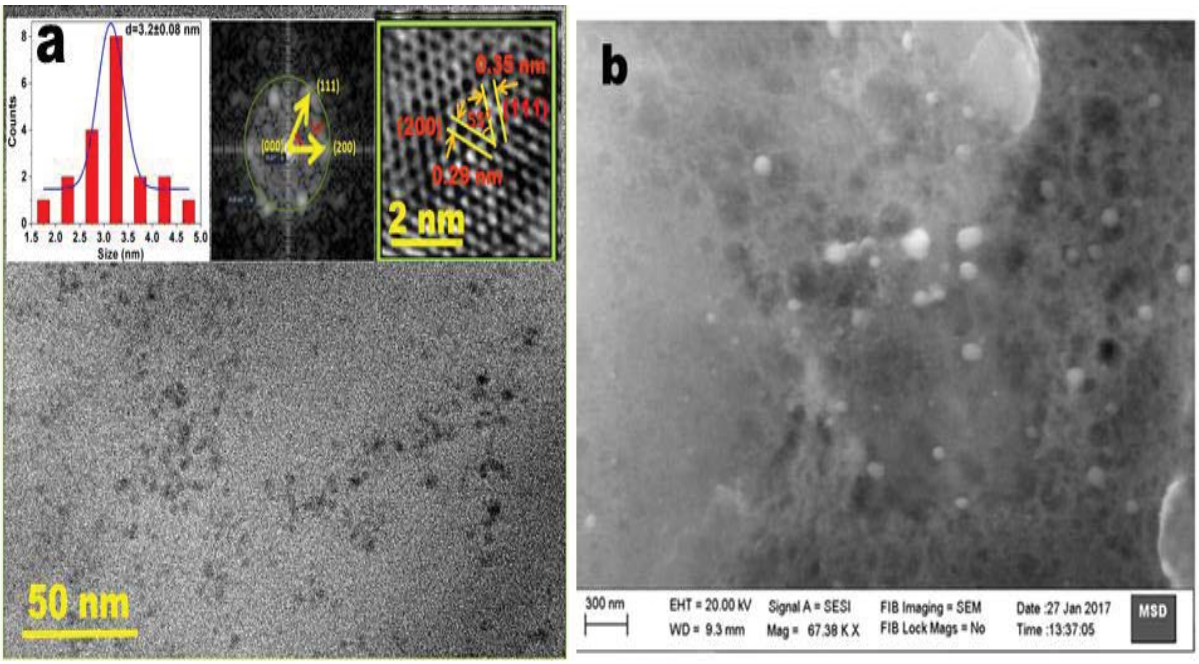

Figure 3.12 *a) TEM image of CdSe QDs (inset 1; particle size distribution, inset 2 FFT pattern and inset 3 HRTEM image showing inter planar distances corresponding to (111) and (200) planes, (b) SEM image showing aggregated morphology of CdSe QDs.*

In the FTIR spectra (Fig. 3.13) the OH stretching peak present in starch (3650-3000 cm^{-1}) is very broad shows the presence of several OH groups, inter and intra molecular hydrogen bonding in starch. The other peaks are at 2900 cm^{-1}(asymmetric C-H stretching), 1640 cm^{-1} (O-H bending of water in starch), 1340 cm^{-1} (angular deformation of C-H bond), 1150 cm^{-1}(C-O and C-C stretching), 1075 cm^{-1} (C-O-H bending), 998 cm^{-1} (skeletal vibration of α 1-4 glyosidic linkage (C-O-C), 926 cm^{-1} (C-C stretching) and 850 cm^{-1} (C_2 deformation) [148]. The starch capped CdSe samples give distinct peaks which indicate the existence of starch on CdSe surface. The extracted QDs were modified by surface functionalized with thiourea to increase its PL quantum yield and stability. In the FTIR spectra of thiourea functionalized CdSe QDs, the characteristics peaks of thiourea at 3365 cm^{-1}, 3275 cm^{-1}, 3150 cm^{-1} (symmetric and

asymmetric stretching of NH, NH_2), 1600 cm^{-1} (NH_2 bending), 1400 cm^{-1} (CN stretching), 1075 cm^{-1} (NH_2 rocking), 734 cm^{-1} (CS asymmetric stretching) and 620 cm^{-1} (CS symmetric stretching) [149] vanishes in thiourea functionalized CdSe QDs, which confirmed the binding

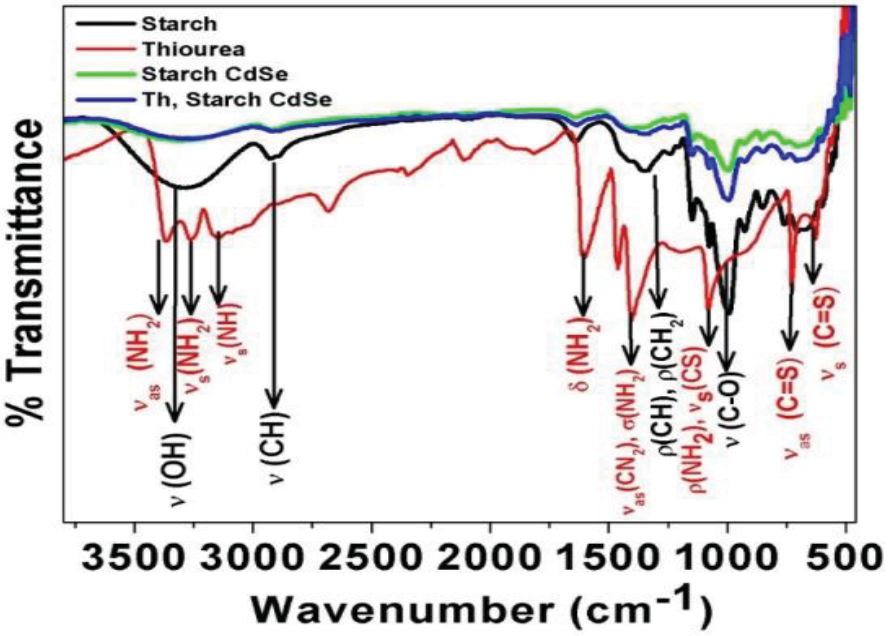

Figure 3.13 *FTIR spectra of starch, thiourea, starch CdSe and starch CdSe with thiourea.*

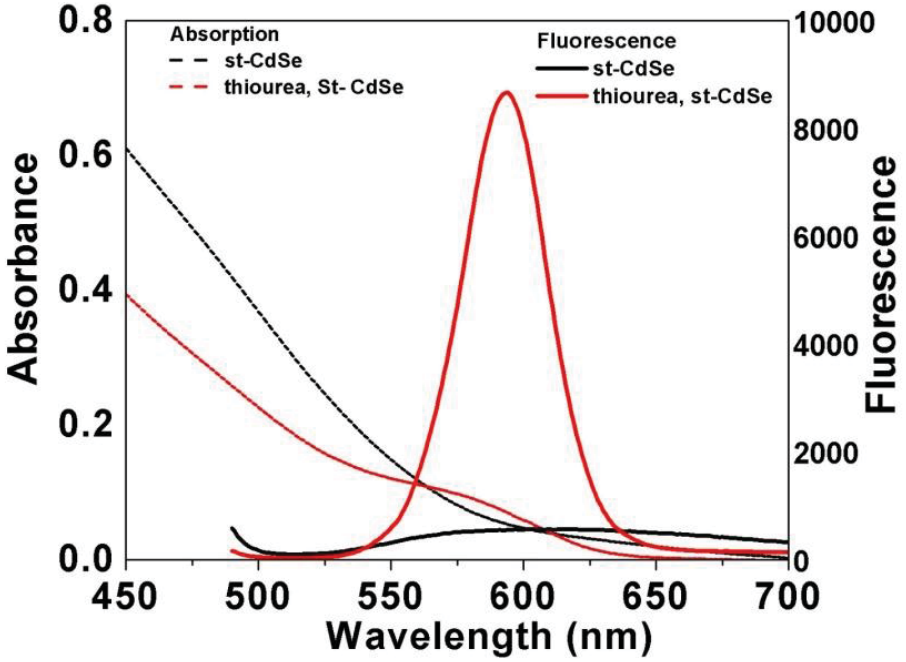

Figure 3.14 *Absorption and photoluminescence spectra of starch capped CdSe QDs and after functionalization with thiourea.*

of thiourea on the surface of the QDs. It is worth to mention here that before functionalization with thiourea the PL spectrum is broad having emission mainly from trap states, however, after functionalization the PL spectrum becomes narrow with very low stokes shift (Fig. 3.14) and therefore it could be mainly arising from the band gap recombination of the charge carriers. Further to confirm the functionalization, we recorded the DLS (dynamic light scattering) measurements of starch capped CdSe QDs both before and after functionalization with thiourea. We found that the hydrodynamic diameter of QDs increases after functionalization from 193 nm to 267 nm (Fig. 3.15). Such an increase in the hydrodynamic diameter clearly indicates the functionalization of QDs [150].

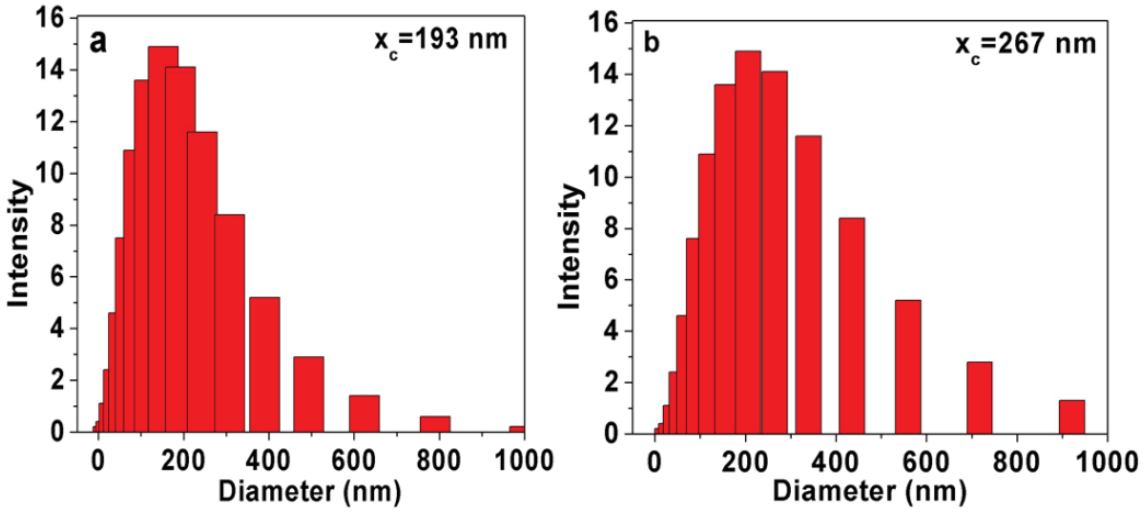

Fig. 3.15 *DLS histograms of starch capped CdSe QDs a) before and b) after functionalization with thiourea.*

3.6.2.3. Effect of temperature and pH on the Pl properties of thiourea functionalized CdSe QDs

The effect of temperature on the Pl properties of thiourea functionalized CdSe QDs was studied by recording the temperature dependent Pl spectra from 5^0C to 80^0C (Fig. 3.16a). From these spectra it is clearly evident that QDs have maximum Pl at 20^0C. Further on increasing or

decreasing temperature the Pl yield decreases. Also the Pl peak position shifts from 592 nm at room temperature to 600 nm at 80^0 C. This red shift can be attributed to minute change in particle size after ligand detachment from the surface of QDs at higher temperature [151].

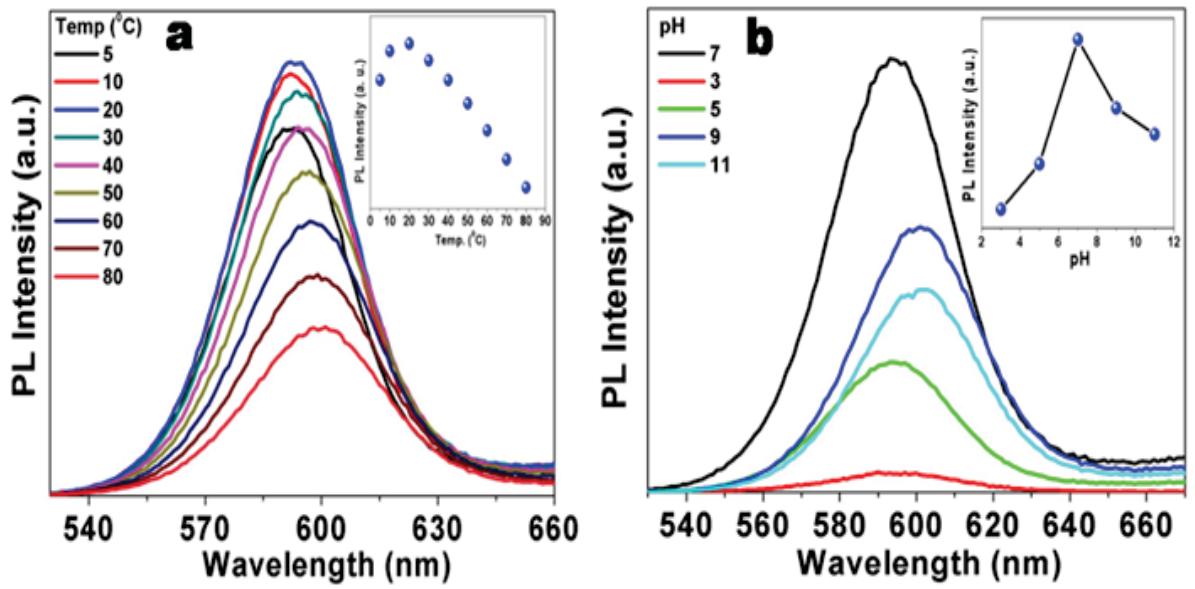

Figure 3.16 *Temperature dependent (a) and pH dependent (b) Pl spectra of thiourea functionalized CdSe QDs.*

On increasing the temperature, the surface capped molecules get detached from the surface of the QDs and create surface defects which enhance the non-radiative recombination of charge carriers and hence there is reduction in Pl Intensity [152] as well as an increase in broadness [153]. It is a well-known fact that the loss of capping ligands from the surface of QDs creates surface defects. The Pl spectra of thiourea functionalized CdSe QDs were also recorded after changing the pH of the colloidal solution from 3 to 11 (Fig. 3.16b). It was found that the Pl yield decreased on either decreasing or increasing from the neutral pH. At lower pH, the thiourea and starch gets protonated and the QDs become destabilized, hence the Pl intensity decreases. At higher pH, the formation of hydrated product on the surface of QDs might cause

a reduction in the Pl intensity. Furthermore, the metal ions also get precipitated as their corresponding hydroxides at higher pH causing a reduction in the Pl intensity/yield [154].

3.6.2.4. Metal ion sensing studies

3.6.2.4.1. Selectivity

Thiourea functionalized CdSe QDs were used in the sensing of various metal ions. 10. 0 μM concentration of Hg^{+}, Hg^{2+}, Co^{2+}, Cr^{3+}, Cr^{6+}, Zn^{2+}, Pb^{2+}, Cd^{2+}, Ni^{2+}, Mn^{2+}, Fe^{3+} or Cu^{2+} were added to the aqueous QDs solution. Out of these metal ions only Cu^{2+}, Cr^{6+} and Hg^{2+}were able to selectively quench the Pl intensity of QDs. (Fig. 3.17). Others metal ions were not able to quench the Pl intensity appreciably.

3.6.2.4.2. Pl quenching by Cu^{2+}, Cr^{6+} or Hg^{2+} ions

The effect of Cu^{2+}, Cr^{6+} or Hg^{2+} ions on the Pl quenching of CdSe QDs among various metal ions is established from their Pl investigations (Fig. 3.17) in presence of different metal ions.

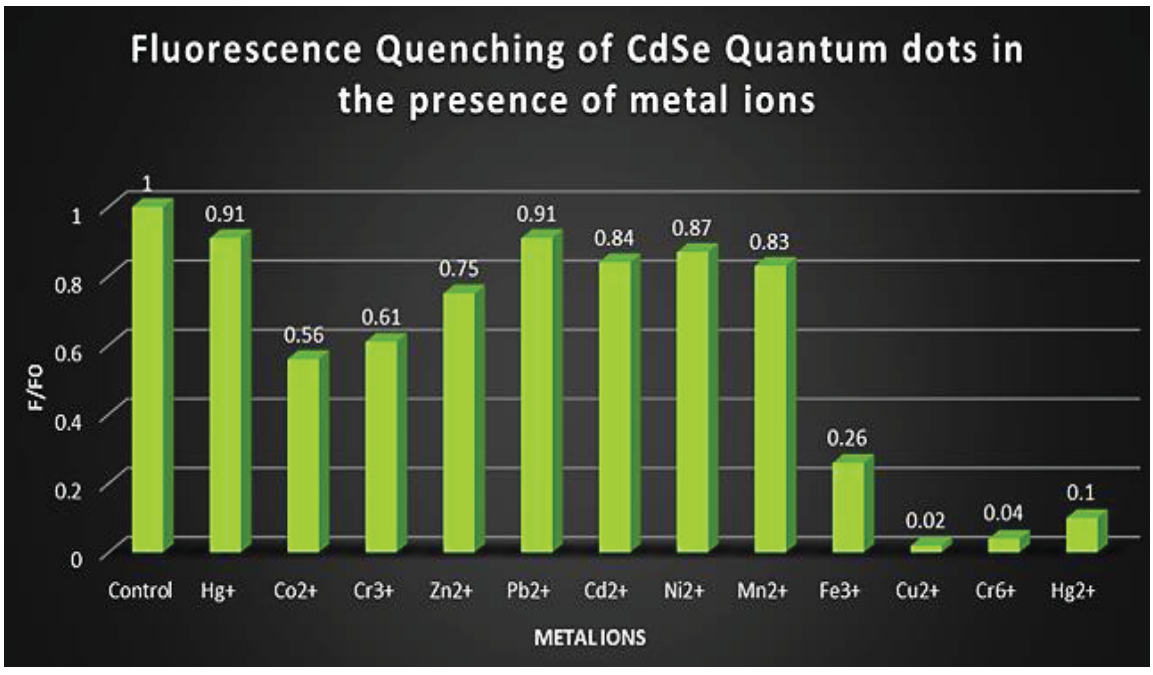

Figure 3.17 *Pl quenching of CdSe QDs in presence of different metal ions.*

So in order to understand the Pl quenching behaviour of CdSe QDs in the presence of these ions different concentration of Cu^{2+}, Cr^{6+}or Hg^{2+}ions were added to the aqueous colloidal solution of CdSe QDs. It was found that the quenching of Pl linearly depends upon the concentration of these metal ions (Fig. 3.18 a, b and c).

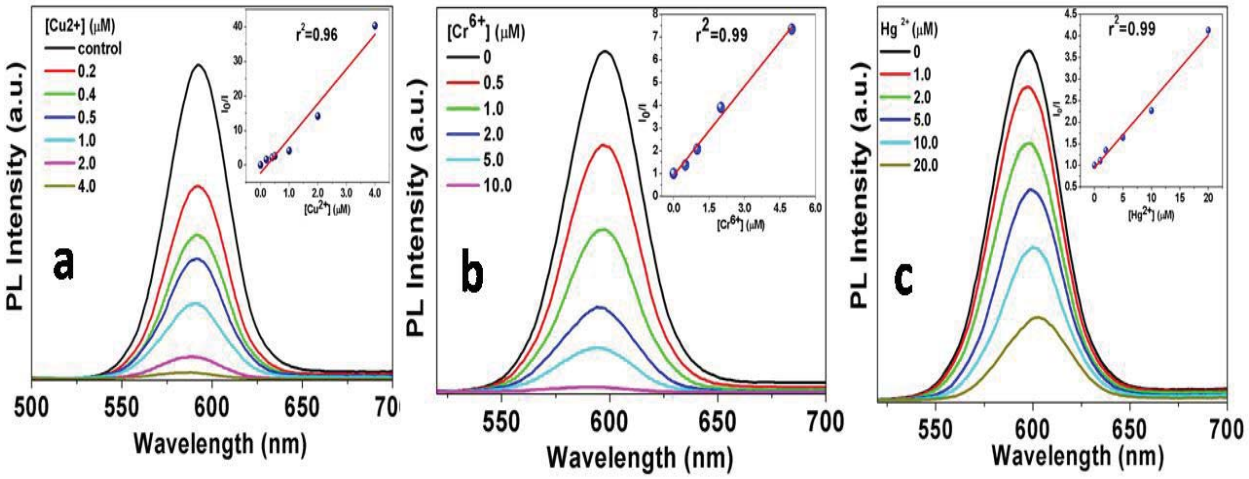

Figure. 3.18 *Pl quenching of CdSe QDs in presence of different metal ions (a) Cu^{2+}, (b) Cr^{6+} and (c) Hg^{2+}, inset- Stern-Volmer plot.*

Therefore, this system can be used as systematic and selective method in sensing of Cu^{2+}, Cr^{6+} and Hg^{2+} ions as well as the 3+ and 6+ oxidation states of Cr and 1+ and 2+ oxidation state of Hg can be differentiated. The Pl quenching data were analyzed using Stern-Volmer equation [109] which can be given as follows.

$$\frac{I_0}{I} = 1 + K_{SV}[Q] = 1 + k_q \tau_0 [Q] \qquad (3.7)$$

where, $K_{sv} = k_q \tau_0$, I_0 and I are the Pl intensity of QDs in the absence and presence of metal ions. K_{sv} is the Stern-Volmer quenching constant, Q is the concentration of the metal ions, k_q is quenching rate constant and τ_0 is the Pl lifetime of the QDs in the absence of metal ions. As

it is clear from these Figures that the plot of I_0/I as a function of metal ion concentration is linear ($r^2 = 0.99$) so the Stern-Volmer description of binding of metal ions with the QDs is valid. The quenching rate constant (k_q) was determined for all the three metal ions are listed in Table 3.3. Further, to confirm it, we recorded the time-resolved Pl decay profiles and determined the lifetime values of the QDs in the absence as well as in the presence of these metal ions (Fig. 3.19). It was found that with all these metal ions the Pl lifetime decreases with increasing the concentration of metal ions which reaffirm the dynamic nature of the PL quenching of the QDs in the presence of these metal ions. The limit of detection (LOD) is evaluated by using the formula 3σ/k, (listed in Table 3.3) where, σ is the standard deviation of the blank signal and k is the slope of the linear calibration plot [155]. It is to be mentioned here that LOD for Cu^{2+} ions is lower than that for Cr^{6+} and Hg^{2+} ions.

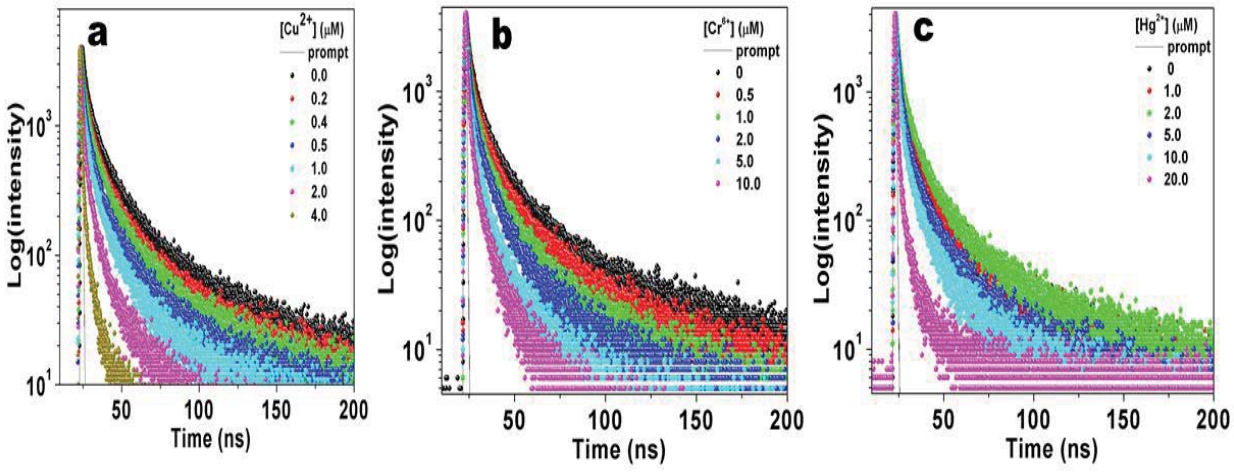

Figure 3.19 *Time-resolved PL decay profiles of CdSe QDs in the presence of different metal ions (a) Cu^{2+}, (b) Cr^{6+} and (c) Hg^{2+}.*

Table 3.3. Limit of detection (LOD) and quenching rate constant (k_q) of metal ions

Metal ion	LOD (μM)	k_q ($M^{-1}s^{-1}$)
Cu^{2+}	27.6	4.66×10^{14}
Cr^{6+}	196.0	8.53×10^{13}
Hg^{2+}	279.2	1.32×10^{14}

3.6.2.4.3. Pl quenching mechanism

Several quenching mechanisms have been proposed by various researchers to explain how metal ions quenches the Pl of functionalized QDs. Non radiative recombination pathway, inner filter effect, electron transfer process, aggregation induced quenching, metal ion replacement, and ion binding interaction are the possible quenching mechanism to explain the Pl quenching phenomena [156]. As we have discussed in the previous section, from the lifetime analysis it is clear that there could be a dynamic Pl quenching of the QDs because the Pl lifetime values decrease on increasing the metal ion concentration [109]. Further to confirm it, we have recorded the absorption spectra of thiourea functionalized CdSe QDs both in absence and the presence of Cu^{2+}, Cr^{6+} and Hg^{2+} (Fig. 3.20).

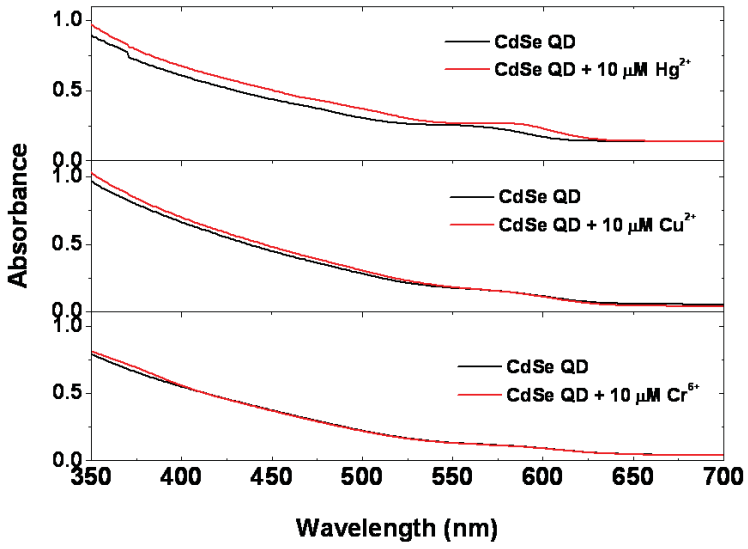

Figure 3.20 *Absorption spectra of thiourea functionalized QDs and QDs with metal ions (Cu^{2+}, Cr^{6+} and Hg^{2+}).*

The presence of Cu^{2+} and Cr^{6+} has no effect on the absorption spectra the QDs but in the presence of Hg^{2+}, the excitonic peak position has been slightly red shifted. This slight red shift in the absorption spectra may be due to nominal increase in the size of QDs in the presence of Hg^{2+} which causes Pl quenching [156]. The quenching rate constant, k_q (Table 3.3) for all the three metal ions are almost 10^3-10^4 times higher than the diffusion-controlled quenching rate constant. This shows that the quenching could also be static in nature even though there is no significant change in the absorption spectra of the QDs in the presence of these metal ions [157]. So from the decrease in the Pl lifetime values of QDs with increase in metal ion concentration and the high quenching rate constant obtained in this case, we suggest that the Pl quenching could be assigned as both static as well as dynamic in nature. In previous literature, it is reported that the metal ions can interact with QDs through the capping layer and can quench their Pl [158,159]. Thiourea has two binding sights through which it can bind with the QDs through the (i) S atom and (ii) two N atoms. It is already confirmed by the FTIR spectra that both N and S atoms of thiourea are involved in the functionalization of CdSe QDs, but the S atom will be predominantly bound to Cd atom of the QDs (according to HSAB principle: soft acid (Cd) and soft base (S)), leaving the N uncoordinated. Scheme 3.3 depicts the possible bindings of thiourea with QDs and metal ions. Being a borderline acid Cu^{2+} can bind with both S and N atom while Hg^{2+} and Cr^{6+} can only bind with S and N atom, respectively.

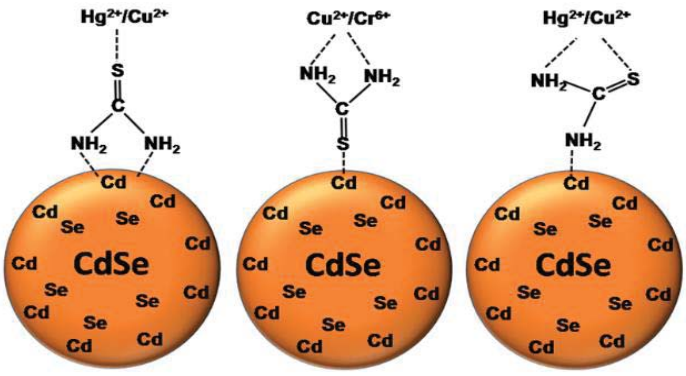

Scheme 3.3 *Possible bindings metal ions with thiourea attached to the surface of CdSe QDs.*

Thus, Cu^{2+} has a strong affinity towards thiourea and hence a lower limit of detection and higher quenching rate constant as compare to Cr^{6+} and Hg^{2+}. It is seen that Cu^{2+}, Cr^{6+} and Hg^{2+} ions predominantly form complexes with thiourea on the CdSe QDs surface, which results in the imperfection of their surface and facilitate the non-radiative e/h recombination. The higher quenching rate constant also favours the association of the metal ions directly to the surface of QDs and photo-induced e transfer from the conduction band of QD to the metal ions.

3.6.2.4.4. Interference effect of Pb^{2+}, $Cd^{2+}$and Fe^{3+} ions

In order to adopt the QDs as a probe for these metal ions it is very essential to study the interference effect of certain other ions. This interference study is focused on the cations which are naturally found along with these metal ions or have adverse effect on human being or environment. Pb^{2+} and $Cd^{2+}$are one of the most hazardous heavy metals along with Hg^{2+}. Fe^{3+} is the constituent metal ion which is found along with copper (chalcopyrite; $CuFeS_2$) and chromium (chromite; $FeCrO_4$). So interference of Pb^{2+}, Cd^{2+} and Fe^{3+}were studied by taking the equal or ten times higher concentration of these interfering ions (Fig 3.21).

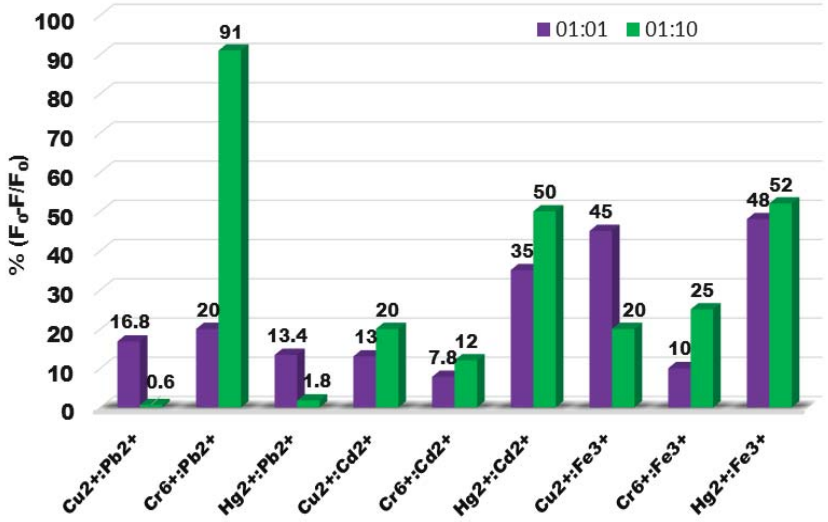

Figure 3.21 *Histograms showing the change in Pl of CdSe QDs in the presence of Pb^{2+}, Cd^{2+} or Fe^{3+} with Cu^{2+}, Cr^{6+} and Hg^{2+} (equal concentration and ten times higher concentration of interfering metal ions).*

From Fig. 3.21 it is clear that the Pb^{2+} is showing very little interference with Cu^{2+} and Hg^{2+} while it is showing adequate interference with Cr^{6+}. On the other hand, Cd^{2+} is showing very little interference with Cu^{2+} and Cr^{6+} but showing good interference with Hg^{2+}. Fe^{3+} is showing good interference with Cu^{2+} and Hg^{2+}.

3.7. Summary and Conclusion

In summary, biomolecules like L-cysteine and starch were used in synthesis of monodispersed CdSe QDs in aqueous solution *via* photochemical route using 300 nm UV irradiation. The photochemical method is a rapid, one-pot, facile alternative method to synthesize monodispersed CdSe QDs in aqueous solution. Their colour, Pl intensity and Pl lifetime strongly depend upon the Cd to Se precursor ratio used during the synthesis. The cytotoxicity study revealed that these QDs were found to be less cytotoxic in comparison to the bare one. A new method has been demonstrated for the extraction of these QDs from the colloidal solution. The extracted QDs after further surface functionalization with thiourea were found to exhibit maximum Pl intensity at room temperature and the neutral pH. It was also demonstrated that the Pl intensity of CdSe QDs can be quenched by Cu^{2+}, Cr^{6+} and Hg^{2+} ions with high sensitivity and selectivity. The mechanism of Pl quenching in the presence of Cu^{2+}, Cr^{6+} and Hg^{2+} could be attributed to the (i) non-radiative charge carrier recombination on the thiourea capping layer as well as (ii) photo induced electron transfer from QDs to metal ions. The different oxidation states of Cr (III and IV) and Hg (I and II) can also be differentiated by the Pl quenching behaviour of these QDs. The thiourea functionalized starch capped CdSe QDs have a potential application in sensing heavy metal ions present in aqueous solutions.

CHAPTER 4
RADIATION CHEMICAL SYNTHESIS OF CdSe NANOPARTICLES

4.1. Introduction

Out of different bottom up approach of synthesis of nanoparticles, radiation induced approach of synthesis is very important because it offers many advantages over the other methods like it is one-pot, facile and rapid method. In radiation induced method of synthesis, we have already discussed about the photochemical synthesis of CdSe QDs in chapter 3. This chapter is devoted to the radiation chemical synthesis of CdSe QDs and effect of various capping agents and the solvent media on its properties. The radiation chemical route is very important because it has advantages over the other routes like - (a) Minimum energy requirement, (b) low concentration of precursors are required, (c) Minimal or no use of harmful chemicals, (d) simple production scheme, (e) large scale production and more importantly (f) tuning the optical and electronic properties of the nanoparticles due to tuning of shape and size of by controlling the dose and dose rate and (g) *In situ* sterilization if required [160-162]. Apart from the method of synthesis, the properties of the nanoparticles/QDs depends strongly on the capping agent and the solvent media used. In this chapter, we have described about- (i) Saccharide capped CdSe QDs grown in aqueous solution *via* electron beam irradiation and (ii) A pulse radiolytic study of dynamics of radiolytic formation of CdSe QDs in aqueous solution containing different alcohols.

4.2. Saccharide capped CdSe QDs grown *via* electron beam irradiation

In this section, we reported a facile electron beam induced synthesis of CdSe QDs in aqueous solution capped with saccharides –fructose, glucose, sucrose and starch. Here aqueous electron was used as the reducing agent which was generated as the primary species in the radiolysis of water by the electron beam. The other species i.e. H• and OH• were quenched by adding tert-butyl alcohol to the solutions. The optical properties of the as synthesized CdSe QDs in all the four saccharides were studies using UV-vis absorption spectrophotometer,

steady state spectrofluorometer and time resolved spectrofluorometer (TCSPC). The transient spectra and their kinetic decay profile was obtained by pulse radiolysis coupled with kinetic spectrophotometry.

4.2.1. Experimental

4.2.1.1. Synthesis of CdSe QDs

High purity chemicals used in the present work comprising cadmium sulfate ($CdSO_4$), sodium sulphite (Na_2SO_3), selenium (Se) powder, and tert-butanol were obtained from Sigma–Aldrich. Saccharides such as glucose, fructose, sucrose and starch were obtained from SDFCL. All the above chemicals were used without further purification. Na_2SeSO_3 solution was prepared by refluxing the solution containing 1 g Se powder and 10 g Na_2SO_3 in 50 ml nanopure water at 70^0 C for 7 hrs [133]. The reaction mixtures were prepared with freshly prepared equimolar (*viz*. 1 mM) ammoniated cadmium sulfate ($Cd[NH_3]_4SO_4$), sodium selenosulfate (Na_2SeSO_3) with a ratio 1:1 containing one of the above mentioned saccharides (20 mM) as the capping agent at a time in nanopure water obtained from a Milipore water purifying system. 1 M tert-butanol was added to the reaction mixture to scavenge the $OH^{\bullet}$ radicals. The solutions were de-aerated with high purity nitrogen. The above mentioned reaction mixtures were continuously irradiated with 2μs electron pulses from a 7 MeV linear accelerator (LINAC). The absorbed dose per pulse was kept at 128 Gy and the samples were irradiated with repeated pulses at a rate of 12 pulses per second accounting for a cumulative dose of 10 kGy.

The transient studies were carried out by the pulse radiolysis technique using a kinetic spectrometer coupled with LINAC. The FWHM of the electron pulse was 500 ns and the absorbed dose was 40 Gy/pulse.

4.2.1.2. Characterization

UV-visible absorption spectra of the reaction mixtures were recorded using a spectrophotometer with a model no. JASCO V650 and a quartz cell with 10 mm optical path length. Room temperature fluorescence (FL) spectra of the QDs were recorded using a spectrofluorometer with a model no. Hitachi F-450. FL lifetime measurements were carried out using a time-resolved spectrofluorometer using time-correlated single photon counting (TCSPC) principle with a model no. Horiba Jobin Yvon IBH 400. X-ray diffraction (XRD) measurements of CdSe QDs were carried out by using a Panalytic (model-X-Pert pro) instrument using Cu K-α source. Transmission electron microscopy (TEM) images were recorded using the instrument Libra 120 keV from Carl Zeiss. Samples for TEM measurements were prepared by putting a drop of the as prepared colloidal solution on thin carbon coated copper grid and consecutively allowing the solvent to evaporate. Fourier transform infrared (FTIR) spectra were recorded with the sample using a SHIMADZU IR-Affinity-1 FTIR instrument in diamond ATR mode.

4.2.1.3. Pulse radiolysis study

Pulse radiolysis experiments were carried out with a 7 MeV linear electron accelerator (LINAC) coupled with a kinetic spectrometer. The solutions were irradiated with electron pulses of FWHM about 500 ns inside a 10 mm x 10 mm flow quartz cell with all the sides transparent to the visible light. The white light from a 450 Watt xenon lamp at a 90^0 angle to the electron beam irradiation was used for the detection of the transient species produced upon radiolysis. The details of the set up are given elsewhere [163]. The absorbed dose was determined by using a chemical dosimeter solution of 10 mM potassium thiocyanate (KSCN), kept in a quartz cell of similar dimensions. The absorbed dose in the pulse radiolysis experiments were 40 Gy. The time-resolved spectra and the kinetic profiles at different probe

wavelengths for the formation and decay of the transient intermediate species produced during radiolysis were obtained during the pulse radiolysis experiments.

4.2.1.4. *In vitro* toxicity studies of CdSe QDs

In vitro cytotoxicity of CdSe QDs was assessed by using standard 3-[4,5-dimethylthialzol-2-yl]-2,5-diphenyltetrazolium bromide (MTT) assay in (CHO, Chinese Hamster Ovary epithelial) cells. The details of MTT assay has already been described in chapter 3 (section 3.5).

4.2.2. Results and discussion

Radiolysis of water produces three primary radicals, hydrated electrons (e_{aq}^-), $H^\bullet$ and $OH^\bullet$ radicals as well as other molecular species like H_2, H_3O^+ and H_2O_2. Among these e_{aq}^- and $H^\bullet$ are reducing radicals whereas $OH^\bullet$ radical is an oxidizing radical. Upon addition of suitable $OH^\bullet$ radical scavengers like tert-butanol or 2-propanol, a perfectly reducing condition can be maintained in the medium. In the present study, tert-butanol has been used to scavenge $OH^\bullet$ radicals. Hydrated electrons, e_{aq}^- reduces $[Cd(NH_3)_4]^{2+}$ ion to form $Cd^{\bullet+}$ and also releases $Se^{\bullet-}$ from $SeSO_3^{2-}$ ion in aqueous solution, which leads to the formation of CdSe nanoparticles [134]. However, these nanoparticles are not stable under ambient conditions, rather they undergo agglomeration to form coagulated CdSe particles. In order to increase their colloidal stability and to avoid their agglomeration, we have used different saccharides in the reaction mixtures. The solutions were irradiated with 10 kGy absorbed dose, where these saccharides do not have any substantial damage/degradation [164,165]. The colour of the reaction mixtures changed from colourless to transparent greenish orange colour upon irradiation and found to be stable for several hours. The camera ready pictures of the colloidal solution containing the as grown CdSe QDs in the presence of different saccharides are shown in the Fig. 4.1.

Figure 4.1 *Camera ready pictures of as grown CdSe QDs synthesized in the presence of different saccharides via electron beam irradiation.*

4.2.2.1. XRD and TEM studies

The materials were separated from the solution and characterized by XRD. Fig. 4.2 shows XRD patterns obtained for the CdSe QDs capped with fructose, glucose, sucrose and starch. The materials were separated from the solution and characterized by XRD. Fig. 4.2 shows XRD patterns obtained for the CdSe QDs capped with fructose, glucose, sucrose and starch. It is seen from this figure that the as grown nanoparticles are of amorphous in nature and resemble to the cubic phase CdSe. The particle sizes of these QDs (Table 4.1) have been estimated from these XRD peaks by using Scherer's formula and are less than the Bohr radius of exciton for the CdSe (i.e. 5.6 nm). The as grown QDs were characterized by TEM measurements. The TEM image and HRTEM image obtained for the CdSe QDs capped with fructose are shown in Fig. 4.3. It is seen from this figure that the sizes of the particles are less than 5 nm, which matches well with those obtained from the XRD data. The HRTEM image shows the well resolved (220) lattice plane with lattice parameter 2.13 Å. Similarly, TEM and HRTEM images of glucose, sucrose and starch capped CdSe is shown in figures 4.4, 4.5 and 4.6 respectively. The HRTEM images of glucose capped CdSe QDs shows the lattice plane with interplannar

distance of 2.05 Å which matches well with the (220) plane of cubic ZB phase of CdSe. For sucrose capped CdSe, the interplannar distance was found to be 1.78 Å which corresponds to the (111) plane of ZB phase of CdSe. In case of starch capped CdSe, again the interplannar distance was found to be 2.24 Å which correspond to the (220) plane. The concentric ring shown in the SAED pattern indicates that the QDs are polycrystalline in nature. The HRTEM image shows the well resolved (220) lattice plane with lattice parameter of 2.24 Å.

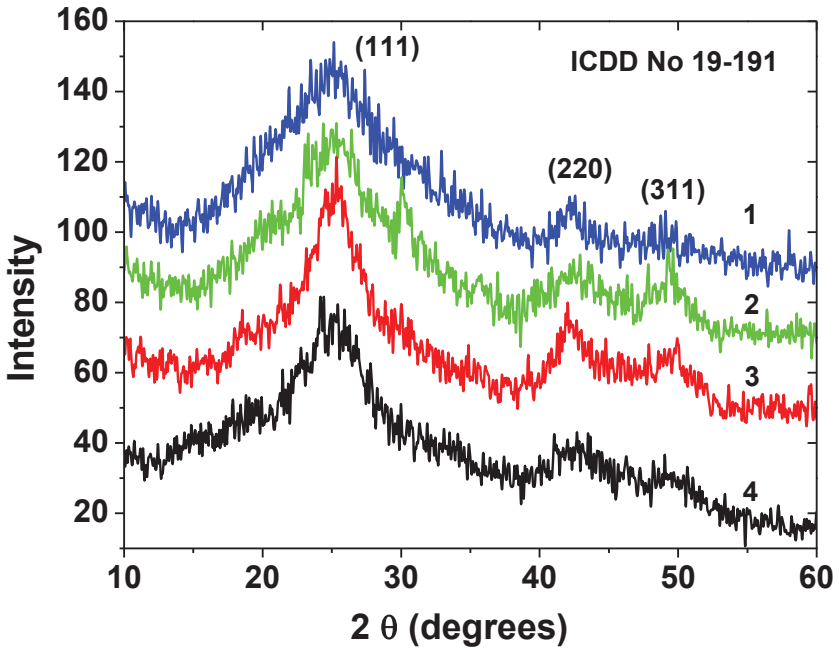

Figure 4.2 *XRD patterns for the CdSe QDs capped with (1) Fructose, (2) Glucose, (3) Sucrose, (4) Starch.*

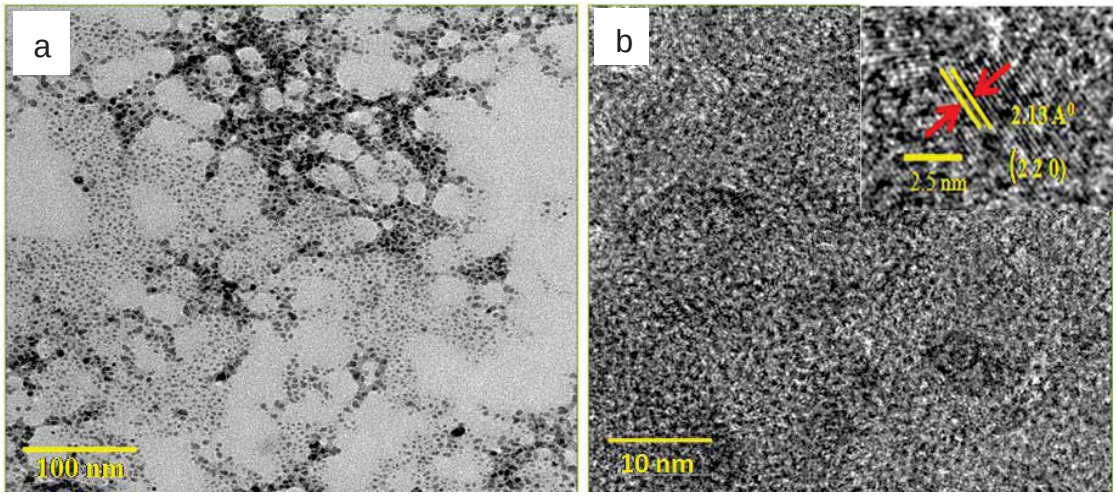

Figure 4.3 *(a) TEM image and (b) HRTEM image of fructose capped CdSe QDs.*

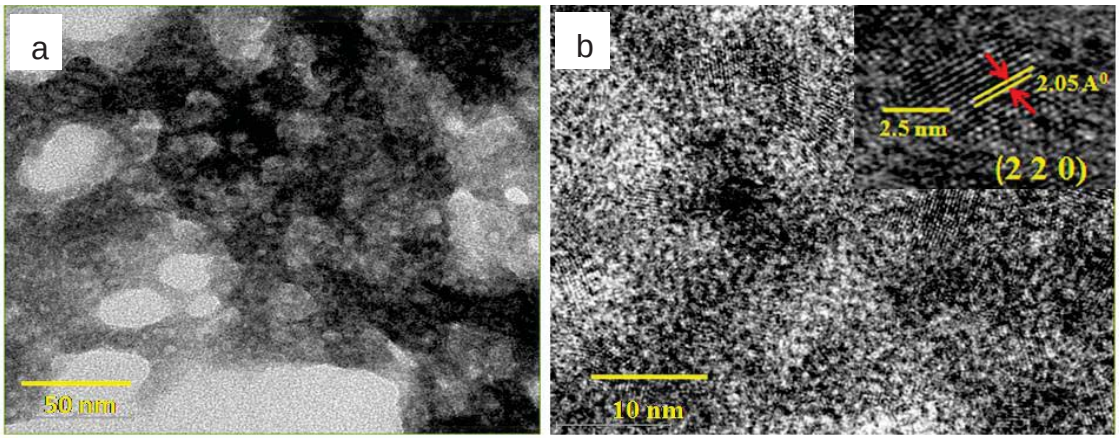

Figure 4.4 *(a) TEM image and (b) HRTEM image of glucose capped CdSe QDs.*

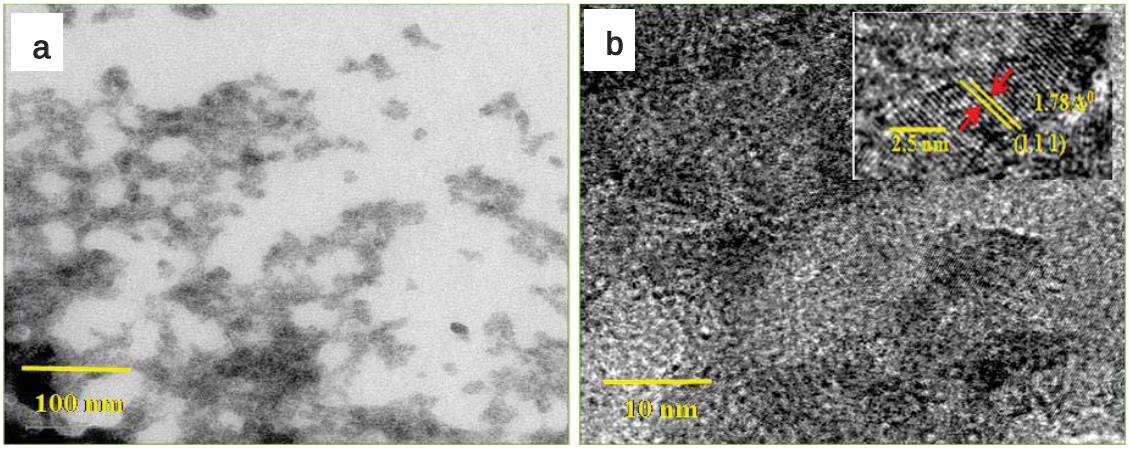

Figure 4.5 *(a) TEM image and (b) HRTEM image of sucrose capped CdSe QDs.*

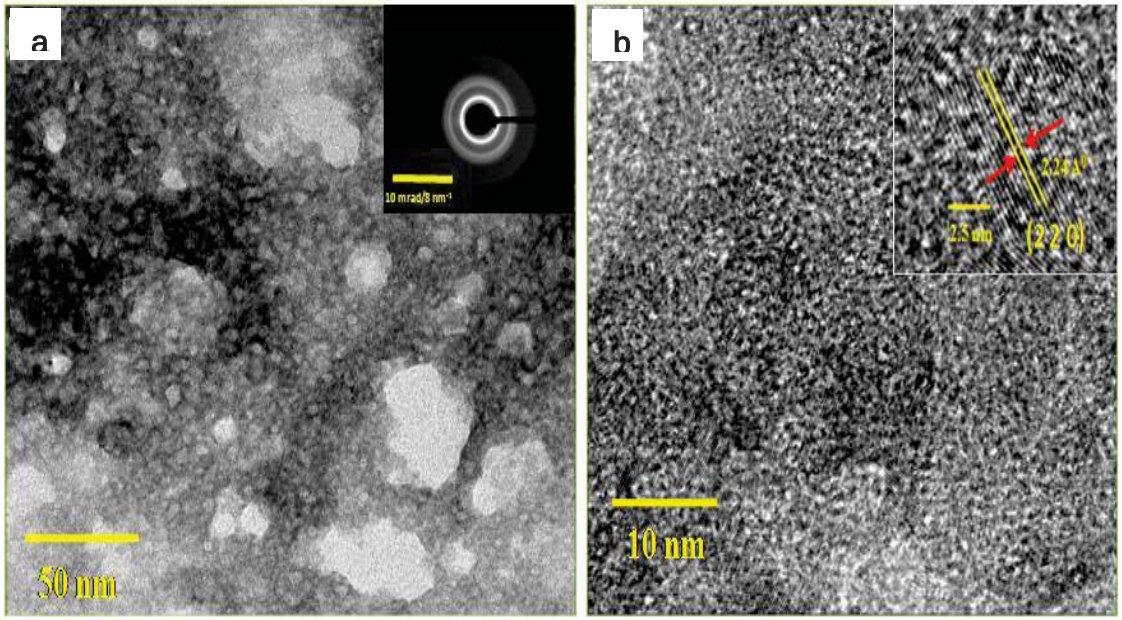

Figure 4.6 *(a) TEM image (inset FFT pattern) and (b) HRTEM image of with starch capped CdSe QDs.*

4.2.2.2. FTIR studies

FTIR spectra obtained for different saccharides and saccharide capped CdSe QDs are shown in Fig. 4.7. The band at 2975 cm^{-1} obtained in the case of fructose, glucose and sucrose and at 2900 cm^{-1} in the case of starch correspond to asymmetric stretching of -CH bond, which vanishes in the case of fructose and glucose capped CdSe QDs, but does not vanish in the case of sucrose and starch capped CdSe QDs. Peaks obtained in the case of fructose and glucose at around 1450 and 1350 cm^{-1} are due to bending mixed vibrational modes of –COH, -CCH, -OCH and –CCH, -OCH respectively. Peaks around 1150,1050 and 990 cm^{-1} are due to asymmetric stretching of –CO and –CC bonds [166]. In the case of sucrose, peaks at 1350 cm^{-1} correspond to –CH rocking vibration, 1050, 990 and 910 cm^{-1} corresponds to –CO stretching vibration [167]. In the case of starch, peak at 2900 cm^{-1} is due to the –CH stretching and the weak peak at 1650 and 1420 cm^{-1} are due to –OH bending of water absorbed and asymmetric and symmetric stretching vibration of –CO group [165]. The broad band near 3300 cm^{-1} in all four saccharides correspond the –OH stretching mode.

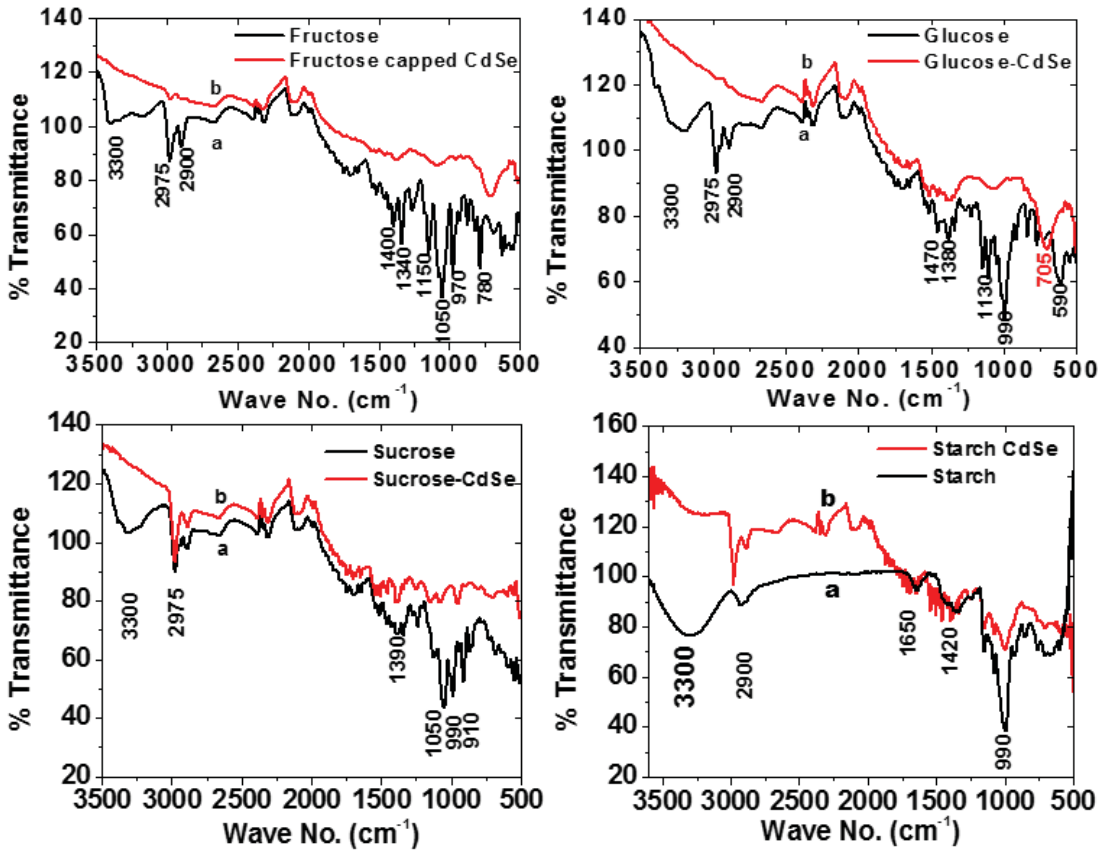

Figure 4.7 *FTIR spectra of different saccharides and saccharides capped CdSe QDs.*

This band is very broad in the case of starch as compared to the other saccharides which is because of being a polysaccharide starch molecule contain many –OH functional groups and they go through intermolecular and intramolecular hydrogen bonding. This band is completely absent in the spectra of saccharide capped CdSe QDs. This clearly indicates the capping of QDs with the hydroxyl group of the saccharides.

4.2.2.3. Optical absorption studies

The optical absorption spectra of the CdSe QDs synthesized by radiolytic method inside the sealed quartz cell containing the above mentioned reaction mixture, are immediately recorded in a spectrophotometer (shown in Fig. 4.8). It is clearly seen from these spectra that these QDs exhibit excitonic absorption peaks. By using the empirical formula reported by Yu

et al. [145] the particle size and the electronic band gap values of these QDs were calculated from their excitonic absorption peak positions (Table 4.1). The particle sizes were within 2 to 3 nm and matches well with those obtained from XRD and TEM measurements.

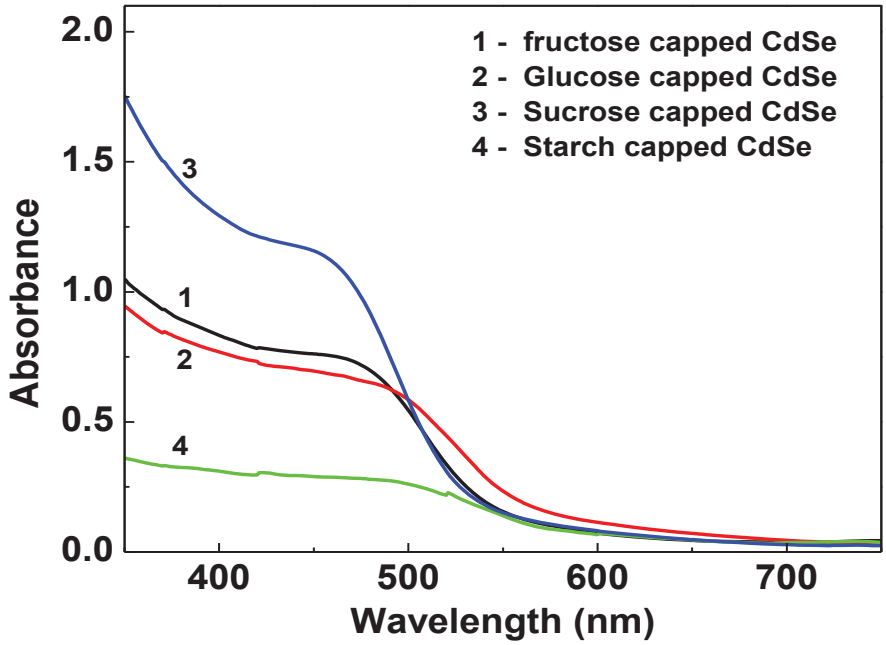

Figure 4.8 *Optical absorption spectra of saccharide capped CdSe QDs.*

Table 4.1. Electronic band gap (E_g) and particle size (nm) of the CdSe QDs determined from the ground state absorption spectra in the presence of different saccharides.

CdSe QDs capped with saccharides	E_g (eV)	Particle size (nm)
Fructose	2.23	2.62
Glucose	2.12	2.96
Sucrose	2.31	2.46
Starch	2.10	3.04

4.2.2.4. Photoluminescence studies

Steady state photoluminescence (Pl) spectra of the fully grown CdSe QDs were recorded at room temperature with an excitation wavelength 400 nm (shown in Fig. 4.9).

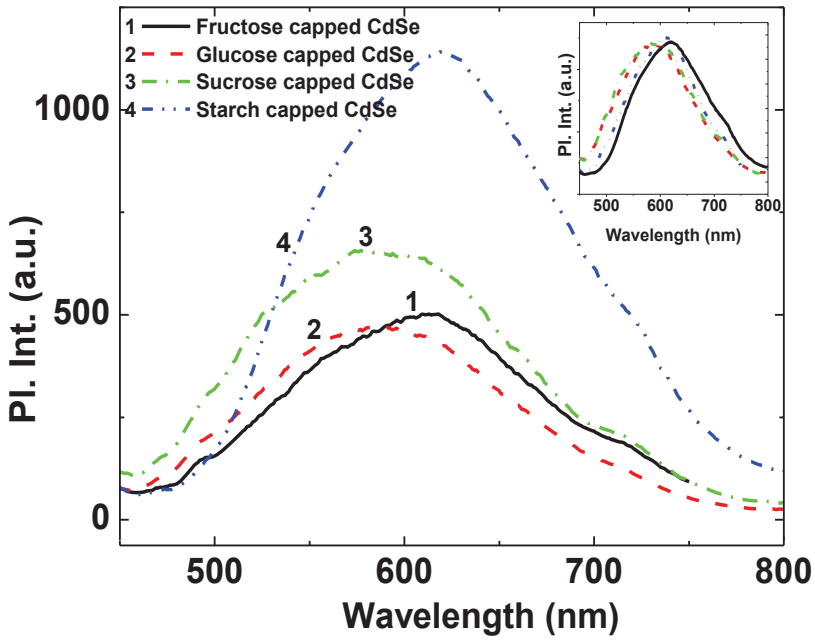

Figure 4.9 *Room temperature steady-state FL spectra of saccharide capped CdSe QDs synthesized via electron beam irradiation in aqueous solution. Insert: Normalized FL spectra of the CdSe QDs. Absorbed dose absorbed = 10 kGy. Excitation wavelength = 400 nm.*

The CdSe QDs studied here were synthesized with reaction mixtures containing equimolar (1 mM:1 mM) concentrations of precursors $[Cd(NH_3)_4]^{2+}$ and $SeSO_3^{2-}$ and different saccharides as the capping agents. It is observed that the Pl spectra are very broad having emission from 480 to 750 nm with the emission maximum at 580 nm and FWHM of 150 nm. The emission intensity was almost similar in the case of fructose and glucose capped QDs, however the intensity was higher in the sucrose and highest in the case of starch capped QDs. This is probably due to the decrease in the surface trap states as well as a strong capping of the CdSe

QDs in the case of starch. It is to be mentioned here that the CdSe QDs synthesized in the presence of starch remains unchanged even after several weeks in the same colloidal solution, which confirms the good stability of QDs by the starch molecules. Here, we get polydispersed CdSe QDs as seen from their TEM images, absorption as well as emission spectra. However, by suitably choosing the concentration of the precursors and the capping agents, as well as tuning the absorbed dose and dose rate, the quality of the QDs might be improved for sharper and stronger emission. The effect of such experimental parameters has been discussed in one of our earlier study on the electron beam induced synthesis of β-cyclodextrin capped CdSe QDs [168].

Time resolved Pl measurements were carried out by using a time correlated single photon counting (TCSPC) instrument to find out the Pl lifetime of the CdSe QDs synthesized in the reaction mixtures as mentioned above (Fig. 4.10). The samples were excited by a diode laser of output wavelength of 405 nm with an IRF of less than 100 ps and Pl was monitored at 580 nm. The instrument response function (IRF) of the setup was measured by collecting the scattered light at 405 nm from a TiO_2 suspension in water. The Pl decay profiles of these CdSe QDs were of multi-exponential behaviour and fitted with tri-exponential fitting function to obtain a chi-square value close to 1. The average lifetime values $<\tau>$ were calculated using the eq. (4.1) below.

$$<\tau> = \frac{a_1\tau_1 + a_2\tau_2 + a_3\tau_3}{a_1 + a_2 + a_3} \qquad (4.1)$$

It was observed that the average lifetime value of the CdSe QDs was least in the case of fructose capped and the maximum in the starch capped (Table 4.2).

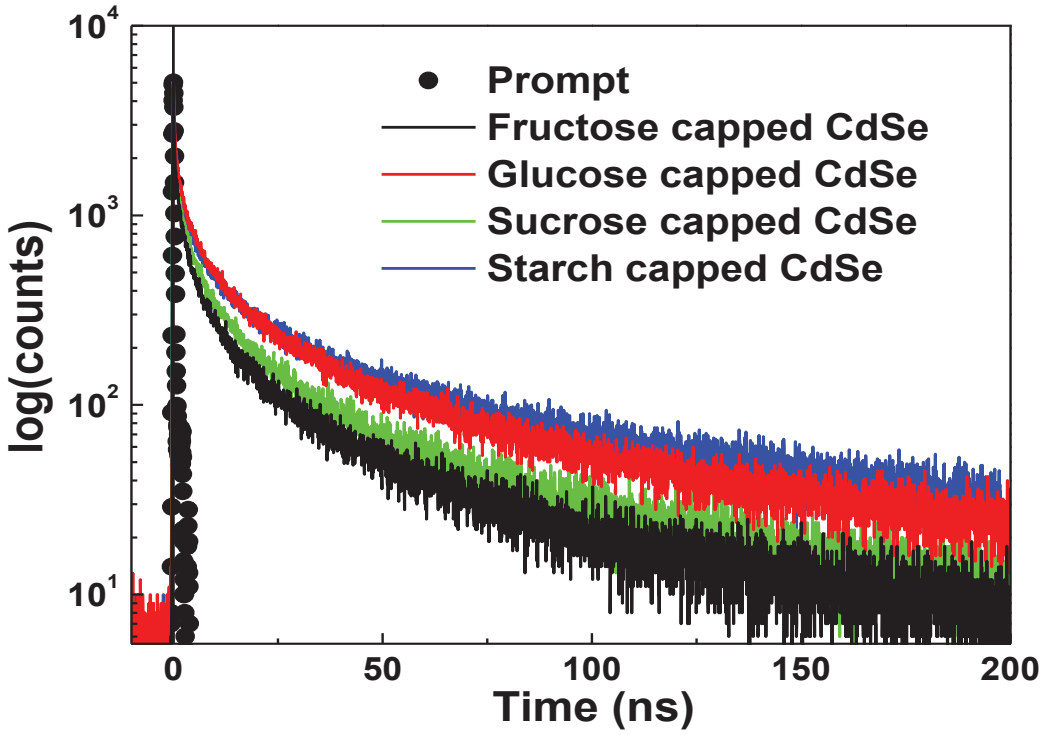

Figure 4.10 *Time-resolved Pl decay profiles of saccharide capped CdSe QDs synthesized via electron beam irradiation in aqueous solution. Absorbed dose absorbed = 10 kGy. Excitation wavelength=400 nm, emission wavelength = 550 nm.*

Table 4.2. Pl lifetime values determined from the lifetime decay profiles by fitting with tri-exponential curve fitting for CdSe QDs capped with different saccharides.

CdSe QDs capped with saccharides	τ_1 (ns)	a_1	τ_2 (ns)	a_2	τ_3 (ns)	a_3	$<\tau>$ (ns)
Fructose	2.24	0.24	20.56	0.66	0.07	0.10	14.14
Glucose	5.25	0.34	36.55	0.54	0.48	0.12	21.40
Sucrose	5.08	0.36	34.84	0.52	0.52	0.11	20.12
Starch	7.89	0.32	45.70	0.60	1.07	0.08	30.03

This could be explained as follows: in the case of fructose there is a lower degree of capping by these molecules, which increases the non-radiative decay pathway, therefore the Pl lifetime value is small; in the case of starch there is higher degree of capping by these molecules, which increases the radiative decay pathway, therefore the Pl lifetime value is higher. A similar explanation could also be made with respect the steady-state Pl spectral observations.

4.2.2.5. Pulse radiolysis studies

The mechanism of the radiolytic formation of these QDs in the presence of different saccharides has been investigated by pulse radiolysis studies. The transient absorption spectra obtained with all the four saccharides capped CdSe QDs. The transient absorption spectra of fructose capped CdSe QDs are shown in Fig. 4.11. The reaction mixtures containing equimolar (1 mM each) cadmium and selenium precursors along with the saccharides either fructose (20 mM), or glucose (20 mM), or sucrose (20 mM) or starch (0.1 g in 50 ml sol) were used for the pulse radiolysis studies. It is clearly evidenced from these figures that the formation of CdSe QDs is always associated with a transient intermediate species having absorption maxima at around 380 and 510 nm, except for the case of capping by fructose, where the peaks are at 360 and 490 nm (Table 4.3). This observation matches very well with that earlier reported by us [134]. The decay rate constants of the transient intermediates having absorption peaks at around 500 nm, have been determined by fitting the kinetic decay profiles obtained at this wavelength with a single exponential fit equation. It was observed that the decay rate constants in all the four saccharides were very close to each other. The signal value at the peak position around 500 nm is the highest in the case of starch. Similarly, the stability of the as grown CdSe QDs in colloidal solution was the highest in case of starch and lowest in case of fructose.

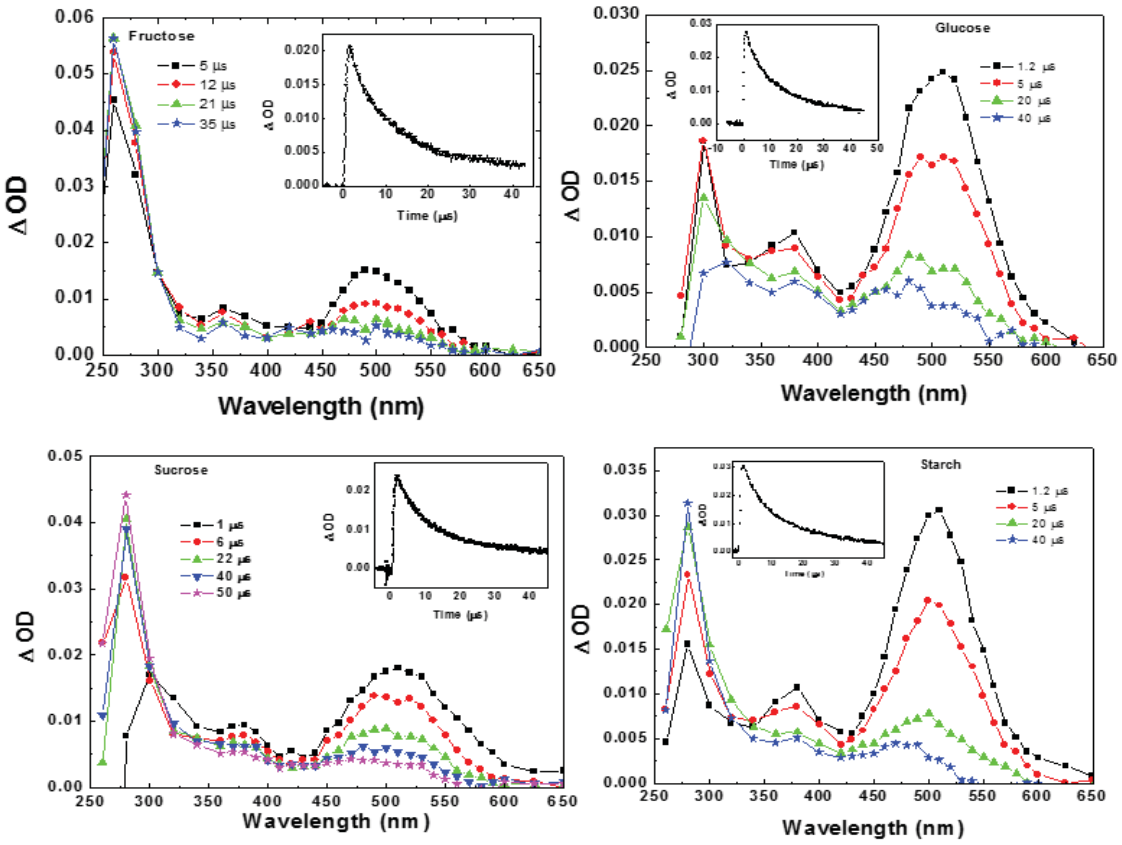

Figure 4.11 *Transient absorption spectra obtained from the pulse radiolysis studies performed on the mixture of 1 mM of each precursors with different saccharides in aqueous tert butanol. Pulse width 500 ns, absorbed dose 40 Gy/pulse. Insert: Kinetic decay profile obtained at 500 nm.*

Table 4.3. Decay rate constants of the transient intermediate species having absorption at 500 nm and position of absorption maximum estimated from the pulse radiolysis studies in the presence of different saccharides and polysaccharides.

Saccharides	λ^{max} (nm) (for transient species)	k (10^5 s^{-1})
Fructose	360, 490	1.9
Glucose	380, 510	1.4
Sucrose	380, 510	1.0
Starch	380, 510	1.2

On comparison of the present observations with that earlier reported by our group [134], it could be concluded that the presence of the saccharides does not interfere with the formation of these QDs, rather they provide an enhanced stability by virtue of capping these nanoparticles. Based on these observations, the reactions leading to the formation of CdSe QDs could be written as follows.

$$H_2O \rightsquigarrow e_{aq}^-, H^\bullet, OH^\bullet, H_2O_2, H_3O^+ \quad (4.2)$$

$$H^\bullet / OH^\bullet + \text{t-Butanol} \longrightarrow (CH_3)_2CH_2{}^\bullet COH \text{ (unreactive)} + H_2 / H_2O \quad (4.3)$$

$$e_{aq}^- + [Cd(NH_3)_4]^{2+} \longrightarrow Cd^{\bullet+} \quad (4.4)$$

$$e_{aq}^- + SeSO_3^{2-} \longrightarrow Se^{\bullet-} + SO_3^{2-} \quad (4.5)$$

$$Cd^{\bullet+} + Se^{\bullet-} \longrightarrow CdSe \quad (4.6)$$

$$CdSe + nCdSe \xrightarrow{\text{saccharide}} \text{saccharide capped CdSe QDs} \quad (4.7)$$

It is to be mentioned here that the saccharides used in this study act only as capping agents for the CdSe QDs. They do not take part in the radiolytic reactions. Their presence in the reaction mixture does not lead to the formation of CdSe QDs in the absence of any electron beam irradiation. So this confirms that these saccharides play only the role of capping or stabilizing agent for the CdSe QDs. As these saccharides are biocompatible and, it can be presumed that these QDs could also have certain biocompatibility effect. This has been investigated in the following cytotoxicity studies.

4.2.2.6. Cytotoxicity studies

The biocompatibility of above CdSe QDs synthesized in the presence of different saccharides was evaluated in epithelial (CHO) cells by monitoring the viability at 48 hr after their addition to cells. The results as shown in Fig. 4.12 indicated that addition of bare QDs to cells with stoichiometry of 1:1. The capped QDs also exhibited concentration dependent

cytotoxicity in the given concentration range however, there was no significant difference in the cytotoxicity values of bare CdSe and fructose and sucrose capped CdSe QDs at relatively higher concentrations, i.e. 5 and 10 μg/ml. This undoubtedly suggests the inability of sucrose and fructose as a strong capping agent to reduce the cytotoxicity of CdSe QDs at relatively higher concentration. It is important to note here that particle sizes of fructose and sucrose capped QDs (2.62 and 2.46 nm respectively) are relatively smaller than those of glucose and starch capped QDs (2.96 and 3.04 nm, respectively).

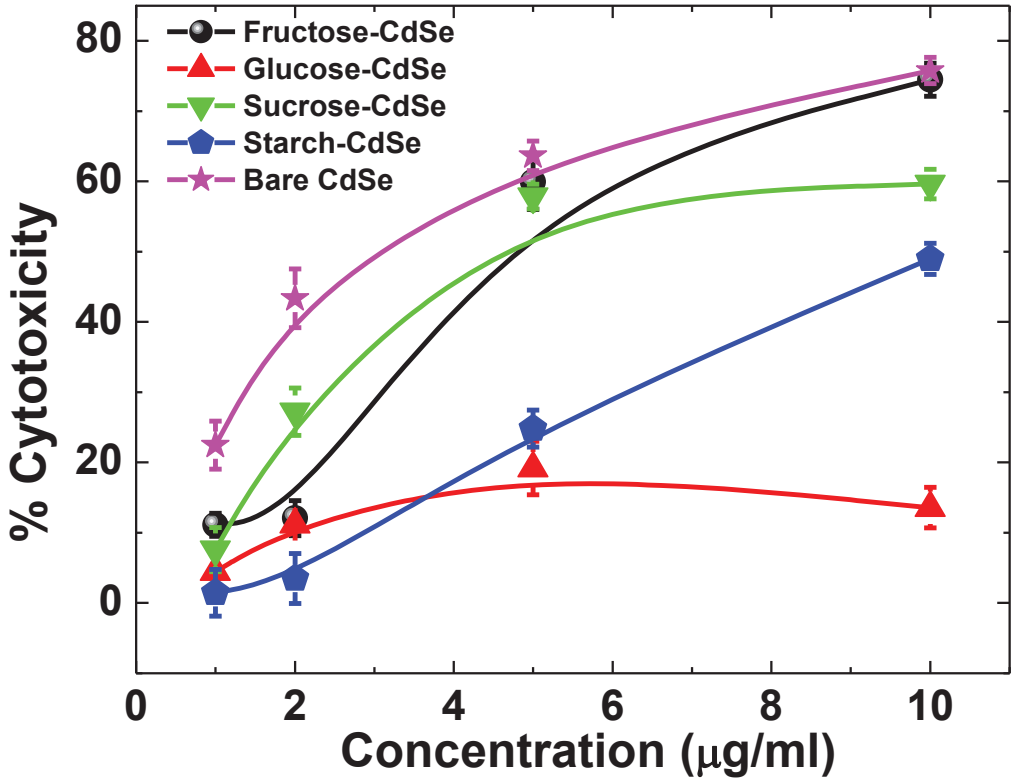

Figure 4.12 *Line graph showing % cytotoxicity of CdSe QDs (uncapped and capped with four different saccharides. The results are presented as mean ±SEM (n=3).*

Therefore, fructose and sucrose capped QDs are expected to have larger surface area as well as more number of Cd atom on the surface compared to others and this may be the reason for their higher cytotoxicity. Now apart from the size, there may be inherent toxicity of fructose and

sucrose in mammalian cells [169,170] contributing to the overall toxicity of these QDs. There is no significant difference in the cytotoxicity values of glucose capped QDs at 2, 5 and 10 μg/ml concentrations. So the toxicity has already attained saturation in this concentration range. However, the lower cytotoxicity of glucose capped CdSe QDs could be due to the relatively higher biocompatibility of glucose as compared to other saccharides. Taken together above results confirmed that capping by various saccharides can be used as a strategy to control the size and subsequent toxicity of radiation induced synthesized CdSe QDs in order to convert them to biocompatible for various biological usage.

4.3. Dynamics of radiolytic formation of CdSe QDs in aqueous solution containing different alcohols: a pulse radiolysis study

In this section we have investigated the reaction dynamics of the radiation induced synthesis of CdSe QDs by different aliphatic alcohol radicals through pulse radiolysis studies. Their optical properties have been investigated and a probable mechanism of their formation has been proposed.

4.3.1. Experimental

4.3.1.1. Chemicals

High purity chemicals cadmium sulphate, sodium sulphite, Se powder methanol, ethanol, 2-propanol, n-propanol and n-butanol were purchased from Sigma Aldrich and used without further purification. Ammoniated cadmium sulphate, $Cd(NH_3)_4SO_4$ and sodium selenosulphate, Na_2SeSO_3 were used as precursors for cadmium and selenium respectively. $Cd(NH_3)_4SO_4$ solution was prepared by adding desired quantity of 25 % NH_3 solution to freshly prepared $CdSO_4$ solution until cleared transparent solution was obtained. Na_2SeSO_3 solution was prepared by refluxing the solution containing 1 g Se powder and 10 g Na_2SO_3 in 50 ml

nanopure water at 70^0 C for 7 hrs [171]. Nanopure water obtained from Millipore water purifying system was used for preparing the solutions. 4 % v/v of different alcohols were taken in reaction mixture of 0.5 mM concentration of the both the precursors.

The reaction mixture was saturated with N_2O (2.5×10^{-2} M) before the electron beam irradiation to quench the hydrated electrons, e_{aq}^-, allowed the different alcohols to react with $H^\bullet/OH^\bullet$ radicals formed after electron beam irradiation to generate different secondary alcohol radicals [80,172]. These secondary alcohol radicals react with the precursors to form different transient intermediate species. The concentrations of both the precursors were changed accordingly to allow the secondary radicals to react with the specific precursor molecule.

4.3.1.2. Pulse radiolysis

Pulse radiolysis experiments were carried out with a 7 MeV linear electron accelerator (LINAC) coupled with a kinetic spectrometer. The details of pulse radiolysis have already been described in section 4.2.1.3.

4.3.1.3. Characterization

UV-vis absorption spectra of the reaction mixtures were recorded using a spectrophotometer with a model no. JASCO V650 and a quartz cell with a 10 mm path length. Room temperature steady state fluorescence spectra were recorded using spectrofluorometer with a model no. Hitachi F-450. X-ray diffraction (XRD) measurements of CdSe QDs were carried out by using a Panalytic model X-Pert pro instrument using Cu K-α source. The transmission electron microscopy (TEM) images were recorded using a Libra 200FE instrument operated at 200 kV accelerating voltage.

4.3.2. Results and discussion

4.3.2.1. Synthesis of CdSe QDs

Radiation-induced synthesis of any materials mainly directed by the process of radiolysis of water because the water molecules are present in ample amount in aqueous solution so the radiation primarily interacts with water molecules leads to radiolysis of water. Radiolysis of water produces three major species, e_{aq}^-, $H^\bullet$ and $OH^\bullet$ radicals. Out of these the e_{aq}^- and $H^\bullet$ are reducing while $OH^\bullet$ is oxidizing in nature [173]. By suitably modifying the solvent medium, it is possible to investigate the reaction of any one of these three primary radicals with the reagents of our interest. A reducing environment containing only hydrated electrons, e_{aq}^-, can be achieved by adding tert-butanol ($(CH_3)_3COH$), which quenches $OH^\bullet$ radicals. On the contrary, an oxidizing environment can be made by saturating the solution with N_2O [134] which generate $OH^\bullet$ radical by reacting with e_{aq}^-. Similarly, a reducing environment can also be created by adding different aliphatic alcohols along with saturating the solution with N_2O, where the $OH^\bullet$ radicals can react with the alcohols to produce secondary radicals, which are reducing in nature. The rate constant of reaction between $OH^\bullet$ and aliphatic alcohols (ROH) is interestingly very high (Table 4.4) [80].

Table 4.4. Rate constants of reactions of $H^\bullet$, $OH^\bullet$ radicals with alcohols [80].

Alcohols	k (M^{-1} s^{-1})	
	$H^\bullet$	$OH^\bullet$
methanol	2.6×10^6	9.7×10^8
ethanol	1.7×10^7	1.9×10^9
1-propanol	2.4×10^7	2.8×10^9
2-propanol	7.4×10^7	1.9×10^9
1-butanol	5.5×10^7	4.2×10^9

Radiolysis of water:

$$H_2O \rightsquigarrow e_{aq}^-,\ OH^\bullet,\ H^\bullet,\ H_3O^+,\ H_2,\ H_2O_2, \quad (4.8)$$

In the presence of tert-butanol:

$$OH^\bullet\ (H^\bullet) + (CH_3)_3COH \longrightarrow {}^\bullet CH_2(CH_3)_2COH + H_2O\ (H_2) \quad (4.9)$$

In the presence of N_2O:

$$e_{aq}^- + N_2O \xrightarrow{H_2O} N_2 + OH^- + OH^\bullet\ (k = 9.1 \times 10^9\ M^{-1}\ s^{-1})^{[6]} \quad (4.10)$$

In the presence of aliphatic alcohols (ROH):

$$ROH + OH^\bullet/H^\bullet \longrightarrow R^\bullet OH + H_2O \quad (4.11)$$

The radiolytic synthesis and the pulse radiolysis study of CdSe QDs using electron beam irradiation in aqueous solution containing equimolar $Cd(NH_3)_4SO_4$ and Na_2SeSO_3 and tert-butanol have been previously reported by us [134]. In this solution the precursor molecules mainly reacted with e_{aq}^-. In the present work, we have synthesized CdSe QDs, also investigated the dynamics of their formation as well as their properties. 4 % v/v of methanol, ethanol, 2-propanol, 1-propanol or 1-butanol were taken in the reaction mixture containing 0.5 mM $Cd(NH_3)_4SO_4$ and Na_2SeSO_3 saturated with N_2O. For different alcohols there is possibility of different secondary radicals depending upon the H-atom abstraction from different positions of aliphatic C-chain (α, β, γ etc.) (Table 4.5). However, the α carbon centered radicals are the major products among all the possible radicals [174]. These radicals can react with the precursor ions to give transient intermediate species which subsequently form the CdSe QDs. These radicals are expected to react with the precursors and initiate the reactions to form CdSe.

Interestingly, the clear colourless solutions were found to change to greening orange colour upon the electron beam irradiation, which clearly confirms the formation of colourful products in the solution (Fig. 4.13).

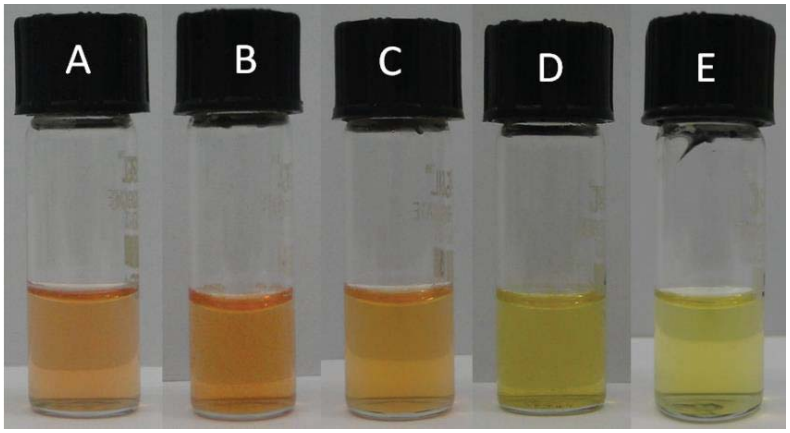

Figure 4.13 *Camera ready pictures of CdSe QDs synthesized in aqueous solutions containing different alcohols (a) MeOH, (b) EtOH, (c) 2-PrOH, (d) n-PrOH, (e) n-BuOH.*

Table 4.5. One-electron reduction potential (E^1) [136] values of the radicals in different solvent systems at pH 3.4 vs NHE at room temperature (25^0C).

Redox couples (solvents system)	E^1 (V) vs NHE at 25^0C
$CH_2O/^{\bullet}CH_2OH$ (4 % methanol)	-1.18
$CH_3CHO/CH_3C^{\bullet}HOH$ (4 % ethanol)	-1.25
$CH_3CH_2CHO/CH_3CH_2C^{\bullet}HOH$ (4 % 1-propanol)	-1.41
$(CH_3)_2CO/(CH_3)_2C^{\bullet}OH$ (4 % 2-propanol)	-1.59
$CH_3CH_2CH_2CHO/CH_3CH_2CH_2C^{\bullet}HOH$ (4 % 1-butanol)	-1.44

The reactions involved in the presence of different alcohols are as follow:

In the case of methanol:

$$CH_2^{\bullet}OH + [Cd(NH_3)_4]^{2+} \longrightarrow Cd^{\bullet+} + HCHO + H^+ \quad (4.12)$$

$$CH_2^{\bullet}OH + SeSO_3^{2-} \longrightarrow SO_3^{2-} + Se^{\bullet-} + HCHO + H^+ \quad (4.13)$$

In the case of ethanol:

$$CH_3CH_2^{\bullet}OH + [Cd(NH_3)_4]^{2+} \longrightarrow Cd^{\bullet+} + CH_3CHO + H^+ \quad (4.14)$$

$$CH_3CH_2^{\bullet}OH + SeSO_3^{2-} \longrightarrow SO_3^{2-} + Se^{\bullet-} + CH_3CHO + H^+ \quad (4.15)$$

In the case of 2-propanol:

$$(CH_3)_2C^{\bullet}OH + [Cd(NH_3)_4]^{2+} \longrightarrow Cd^{\bullet+} + (CH_3)_2CO + H^+ \quad (4.16)$$

$$(CH_3)_2C^{\bullet}OH + SeSO_3^{2-} \longrightarrow SO_3^{2-} + Se^{\bullet-} + (CH_3)_2CO + H^+ \quad (4.17)$$

In the case of 1-propanol:

$$CH_3CH_2CH_2^{\bullet}OH + [Cd(NH_3)_4]^{2+} \longrightarrow Cd^{\bullet+} + CH_3CH_2CHO + H^+ \quad (4.18)$$

$$CH_3CH_2CH_2^{\bullet}OH + SeSO_3^{2-} \longrightarrow SO_3^{2-} + Se^{\bullet-} + CH_3CH_2CHO + H^+ \quad (4.19)$$

In the case of 1-butanol:

$$CH_3CH_2CH_2CH_2^{\bullet}OH + [Cd(NH_3)_4]^{2+} \longrightarrow Cd^{\bullet+} + CH_3CH_2CH_2CHO + H^+ \quad (4.20)$$

$$CH_3CH_2CH_2CH_2^{\bullet}OH + SeSO_3^{2-} \longrightarrow SO_3^{2-} + Se^{\bullet-} + CH_3CH_2CH_2CHO + H^+ \quad (4.21)$$

Finally, these radicals will react with each other to form new transient intermediate species, which finally undergo several steps to form CdSe QDs.

$$Cd^{\bullet+} + Se^{\bullet-} \longrightarrow [Cd^{\bullet}:Se^{\bullet-}] \text{ (transient intermediate)} \quad (4.22)$$

$$[Cd^{\bullet}:Se^{\bullet-}] \longrightarrow CdSe \quad (4.23)$$

$$CdSe + nCdSe \longrightarrow CdSe\ QDs \quad (4.24)$$

The absorption spectra (Fig. 4.14) recorded before and after the electron beam irradiation in the case of all the five different types of alcohols, and found that there is a remarkable change

in the spectral patterns confirming the formation of CdSe QDs. The excitonic peak position was found to be different in all the five alcohols.

4.3.2.2. Characterization of CdSe QDs

The CdSe QDs used for XRD and TEM characterization was synthesized by giving a cumulative dose of 10 kGy with a pulse repetition rate of 12.5 pulses per second and 100 Gy/pulse of dose rate for 8 second of e beam irradiation in a solution containing 1.0 mM of each $Cd(NH_3)_4SO_4$ and Na_2SeSO_3, 4 % v/v 2-propanol and saturated with N_2O.

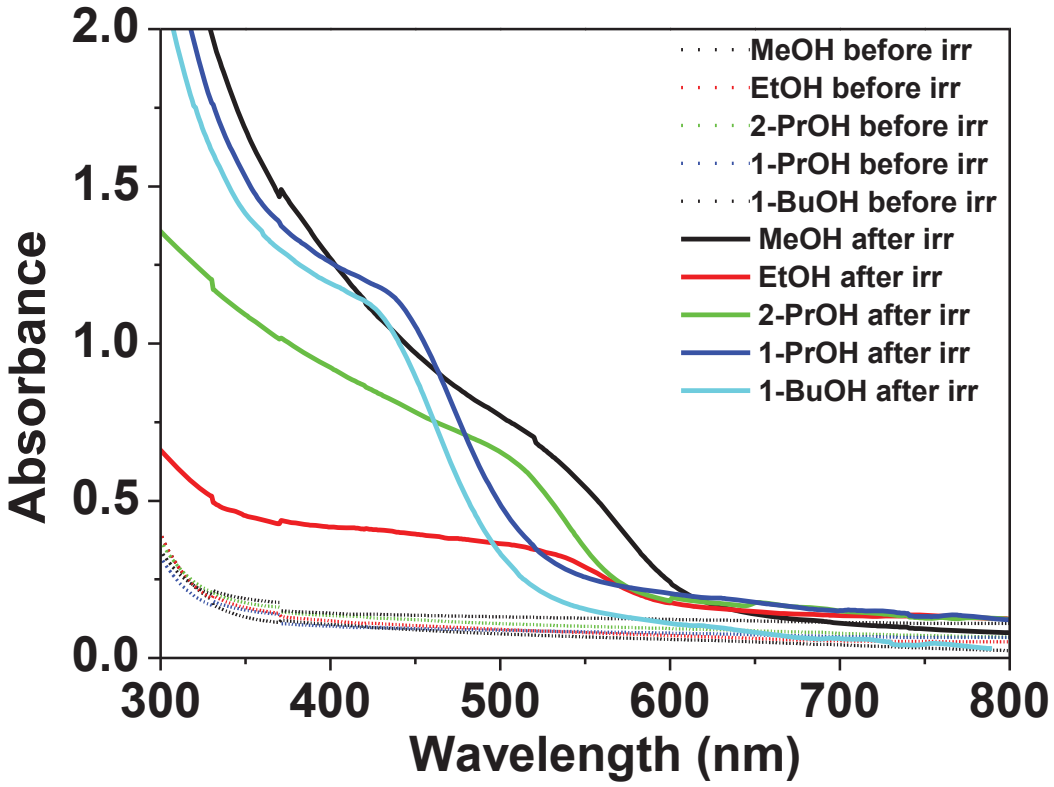

Figure 4.14 *Absorption spectra of CdSe QDs synthesised in the presence of different alcohols, before irradiation (a) dotted line and after irradiation (b) continuous line and their excitonic position (in nm).*

From the XRD pattern shows three peaks at 25.55°, 42.48° and 49.35° which correspond to (111), (220) and (311) plane of cubic zinc blende crystal structure of CdSe (Fig. 4.15). The XRD pattern was found in good agreement with that of ICDD no. 19-191.

The crystallite size was calculated using the Scherrer formula:

$$d = \frac{0.9\lambda}{\beta \, \mathrm{Cos}\theta} \qquad (4.25)$$

Where λ is the wavelength of Cu K-α i.e. 1.5406 Å, β is the broadening at half of maximum intensity (FWHM), θ is the Brag's angle (in degrees). The crystallite size obtained was 2.2 nm. The broadening of the peaks indicates that the CdSe particles synthesized during radiolysis are of nano dimension. TEM samples were prepared by depositing a drop of the colloidal solution of CdSe synthesized in 2-propanol on carbon coated copper grids followed by drying under IR lamp for ten minutes.

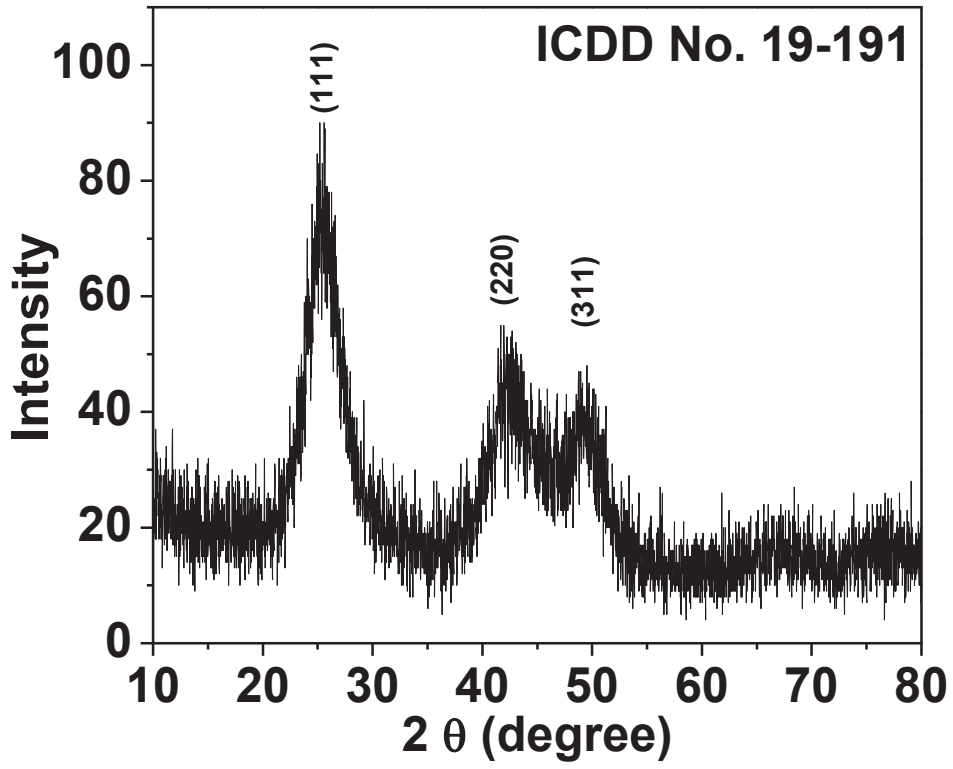

Figure 4.15 *XRD pattern of CdSe QDs synthesized in the presence of 2-propanol.*

From TEM image (Fig. 4.16a) it is clearly shown that the CdSe particles are agglomerated with a primary particle size of 2-3 nm. The agglomeration occurred due to the absence of capping agent. The particle size of the individual grain obtained from TEM, XRD and Absorption spectra were found to be in good agreement. From HRTEM image the lattice spacing was calculated and was found to be 0.238 nm (Fig. 4.13b) which was in good agreement with the (220) plane lattice spacing of zinc blende cubic crystal structure of CdSe (a=0.607 nm). So, from both the XRD as well as TEM it is confirmed that the particle size of CdSe QDs are well within the limit of Bohr radius (5.7 nm for CdSe). So the as synthesized QDs are CdSe QDs.

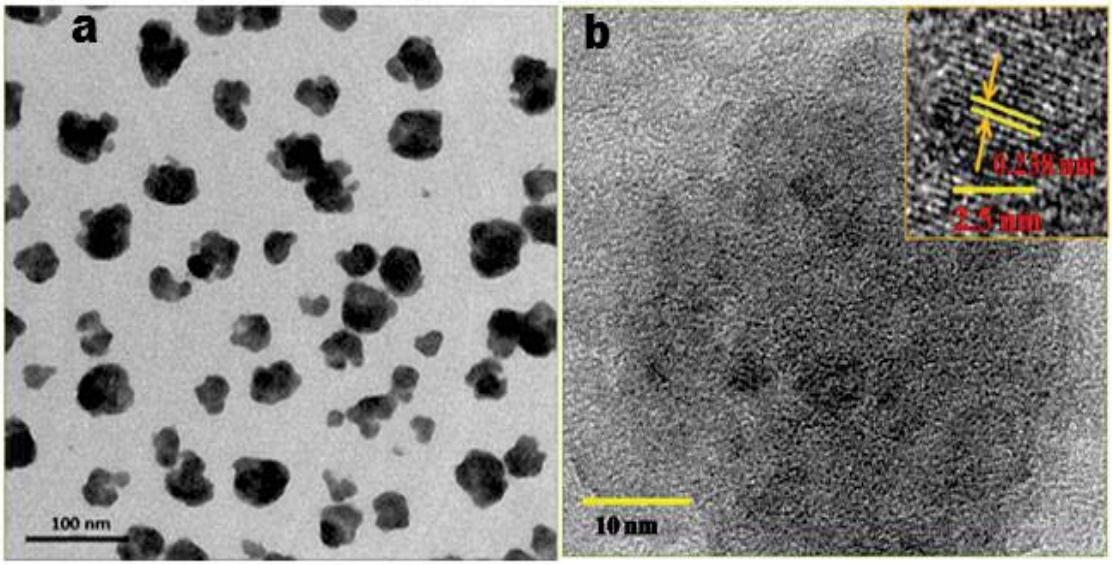

Figure 4.16 *(a)TEM image and (b) HRTEM image of CdSe QDs synthesised in the presence of 2-PrOH (inset the lattice spacing corresponding to 220 plane).*

4.3.2.3. Photoluminescence of CdSe QDs

The steady-state photoluminescence (Pl) spectra of colloidal solution containing CdSe QDs synthesized in the presence of different alcohols were recorded at room temperature. The shape of the Pl spectra was very much different for CdSe QDs synthesized in the presence of different alcohols (Fig. 4.17). The CdSe QDs synthesized in methanol, ethanol and 2-propanol

exhibit very little Pl, however, those synthesized in the presence of 1-propanol and 1-butanol exhibit good Pl. The Pl observed in the case of 1-propanol was very narrow in the region 500 to 550 nm while that in the case of 1- butanol is very broad from 500 nm to beyond 650 nm. This observation confirms that the structure and properties of CdSe QDs obtained in the presence of different alcohols certainly have a correlation among them. It is thus proposed here that the relatively large structure of 1-propanol and 1-butanol as compared to the others used in this study, are providing a better microenvironment and thereby enhances the radiative pathway for the carrier relaxation in the photo excited CdSe QDs.

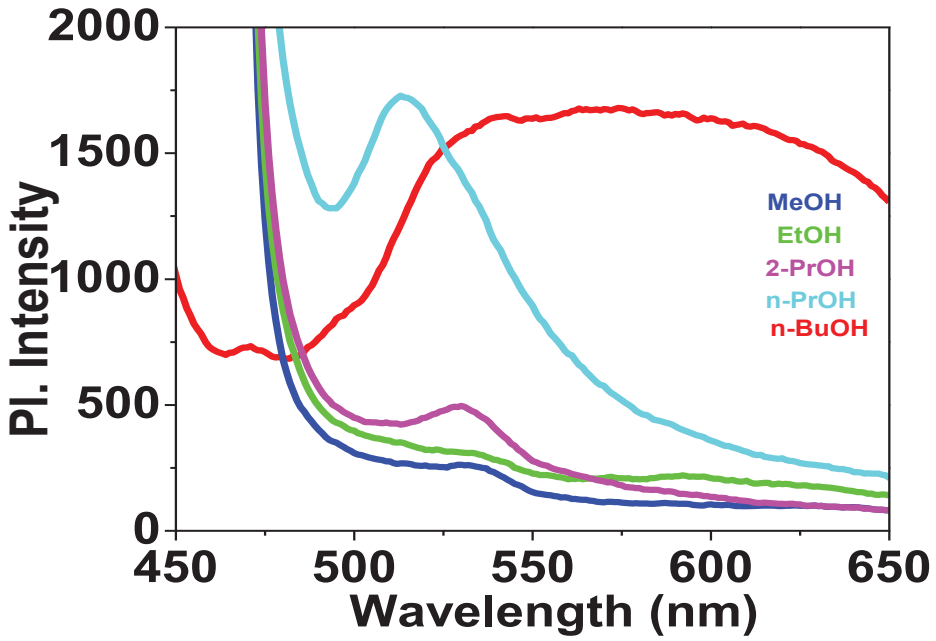

Figure 4.17 *Pl spectra of CdSe QDs synthesised in the presence of different alcohols.*

4.3.2.4. Pulse radiolysis studies

The dynamics of the radiolytic formation of these QDs has been investigated by monitoring transient intermediate species formed upon the reaction of precursors with alcohol radicals through pulse radiolysis studies. The pulse radiolysis studies have been carried out with the solutions containing (i) $[Cd(NH_3)_4]^{2+}$, (ii) SeO_3^{2-} or (iii) both $[Cd(NH_3)_4]^{2+}$ and SeO_3^{2-}.

A 4 % (v/v) (~500 mM) above mentioned alcohol was added to these solutions and was saturated with N_2O prior to the pulse radiolysis experiments. The absorbed dose was kept at 40 Gy/pulse in each case.

The formation as well as decay profiles of the transient species formed in all the three situations were monitored. It was observed that the formation of the transient species (i.e. $Cd^{\bullet+}$) in the case of solutions containing the above mentioned alcohol and only Cd precursor is very fast and complete within the pulse width (FWHM 50 ns) of the electron beam used for the study as well as has very low absorbance. Therefore, it is expected here that the rate constant of the formation of this transient species could be similar to that in our earlier work, i.e. reaction between e_{aq}^- and $[Cd(NH_3)_4]^{2+}$ [134].

In the reaction 4.27, R' represents the aliphatic chain with one carbon atom less than the aliphatic chain represented by R in the alcohol radical, $R^{\bullet}OH$.

$$e_{aq}^- + [Cd(NH_3)_4]^{2+} \longrightarrow Cd^{\bullet+} \ (k = 3.1 \times 10^{10}\ M^{-1}\ s^{-1}) \qquad (4.26)$$

$$R^{\bullet}OH + [Cd(NH_3)_4]^{2+} \longrightarrow Cd^{\bullet+} + R'CHO + H^+ \qquad (4.27)$$

The reaction between $SeSO_3^{2-}$ with the alcohol radicals was also investigated through the pulse radiolysis studies. It was observed that the alcohol radicals react with $SeSO_3^{2-}$ in a similar manner as in the case of reaction between e_{aq}^- [134].

$$e_{aq}^- + SeSO_3^{2-} \longrightarrow Se^{\bullet-} + SO_3^{2-} \ (k = 2.3 \times 10^{9}\ M^{-1}\ s^{-1}) \qquad (4.28)$$

$$R^{\bullet}OH + SeSO_3^{2-} \longrightarrow SO_3^{2-} + Se^{\bullet-} + R'CHO + H^+ \qquad (4.29)$$

In our previous study the growth rate constant for the reaction of e^-_{aq} with $SeSO_3^{2-}$ was determined, $k = 2.3 \times 10^9\ M^{-1}s^{-1}$ [168]. It was found that the growth rate constant for the reaction of $SeSO_3^{2-}$ with different alcohol radicals was lower (Table 4.6) than that for the reaction with e^-_{aq}.

Table 4.6 Growth and decay rate constants for $Se^{\bullet-}$ produced in the case of different alcohols.

Alcohols	k_{growth} (M^{-1} s^{-1})	k_{decay} (M^{-1} s^{-1})
methanol	4.0×10^8	5.7×10^5
ethanol	2.8×10^8	7.6×10^5
1-propanol	3.0×10^7	3.7×10^6
2-propanol	2.4×10^8	2.4×10^5
1-butanol	3.0×10^7	1.2×10^5

It was observed that the growth and decay rate constants of the transient intermediate, $Se^{\bullet-}$ in these cases were of the order of 10^8 M^{-1} s^{-1} and 10^5 M^{-1} s^{-1} respectively except for n-propanol, where growth rate constant is one order lower and the decay rate constant is one order higher than the above values. The reactions between (i) $Cd^{\bullet+}$ radicals and $SeSO_3^{2-}$ ions and (ii) $Se^{\bullet-}$ radicals and $[Cd(NH_3)_4]^{2+}$ ions have also been investigated by suitably choosing their initial concentrations in the pulse radiolysis studies. In the first case, the concentration of $[Cd(NH_3)_4]^{2+}$ was kept higher as compared to that of $SeSO_3^{2-}$ whereas, it is in the reverse order in the second case. The reactions happening in these cases can be written as:

$$Cd^{\bullet+} + SeSO_3^{2-} \longrightarrow Cd^{\bullet+} : SeSO_3^{2-}] \text{ (transient intermediate)} \quad (4.30)$$

$$Se^{\bullet-} + [Cd(NH_3)_4]^{2+} \longrightarrow [Se^{\bullet-} : [Cd(NH_3)_4]^{2+}] \text{ (transient intermediate)} \quad (4.31)$$

The growth as well as decay rate constants of these transient intermediate species have been determined by monitoring the kinetic profiles at their peak wavelengths (Table 4.7 and 4.8). The growth rate constants were found to be in the order of 10^8 M^{-1} s^{-1} in the first case (reaction 4.30) and 10^9 M^{-1} s^{-1} in the second case (reaction 4.31).

Table 4.7. Growth and decay rate constants of the transient species formed by the reactions between $Cd^{\bullet+}$ and $SeSO_3^{2-}$ ions.

Alcohols	k_{growth} (M^{-1} s^{-1})	k_{decay} (M^{-1} s^{-1})
methanol	4.26 x 10^8	2.88 x 10^7
ethanol	2.47 x 10^8	2.88 x 10^7
1-propanol	2.42 x 10^8	2.88 x 10^7
2-propanol	7.20 x 10^8	6.17 x 10^7
1-butanol	3.13 x 10^8	2.88 x 10^7

Table 4.8. Decay and growth rate constants of the transient species formed by the reactions between $Se^{\bullet-}$ and $[Cd(NH_3)_4]^{2+}$ ions.

Alcohols	k_{growth} (M^{-1} s^{-1})	k_{decay} (M^{-1} s^{-1})
methanol	1.5 x 10^9	1.0 x 10^7
ethanol	2.0 x 10^9	1.1 x 10^7
1-propanol	3.0 x 10^9	1.1 x 10^7
2-propanol	2.8 x 10^9	1.2 x 10^7
1-butanol	1.8 x 10^9	1.4 x 10^7

The pulse radiolysis studies were also performed in the aqueous solution containing equimolar concentrations of both the precursors, $[Cd(NH_3)_4]^{2+}$ and SeO_3^{2-} along with the above mentioned alcohols. In such case, both the precursors can react with the alcohol radicals to produce the transient intermediate species mentioned in the reactions 4.22. It was interestingly observed that these transient intermediate species have a well-defined absorption maximum at around 500 nm along with a shoulder at around 380 nm, in all of these five different alcohols (Fig. 4.18).

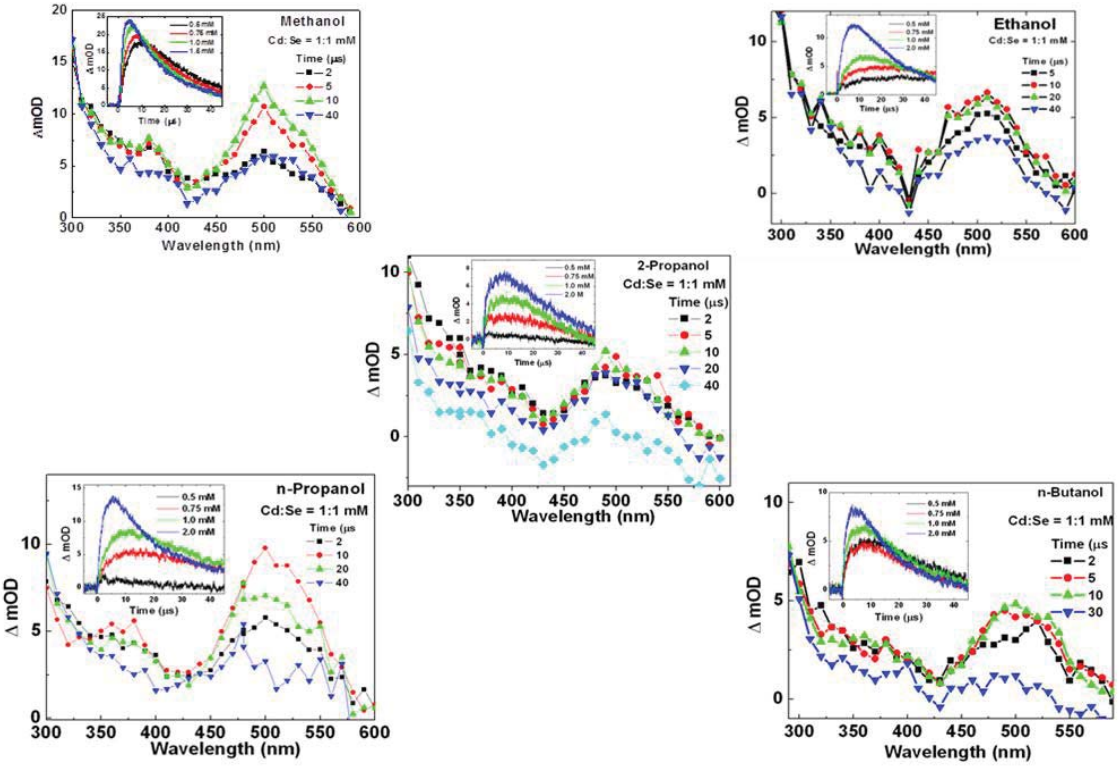

Figure 4.18 *Transient absorption spectra of 1.0 mM each Cd^{2+} and $SeSO_3^{2-}$ in the presence of different alcohols. (Inset: Kinetic profiles at different concentrations of precursors).*

The growth and decay rate constants (Table 4.9) of these transient intermediate species were determined from their kinetic profiles monitored at 500 nm (insets of Fig. 4.18) and it was observed that the growth rate constant was of the order of 10^8 M^{-1} s^{-1}, which match with those obtained in the case of the reactions 4.29 and 4.30. From these results, it is clear that the

formation of transient intermediate species as mentioned in the reactions 4.30 and 4.31 cannot be ruled out in this case where both the precursors are present in the equimolar concentrations. The decay rate constants of the transient intermediate species obtained through the reactions 4.22, 4.30 and 4.31 were found to be very much similar, of the order of 10^7 M^{-1} s^{-1}. It is to be mentioned here that the rate constants of the reactions (i) $Cd^{\bullet+}$ and $SeSO_3^{2-}$ and (ii) $Se^{\bullet-}$ and $[Cd(NH_3)_4]^{2+}$ are 1.9 x 10^{10} M^{-1} s^{-1} and 5.5 x 10^{10} M^{-1} s^{-1} respectively as obtained in our earlier study [134], which are higher than those obtained in the present study. A schematic representation of various transient intermediate involved in the synthesis and their formation rate constant is shown in scheme 4.1. The relatively slower rate constants obtained in the present study could be correlated with the (i) nature of the alcohol radicals which carry out the reactions and (ii) the nature of the solvent systems which supports the stability of the individual transient intermediate species. It is thus concluded that the kinetics of the formation of CdSe QDs is slower when the synthesis is carried out through the aliphatic alcohol radicals as compared to those obtained through the hydrated electrons, e_{aq}^-.

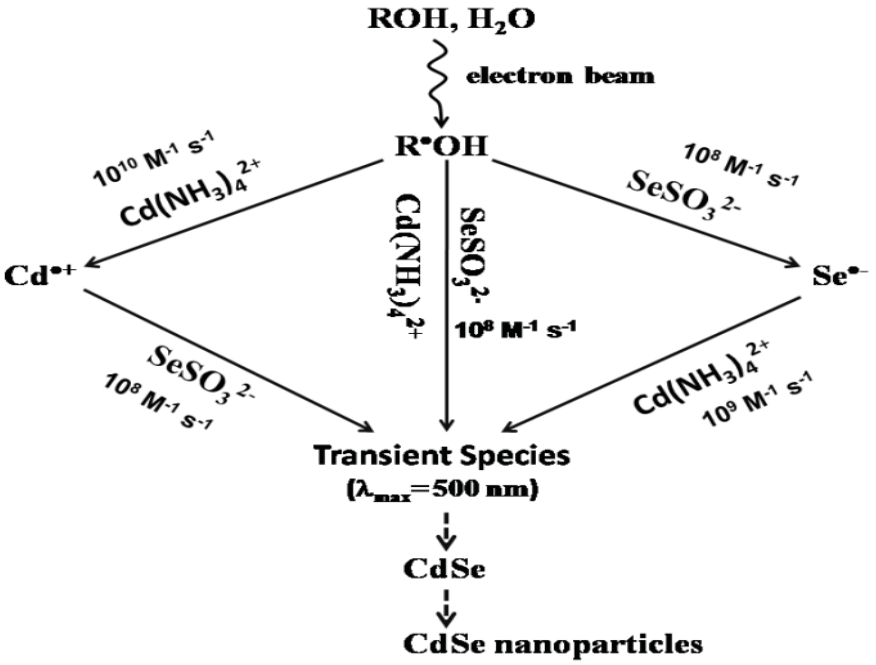

Scheme 4.1 *Transient species involved and their formation rate constant.*

Table 4.9. Growth and decay rate constants of the transient species formed by the reaction between $Cd^{\bullet+}$ and $Se^{\bullet-}$, along with their peak absorbance values observed in the case of different alcohols.

Alcohols	k_{growth} (M^{-1} s^{-1})	k_{decay} (M^{-1} s^{-1})	ΔmOD
methanol	3.69×10^8	4.90×10^7	13.0
ethanol	2.17×10^8	1.77×10^7	6.4
1-propanol	3.39×10^8	1.05×10^7	8.5
2-propanol	2.42×10^8	2.73×10^7	4.6
1-butanol	3.04×10^8	2.20×10^7	6.3

4.4. Conclusion

In summary, we have synthesized different saccharide capped CdSe QDs in aqueous solution via electron beam irradiation. The stability of the as grown QDs was found to be superior as compared to those synthesized without any capping agents in the aqueous medium. The mechanism of the formation of these QDs was investigated by the pulse radiolysis studies. The studies found that the starch capped CdSe QDs were more stable as well as exhibit higher fluorescence as compared to other saccharide capped QDs (scheme 4.2). The glucose capped CdSe QDs were found to be less cytotoxic as compared to the uncapped as well capped with other saccharides. It is expected that these QDs could find importance in the biological applications. Dynamics of radiolytic formation of CdSe QDs in aqueous solution containing different aliphatic alcohols was studied. It was found that the formation of CdSe QDs proceeds *via* formation of short lived transient intermediate species having absorption maximum at 500

nm which are formed by the reaction of different secondary alcohol radicals with the precursor molecules.

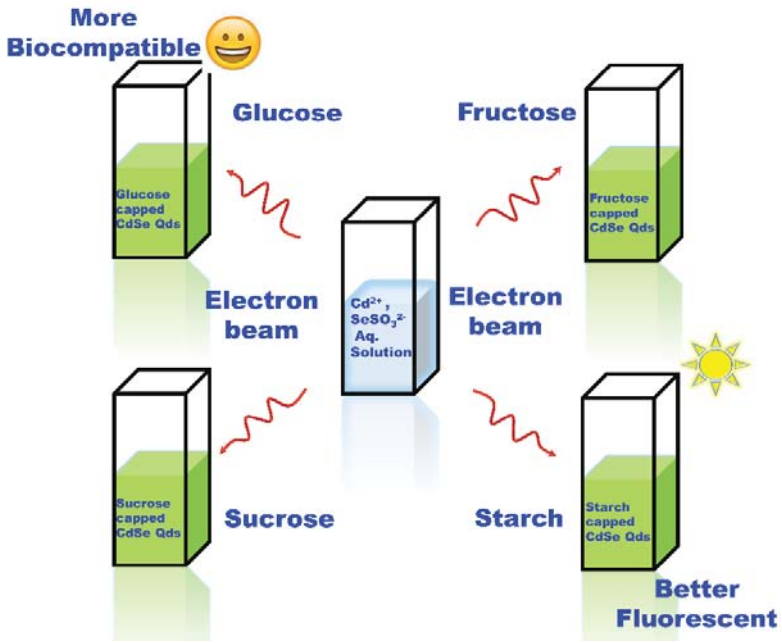

Scheme 4.2 *Relative properties of different saccharide capped CdSe QDs.*

The rate constant for the formation of transient intermediate species formed by the reaction of the alcohol radicals with Cd and Se precursors is lower than the rate constants for the formation of transient intermediate species formed by the reaction of hydrated electrons, e_{aq}^- with the Cd and Se precursors. The optical properties of the QDs synthesized with different alcohol radicals is also different.

CHAPTER 5
ROOM TEMPERATURE SYNTHESIS OF CdSe NANOPARTICLES

5.1. Introduction

Nanoparticles can be synthesized using various methods like- organometallic route, laser ablation, sol-gel method, hydrothermal/solvothermal, sonochemical, radiation chemical, photochemical and normal chemical methods etc. Out of these methods, organometallic route, laser ablation, sol-gel method, hydrothermal/solvothermal methods involve high temperature, high pressure or vacuum, toxic and hazardous chemicals and well equipped laboratories. Sonochemical, radiation and photochemical methods require complicated and costly instrumentation and their maintenance is quite cumbersome. Synthesizing nanoparticles by using normal chemical method does not involve high temperature, pressure, complicated instrumentations and specific laboratory conditions [175]. Various biomolecules and bio compatible molecules like- Bovine Serum Albumin (BSA), different thiol group containing compounds like- glutathione, l-cysteine and thioglycerol can used as reducing as well as capping agents which are not hazardous and provide very good stable and monodispersed nanoparticles [176-180]. However, the nanoparticles synthesized by the green synthesis route usually won't possess comparable optical properties (e.g. sharp excitonic absorption and narrow-tunable emission) as of those obtained through the high temperature route [175]. CdSe nanoparticles or Quantum dots (QDs) synthesized with the help of biomolecules have been used as the biomarkers or probes for understanding the shapes and structures of macromolecules of biological interests [130,181,182]. This is mainly due to the intense fluorescence obtained from the CdSe QDs and their robust stability in the diverse chemical environments. One of the most important method (based on the fluorescence properties) widely performed to understand the interaction between nanoparticles and the species (such as dyes, and biomolecules) conjugated to them is the Foster's resonance energy transfer (FRET). It is well known that the FRET takes place predominantly in those cases, where the distance between the donor and the accepter is within 10 nm [183,184]. Often in this kind of studies,

nanoparticles act as donors and conjugated species act as accepters. Willard *et al*. [185] observed enhanced fluorescence caused by FRET from the CdSe−ZnS core−shell QD donors to the tetramethylrhodamine-labeled streptavidin (SAv−TMR) acceptors. Zhang *et al*. [186] demonstrated a QD based DNA nano sensor, wherein the QDs coated with streptavidin function as a FRET donor.

In this chapter, we have described about green synthesis of CdSe QDs using (i) 1-thioglycerol and (ii) BSA in two separate sections (5.2 and 5.3 respectively). In section 5.2 we have reported about the synthesis of CdSe QDs through a facile, one pot, single step and green route at room temperature using 1-thioglycerol as a capping as well as reducing/catalysis agent. The absorbance, fluorescence and the fluorescence lifetime properties of the CdSe QDs synthesized with different stoichiometric ratios of Cd and Se precursors have been extensively studied. All these QDs have a sharp excitonic absorption peak at around 420 nm which is usually not found in QDs synthesized at ambient conditions. A systematic in-depth analysis of their formation mechanism as well as optical properties has been made. The above mentioned studies of optical properties and the reaction mechanism of the synthesis provide a valuable platform to synthesize the CdSe QDs of the desired properties in aqueous solution *via* green synthesis route.

In section 5.3, we investigated the growth kinetics of CdSe QDs in aqueous solution in the presence of BSA. Since, there is always a nucleation followed by growth of the nanoparticles, which is terminated at an early stage in order to restrict them from the precipitation. This termination is achieved by adjusting various factors such as the precursor concentrations, release of the precursors during the reaction, concentration of capping agents, etc. The kinetics of growth can be different for different synthesis methods and types of precursors used. Nonetheless, in the present work, the growth was studied by monitoring the changes in the optical absorption spectra of the QDs as well as the room temperature fluorescence spectra of

BSA and QDs with the reaction time. The interaction between the BSA molecules and the CdSe QDs was investigated by the FRET analysis, where BSA molecules were found to be the donors and the CdSe QDs played the role of accepters. Of course, the synthesis of protein encapsulated nanomaterials or QDs and their characterization studies have been reported in the literature [187,188]. However, the detailed analysis of the growth kinetics of the QDs (synthesized *in situ* in the protein milieu) with their time dependent photophysical properties may contribute in better understanding of the correlation between different processes (such as crystal growth, defect formation, energy transfer) taking place in the system.

5.2. Facile and green synthesis of 1-thioglycerol capped CdSe QDs in aqueous solution

5.2.1. Experimental section

5.2.1.1. Materials

High purity chemicals 1-thioglycerol ($C_3H_8O_2S$), cadmium sulphate ($CdSO_4$), sodium sulphite (Na_2SO_3) and selenium powder (Se) were obtained from Sigma Aldrich and used without further purification. Aqueous solutions were prepared by using nanopure water (resistivity 18.2 megaohm cm) obtained from the Millipore water purifying system. Ammoniated cadmium sulphate $Cd(NH_3)_4SO_4$ was used as the cadmium precursor and sodium selenosulphate (Na_2SeSO_3) was used as the selenium precursor for the synthesis of CdSe QDs. Na_2SeSO_3 was prepared by refluxing the reaction mixture containing 10 g Na_2SO_3, 1 g Se powder and 50 ml water at 70^0C for 7hrs [133].

5.2.1.2. Synthesis

The synthesis of CdSe QDs was carried out as follows: 50 µl of the 1-thioglycerol solution (Stock 11.5 M) was added to 5 ml of 1.0 mM ammoniated cadmium sulphate, $Cd(NH_3)_4SO_4$.

This reaction mixture was equilibrated for 5 minutes. Then 5 ml solution of 1.0 mM sodium selenosulphate, Na_2SeSO_3 solution was added to it with constant stirring. This solution was considered as 1:1 CdSe QDs. The exact concentration of cadmium, selenium precursor and 1-thiogycerol was 0.5 mM, 0.5 mM and 57.5 mM respectively. However, lower concentrations (5 and 15 mM) of 1-thioglycerol were also used in the synthesis for a comparison purpose. All these experiments were carried out room temperature under ambient conditions. For different stoichiometric ratios, the concentrations of $Cd(NH_3)_4SO_4$ and sodium selenosulphate were taken as 2.0 mM and 1.0 mM (called as 2:1); 1.0 mM and 2.0 mM (called as 1:2); 1-thioglycerol concentration was fixed at 57.5 mM in all these three cases. As soon as the selenium precursor was added to the equilibrated solution of Cd-thioglycerol, the colour of the solution started to change from colourless to greenish yellow. This evolution of colour indicates the formation of colloidal semiconductor QDs. The as prepared colloidal solutions were used to record the absorption spectra, steady-state and time-resolved fluorescence spectra.

5.2.1.3. Materials characterization

UV-visible absorption spectral measurements were carried out by using a spectrophotometer with a model no. JASCO V650, and solution taken in a quartz cell with 10 mm optical path length. Steady-state fluorescence measurements were carried out at room temperature by using a Hitachi F-4500 spectrofluorometer. Fluorescence lifetime measurements were carried out using a time-resolved spectrofluorometer using time-correlated single photon counting (TCSPC) principle with a model no. Horiba Jobin Yvon IBH 400. X-ray diffraction (XRD) measurements of CdSe QDs were carried out by using a Panalytic (Model-X-Pert pro) instrument using Cu K-α source. Transmission electron microscopy (TEM) images were recorded using the instrument Libra 120 keV from Carl Zeiss. Samples for TEM measurements were prepared by putting a drop of the as prepared colloidal solution on thin carbon coated

copper grid and consecutively allowing the solvent to evaporate. Fourier transform infrared (FTIR) spectra were recorded with the sample put on a KBr pellet using a SHIMADZU IR-Affinity-1 FTIR instrument in diamond ATR mode. Raman spectral studies were carried out on Seki's STR300 Raman spectrometer equipped with a single monochromator (Princeton instruments) and a peltier cooled charge coupled device (CCD). A fiber coupled diode-pumped solid-state laser (DPSSL) source was used as an excitation source with a wavelength of 532 nm. The spectral and spatial resolution of the Raman system was nearly 3 cm^{-1} and 5 cm^{-1}, respectively.

5.2.1.4. Pulse radiolysis

Pulse radiolysis experiments were carried out with a 7 MeV linear electron accelerator (LINAC) coupled with a kinetic spectrometer, the details of which has already been described in section 4.2.1.3.

5.2.1.5. Cyclic voltammetry

Cyclic voltammetric measurements were carried out using the PGSTAT 302 N potentiostat. Saturated calomel electrode (SCE) was used as reference electrode whereas glassy carbon electrode and platinum foil were used as working and counter electrodes respectively. 0.1 M Na_2SO_4 solution was used as supporting electrolyte. The working electrode was polished over a microcloth after each run using 0.05 micron alumina paste and was thoroughly rinsed with nanopure water. The cyclic voltammetry was performed at 20, 40, 60, 80 and 100 mV/s scan rates. The concentration of TG was kept at 6.0 mM and concentration of ammoniated cadmium sulphate and sodium selenosulphate was kept at 0.5 mM. The pH was adjusted to 11.0.

5.2.3. Results and discussion

5.2.3.1. Synthesis and characterization

The reaction mixture containing the precursors ammoniated cadmium sulphate and sodium selenosulphate either 0.5 mM each (1:1) or 1 mM and 0.5 mM (2:1) or 0.5 mM and 1 mM (1:2) respectively, did not exhibit any change in its colour even after several days under ambient laboratory conditions. However, these reaction mixtures in the presence of 1-thioglycerol (TG) exhibit a noticeable colour change from clear colourless to greenish yellow at room temperature under ambient laboratory conditions within a few minutes. This clearly confirms the formation of new species which have a strong absorption in the visible region. Fig. 5.1 shows the camera-ready pictures of reaction mixtures (1:1) in the absent (clear colourless solution) and presence (coloured solution) of 57.5 mM TG (50 µl ml TG in 10 ml solution). The expected products are CdSe nanoparticles only in the present case.

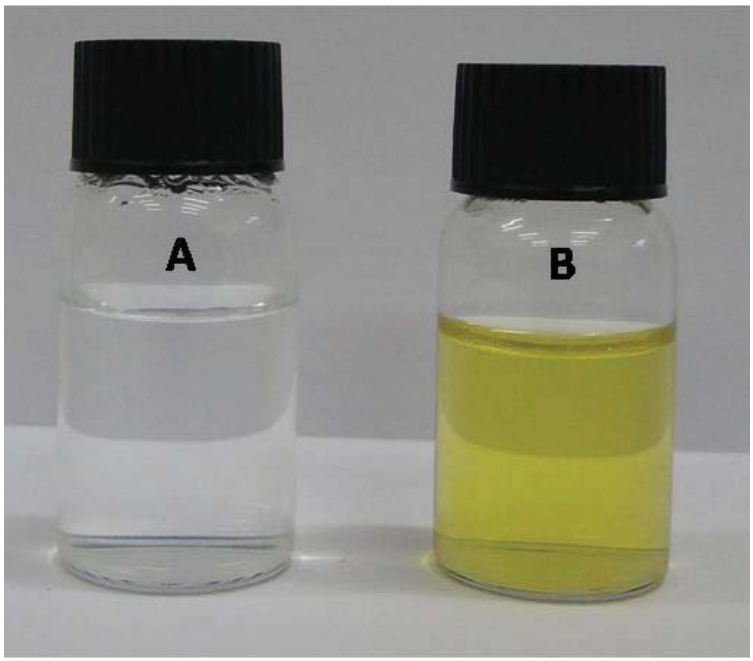

Figure 5.1 *Camera ready pictures of reaction mixture containing a) Cd and Se precursors, b) Cd and Se precursor along with 1-thioglycerol.*

Fig. 5.2 represents the absorption spectra recorded for (i) individual precursors (i.e. 0.5 mM $Cd(NH_3)_4SO_4$, 0.5 mM Na_2SeSO_3), (ii) only TG (57.5 mM), (iii) individual precursors in the presence of TG (i.e. 0.5 mM $Cd(NH_3)_4SO_4$ and 57.5 mM TG; 0.5 mM Na_2SeSO_3 and 57.5 mM TG), (iv) reaction mixture in the absence of TG (i.e. solution containing 0.5 mM $Cd(NH_3)_4SO_4$ and 0.5 mM Na_2SeSO_3 only) and (v) reaction mixture in the presence of TG (i.e. 0.5 mM $Cd(NH_3)_4SO_4$ and 0.5 mM Na_2SeSO_3 and 57.5 mM TG).

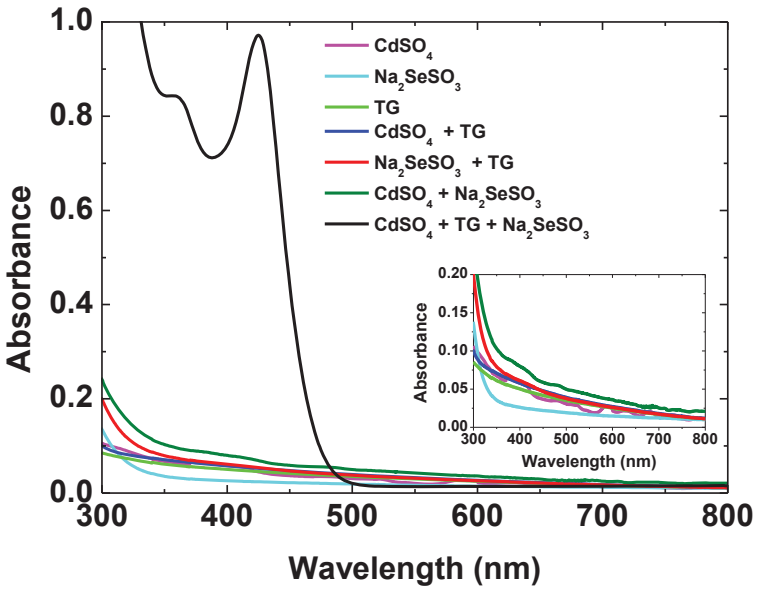

Figure 5.2 *Absorption spectra of different systems used in the synthesis of CdSe QDs.*

This confirms that TG catalyzes/induces the formation of CdSe nanoparticles in the present case. Similar experiments were also carried out with lower concentrations of TG (i.e. 5 and 15 mM), and the change in the colour of the reaction mixtures was almost identical to the naked eye, however, there was a remarkable change in their absorption spectra (Fig. 5.3). It is clear from these spectral patterns that the CdSe nanoparticles obtained in the case of relatively higher concentration of TG (57.5 mM) are better, as the excitonic peak is very sharp with reduced band edge absorption. It is to be mentioned here that such a sharp excitonic absorption peak along with an additional peak at lower wavelength (higher energy peak) is usually observed

only in the case of CdSe nanoparticles or QDs synthesized at elevated temperature under inert atmosphere using TOPO/TOP as the capping agents [189]. However, we have observed such results in the case of CdSe nanoparticles synthesized at just room temperature in the presence of 1-thioglycerol without any additional effort. The CdSe nanoparticles have been synthesized with 57.5 mM TG for further characterization and investigations throughout the text.

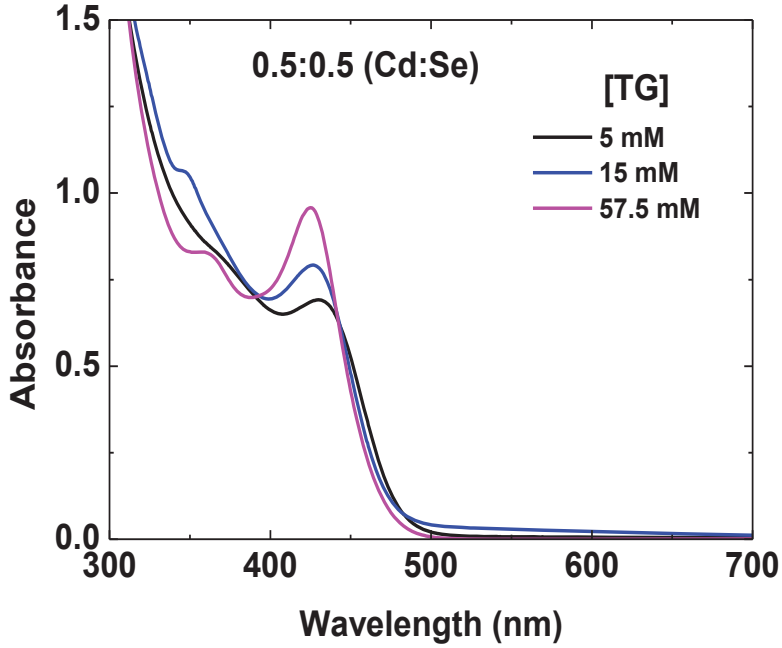

Figure 5.3 *Absorption spectra of CdSe QDs synthesized with three different concentrations of 1-thioglycerol.*

These CdSe nanoparticles have been characterized by XRD measurements. One typical XRD pattern obtained in the case of CdSe nanoparticles synthesized with the 1:1 reaction mixture is shown in the Fig. 5.4. From this figure three distinct peaks at 25.7^0, 42.9^0 and 50.7^0 were observed. These peak positions correspond to (111), (220) and (311) diffraction planes respectively. Thus obtained pattern clearly indicates the formation of cubic ZB phase CdSe by comparing with the standard ICDD card no. 19-191. The peak broadening in the XRD pattern was due to the formation of nano sized crystals. The crystallite sizes have been estimated using

the Scherrer's formula (4.25). The average crystallite size thus estimated was ~1.9 nm in the case of CdSe nanoparticles obtained from the 1:1 reaction mixtures. Similar results were obtained in the case of other two reaction mixtures too.

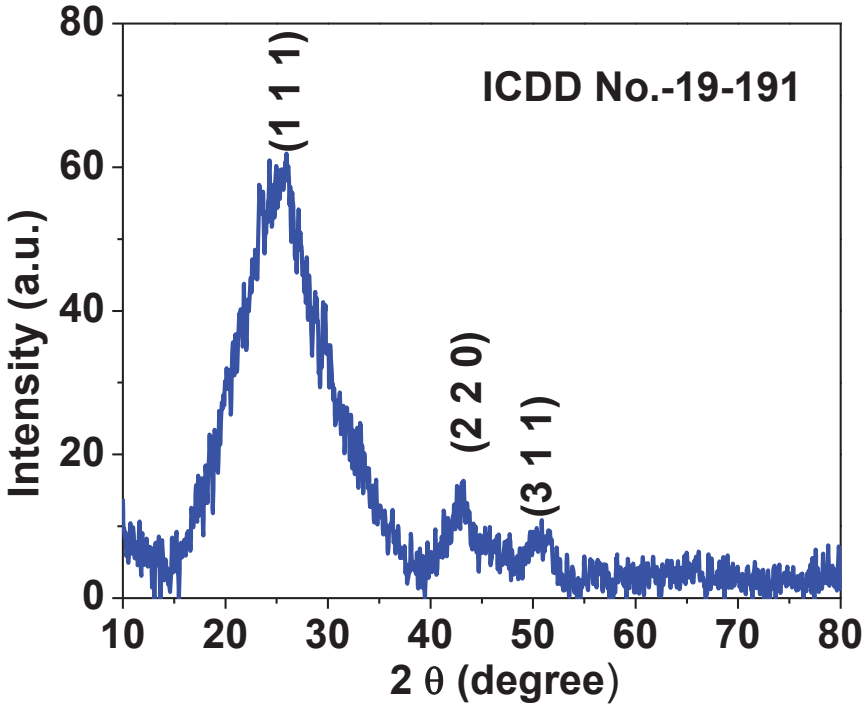

Figure 5.4 *XRD pattern of thioglycerol capped CdSe QDs.*

The particle sizes of these nanoparticles are less than the Bohr radius of exciton for CdSe (i.e. 5.6 nm) and hence these nanoparticles can be called as QDs. These QDs have also been characterized by Raman as well as FTIR spectroscopy. One representative Raman spectra for the CdSe QDs synthesized from the 1:1 reaction mixture is shown in the Fig. 5.5. Raman spectra of as grown CdSe QDs comprised of peaks for fundamental longitudinal optical (LO1) phonon mode at 202 cm^{-1} and the second longitudinal optical (LO2) phonon mode at 404 cm^{-1} [190,191]. In between these two peaks there are peaks at 242, 280, 321 and 350 cm^{-1} which may be surface optic modes [192] These types of surface optic modes have been reported earlier in very small size QDs, which arise due to more no. of atoms on the surface in a

nanostructures behaving like molecules [192]. A shoulder occurring at 187 cm^{-1} can also be noticed which can be attributed to transverse optical (TO) phonon mode [192].

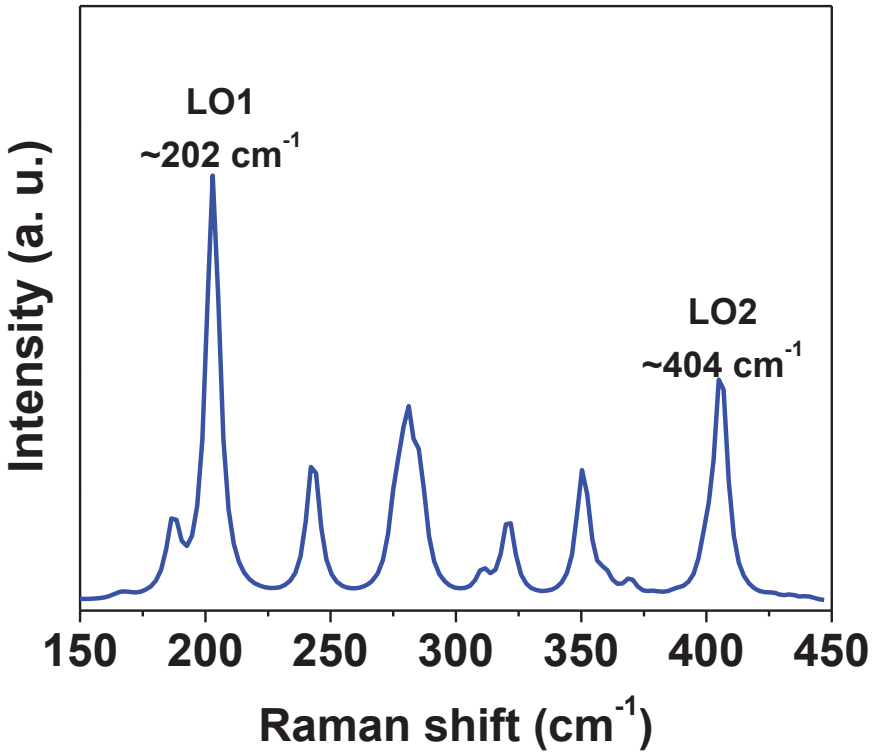

Figure 5.5 *Raman Spectrum of thioglycerol capped CdSe QDs.*

FTIR spectra of TG and CdSe QDs synthesized from the 1:1 reaction mixture are shown in the Fig. 5.6. It is clear from these spectra that TG binds with the CdSe QDs. It is seen from this figure that the peak at 2550 cm^{-1} due to S-H stretching vibration mode is present in the FTIR spectra of TG, while in the case of thioglycerol capped CdSe it is absent. This clearly shows the binding of sulphur atom of the TG molecule with the Cd atom of CdSe QDs which is also in good agreement with hard soft acid base (HSAB) principle. The broad band at 3650-3000 cm^{-1} which is present in both the thioglycerol as well as the CdSe is due to the O-H stretching and C-H stretching modes. The band is broadened so much because of the aqueous solution. The bands at 2930 and 2880 cm^{-1} which corresponds to -CH_2 asymmetric and symmetric

stretching modes are interestingly found only in thioglycerol. Band at 1640 cm^{-1} which corresponds to O-H bending of water was present in both the spectra. Further the bands at 1420 and 1030 cm^{-1}in the thioglycerol are due to -CH_2 bending and due to C-O and C-C stretching respectively. In the case of thioglycerol, the band at 940 cm^{-1} corresponds to C-S stretching which is absent in the case of CdSe [193]. This result clearly indicates that the surface passivation of CdSe QDs with higher Cd:Se ratio by the TG molecules is better than those with the lower Cd:Se ratio.

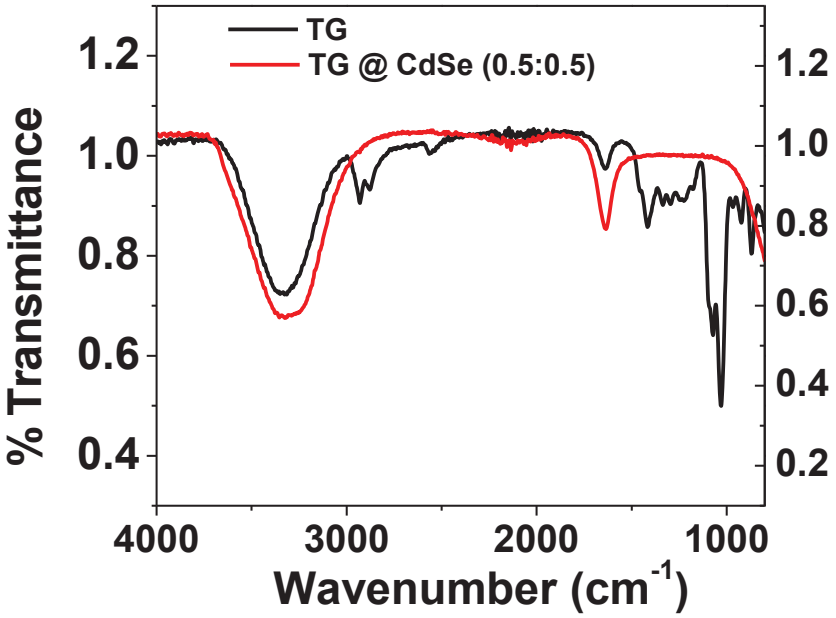

Figure 5.6 *FTIR spectra of thioglycerol and thioglycerol capped CdSe QDs.*

The morphology and shapes and sizes of these QDs have been determined from their SEM and TEM images respectively. Two representative SEM images for the CdSe QDs synthesized from the 2:1 reaction mixture are shown in the Fig. 5.7, a and b for lower and higher magnifications, respectively. It is seen from these figures that these QDs exist in the agglomerated form as rod shaped with diameter about a few micron and length about a few

tens of micron with a high aspect ratio about 10. Spherical and rod shaped mixed morphology was also obtained in the case of CdSe QDs synthesized from the 1:1 reaction mixture (Fig. 5.8a). Rod shaped morphology was again obtained in the case of QDs synthesized from the 1:2 reaction mixture (Fig. 5.8b).

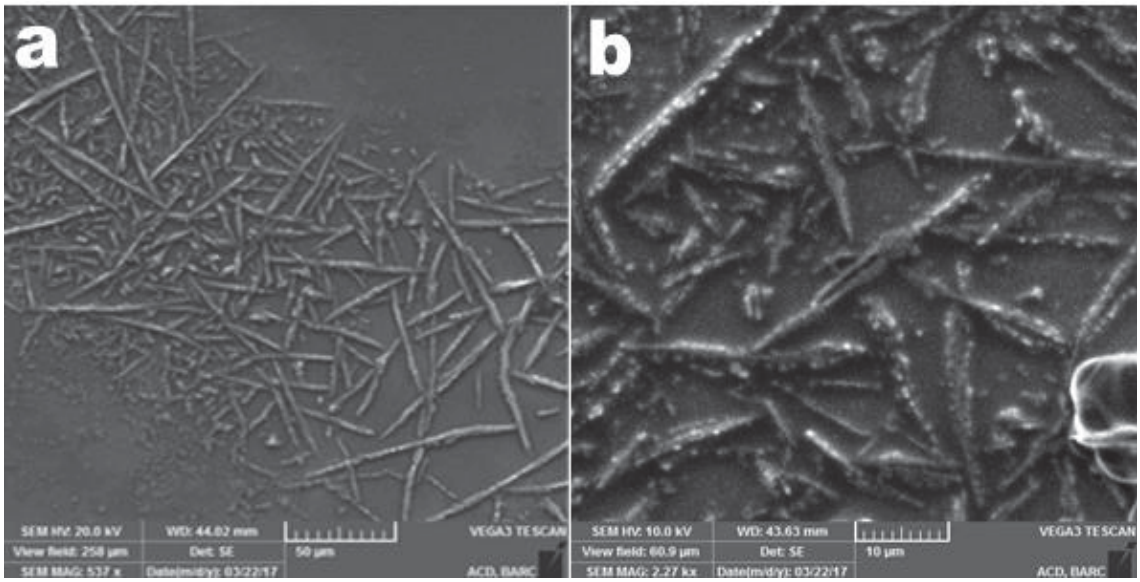

Figure 5.7 *SEM images of 1.0:0.5 mM Cd:Se QDs (a) low magnification and (b) high magnification.*

However, the sizes of the rods in the case 1:2 were less as compared to those obtained in the case of 2:1. It is inferred from these observations that the morphology of the agglomerated CdSe QDs strongly depends on the stoichiometric compositions used during their synthesis. The morphology becomes anisotropic (rod shaped structure) when the Cd:Se ratio changes in the either way and on the contrary, both isotropic and anisotropic structures exist in the case stoichiometric composition. One representative TEM image obtained for the CdSe QDs synthesized from the 2:1 reaction mixture is shown in the Fig. 5.9. It is clear from this image that the sizes of the CdSe QDs are around 3 nm and are mostly homogeneous in nature (inset

of Fig. 5.9). Similar observations were also observed for the other two cases (Fig. 5.10 for CdSe QDs synthesized with the 1:1 reaction mixture).

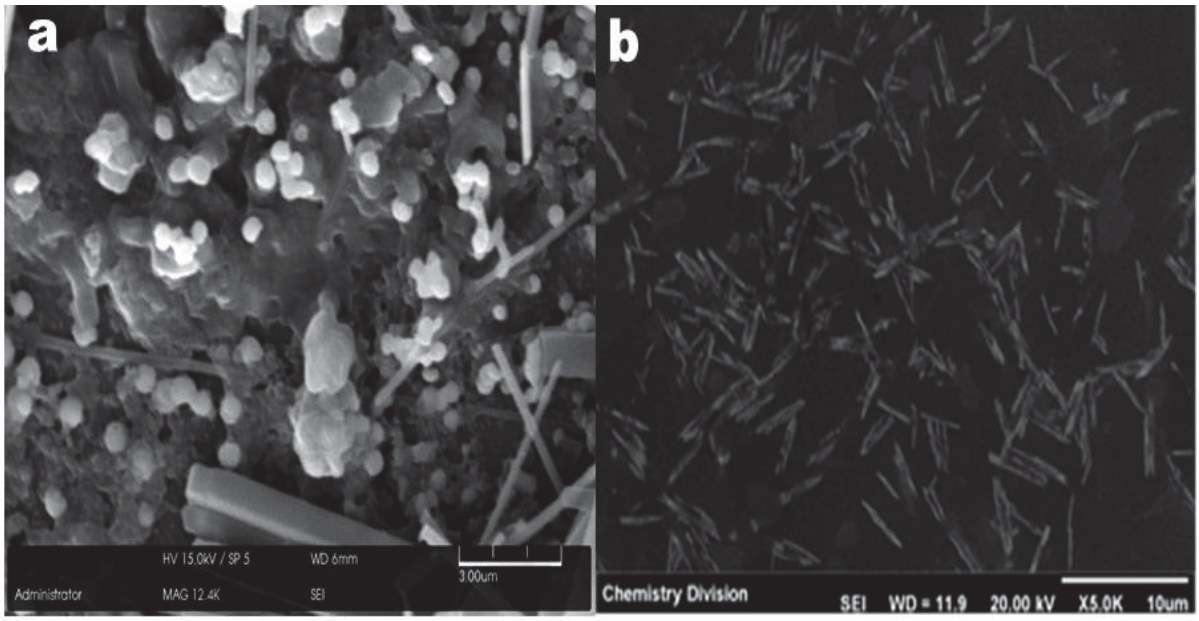

Figure 5.8 *SEM images of (a) 0.5:0.5 mM and (b) 0.5:1.0 mM Cd:Se quantum dots.*

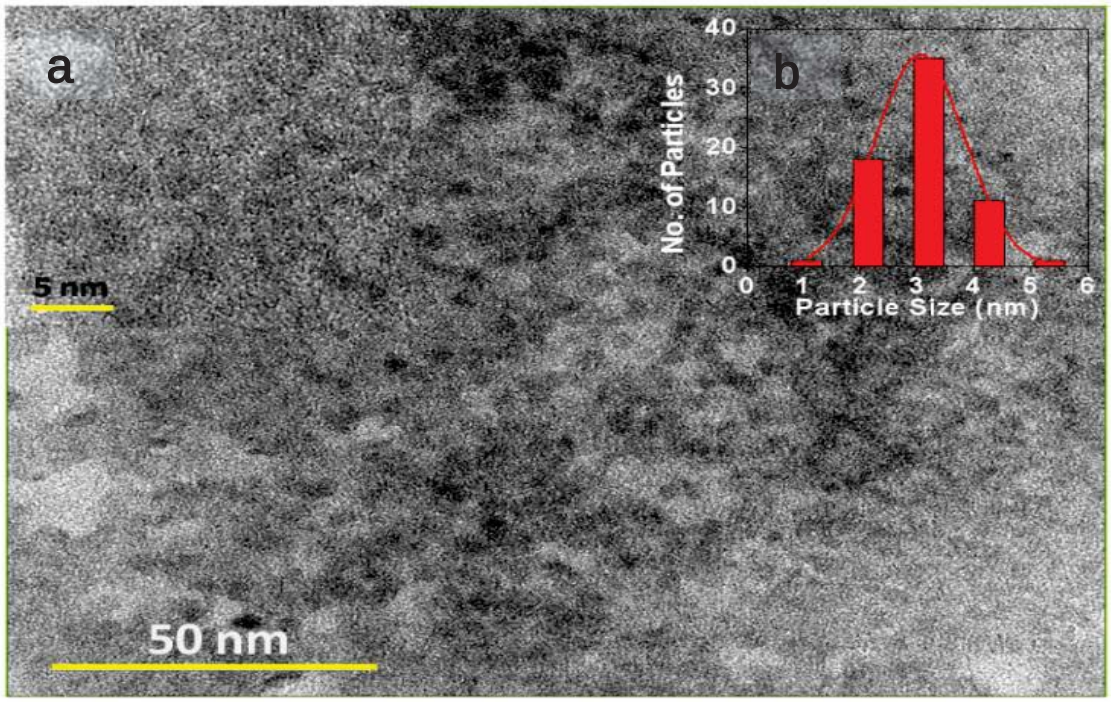

Figure 5.9 *TEM image of CdSe QDs, inset (a) HRTEM image and (b) Particle size distribution.*

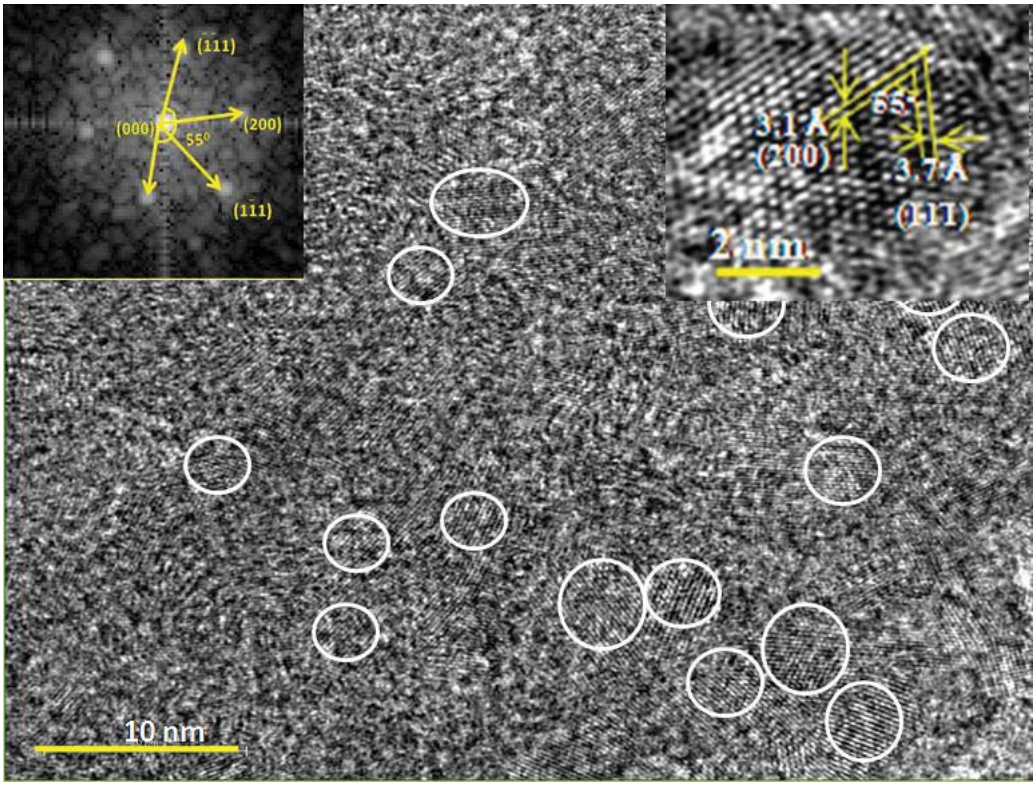

Figure 5.10 *TEM image of 0.5:0.5 mM Cd:Se quantum dots (inset FFT pattern and HRTEM image showing the planes of the crystal).*

5.2.3.2. Optical properties

5.2.3.2.1. UV-visible absorption studies

The absorption spectra of CdSe QDs synthesized with different stoichiometric ratio of Cd:Se were recorded after a few minutes of mixing of the two precursor solutions at room temperature (see Fig. 5.11). In all the three cases, a sharp excitonic absorption peak along with a second higher energetic peak was observed. There was a blue shift in the first excitonic peak position with an increase in the Cd:Se ratio (λ_{max} for 1:1 was 425 nm and 2:1 was 417 nm) however no noticeable shift was observed with decrease in this ratio (λ_{max} for 1:1 was 425 nm and 1:2 was 426 nm). The energy values of band gap (E_g) were calculated from the Tauc plot (see the inset of Fig. 5.11). The particle sizes for all the samples were calculated using the modified Brus equation (eq. 5.1) [10].

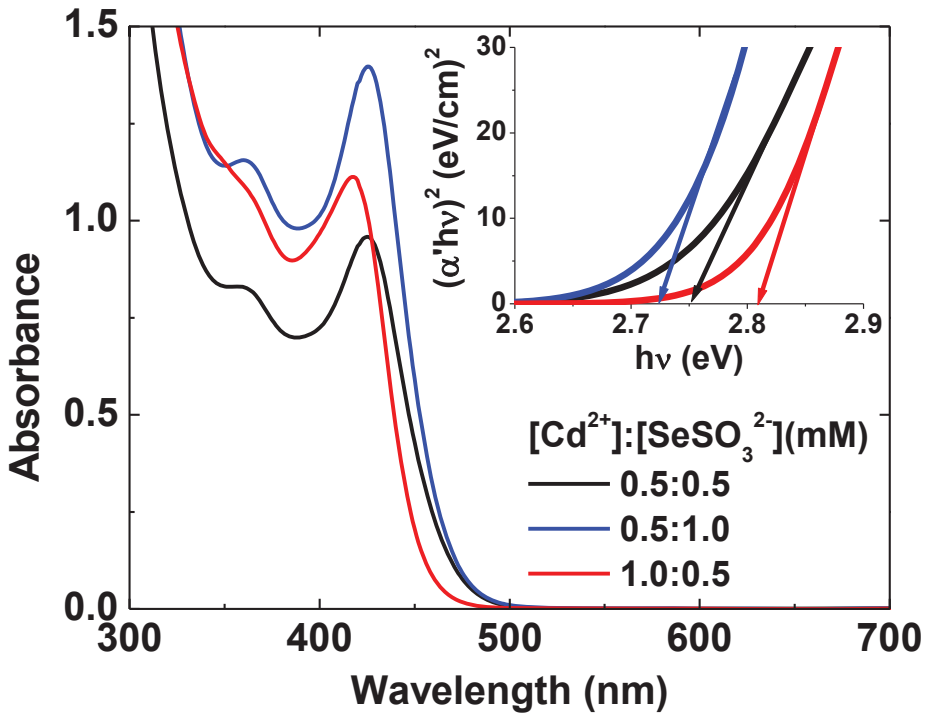

Figure 5.11 *UV-vis absorption spectra of CdSe QDs synthesized with different Cd^{2+} and Se^{2-} ratios (Inset: Tauc plot for different Cd:Se ratios).*

$$E_g = E_g(0) + \alpha/d^2 \qquad (5.1)$$

where, $E_g(0)$ = 1.75 eV is the bulk band gap of CdSe, α = 3.7 eVnm^2, d is the particle size in nm. E_g is the band gap value in eV obtained from Tauc plot. The band gap (E_g) values were determined from the Tauc plots of $(\alpha` h\nu)^2$ *vs* $h\nu$, as this is a direct band gap semiconductor [194]. The symbol 'a`' represents the absorption coefficient multiplied with the concentration of the CdSe nanoparticles, which was obtained from the relation (2.303A/l), where 'A' is the absorbance and 'l' is the optical path length of the cell (10 mm). The term '$h\nu$' represents the photon energy. The particle sizes were also estimated by using empirical equation postulated by Peng and his group. [145] (eq 5.2) and both the values match well.

$$D = (1.6122 \times 10^{-9})\lambda^4 - (2.6575 \times 10^{-6})\lambda^3 + (1.62425 \times 10^{-3})\lambda^2 - (0.4277)\lambda + 41.57 \qquad (5.2)$$

where, D is the particle size and λ is the wavelength of first excitonic absorption peak position (in nm). The particle sizes were found to be about 2 nm. The first excitonic absorption peak was assigned to the 1S(h) to 1S(e) transition and the second peak was assigned to the 1P(h) to 1P(e) transition (Fig. 5.12) [195, 196].

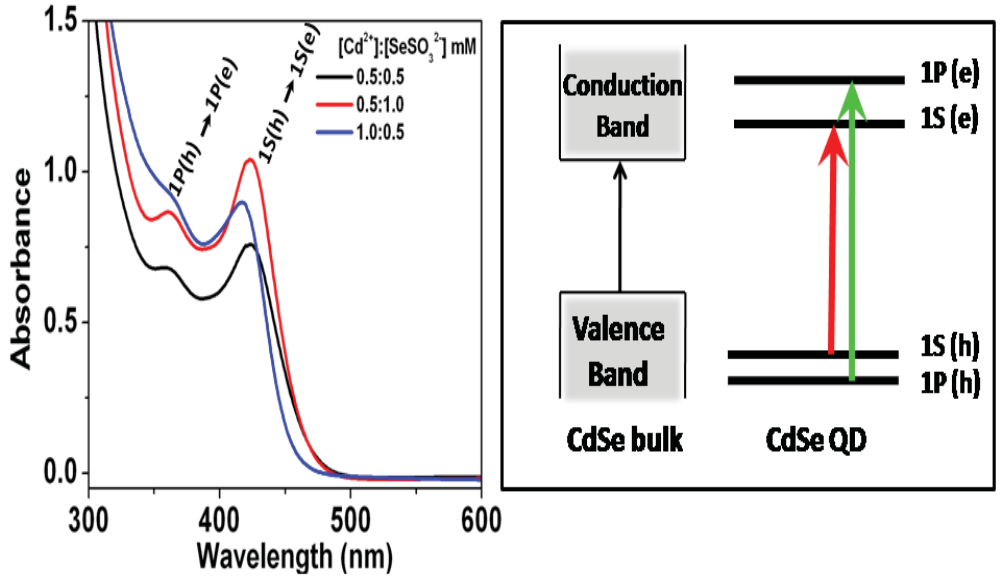

Figure 5.12 *Band assignment of absorption spectra of CdSe QDs and schematic representation of electronic absorptions to corresponding bands.*

The appearance of the excitonic peak indicates the formation of the CdSe QDs. Therefore, the rate of formation of these QDs has been estimated from the plot of the absorbance value recorded at 420 nm *vs* different time just after the mixing of the two precursors. The rate constants were determined by fitting the experimental data points with a first order kinetics, and found to be $k_{0.5:0.5} = 7.5 \times 10^{-3}$ s^{-1}, $k_{1.0:0.5} = 4.4 \times 10^{-3}$ s^{-1} and $k_{0.5:1.0} = 3.1 \times 10^{-2}$ s^{-1}. It was observed that the rate of formation of these QDs followed the order, 2:1 < 1:1 < 1:2.

5.2.3.2.2. Photoluminescence studies

The steady-state emission and excitation spectra of CdSe QDs synthesized with different stoichiometric ratios of Cd:Se were recorded after a few minutes of mixing of the two precursor solutions (see Fig. 5.13).

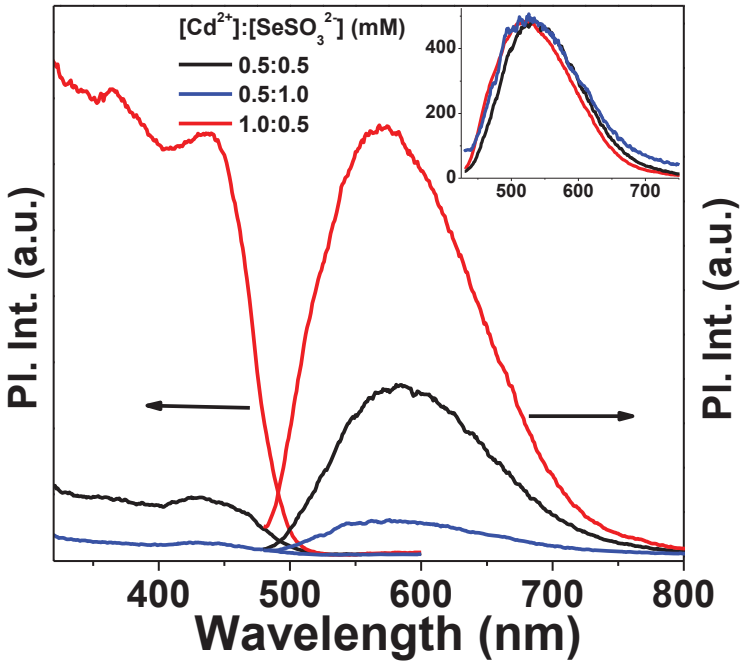

Figure 5.13 *Steady state Pl spectra for different Cd:Se ratio. (Inset: Normalised Pl spectra).*

There was no excitation wavelength dependent emission observed from these QDs confirming their homogeneity. The Pl intensity was found to be highly dependent on the stoichiometric ratios of Cd and Se precursors and followed the order, 1:2 < 1:1 < 2:1. As in the previous section discussed, the formation rate constant of the QDs follows the order 1:2 > 1:1 > 2:1 i. e. the formation rate constant is decreasing with increasing Cd:Se precursor ratio. The slower the rate of formation of a crystal yield good quality of crystal with less no. of trap states which exhibit better Pl yield. Hence, the QDs synthesized with 2:1 Cd:Se ratio is having more Pl. There was a spectral shift among these QDs too, for 1:1 case λ_{em}^{max} = 535 nm, for 2:1 it was 515 nm and for 1:2 it was 525 nm (normalized emission spectra in the inset of Fig. 5.13).

There was good match between the absorption and excitation spectra indicating the genuinity of the material. It was observed that there was a large stokes shift associated with these Pl and the excitation spectra, which clearly indicates these Pl could be due to trap states only. As the Pl spectra were very broad, it could be composed of both shallow as well as deep trap states (Scheme 5.1).

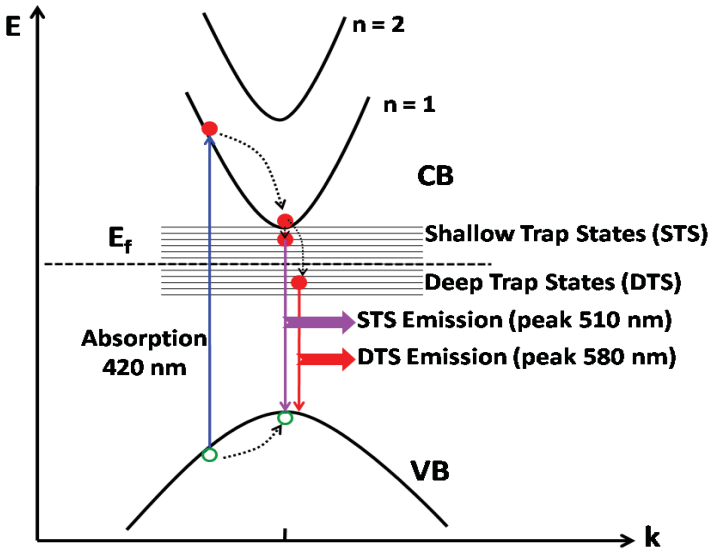

Scheme 5.1 *Representation of excitation and de-excitation of charge carriers in the CdSe QDs capped with 1-thioglycerol.*

These two different trap state emissions were resolved from the photoluminescence spectra with multiple curve fitting method (Fig. 5.14). It was found that both the shallow and deep trap state emissions increase on increasing the Cd:Se precursor ratio up to 1.0:0.5 mM. The relative band gap intensity and the relative trap state intensity with the Cd:Se precursor ratio was also plotted and it was found that the fraction of band gap increases with increasing the Cd:Se ratio however it does not change much from 0.5:0.5 mM to 1.0:0.5 mM. The fraction of trap state emission decreases with the Cd:Se precursor ratio.

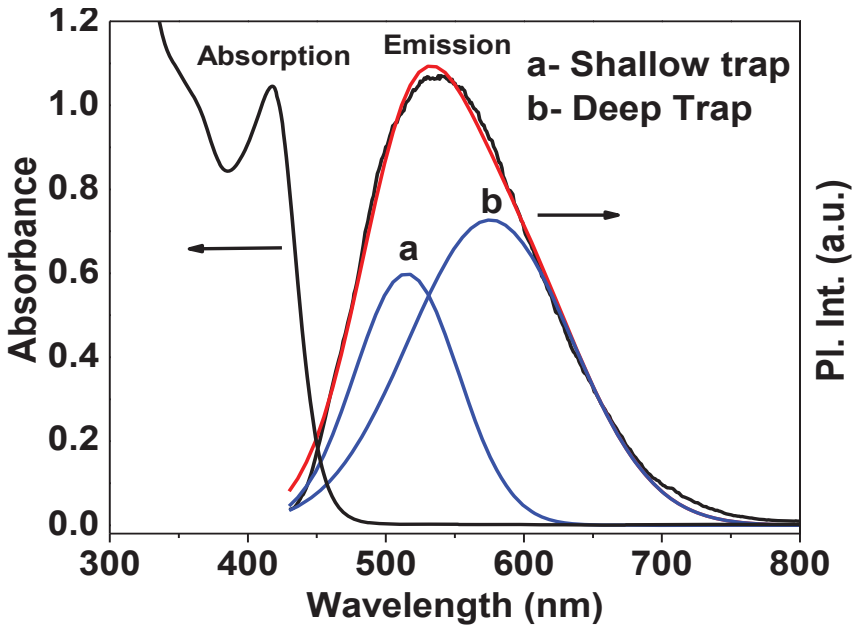

Figure 5.14 *Multiple curve fitting of Pl spectra along with absorption spectra of 0.5:0.5 mM Cd:Se quantum dots.*

Pl quantum yield for different stoichiometry of CdSe QDs were measured using Cumarin-153 (Cm-153) dye as a reference. The absorption and emission spectra of Cm-153 matches very well in the wavelength range of absorption and emission of the as synthesized CdSe QDs. The quantum yield was calculated by the following formula

$$\phi_s = \phi_r \frac{A_s}{A_r} \frac{OD_r}{OD_s} \left(\frac{\eta_s}{\eta_r} \right)^2 \qquad (5.3)$$

where, ϕ_r is the quantum yield of reference (Cm-153) which is 0.54 [197], A_s is the integrated Pl intensity of QDs, A_r is the integrated Pl intensity of reference (Cm-153), OD_r is the optical density of reference (Cm-153), OD_s is the optical density of QDs, η_s is the refractive index of the solvent of QDs (for aqueous $\eta_s = 1.33$) and η_r is the refractive index of solvent of Cm-153 (for acetone $\eta_r = 1.36$). The quantum yield was found maximum for 1.0:0.5 Cd:Se precursor ratio which was 1.91 % followed by 0.5:0.5 mM precursor ratio which was 1.86 % (see Table 5.1).

Table 5.1 Band gap values, particle sizes, quantum yield and zeta potentials of TG capped CdSe QDs synthesized with different stoichiometric compositions.

Cd:Se	Band Gap, Eg (eV)	Particle Size (nm)		% Quantum Yield	Zeta potential
		Peng Eq	Brus Eq		
0.5:0.5	2.75	1.76	1.91	1.86	35.3
0.5:1.0	2.72	1.76	1.92	1.22	21.5
1.0:0.5	2.81	1.71	1.86	1.91	15.4

As observed in the FTIR studies, a better surface passivation by the TG molecules in the case of QDs synthesized with the higher Cd:Se ratio leads to the higher Pl yield of these QDs. Further, such a higher Pl in the case of higher Cd:Se ratio could also be correlated to their anisotropic structure as observed from the SEM images. However, due to a relatively lower surface passivation by the TG molecules in the case of QDs synthesized from the lower (1:2) Cd:Se precursor ratio, there was a week Pl in this case, even though the morphology of the particles matches with that in the case of a higher Cd:Se ratio. The Pl lifetime measurements were carried out with these QDs at room temperature. It was observed that there was an increase in the lifetime with the increase in the Pl monitoring wavelength. The decay profiles were fitted with bi-exponential fit and the lifetime values along with the pre-exponential factors are listed in the Table 5.2. The Pl lifetime values were found to be in the order of 1:1 > 2:1 > 1:2 (one set of representative decay profiles are shown in the Fig 5.15 with the monitoring wavelength of 560 nm for all the three cases).

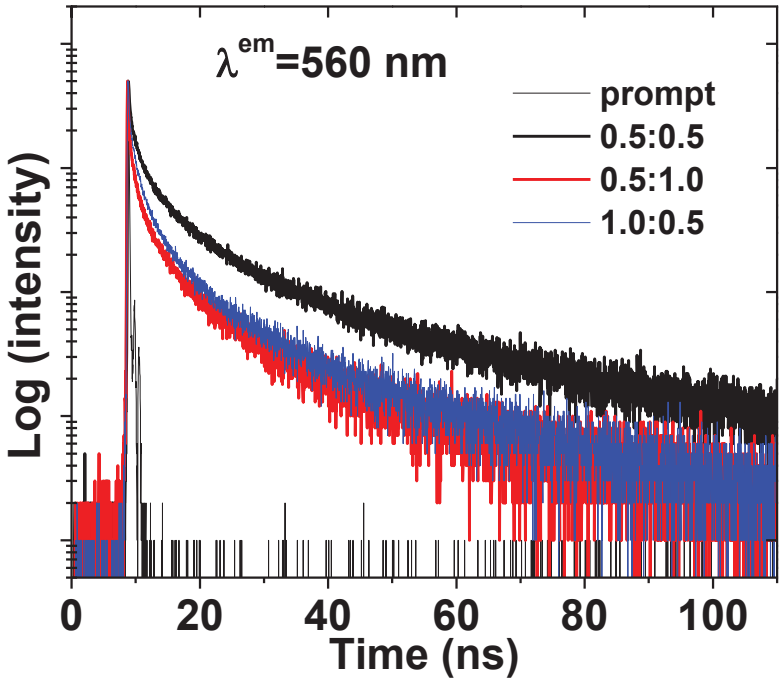

Figure 5.15 *Pl. lifetime decay profiles obtained for the quantum dots with different stoichiometric composition monitored at 560 nm. The excitation wavelength was 420 nm.*

Table 5.2 Pl lifetime values at different emission wavelength of TG capped CdSe QDs synthesized with different stoichiometric compositions.

Cd:Se	0.5:0.5			0.5:1.0			1.0:0.5		
	520 nm	560 nm	600 nm	520 nm	560 nm	600 nm	520 nm	560 nm	600 nm
τ_1	0.74	1.08	1.63	0.24	0.51	0.64	0.64	0.98	1.18
a_1	0.37	0.29	0.28	0.45	0.40	0.33	0.48	0.47	0.42
τ_2	8.37	11.38	14.97	4.17	8.11	8.82	6.06	9.87	11.47
a_2	0.63	0.71	0.72	0.55	0.60	0.67	0.52	0.53	0.58
$<\tau>$	5.55	8.39	11.23	2.40	5.07	6.12	3.46	5.70	7.15

5.2.3.3. Reduction potential studies

The formation of CdSe QDs in the presence of TG definitely confirms that these molecules are involved in the reaction processes. In the case of radiation induced synthesis of CdSe QDs in the aqueous solution containing very low concentrations (≤ 1mM) of $Cd(NH_3)_4SO_4$ and Na_2SeSO_3, the formation of CdSe takes place through the reaction of the precursor ions with a strongly reducing agent like hydrated electron, e_{aq}^- or secondary alcohol radicals [134]. Therefore, it is also expected here that the TG molecules might be doing a similar role as a strongly reducing agent. So in order to find out the reduction potential (E^1) of TG, we have carried out cyclic voltammetric as well as pulse radiolysis studies of these molecules under various experimental conditions. The pH of the reaction mixtures was around 10, so, the TG molecules are mostly be present in their deprotonated for, i.e. $HOCH_2CH(OH)CH_2S^-$ (pK_a ($HOCH_2CH(OH)CH_2SH$/ $HOCH_2CH(OH)CH_2S^-$) = 9.51) [198]. The reduction potential value of its structural analogue molecule, i.e. $OHCH_2CH_2SH$ is E^1 = +0.750 V ($OHCH_2CH_2S^{\bullet}/OHCH_2CH_2S^-$) vs NHE [136]. It is expected that the reduction potential value of this compound should also be close to the above value.

5.2.3.3.1. Pulse radiolysis studies

One-electron reduction potential value of a compound can be determined from the pulse radiolysis studies by taking suitable reference standard and by monitoring their growth/decay kinetics at different experimental conditions [199]. In order to find out the one-electron reduction potential value of the 1-thioglycerol ($OHCH_2CH(OH)CH_2SH$) *via* pulse radiolysis studies, sodium azide (NaN_3) was chosen as the suitable redox couple. The solutions containing 50 mM NaN_3 and 10 mM TG at pH around 6 was saturated with N_2O gas just before the experiment. The one-electron reduction potential value of the radical $N_3^{\bullet}$ is +1.33 V ($N_3^{\bullet}/N_3^-$) *vs* NHE [200]. It is expected that these radicals will oxidize TG. The transient absorption

spectra of the one-electron oxidized radicals of TG anions are shown in Fig. 5.16. The kinetic growth and decay profiles monitored at the absorption peak position 430 nm with different concentrations of TG are shown in the inset of Fig. 5.16.

The water radiolysis produces mainly three primary radicals, e_{aq}^-, $H^\bullet$ and $OH^\bullet$ radicals. The expected reactions taking place in this system are written below.

$$N_2O + e_{aq}^- \longrightarrow N_2 + OH^\bullet + OH^- \quad (5.4)$$

$$OH^\bullet + N_3^- \longrightarrow OH^- + N_3^\bullet \quad (5.5)$$

$$N_3^\bullet + TG \longrightarrow N_3^- + TG^{\bullet+} \quad (5.6)$$

Assuming the reaction to (5.6) be an equilibrium reaction, equilibrium constant, K can be found out as follows.

$$k_{observed} = k_1 [TG]_0 + k_2 [N_3^-]_0 \quad (5.7)$$

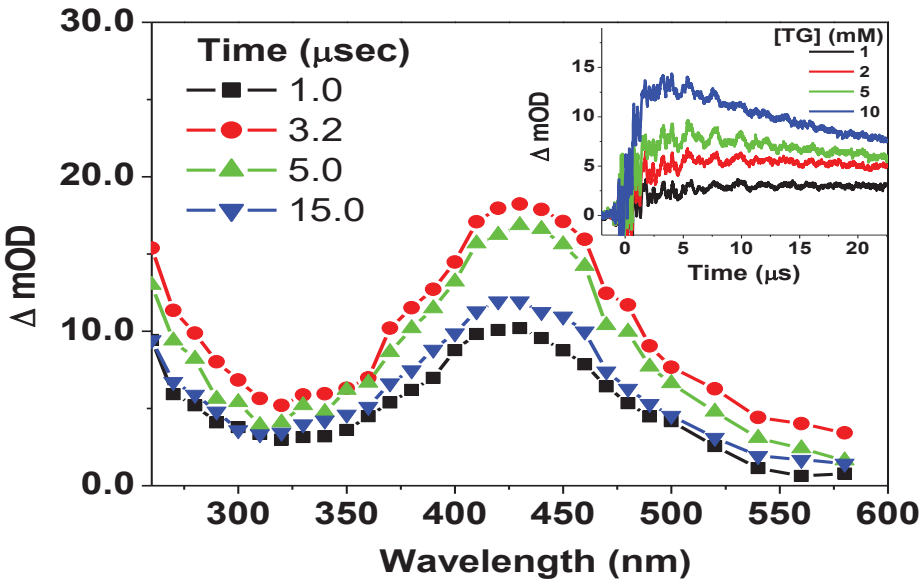

Figure 5.16 *Transient absorption spectra of thioglycerol cation radical obtained in the pulse radiolysis studies in the presence of azide ($N3^{\bullet-}$) radicals. Inset: Formation and decay profiles of thioglycerol cation radicals obtained in the pulse radiolysis studies in the presence of azide ($N_3^{\bullet-}$) radicals monitored at 430 nm at different TG concentrations.*

where, k_1 and k_2 are the rate constants for the forward and backward reactions of the equilibrium reaction (5.6) respectively. $[TG]_0$ and $[N_3^-]_0$ are the initial concentrations of 1-thioglycerol and sodium amide respectively. The rate constant, $k_{observed}$ is the measured value from the observed kinetic growth profile of the $TG^{\bullet+}$ radicals. From the plot of $k_{observed} / [N_3^-]_0$ *vs* $[TG]_0 / [N_3^-]_0$ we can get the values of k_1 and k_2 and hence the equilibrium constant K can be calculated as k_1/k_2. The one-electron reduction potential value of the $TG^{\bullet+}/TG$ couple can be found by the relation,

$$E^1 (TG^{\bullet+}/TG) = E^1 (N_3^{\bullet}/N_3^-) - 0.059 \log K \quad (5.8)$$

$E^1 (TG^{\bullet+}/TG)$ value found here +1.26 V *vs* NHE at room temperature and pH ~ 6. However, this value was normalized to pH 10 and found to be +1.0 V *vs* NHE. At this pH the oxidized form of TG^- would be $TG^{\bullet}$.

5.3.3.2. Cyclic voltammetric studies

Cyclic voltammetric (CV) measurement of 1-thioglycerol in neutral medium resulted in neither cathodic nor anodic peak. But in alkaline medium (pH 11.0), a broad anodic irreversible peak at +0.55 V *vs* SCE was observed (Fig. 5.17). The peak position remained the same with varying scan rate indicating a rapid kinetics, while the linear variation of the peak current with respect to the square root of scan rate indicates that the corresponding Faradic process is diffusion controlled. In alkaline pH, sodium selenosulphate alone has shown neither cathodic nor anodic peak in the potential window of -1.0 to +1.0 V *vs*. SCE, but a sharply rising anodic current was observed beyond +0.70 V *vs*. SCE. However, a mixture of sodium selenosulphate and 1-thioglycerol has shown two irreversible anodic peaks (Fig. 5.17). One peak was at around +0.07 V (peak 1) *vs* SCE while the other one was at around +0.54 V (peak 2) *vs* SCE (same position as in the case of TG alone). Both peak positions have shifted to positive potentials

with increasing scan rate indicating a sluggish kinetics. The variation of peak current with scan rate has shown a better linear fit as compared to that with the square root of scan rate for the first peak (i.e. +0.07 V *vs.* SCE) indicating that the corresponding Faradic process is surface controlled process. For the second peak, the variation of peak current has shown a better linear fit to the square root of the scan rate as compared to that with the scan rate itself. This indicates that the corresponding Faradic process is diffusion controlled.

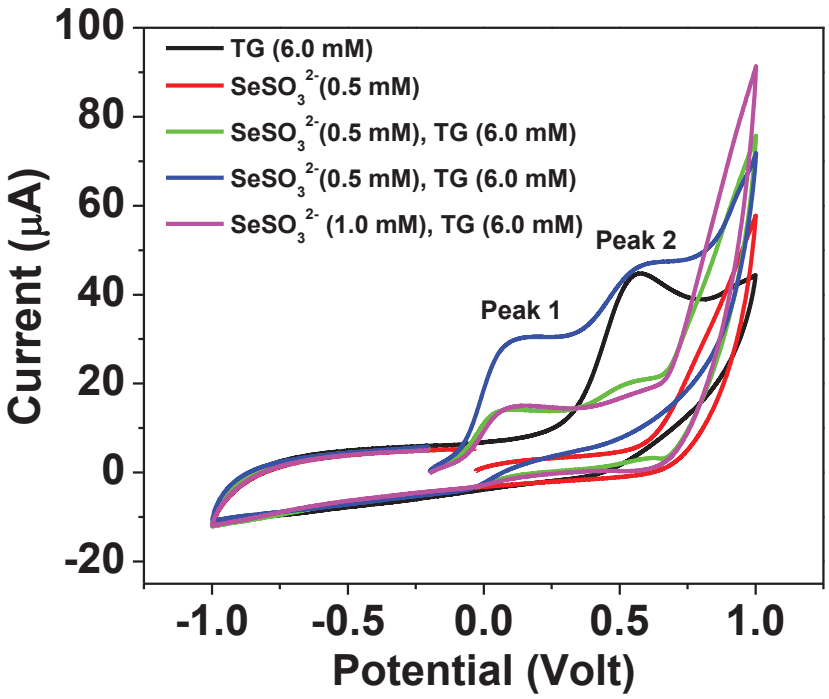

Figure 5.17 *Cyclic Voltammograms of 1-thioglycerol, sodium selenosulphate, sodium selenosulphate with thioglycerol, increased concentration of sodium selenosulphate with 1-thioglycerol and sodium selenosulphate with increased concentration of 1-thioglycerol (Scan Rate- 40 mV/s).*

The voltammograms were also obtained for mixtures with different concentrations of sodium selenosulphate and 1-thioglycerol. There is an increase in both the peaks with the increase in the concentration of 1-thioglycerol, but the peak current ratio (I_{a1}/I_{a2}) decreased for all scan rates by more than two times (table 5.3) on doubling the concentration of Se. The

appearance of the first anodic peak (a_1) for the mixture indicates that there is a formation of an adduct of selenosulphate and 1-thioglycerol. 1-thioglycerol seems to facilitate the oxidation of Se^{2-} to Se^{-} (Se^{2-} in $SeSO_3^{2-}$) in this adduct along with its self- oxidation, which is substantiated by the variation in the peak current upon changing the concentration of 1-thioglycerol as well as that of sodium selenosulphate (Fig. 5.17).

Table 5.3 Comparison of ratios of anodic peak currents for TG to that for Se oxidation for different concentrations of TG.

Scan rate (mV/sec)	Peak 2 (TG) / Peak 1 (Se) [TG] = 12. 0 mM (I_{a1})	Peak 2 (TG) / Peak 1 (Se) [TG] = 6.0 mM (I_{a2})	I_{a1}/I_{a2}
20	0.20	0.09	2.2
40	0.44	0.18	2.4
60	0.67	0.26	2.6
80	0.90	0.29	3.1
100	1.10	0.33	3.3

For the second anodic peak of the mixture, variation of peak current has shown better linear fitting to the square root of the scan rate. The second peak position is similar to that for 1-thioglycerol alone, but the peak current has significantly reduced as compared to that for 1-thioglycerol alone upon addition of $SeSO_3^{2-}$. This peak has almost disappeared upon doubling the concentration of sodium selenosulphate (Fig. 5.17), which indicates that the sodium selenosulphate strongly interferes with the redox behaviour of 1-thioglycerol in the adduct. It may be noted that the concentration of 1- thioglycerol is still six times higher than that of selenosulphate, but the second anodic peak has still disappeared.

Hence, the cyclic voltammetric studies have established that 1-thioglycerol has an important role in electrochemical activation of sodium selenosulphate. The role of sulphur from 1-thioglycerol for this electrochemical activation was investigated by repeating these studies with glycerol instead of 1-thioglycerol. However, with glycerol, no changes in the voltammograms of sodium selenosulphate were observed (Fig. 5.18). This indicates that sulphur of 1-thioglycerol plays an important role in the electrochemical activation of sodium selenosulphate.

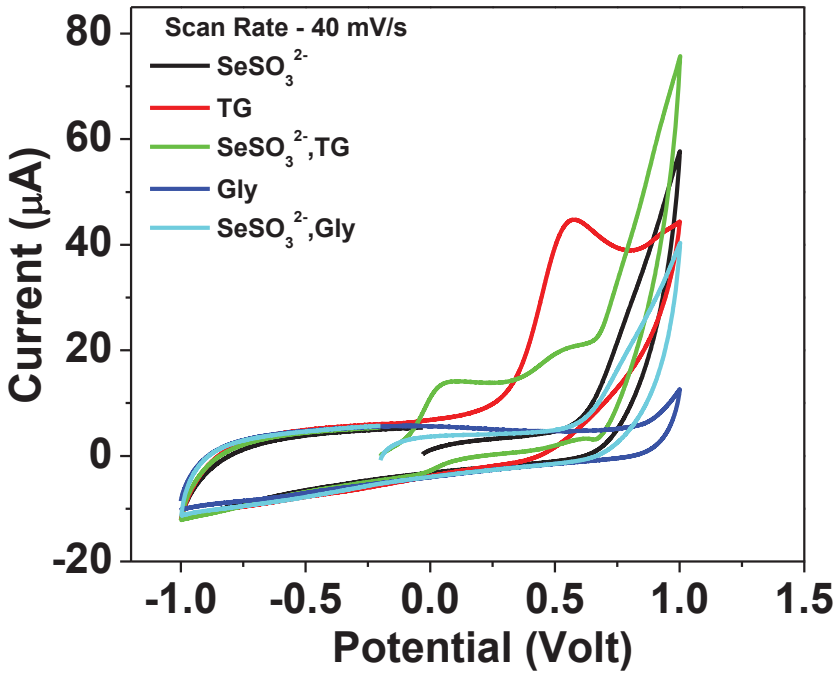

Figure 5.18 *Cyclic voltammograms of sodium selenosulphate, 1-thioglycerol, sodium selenosulphate in the presence of 1-thioglycerol, glycerol and sodium selenosulphate in the presence of glycerol (at pH 11.0).*

The cyclic voltammogram of ammoniated $CdSO_4$ is shown in Fig. 5.19. There is a sharp cathodic peak at around -0.95 V *vs* SCE, which corresponds to the two-electron reduction of Cd^{2+} in alkaline medium. The corresponding anodic peak has been obtained at -0.77 V. On anodic side, there are two peaks, one is at around +0.55 V *vs* SCE (same position as in the case of TG alone) and the other is at around +0.72 V *vs* SCE. This new anodic peak at around +0.72

V *vs* SCE could arise due to the one-electron oxidation of TG in the presence of Cd^{2+} ions. This sharp cathodic peak indicates that there are two successive one-electron transfer processes. In the presence of 1-thioglycerol, the voltammogram of ammoniated cadmium sulphate has shown similar behaviour to that of the later alone. However, the peaks have shifted towards more negative side, which indicates a complexation of cadmium ion with 1-thioglycerol. The peak current has shown a discrete variation with scan rate and it decreases at higher scan rate. The cathodic peak shape changes from a sharp one to a blunt one with increasing scan rate and the peak has finally vanished at the scan rate of 100 mV/s. This indicates that the competing process of hydrogen evolution has a better kinetics.

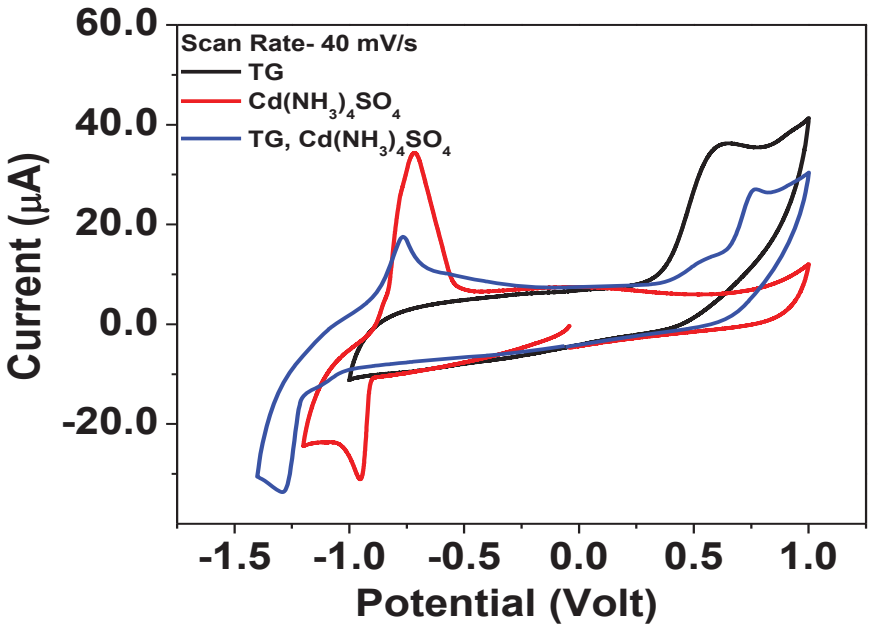

Figure 5.19: *Cyclic Voltammograms of thioglycerol, cadmium sulphate, and cadmium sulphate along with thioglycerol (Scan Rate- 40 mV/sec).*

The feasibility of hydrogen evolution at such low concentrations of Cd^{2+} ion has been reported earlier [201]. The narrow width of cathodic peak indicates that it is a two-electron transfer process. The peak position remained same with scan rate, which indicates the rapid kinetics. In the presence of ammoniated cadmium sulphate, 1-thioglycerol and sodium

selenosulphate, the peak corresponding to cadmium ion reduction and selenium ion oxidation have disappeared while a hump is seen at the position of 1-thioglycerol oxidation. This indicates that the CdSe QDs are electrochemically inert on the glassy carbon electrode. In the presence of ammoniated cadmium sulphate, 1-thioglycerol and sodium selenosulphate, the peaks corresponding to cadmium ion reduction, selenium ion oxidation and 1-thioglycerol oxidation vanishes. It confirms the formation of CdSe QDs (Fig. 5.20).

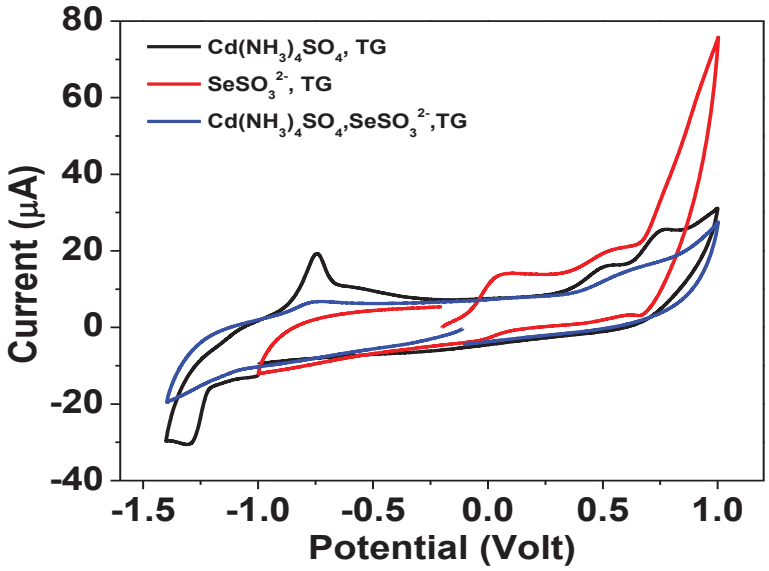

Figure 5.20 *Cyclic Voltammograms of cadmium sulphate with thioglycerol, sodium selenosulphate with thioglycerol and cadmium sulphate and sodium selenosulphate along with thioglycerol (Scan Rate- 40 mV/s).*

5.2.3.4. Reaction mechanism

Therefore, based on the above observations, it can be concluded that 1-thioglycerolate anion can reduce the $Cd(NH_3)_4^{2+}$ to Cd^+ ion ($E^1(Cd^{2+}/Cd^+)$ = +1.1 V vs NHE) [202]. It is reported in the literature that the hydrated electrons e_{aq}^- on water radiolysis, react with $S_2O_3^{2-}$ ions releasing $S^{\bullet-}$ and SO_3^{2-} with a rate constant k = 1.5 x 10^8 M^{-1} s^{-1} [80]. Similarly, we have also reported that hydrated electrons react with $SeSO_3^{2-}$ releasing $Se^{\bullet-}$ and SO_3^{2-} with a rate constant k = 2.27 x 10^9 M^{-1} s^{-1} [133]. Therefore, it is too expected that the TG molecules

(reducing agent like hydrated electrons) could react with $SeSO_3^{2-}$ to release $Se^{\bullet-}$, which is supported from the above cyclic voltammetric studies. Further, in alkaline medium it is reported that $SeSO_3^{2-}$ gives HSe^- [203]. Then HSe^- ions get converted to Se^{2-} by the OH^- ions. Finally, Cd^+ ions could react with $Se^{\bullet-}$ or HSe^-, or Se^{2-}; and Cd^{2+} ions also could react with Se^{2-} ions to form CdSe QDs. The bond between $OHCH_2CH(OH)CH_2S^-$ and Cd on the surface of CdSe inhibits the growth and hence we get CdSe QDs of very small size. The overall reactions those are possible to finally lead to the formation of CdSe QDs are written below:

$$OHCH_2CH(OH)CH_2S^- + [Cd(NH_3)_4]^{2+} \longrightarrow Cd^+ + OHCH_2CH(OH)CH_2S^{\bullet} \quad (5.9)$$

$$SeSO_3^{2-} + OH^- \longrightarrow HSe^- + SO_4^{2-} \quad (5.10)$$

$$HSe^- + OH^- \longrightarrow Se^{2-} + H_2O \quad (5.11)$$

$$Se^{2-} + Cd^+ + OHCH_2CH(OH)CH_2S^{\bullet} \longrightarrow CdSe + OHCH_2CH(OH)CH_2S^- \quad (5.12)$$

$$Cd^+ + HSe^- \longrightarrow CdSe + H^{\bullet} \quad (5.13)$$

$$SeSO_3^{2-} + OHCH_2CH(OH)CH_2S^- \longrightarrow Se^{\bullet-} + SO_3^{2-} + OHCH_2CH(OH)CH_2S^{\bullet} \quad (5.14)$$

$$Cd^{\bullet+} + Se^{\bullet-} \longrightarrow CdSe \quad (5.15)$$

$$OHCH_2CH(OH)CH_2S^{\bullet} + H^{\bullet} \xrightarrow{OH^-} OHCH_2CH(OH)CH_2S^- + H_2O \quad (5.16)$$

$$CdSe + nCdSe \longrightarrow CdSe\ QDs \quad (5.17)$$

These reactions finally lead to the formation of CdSe QDs stabilized by 1-thioglycerol where the later one acts as catalyst cum stabilizer.

5.3. An insight into the optical properties of CdSe QDs during their growth in bovine serum albumin solution

5.3.1. Experimental details

5.3.1.1. Materials

High purity chemicals, cadmium sulfate ($CdSO_4$), sodium sulfite (Na_2SO_3), selenium powder (Se) and bovine serum albumin (BSA) were obtained from Sigma-Aldrich and used without further purification. Aqueous solutions were prepared by using nanopure water (resistivity > 18 megaohm cm) obtained from the Millipore water purifying system (Barnsted System, USA). $CdSO_4$ was used as the cadmium precursor and sodium selenosulfate (Na_2SeSO_3) was used as the selenium precursor for the synthesis of CdSe nanoparticles. Na_2SeSO_3 was prepared by refluxing the reaction mixture containing 10 g Na_2SO_3, 1 g Se powder and 50 ml water at 70^0C for 7hrs [133].

5.3.1.2. Synthesis of CdSe nanoparticles

The synthesis of CdSe nanoparticles was carried out as follows. First, 2 ml solution of 10 mM $CdSO_4$ was added to 4 ml aqueous solution containing 1 mg/ml BSA and the solution was equilibrated for about 1 hr. Then, 2 ml solution of 10 mM Na_2SeSO_3 was added to this BSA-$CdSO_4$ solution. This solution was named as 10:10 reaction mixture, where the exact concentrations of BSA, Cd^{2+} and $SeSO_3^{2-}$ were 0.5 mg/ml, 2.5 and 2.5 mM, respectively. Similarly, two other reaction mixtures were prepared, where in one case, 5 mM Na_2SeSO_3 and

in another case 20 mM Na_2SeSO_3 were used, keeping the initial concentrations of $CdSO_4$ and BSA the same as in the case of 10:10 reaction mixture. These two solutions have been named as 10:5 and 10:20 reaction mixtures, respectively. The exact concentrations of Cd^{2+} and $SeSO_3^{2-}$ were 2.5 and 1.25 mM in the case of 10:5 reaction mixture; 2.5 and 5.0 mM in the case of 10:20 reaction mixture. The mixing of two aforesaid solutions was followed by stirring, which resulted in the evolution of colour depending on the molar ratios of the Cd and the Se precursors. This emergence of colour can be regarded as the primary signature for the formation of CdSe QDs. The as prepared colloidal sols were used to record the changes in the absorption spectra, and both steady-state and time-resolved room temperature Pl spectra at different time intervals after the mixing of the precursors. It is to be mentioned here that the concentration of the precursor solutions kept in such a way that no chemical reaction would occur leading to the formation of CdSe QDs in the absence of BSA.

5.3.1.3. Characterization

Optical absorption measurements were carried out by using a JASCO V-650 absorption spectrophotometer. Steady-state Pl measurements were carried out at room temperature by using a Hitachi F-4500 spectrofluorometer. Time-resolved Pl measurements were carried out by using a time correlated single photon counting (TCSPC) instrument (model: IBH, UK) to determine the Pl lifetimes. The instrument response function (IRF) of the setup was measured by collecting the scattered light from a TiO_2 suspension in water. In all these measurements, the reaction mixture was taken in 10 mm x 10 mm x 60 mm (length x breadth x height) quartz cell with completely filled and tightened with a stopper. The solution was not disturbed during the optical measurements. The samples were excited by a diode laser of output wavelength, 290 nm with an IRF of less than 100 ps and the Pl was monitored at 350 nm.

5.3.1.4. Stopped-flow measurements

The initial time dependent Pl from the reaction mixture containing BSA-Cd^{2+} and $SeSO_3^{2-}$ (i.e. from the time when Na_2SeSO_3 solution is added to the solution containing BSA and $CdSO_4$) was studied by employing a Biologic SFM-300 stopped flow spectrometer (from Biologic Scientific Instruments, France) equipped with a xenon lamp as a light source in the single mixing mode. The flow cell has a path length of 1.5 mm. The sample was excited at 290 nm and the total Pl was collected above 320 nm at right angle geometry after the mixing of the two reactants and was monitored as a function of time.

5.3.2. Results and Discussion

Aqueous solutions containing BSA, Cd^{2+} and $SeSO_3^{2-}$ ions were found to exhibit a change in colour from transparent colourless to dark orange red with time. This orange red coloured solution was also transparent. Neither had it settled down even after several months, nor the intensity of the colour decreased. These nanoparticles have already been characterized by XRD, SEM and TEM measurements in our previous study [204]. Nonetheless, one representative TEM image recorded for the CdSe QDs obtained from the reaction mixture 10:10 is shown in Fig. 5.21. Apart from these, it was also observed that the optical properties i.e. the absorption and photoluminescence behaviors of the grown nanoparticles have strong correlation with the proportions of precursor concentrations used in the synthesis. However, the optical properties investigated in the previous study [204] were limited to completion of initial growth of the CdSe nanoparticles. In this work, we have performed a systematic in-depth study on the growth of the CdSe QDs by monitoring the time dependent absorption and fluorescence properties.

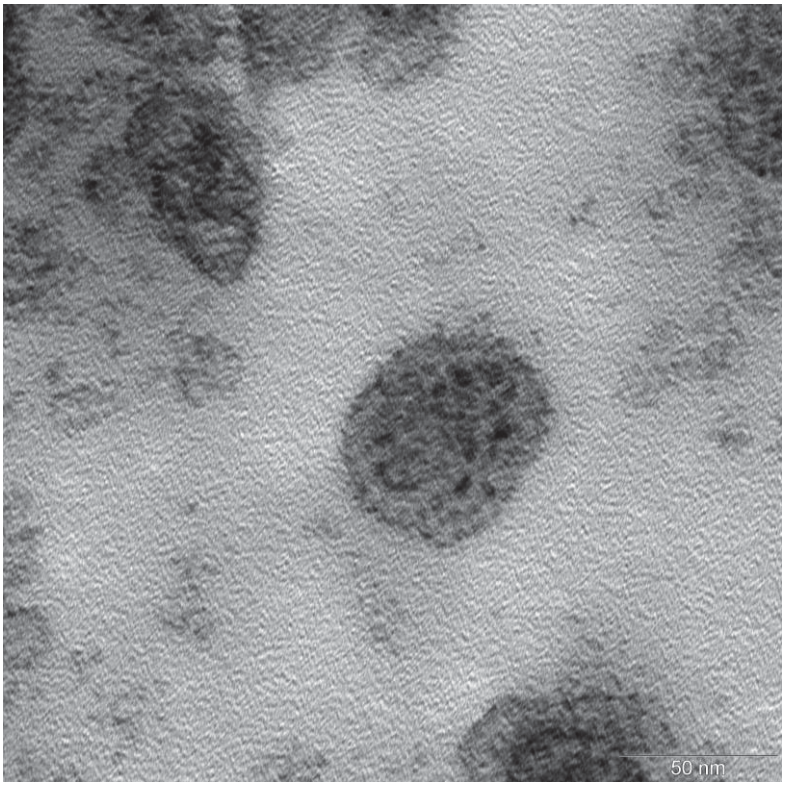

Figure 5.21 *TEM image of CdSe QDs synthesized from the reaction mixture 10:10.*

It is to be noted here that no chemical reaction (neither UV-Vis absorption nor colour appearance signaling the formation of CdSe QDs) was observed in the absence of BSA, even after 4 hrs [204] of mixing. Taking this into account, it can be said that BSA, apart from capping the nanoparticles, might be playing a role of reducing agent as well as a catalyst. This has been explained as follows. It is a well-known fact that proteins/enzymes/peptides possess micro cavities, which catalyze the synthesis of materials [205]. Furthermore, the pH of the reaction mixture was slightly alkaline (7.0–8.0), which facilitates the release of Se^{2-} ions from the Se precursor (Na_2SeSO_3) in such conditions [203]. At the same time, it may be possible that the amino acid residues of BSA might be reducing Na_2SeSO_3, leading to the release of Se^{2-} ions. Essentially, some of these amino acids bearing hydroxyl groups can serve as a mild reducing agent [206]. Considering these arguments, it is inferred that BSA plays a vital role in controlling the formation and stabilization of CdSe QDs. The possible mechanism of the

formation of CdSe nanoparticles in this situation is supposed to take place *via* these reactions as mentioned below [204].

$$Na_2SO_3 + Se \longrightarrow Na_2SeSO_3 \quad (5.18)$$

$$BSA + Cd^{2+} \longrightarrow BSA\text{-}Cd^{2+} \quad (5.19)$$

$$SeSO_3^{2-} + BSA\ (amino\ acids) / OH^- (alkaline) \longrightarrow Se^{2-} \quad (5.20)$$

$$BSA\text{-}Cd^{2+} + Se^{2-} \longrightarrow BSA\text{-}CdSe \quad (5.21)$$

$$BSA{:}CdSe + nCdSe \longrightarrow BSA{:}(CdSe)_{nanoparticle} \quad (5.22)$$

5.3.2.1. UV-visible absorption studies

UV-visible absorption spectra of the three reaction mixtures, 10:5, 10:10 and 10:20 have been recorded at different time intervals after the mixing of the precursor solutions inside a quartz cell, which was sealed with a cap and the cell was completely filled. The quartz cell was not disturbed during the recording of the spectra. Absorption spectra of these three reaction mixtures, 10:5, 10:10 and 10:20, recorded at several different time intervals have been shown in Figs. 5.22a, b and c, respectively. It is clear from these three figures that (i) there is a growth of CdSe nanoparticles with time, (ii) the finally grown CdSe nanoparticles has a noticeable excitonic absorption peak, and (iii) there is an increase in the absorbance value in the order, 10:5 < 10:10 < 10:20.

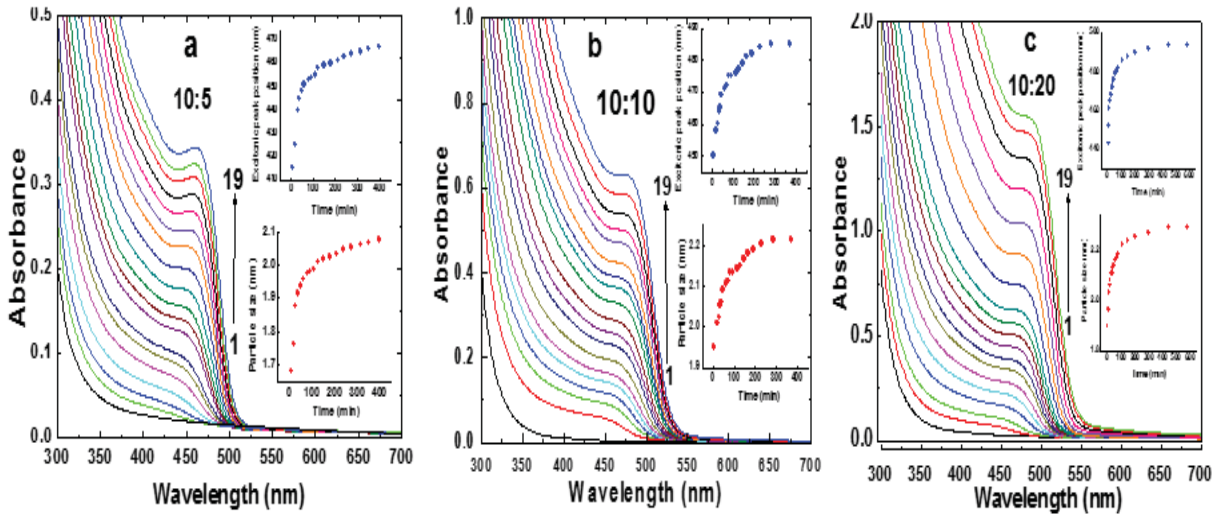

Figure 5.22 *Absorption spectra recorded at different time intervals for (a) 10:5, (b) 10:10 and (c) 10:20 reaction mixtures.*

The excitonic peak positions have been plotted against time and are shown in the insets of each of these Figs. 5.22a, 5.22b and 5.22c for the corresponding reaction mixtures. The particle sizes of the nanoparticles have been calculated from the exciton peak positions using the empirical formula given by Yu *et al*. [145]. The estimated values of the particle sizes were found to be within 1.5 to 3 nm, which are less than the exciton Bohr radius of CdSe (which is 5.6 nm) and therefore confirmed these nanoparticles as the quantum dots (QDs). The sizes of these QDs have been plotted against time and are shown in the insets of Figs. 5.22a, 5.22b and 5.22c for the corresponding reaction mixtures. It is observed that there is an increase in the particle size with time and after about 2 hrs from the time of mixing of the two precursor solutions, the sizes of the CdSe QDs do not increase further and become constant at about 2.1, 2.2 and 2.3 nm, respectively for the case of 10:5, 10:10 and 10:20 reaction mixtures. The growth rate constants (k_{g1}) for the QDs have been determined by applying a first-order growth kinetic equation on the plots of particle sizes vs time and are shown in Table 5.4.

Table 5.4 Kinetic parameters determined from the excitonic absorption peak positions vs time, which was obtained from time dependent absorption spectra at different time intervals after mixing of the two precursor solutions, by fitting with first order equation, $y = y_0 + ae^{-kt}$.

Cd:Se	k_{g1} (s^{-1})
10:5	1.9×10^{-4}
10:10	2.4×10^{-4}
10:20	4.1×10^{-4}

However, in all these three situations, three main observations were drawn from the plots of particle size *vs* time: (i) the sizes of the particles at the initial time are more than 1.5 nm, (ii) there is only a marginal increase in the particle size of about 0.4 nm from the time of mixing of the precursor solutions up to about 5 hrs and (iii) k_{g1} of the particles are in the order 10:5 < 10:10 < 10:20. From these observations, it is clear that the sizes of the CdSe QDs at the initial stage i.e. within a few minutes of mixing of the precursor solutions, are being overestimated from the absorption spectra. This could be due to an error in finding out the exact exciton peak positions in the initial times. However, in all the cases the exciton peak positions were obtained from the intersection of two tangents drawn near the exciton peak. Nevertheless, the fully grown CdSe QDs exhibit sharp excitonic absorption peaks in the range 450 to 550 nm, with a red shift in the order 10:5 < 10:10 < 10:20.

5.3.2.2. Room temperature fluorescence studies

5.3.2.2.1. Steady-state fluorescence

Room temperature fluorescence of BSA was found to be marginally affected upon the addition of Cd^{2+} after the equilibration for about 1 hr [204]. The fluorescence intensities as well

as the lifetime values were reduced very little in the case of the equilibrated solution containing BSA and Cd^{2+}. However, it was observed that the fluorescence from BSA was immediately quenched upon addition of $SeSO_3^{2-}$ to the BSA solution without any shift in the peak position. There was no further quenching with time (Fig. 5.23 for solution containing 0.5 mg/ml BSA and 2.5 mM $SeSO_3^{2-}$).

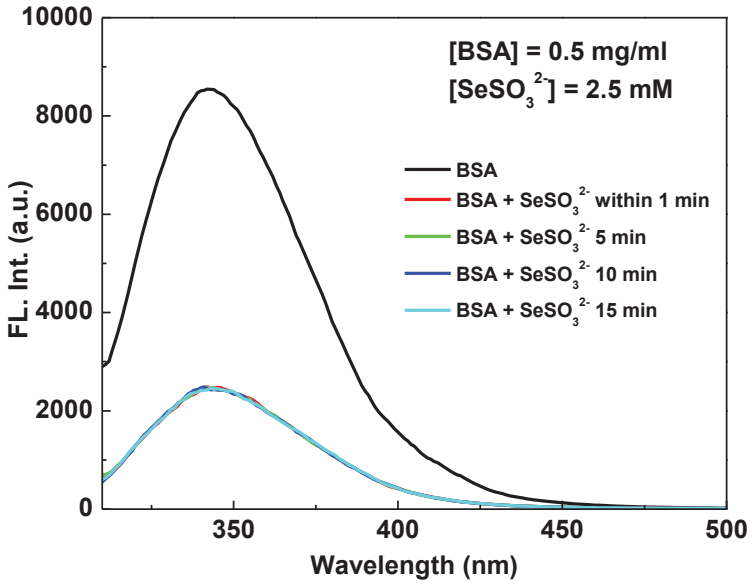

Figure 5.23 *Room temperature steady-state fluorescence spectra recorded with the solution containing 0.5 mg/ml BSA only and 0.5 mg/ml BSA along with 2.5 mM $SeSO_3^{2-}$ at different time intervals: within 1 min, 5 min, 10 min and 20 min. Excitation wavelength was fixed at 290 nm.*

From the fluorescence quenching studies, using Stern-Volmer plot, the fluorescence quenching rate constant, k_q (BSA-$SeSO_3^{2-}$) has been determined to be 2.9 x 10^{11} M^{-1} s^{-1}. However, while $SeSO_3^{2-}$ was added to the equilibrated solution of BSA and Cd^{2+}, there was a time-dependent quenching of BSA fluorescence without any change in its peak position, which was not the case in absence of Cd^{2+} in the solution (Fig. 5.24 for 10:10 reaction mixture containing 0.5 mg/ml BSA, 2.5 mM Cd^{2+} and 2.5 mM $SeSO_3^{2-}$).

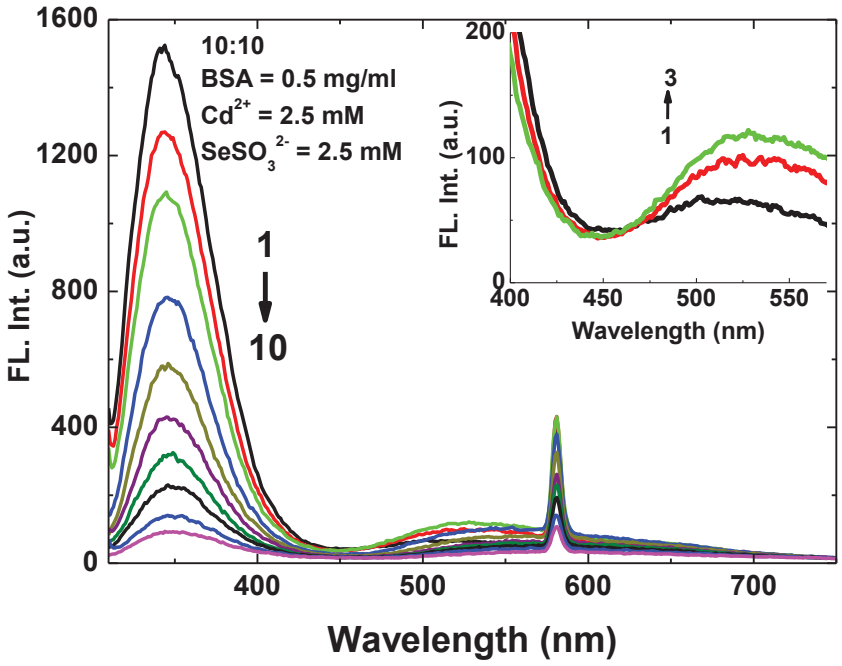

Figure 5.24 *Room temperature steady-state fluorescence spectra recorded at different time intervals for 10:10 reaction mixture. Excitation wavelength-290 nm. Inset: Fluorescence spectra shown in expanded scale for three different time intervals.*

This was associated with a new fluorescence peak at around 540 – 560 nm, intensity of which increases with time. However, at later stage the intensity decreases with time (Fig. 5.24 for the 10:10 reaction mixture). The decrease in BSA fluorescence with peak at 345 nm and the simultaneous increase in the new fluorescence with peak at around 540 – 560 nm were associated with an isoemissive point at 470 nm during the early time within 6 minutes from the time of mixing of two precursors (inset of Fig. 5.24). Similar observations were found for other two reaction mixtures, 10:5 and 10:20. From the plot of BSA fluorescence intensity at 345 nm *vs* time (Fig. 5.25) for both the cases, it is confirmed that $SeSO_3^{2-}$ strongly quenches the BSA fluorescence; however, in the presence of Cd^{2+} the quenching efficiency is decreased. This is because of the interaction of $SeSO_3^{2-}$ with Cd^{2+}, which leads to the formation of CdSe QDs in the presence of BSA.

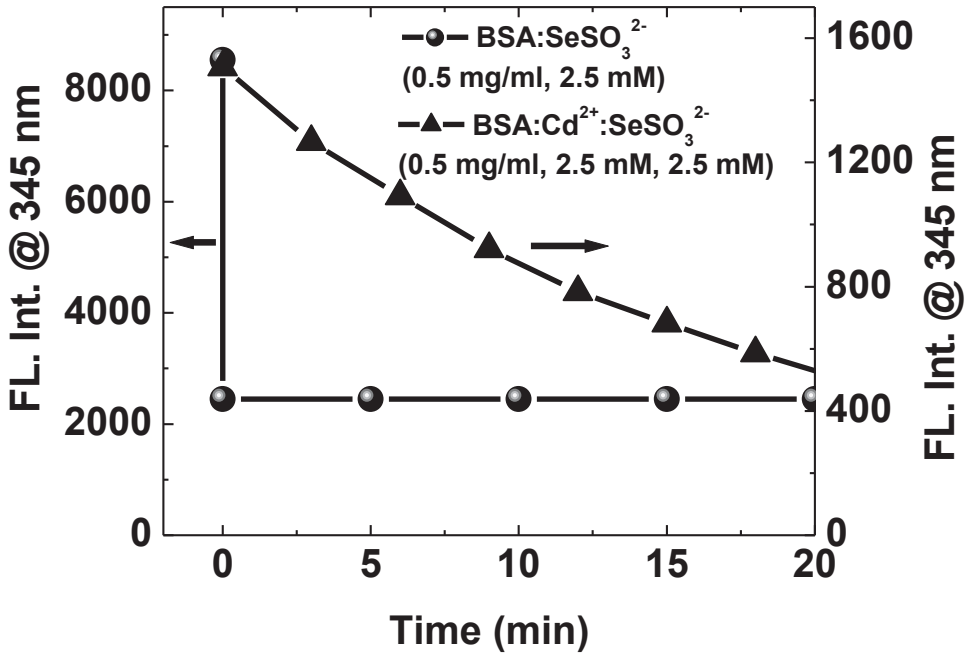

Figure 5.25 *Plot of BSA fluorescence intensity at 345 nm vs time for the solution containing 0.5 mg/ml BSA and 2.5 mM $SeSO_3^{2-}$; 0.5 mg/ml BSA, 2.5 mM Cd^{2+} and 2.5 mM $SeSO_3^{2-}$.*

The long wavelength fluorescence with the peak at around 540 – 560 nm could be assigned due to originating from these newly formed CdSe QDs. It is to be noted here that the excitation wavelength used for getting the fluorescence from BSA is 290 nm. In this situation, the quenching of BSA fluorescence at 345 nm and the simultaneous appearance as well as increase in the Pl from CdSe QDs at the initial time period, associated with an isoemissive point clearly indicates that there is an energy transfer from excited state of BSA to the newly formed CdSe QDs. This part will be discussed in details separately in a different section. It is seen from the Fig. 5.24 that along with the fluorescence from BSA and CdSe QDs the second order diffraction peaks of (i) the excitation wavelength (i.e. 290 nm) as well as the (ii) BSA fluorescence, appears at 580 and 645 nm, respectively. This is mainly originated from the fluorescence spectrometer instrument. As the fluorescence spectra were recorded from 310 to 750 nm, there was no scope for getting rid of those two second order diffraction peaks. Therefore, in order to

have a detailed investigation on the insight into the interaction between BSA and CdSe QDs as well as the growth of these QDs based on their fluorescence properties, the Pl from the CdSe QDs was monitored by exciting the solutions with 420 nm. Pl spectra recorded at longer wavelength region from 450 to 750 nm at several different time intervals up to about 3 hrs from the time of mixing of the two precursor solutions are shown in Fig. 5.26 for the 10:10 reaction mixture with an excitation wavelength 420 nm. The Pl spectra recorded for the other two reaction mixtures, 10:5 and 10:20 also exhibit similar behaviour. It is to be noted here that there was no difference in the Pl spectra recorded in the longer wavelength region with the excitation wavelengths 290 and 420 nm, except for the appearance of the second order diffraction peaks of 290 nm and BSA fluorescence.

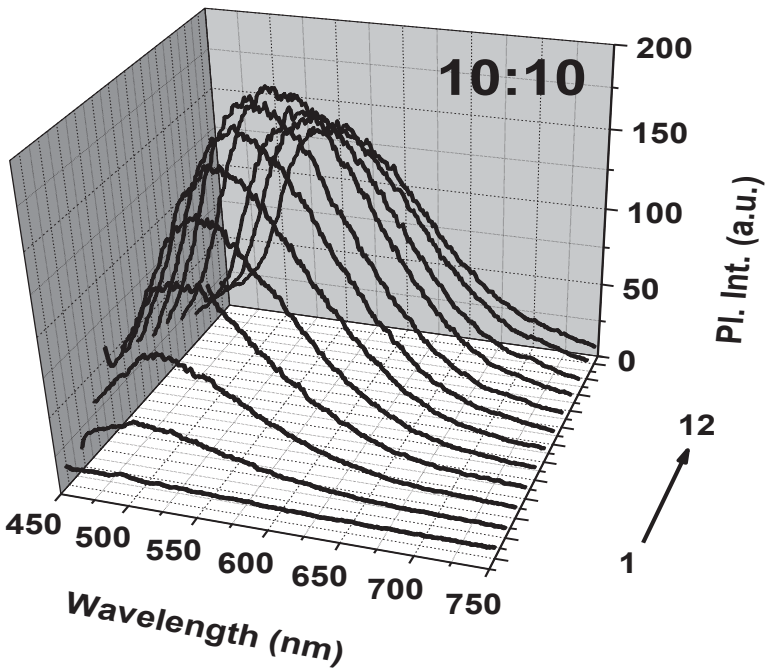

Figure 5.26 *Room temperature steady-state CdSe Pl spectra recorded at different time intervals for the 10:10 reaction mixture 1) 0, 2) 3, 3) 6, 4) 9, 5) 12, 6) 15, 7) 18, 8) 24, 9) 30, 10) 36, 11) 45, 12) 75 min. Excitation wavelength was fixed at 420 nm.*

However, we have also recorded the wavelength dependent emission as well as excitation spectra which corroborate the above observation. No peak shift was observed in these spectra indicating uniformity in the material. From the Figs. 5.24 and 5.26, it is observed that (i) there is an increase in the Pl intensities of CdSe QDs associated with a red shift in the spectral peak position during initial time period of about a few minutes, (ii) afterwards it decreases along with a further red shift in the spectral peak position and (iii) finally after long time of about 3 hours there is no change in Pl intensities as well as shift in the spectral peak position. This suggests that there is a growth of the CdSe QDs as well as an increase in its concentration which gives rise to the red shift in the fluorescence spectral peak positions as well as an increase in the intensities. However, after certain stage further growth of these QDs leads to the formation of trap states, which actually capture the photo excited carriers (mainly electrons) leading to the reduction in the Pl intensity.

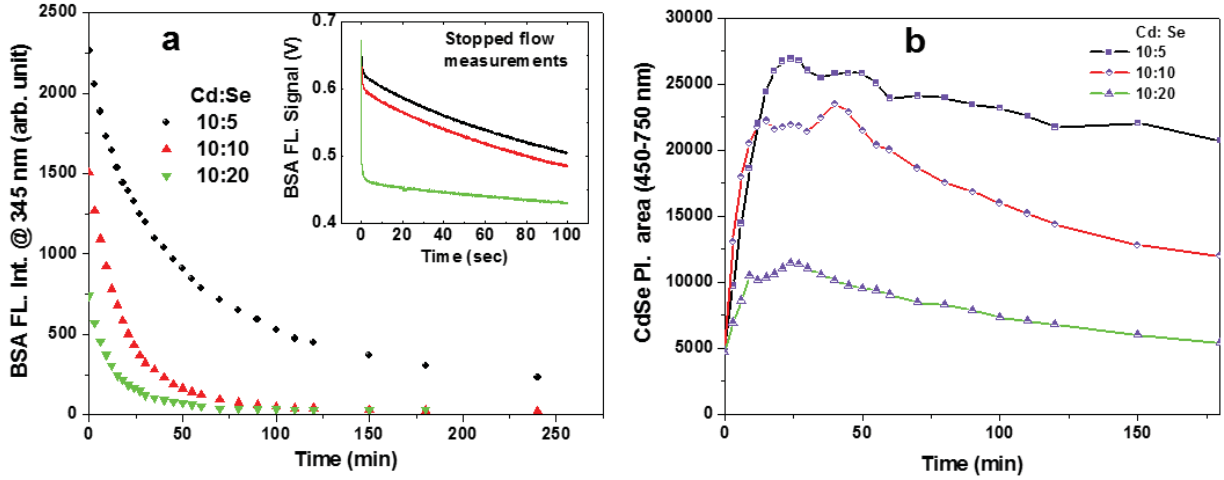

Figure 5.27 *(a) Plot of room temperature BSA fluorescence intensities recorded at 345 nm vs time for the three reaction mixtures, 10:5, 10:10 and 10:20. Inset: Plot of BSA fluorescence signal vs time obtained from the stopped flow measurements for the three reaction mixtures, 10:5, 10:10 and 10:20. (b) Plot of area under the CdSe Pl spectra in the range from 450 to 750 nm vs time for the three reaction mixtures, 10:5, 10:10 and 10:20.*

The BSA fluorescence intensities at 345 nm were plotted against time (Fig. 5.27a) for all the three cases and the rate of decay of the fluorescence was determined from the first order curve fit (see Table 5.5).

Table 5.5 Kinetic parameters obtained from the fluorescence intensity of BSA at 345 nm vs time and the Pl (total area under the curve) of CdSe QDs vs time, which were obtained from the steady-state fluorescence measurements at different time intervals after mixing of the two precursor solutions, by fitting with first order equation, $y = y_0 + ae^{-kt}$; as well as from the stopped flow measurements in the fluorescence mode (that is mainly BSA fluorescence) by fitting with second order equation, $y = y_0 + a_1e^{-k(1)t} + a_2e^{-k(2)t}$.

Cd:Se	k_{d1}(BSA-Pl) (s^{-1})		k_{d2}(BSA-Pl)	k_{g2}(CdSe-Pl)	k_{d3}(CdSe-Pl)
	$k_{d1\text{-}1}$	$k_{d1\text{-}2}$	(s^{-1})	(s^{-1})	(s^{-1})
10:5	1.637	9.64×10^{-3}	0.39×10^{-3}	1.52×10^{-3}	1.11×10^{-4}
10:10	1.557	9.29×10^{-3}	0.91×10^{-3}	3.98×10^{-3}	1.87×10^{-4}
10:20	0.677	7.33×10^{-3}	1.25×10^{-3}	2.59×10^{-3}	1.62×10^{-4}

It was observed that the rate of decay (k_{d2}) was increased in the order, 10:5 < 10:10 < 10:20. It is expected that the fluorescence intensities of BSA at the time of mixing of the two precursors remain same for all the three reaction mixtures. However, as seen from Fig. 5.27a, the initial fluorescence intensities are not the same. This is believed to be due to real time lapse between mixing of precursors and measurement, which is unavoidable as the fluorescence spectra were recorded in a normal steady-state spectrofluorometer. Therefore, in order to investigate the change in the BSA fluorescence intensities at the early time (up to about 2 minutes), the stopped flow experiments were carried out in the fluorescence mode. In this experiment, the signals were collected in the right-angle geometry for all the three reaction mixtures and are shown in the inset of Fig. 5.27a. It is now clearly seen that the initial fluorescence intensities were almost

same in all the three cases but, decayed differentially depending on the composition of the reaction mixtures. These decay curves were fitted with second order kinetics and the results are shown in Table 5.5. Among the two decay rate constants, one (k_{d1-1}) was very high as compared to the other (k_{d1-2}) in all the three cases and both of these were found to be in the order, 10:5 > 10:10 > 10:20. The first decay rate constant, k_{d1-1} could be assigned due to the initial dynamic quenching of the BSA by the $SeSO_3^{2-}$ ions within a few seconds only. The second decay rate constant, k_{d1-2} could be assigned due to both dynamic quenching as well as the excited state energy transfer from BSA to CdSe QDs, as the formation of these QDs takes place after a few seconds. The quenching here is assigned as the dynamic and not static because there is no ground state interaction between BSA and $SeSO_3^{2-}$ as seen from the UV visible absorption spectra rather there is the formation of CdSe QDs. Similarly, the Pl spectra originated from CdSe QDs were analyzed considering the total areas under the curve (Fig. 5.27b) because the Pl spectra were associated with a peak shift. Up to a few minutes an increase in the Pl area is observed, thereafter it decreases and finally remains almost unchanged at a lower value. The first part of the growth was fitted with first order growth kinetics and the second part was fitted with first order decay kinetics. The rate constant for the increase in the CdSe Pl (k_{g2}) during the initial time period up to about 60 minutes and rate constant for the decrease in this Pl (k_{d3}) during subsequent time period are listed in the Table 5.5. It is observed that the yield of the CdSe Pl (area under the curve) decreases in the reaction mixtures in the order of, 10:5 > 10:10 > 10:20. This indicates that the presence of higher $SeSO_3^{2-}$ contents in the solution increases the density of trap states, which reduce the overall Pl from the CdSe QDs. However, the rate constants for the increase and decrease in the Pl intensities with time does not follow any order as indicated above.

From the broad nature of the Pl spectra of the CdSe QDs, it is expected that there could be the existence of both band gap Pl (BG-Pl) and trap state Pl (TS-Pl). Therefore, in order to

separate these two Pl peaks, multiple curve fitting was performed in all the Pl spectra (one set of representative spectra are shown in Fig. 5.28). The extracted Pl peaks i.e. $\lambda_{1\text{-fit}}^{max}$ and $\lambda_{2\text{-fit}}^{max}$ after double curve fitting along with the observed Pl peak i.e. λ_{obsd}^{max} values are plotted against time as shown in Fig. 5.22a, b and c for the three reaction mixtures 10:5, 10:10 and 10:20, respectively. It is observed from these figures that the λ_{obsd}^{max} values increases with time and finally saturates at a certain value for all the three cases. Similar observations were also found for the $\lambda_{1\text{-fit}}^{max}$ and $\lambda_{2\text{-fit}}^{max}$ values for all the three cases.

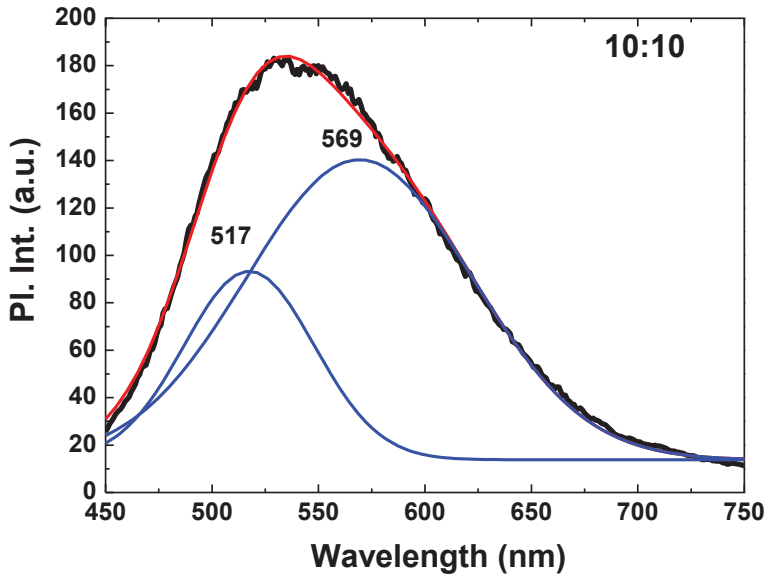

Figure 5.28 *Room temperature steady-state CdSe Pl spectrum (black) recorded for the 10:10 reaction mixture at 30 minute. Excitation wavelength was fixed at 420 nm. Red line shows the multiple curve-fitting spectrum matching with the observed spectrum (black) and blue lines show the two fitted spectra shown with their peak positions.*

There is a remarkable difference in the initial (i.e. from the first Pl spectrum recorded at 0 minute) and final (i.e. from the last Pl spectrum recorded after 3 hrs) values of λ_{obsd}^{max}, $\lambda_{1\text{-fit}}^{max}$ and $\lambda_{2\text{-fit}}^{max}$ whereas, much change in their FWHM values (shown in the table 5.6) were not observed.

It is clear from these observations that there is an increase in the observed as well as the extracted Pl peak positions in the order, 10:5 < 10:10 < 10:20. This observation is consistent with our earlier findings and suggests a red shift in the Pl peak position with increase in the ratio, Se:Cd whereas a blue shift occurs with an increase in the ratio, Cd:Se [204]. The extracted Pl peaks, $\lambda_{1\text{-fit}}^{max}$ and $\lambda_{2\text{-fit}}^{max}$ are assigned to the BG-Pl and TS-Pl peak positions, respectively. It is seen that the $\lambda_{1\text{-fit}}^{max}$ value at longer time matches well with the $\lambda_{2\text{-fit}}^{max}$ value at initial time.

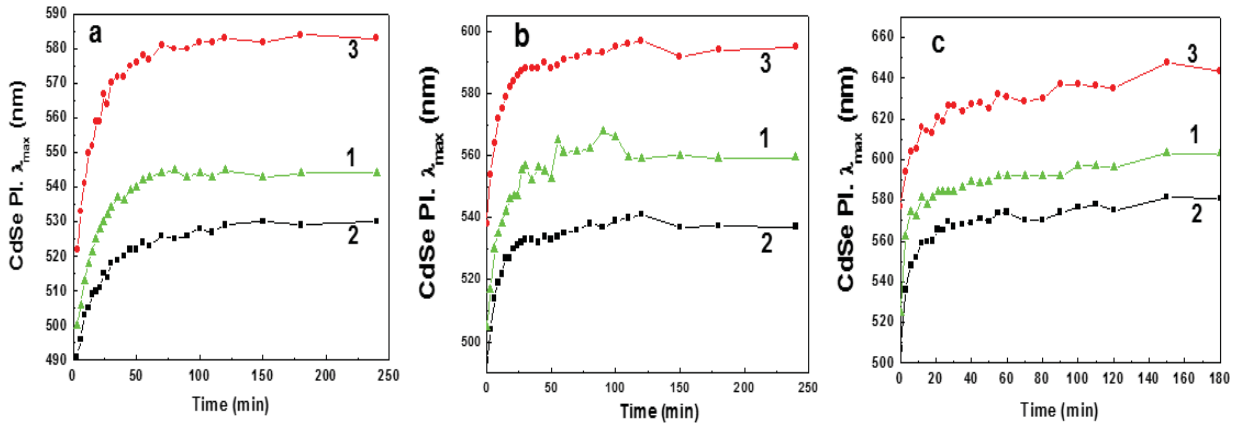

Figure 5.29 *Plot of CdSe Pl peak positions for as observed (λ_{obsd}^{max}, 1) and the fitted ones ($\lambda_{1\text{-}fit}^{max}$, 2 and $\lambda_{2\text{-}fit}^{max}$, 3 for the short and long wavelength peak positions respectively) vs. time for the three reaction mixtures: (a) 10:5, (b) 10:10, (c) 10:20.*

This indicates that the Pl observed from the CdSe QDs at about 3 hrs (corresponding to final values) could arise from (i) only trap states, where $\lambda_{1\text{-fit}}^{max}$ is from shallow traps and $\lambda_{2\text{-fit}}^{max}$ from deep traps, (ii) relatively larger size QDs where the band gap is comparable to the trap state of the initially formed QDs, so therefore $\lambda_{1\text{-fit}}^{max}$ is from band gap and $\lambda_{2\text{-fit}}^{max}$ from overall trap states. On the contrary, the Pl observed from the CdSe QDs within a few minutes, is from band gap as well as trap states, because the Pl spectra are very broad even during this initial time period.

Table 5.6 Pl peak positions (observed as well as fitted values) of CdSe QDs at initial time (about 0 to 5 min) and after long time duration (about 2 hrs) from the time of mixing of the two precursor solutions, in different precursor ratio conditions.

Reaction mixture	λ_{obsd}^{max} (nm)		$\lambda_{1\text{-}fit}^{max}$ (nm) (FWHM)		$\lambda_{2\text{-}fit}^{max}$ (nm) (FWHM)	
	initial	final	initial	final	initial	final
10:5	500	544	491 (57)	529 (51)	522 (122)	583 (100)
10:10	505	555	494 (68)	538 (58)	538 (128)	594 (100)
10:20	525	598	507 (65)	581 (93)	577 (118)	658 (119)

FWHM values are shown in parentheses.

The presence of trap states in these QDs might be intrinsic in nature and are being unintentionally incorporated during their nucleation and growth process in the present cases.

The rate constants for the growth processes were also estimated from the plots of emission peak positions vs time (table 5.7). From these growth rate constants, k_{g1} (estimated from the time dependent UV-visible absorption measurements), k_{g2} (estimated from the time dependent CdSe Pl area measurements) and k_{g3} (estimated from the time dependent CdSe Pl peak position measurements), it is clear that the growth rate constants estimated from the Pl measurements are about one order higher than those estimated from the absorption measurements.

5.3.2.2.2. Time-resolved fluorescence

Fluorescence lifetime measurements were also carried out by monitoring the time-resolved Pl decay at room temperature at different time intervals from the time of mixing of the precursor solutions. The samples were photo excited with 290 nm light from a light emitting diode (LED) with an instrument response time of about 1 ns. The emission signal was collected at 345 nm

corresponding to the BSA fluorescence. The fluorescence decay profiles obtained at different time intervals for all the three reaction mixtures, 10:5, 10:10 and 10:20 are shown in Figs. 5.30a, b and c respectively.

Table 5.7 First-order growth rate constants k_{g3} determined by the fitting the plots of observed and fitted values of Pl peak positions of CdSe QDs against time with first order equation, $y = y_0 + ae^{-kt}$.

Cd:Se	k_{g3} @ λ_{obsd} (s^{-1})	k_{g3} @ $\lambda_{1\text{-fit}}$ (s^{-1})	k_{g3} @ $\lambda_{2\text{-fit}}$ (s^{-1})
10:5	0.91×10^{-3}	0.69×10^{-3}	0.94×10^{-3}
10:10	1.16×10^{-3}	1.44×10^{-3}	1.50×10^{-3}
10:20	2.12×10^{-3}	1.85×10^{-3}	0.85×10^{-3}

The fluorescence decay profiles were fitted with bi-exponential decay curve fit and the results are listed in Table 5.7. It is observed from this table that the BSA fluorescence has two lifetimes, a relatively short lifetime (τ_1) less than 1.5 ns with a lower percentage and a relatively long lifetime (τ_2) 4.7 – 6.0 ns with a higher percentage. The weighted average lifetime $<\tau>$ values are plotted against time for all the three reaction mixtures as shown in Fig. 5.30.

It is seen from these results that the weighted average lifetime values in the case of all the three reaction mixtures decrease linearly from 5.0 - 5.3 ns to 3.3 - 3.7 ns. The shorter lifetime (τ_1) and longer lifetime (τ_2) values are separately plotted against time as shown in the insets of Fig. 5.31 as a and b, respectively. It is seen from these figures that the shorter lifetime (τ_1) component decreases very fast up to about 90 minutes from the time of mixing of the two precursor solutions and after this time its decrease is very slow.

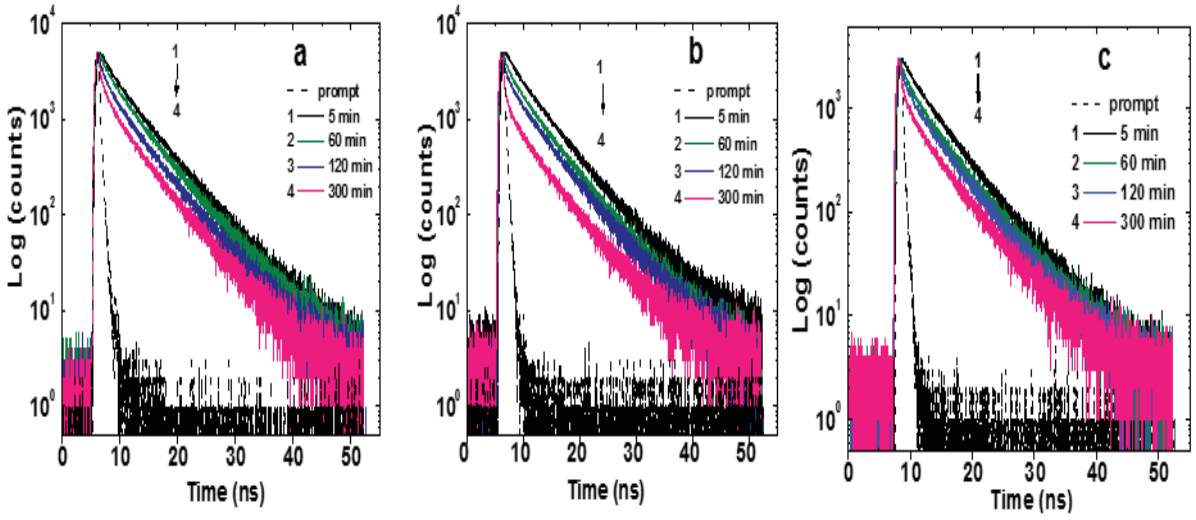

Figure 5.30 *Room temperature BSA fluorescence decay profiles monitored at 345 nm at different time intervals, 5, 60, 120, 300 min along with the prompt profile for the three reaction mixtures, (a) 10:5, (b) 10:10, (c) 10:20.*

Table 5.8 Fluorescence lifetime values (ns) of BSA obtained at different time intervals (min) after mixing of the precursors in the case of three different precursor concentrations.

Rea Mix.	10:5				10:10				10:20			
Time(min)	5	60	120	300	5	60	120	300	5	60	120	300
τ_1	1.46	0.85	0.30	0.14	1.39	0.38	0.21	0.08	1.35	0.81	0.26	0.15
a_1	0.14	0.13	0.17	0.25	0.11	0.13	0.17	0.34	0.12	0.11	0.16	0.25
τ_2	5.93	5.48	5.10	4.75	5.85	5.39	5.28	4.8	5.53	5.45	5.14	4.96
a_2	0.86	0.87	0.83	0.75	0.89	0.87	0.83	0.66	0.88	0.89	0.84	0.75
$<\tau>$	5.33	4.86	4.27	3.59	5.34	4.73	4.41	3.3	5.00	4.94	4.36	3.75

Similar observations are also found in the case of longer lifetime (τ_2) component. The shorter lifetime (τ_1) component is assigned to the quenching of the BSA fluorescence by the $SeSO_3^{2-}$

ions as well as short range energy transfer from excited state BSA to CdSe QDs whereas the longer lifetime (τ_2) component is assigned mainly due to the energy transfer from excited state BSA to CdSe QDs. In this context, it may be noted here that BSA has two tryptophan units (Trp-134 and Trp-213) which contribute to its overall fluorescence [118]. Therefore, from these results it could be relevant that the sharp decrease in the short lifetime (τ_1) could arise due to the close proximity of one of the fluorophores (Trp-134) to $SeSO_3^{2-}$ or CdSe and the slow decrease in the long lifetime (τ_2) could arise due to the location of the other fluorophore (Trp-213) away from $SeSO_3^{2-}$ or CdSe [207-209].

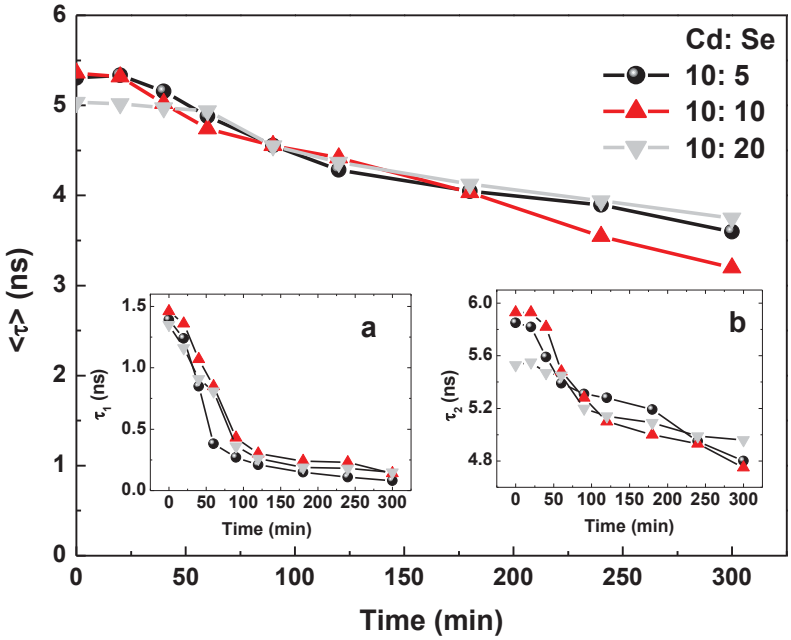

Figure 5.31 *Plot of average Pl lifetime (<τ>) vs time for the three reaction mixtures, 10:5, 10:10 and 10:20. Inset: (a) Plot of short lifetime, τ_1 vs time and (b) Plot of long lifetime, τ_2 vs time for these above three reaction mixtures.*

Based on these observations, the overall processes occurring in the reaction mixtures from the time of mixing of the two precursor solutions till the complete formation of CdSe QDs, which include (i) photoexcitation of BSA by 290 nm, (ii) fluorescence from BSA with peak at

345 nm, (iii) Pl from CdSe QDs at the initial time and (iv) both band gap as well as trap state Pl from the CdSe QDs at longer time associated with their growth. All these processes are shown in the Scheme 5.2.

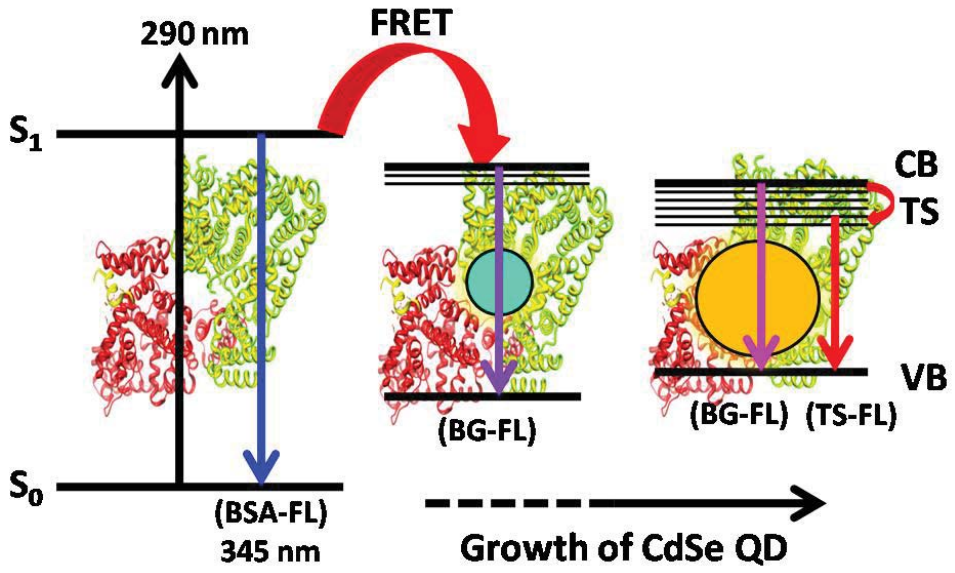

Scheme 5.2*: Schematic representations showing the photo-excitation of BSA followed by (i) emission from BSA excited states, (ii) FRET from excited state BSA to the conduction band of CdSe QDs at the initial time, (iii) emissions from the CdSe QDs and (iv) growth of these QDs.*

5.3.2.3. FRET analysis and growth of CdSe QDs

It is now clearly understood that the initial appearance and growth in the fluorescence from the CdSe QDs mainly arise due to the energy transfer from excited state BSA to the CdSe QDs along with its growth. However, the extent of energy transfer is higher as compared to the growth, as in the initial time period of about a few minutes from the time of mixing of the two precursor solutions, the growth of the CdSe QDs might not have occurred sufficiently enough to contribute towards its Pl. However, after some time delay, the QDs could have grown sufficient enough to have their own Pl properties in addition to the energy transfer from excited

state BSA to these QDs. Essentially, BSA has an absorption band at this wavelength, while in the case of CdSe QDs this wavelength corresponds to a very high excitation level close to the continuum. Therefore, it is expected that BSA will be easily photo excited to its first excitation level, whereas even though the excited states get populated in the case of CdSe QDs, there are several relaxation pathways exist from such higher excited levels, of which the radiative channels could be very low. Nevertheless, as already mentioned earlier, there exists an isoemissive point in the fluorescence spectra of BSA-CdSe solution at the initial time scale (inset of Fig. 5.31, 5.32). This certainly suggests that the BSA emission is getting converted to the emission from CdSe QDs at the initial time, which confirms the possibility of an energy transfer between BSA and CdSe QDs. In the present situation, BSA acts as a stabilizing agent for the synthesis of CdSe QDs. Therefore, it is expected that fluorophore of BSA and CdSe QDs might be in close proximity to each other. Hence, the quenching of BSA fluorescence and the simultaneous growth of the CdSe Pl during the initial time could be explained by the Forster's non-radiative energy transfer theory (also known as Forster's resonance energy transfer, FRET).

The main criteria for this to occur are (i) the overlap between the donor emission spectrum and accepter absorption spectrum and (ii) the distance between the donor and accepter should be less than 10 nm [210-212]. Both the criteria are satisfied in the present cases and hence FRET analysis can be safely applied to investigate the Pl behaviours. The absorption spectra of the reaction mixtures 10:5, 10:10 and 10:20 showing the absorption characteristics of CdSe QDs during the initial time period up to a few minutes along with the BSA fluorescence spectra are shown in Figs 5.32a, b and c respectively.

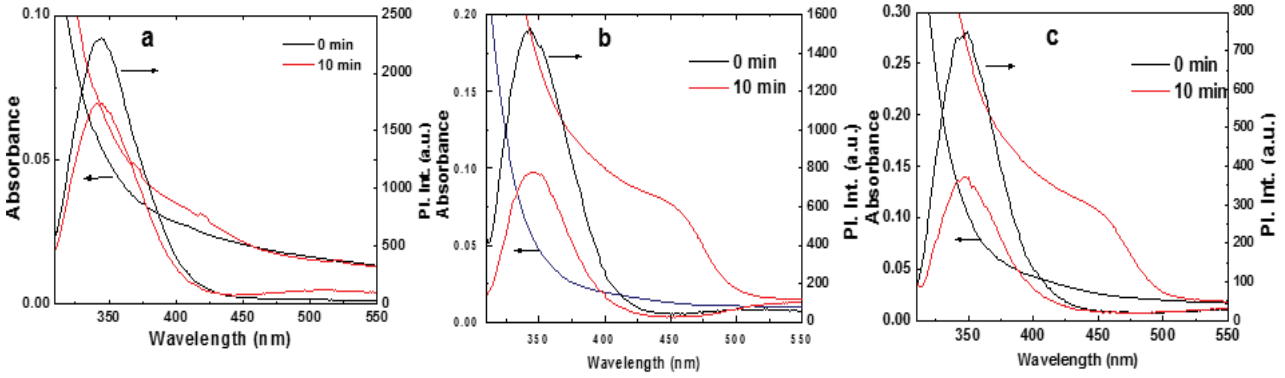

Figure 5.32 *Absorption spectra (of CdSe QDs) and room temperature fluorescence spectra (of BSA) at initial time intervals plotted in the same wavelength scale in order to show the overlap between them for the three reaction mixtures: (a) 10:5, (b) 10:10 and (c) 10:20.*

In this mechanism, the energy is transferred from excited state BSA to CdSe QDs via non-radiative pathway and dependent on the spectral overlap between the absorption spectra of CdSe QDs and the fluorescence spectra of BSA as well as the distance between these two species. In the present situation, BSA acts as a donor and the CdSe QDs acts as receptors. The rate of energy transfer, k_{FRET} is given by the equation

$$k_{FRET} = \frac{1}{\tau_D}\left(\frac{R_0}{r}\right)^6 \qquad (5.23)$$

where, τ_D is the lifetime of the donor, BSA (5.56 ns) in the absence of acceptor, i.e. CdSe QD, r is the distance between donor and acceptor, R_0 is the critical transfer distance. The value of the critical energy transfer distance, R_0 (in angstrom) is the distance between donor and acceptor, when the energy transfer efficiency is 50 % and given by the equation

$$R_0 = 0.211\left(\frac{k^2 \varphi_D J}{n^4}\right)^{1/6} \qquad (5.24)$$

where, k^2 is the orientation factor relating to the geometry of donor and acceptor dipoles, which is equal to 2/3 for the isotropic donor and acceptor, n is the refractive index of the solvent (in the present case it is water and n = 1.333), ϕ_D is the fluorescence quantum yield of donor (in

the present case it is BSA and $\phi_D = 0.101$) in the absence of acceptor (in the present case it is CdSe QD) and J is the overlap integral between the donor fluorescence spectra and the acceptor absorption spectra. The spectral overlap integral (J) was determined by the equation

$$J = \int_0^\infty F_D(\lambda)\varepsilon_A(\lambda)\lambda^4 d\lambda / \int_0^\infty F_D(\lambda)d\lambda \qquad (5.25)$$

where, $F_D(\lambda)$ and $\varepsilon_A(\lambda)$ are the fluorescence intensity of donor, BSA and the molar extinction coefficient of the acceptor CdSe QDs, respectively, at the wavelength, λ. The concentrations of the accepter, i.e. CdSe QDs have been estimated from the empirical formula given by Yu *et al.* [56]. The molar extinction coefficients of the accepters, ε_A, have been calculated from the absorbance values and the concentration of the QDs, for the estimation of spectral overlap integral J. The efficiency of FRET (E_{FRET}) is related to the distance (r) between donor and acceptor by the equation,

$$E_{FRET} = \frac{R_0^6}{R_0^6 + r^6} = 1 - \frac{\tau}{\tau_D} \qquad (5.26)$$

where, τ and τ_D are the fluorescence lifetimes of the donor (BSA) in the presence and absence of the acceptors (CdSe QDs), respectively. In the present situation, τ_D is the fluorescence lifetime of BSA (5.56 ns) before addition of $SeSO_3^{2-}$ ions and τ is the fluorescence lifetime of BSA after mixing of the two precursors (see Table 5.8). For the calculation of E_{FRET} the weighted average lifetime values were taken. All the parameters calculated by using the above equations (5.24-5.27), are listed the Table 5.7 for all the three reaction mixtures at different time intervals.

Table 5.9 FRET parameters determined for all the three reaction mixtures at different time intervals (initial period within 10 minutes, later period at about 60 minutes) from the time of mixing of the two precursor solutions.

Rean Mix.	Time period	J (M^{-1} cm^{-1} nm^4)	R_0 (Å)	E_{FRET}	r (Å)	k_{FRET} (s^{-1})
10:5	10 min	7.20×10^{14}	33.3	0.041	56.3	7.68×10^6
	60 min	9.45×10^{14}	34.8	0.126	48.1	2.59×10^7
10:10	10 min	1.86×10^{15}	39.0	0.039	66.5	7.29×10^6
	60 min	1.55×10^{15}	37.8	0.149	50.5	3.15×10^7
10:20	10 min	1.32×10^{15}	36.8	0.101	53.0	2.02×10^7
	60 min	1.52×10^{15}	37.7	0.111	53.3	2.24×10^7

The efficiency of energy transfer, E_{FRET} and the rate of energy transfer, k_{FRET} were found to increase with time for all the three reaction mixtures. However, the overall Pl from the CdSe QDs was decreased at a later time. This could be due to the quenching of fluorescence by the trap states and defects in the QDs. The distance between the donor BSA and the accepter CdSe QDs was found to be within 7 nm throughout the growth period. This suggests that the CdSe QDs are always in the close vicinity of the tryptophans in BSA tertiary structure. It is now clearly understood from these results that because the FRET is associated with the growth of the CdSe QDs, the growth rate constants for CdSe QDs estimated from the Pl studies are always higher than those estimated from the absorption studies.

5.4. Conclusion

In summary, we have synthesized CdSe QDs using molecules like- 1-Thioglycerol and BSA in aqueous solution at ambient conditions without using any other reducing agents through highly facile and green route. Here, both the molecules i.e. 1-thioglycerol and BSA act as a capping as well as a catalyzing agent.

We have investigated the optical properties of the CdSe QDs synthesized in the presence of 1-thioglycerol in aqueous solution. The as grown QDs were found exhibit sharp excitonic absorption peaks at around 420 nm, which is very unusual in the case of the CdSe QDs synthesized at room temperature and ambient conditions. The excitonic absorption peak position could be nicely tuned by varying the stoichiometric compositions of the precursors, i.e. ammoniated cadmium sulphate and sodium selenosulphate. However, these QDs exhibit a very broad Pl with a large stokes shift at room temperature, which is rather contrast to those are synthesized at high temperature using TOPO and TOP with a sharp excitonic absorption as well as sharp band gap emission with very less stokes shift. The fluorescence lifetime values were found to increase with the increase in the emission wavelength indicating a longer lifetime for the deep trap states as compared to the shallow trap states. The lifetime values were higher in the case of Cd:Se ratio as 0.5:0.5 and these values decrease with a variation in this stoichiometry. This indicates an increased contribution of the non-radiative deactivation of the photo excited carriers upon deviation in the perfect stoichiometric composition in the CdSe QDs synthesized in the presence of 1-thioglycerol in aqueous solution. The mechanism of synthesis was investigated using the Cyclic Voltammetry and it was found that the S atom of 1-thioglyceol had an important role.

We have also synthesized the CdSe QDs in BSA protein matrix in aqueous solution and we have investigated the optical properties of *in situ* growth of CdSe QDs in detail. The growth of these QDs was found to follow a first order kinetics. The room temperature steady-state

fluorescence of BSA was found to be quenched by $SeSO_3^{2-}$, however, in the presence of Cd^{2+}, the quenching was found to be decreased along with the formation of CdSe QDs without any change in its peak position. This was associated with an appearance as well as a subsequent increase in the Pl from the CdSe QDs. However, the Pl from CdSe QDs was found to be associated with several features: (1) red-shift in its peak position, (2) increase in intensity with an isoemissive point at the initial time period up to about 10 minutes from the time of mixing of the two precursors and (3) subsequent decrease in intensity reaching a minimum value, which remains almost unchanged with time. The growth rate constant obtained from the absorption measurements was found to be one order lower as compared to that obtained from the steady-state fluorescence measurements. The decrease and increase in the fluorescence from BSA and CdSe QDs, respectively have been explained on the basis of FRET as well as the simultaneous growth of these QDs. In the present situation, BSA acts as a donor and CdSe QD acts as an acceptor. From these studies, it is clear that the CdSe QDs are formed in the close proximity to the BSA molecules so that FRET could occur and the tertiary structure of BSA provides a suitable environment so that these QDs do not undergo any substantial agglomeration leading to their precipitation.

CHAPTER 6
SUMMARY AND OUTLOOK

6.1. Summary

The present thesis is an endeavor to explore the nanoparticles synthesis in aqueous solution at ambient conditions without using high temperature, high pressure and specific laboratory requirements. Along with the materials and capping molecules, the methods of synthesis also influence the properties of the nanoparticles. Synthesizing good quality nanomaterials in aqueous solution at ambient conditions is very challenging exercise for researchers and scientists. In this direction, we have explored the synthesis of CdSe nanoparticles using radiation and photochemical methods along with normal chemical methods. The methods which are used here for synthesis are rapid, one-pot and facile. It is fundamental principle that capping the nanoparticles with biocompatible molecules, especially with biomolecules reduce the cytotoxic effect of the nanoparticles. Furthermore, the nanoparticles capped/passivated with biomolecules are used in various biological applications. So capping of nanoparticles with biocompatible molecules is very important synthesis strategy. In this thesis, biomolecules like- L-cysteine, BSA, various saccharides like- glucose, fructose, sucrose and starch and 1-thioglycerol have been used as capping agents. Tuning the optical properties of nanoparticles were explored and the fundamental processes involved were attempted to understand. The mechanistic aspects of the synthesis were studied using various techniques. This thesis consists of 6 chapters. Chapter 1 and 2 are the introductory chapters. **Chapter 1** deals with the fundamentals of nanoscience and nanotechnology, its applications, structures, kinetics and thermodynamics of growth of nanoparticles, synthesis methodology and their pros and cons. The fundamentals of the methods of synthesis used in this thesis like – radiation chemical, photochemical and room temperature chemical methods were discussed in brief. In this chapter, we have also described about the basics of semiconductor nanoparticles and the quantum confinement, their photophysical properties and the cause of their cytotoxicity. **In chapter 2**, the details of instrumentations involved in the synthesis and characterization of

nanoparticles have been described. The fundamentals of pulse radiolysis technique, the various components of linear electron accelerator (LINAC) and the kinetic treatments of the data has been explained. A brief discussion about the schematics and working principles of characterization techniques like- XRD, TEM, SEM, FTIR and Raman spectroscopy has been given. The techniques to study the optical properties of the nanoparticles like- UV-vis spectrophotometer, steady state spectrofluorometer and time correlated single photon counting (TCSPC) has also been discussed in this chapter.

The summary of important finding of the works carried out has been described in chapter 3, 4 and 5 and their outlook has been consequently presented here.

In chapter 3, we have described about the synthesis of CdSe QDs by photochemical route, using 300 nm lamps inside the photoreactor is used as the light source. *In situ* generated isopropyl radicals in the reaction mixture was used as reducing agent. We have used two different capping molecules i. e.- L-Cysteine and starch to stabilize the QDs. These QDs were characterized using XRD, Raman, TEM, SEM and FTIR. It was observed that the Pl yield as well as the Pl lifetime of these QDs could be tuned by changing the Cd and Se ratio in the reaction mixture. The L-cysteine capped CdSe QDs synthesized with 1.0:0.5 mM of Cd:Se precursor ratios were found to be comparatively smaller (~ 3 nm) and more monodispersed in size as compared to those synthesized with 1.0:1.0 mM of Cd:Se precursor ratios. Also the QDs synthesized with 1.5:0.5 mM of Cd:Se ratio were found to have more Pl and longer Pl life time (~ 57 ns) as compared to the QDs synthesized with other Cd:Se ratios. The decreased in the surface trap states in the CdSe QDs with an increase in the Cd content emerged because of better surface passivation by L-cysteine with Cd. From the FTIR studies, we found that the QDs are attached with L-cysteine *via* thiol group. The *in vitro* cytotoxicity study revealed that the QDs synthesized with 1.0:0.5 Cd:Se ratio was more bio-compatible as compared to those

synthesized with 1.0:1.0 mM with and without capping agent. Therefore, the cytotoxicity study exhibits that the capping molecules are able to reduce the cytotoxicity of the QDs adequately. Starch capped CdSe QDs were synthesized by irradiating the reaction mixture containing 0.5 mM each of $CdSO_4$ and Na_2SeSO_3, 0.5 mg/mL of starch solution, 2% v/v of acetone and 2% v/v of 2-propanol. After photoirradiation, the colourless solution changed to orange coloured colloidal solution, which indicates the formation of CdSe QDs. Growth of the QDs were monitored by recording the absorption spectra at different time of photo irradiation. They were characterized by XRD, TEM, SEM, Raman and FTIR techniques. From the TEM studies the particle size obtained of the as synthesized QDs were ~3.0 nm. The Pl intensity increased with increase in Cd:Se ratio and was maximum for CdSe QDs synthesized with 1.5:0.5 mM. The Pl life time was found to increase from 26 ns to 32 ns on increasing the Cd containts from 1.0:0.5 mM Cd:Se to 2.0:0.5 mM Cd:Se. The Pl lifetimes of the CdSe QDs have two components (τ_1 and τ_2), which is expected to be originated from the band gap (τ_1) and trap states (τ_2). The QDs synthesized with different Cd:Se ratio were extracted from the colloidal solution by first freezing, then defreezing at room temperature. The powder form of the extracted QDs synthesized with 1.5:0.5 mM of Cd:Se from the aqueous colloidal solution was functionalized with thiourea and temperature and pH conditions were optimized for maximum Pl. These thiourea functionalized QDs were used in the fluorimetric detection of heavy metal ions. Out of various heavy metal ions the Pl of these QDs were found to quenched in the presence of Cu^{2+}, Cr^{6+} and Hg^{2+}. The limit of detection (LOD) and quenching rate constant for these metal ions were determined. The limits of detection for these metal ions were in the micro molar range. The quenching rate constant were different with different metal ions and were of the order of 10^{14} $M^{-1}s^{-1}$. A mechanism for the Pl quenching was proposed in which possibility of both static and dynamic quenching was discussed. The dynamic quenching was confirmed with decrease in Pl lifetime on increasing the metal ion concentration whereas, the binding of these

metal ions on the surface of QDs as well as with the capping ligands attributed to the static quenching.

In chapter 4, we have used e-beam irradiation to synthesize CdSe QDs. These QDs were synthesized using e^-_{aq}. as reducing agent. Here, we have used different saccharides like – glucose, fructose, sucrose and starch as capping agents in the e-beam induced synthesis of CdSe QDs. The stability of the as grown QDs were found to be superior to those which were synthesized without any capping agents in the aqueous solution. These QDs were characterized by XRD, TEM and FTIR techniques. The size of the QDs were found to be around 3.0 nm as revealed by TEM. From the FTIR studies it is revealed that these QDs were functionalized by binding with the -OH group presents in all the saccharides. The mechanism of formation of these QDs was investigated by pulse radiolysis and it was found that the reaction goes through the formation of transient intermediate having absorption maximum at 500 nm in presence of all the four saccharides. The studies of optical properties of the as synthesized QDs reveals that the particle size as well as ε (molar extinction coefficient) of the CdSe QDs were different in different saccharides. The Pl intensity was also found to be different having maximum in starch followed by sucrose and for glucose and fructose, it was nearly equal. The Pl life time was found to be maximum (~30 ns) for starch capped CdSe followed by sucrose and glucose capped CdSe (~20 ns) and was least for fructose capped CdSe QDs (~14 ns). From the cytotoxicity study we found that all the saccharide capped CdSe QDs are less cytotoxic than the uncapped CdSe QDs. Among the saccharide capped QDs, glucose capped CdSe QDs were found to be least cytotoxic followed by starch and fructose capped CdSe was found to be the most cytotoxic followed by sucrose.

In different set of work, we have studied about the dynamics of formation of CdSe QDs synthesized using different secondary aliphatic alcohol radicals as reducing agents. Different aliphatic alcohols like- methanol, ethanol, 2-propanol, 1-propanol and 1-butanol have been

used to generate the corresponding secondary reducing radicals after the reaction of primary $H^{\bullet}$ and $OH^{\bullet}$ radicals produced upon the radiolysis of water. It was found that the formation of CdSe QDs proceeds *via* formation of short lived transient intermediate species having absorption maximum at 500 nm which are formed by the reaction of different secondary alcohol radicals with the precursor molecules. The rate constant for the formation of transient intermediate species formed by the reaction of the alcohol radicals with Cd and Se precursors were lower than the rate constants for the formation of transient intermediate species formed by the reaction of hydrated electrons, e_{aq}^- with the Cd and Se precursors. The optical properties of the QDs synthesized with different alcohol radicals were found to be different. The excitonic peak positions of the CdSe QDs was different in different alcohols. It was found to be blue shifted on increasing the no. of carbon atoms in the alcohols i. e. it shifted from 536 nm synthesized in methanol to 436 nm synthesized in n-butanol. The shape of the Pl spectra was very much different for CdSe QDs synthesized in the presence of different alcohols. The CdSe QDs synthesized in methanol, ethanol and 2-propanol exhibit very little Pl, however, those synthesized in the presence of 1-propanol and 1-butanol exhibit good Pl. The Pl observed in the case of 1-propanol was very narrow while that in the case of 1- butanol is very broad. These observations validate the correlation of different alcohols with the structure and properties of CdSe QDs. The relatively large structure of 1-propanol and 1-butanol as compared to the other alcohols, could provide a better microenvironment around the QDs which enhanced the radiative pathway for the carrier relaxation in the photo excited CdSe QDs.

The rate constants for the formation and decay of transients formed after the reaction of alcohol radicals with the Cd and Se precursors were found to be slower in comparison to that of hydrated electrons, e_{aq}^- with the Cd and Se precursors. This study could be correlated with the nature of the alcohol radicals and the nature of the solvent systems which supports the stability of the individual transient intermediate species. Thus it could be concluded that the

kinetics of the formation of CdSe QDs is slower when the synthesis is carried out through the aliphatic alcohol radicals as compared to those obtained through the hydrated electrons, e_{aq}^- providing different environment around the QDs and hence different optical properties and stability.

Chapter 5 is devoted to the green synthesis of CdSe quantum dots at ambient conditions. In this chapter no radiation or photon was used in the synthesis. Molecules with reducing nature like 1-thioglycerol and BSA was used in the synthesis of CdSe QDs. Our study revealed that both 1-thioglycerol and BSA acted as catalyzing and capping agent. Synthesis and study of the properties of CdSe QDs using these two molecules have been described in two sections separately. The QDs synthesized using 1-thioglycerol have a sharp excitonic absorption peak at around 420 nm which is usually not found in QDs synthesized at ambient conditions. The excitonic peak positions and hence the band gap of the QDs could be tuned from 2.72 to 2.82 eV by changing the Cd:Se ratio. The Pl quantum yield as well as Pl life time could also be effectively tuned by changing the Cd:Se precursor ratio. The Pl quantum yield was found to followed the order, 1:2 < 1:1 < 2:1. A large stokes shift associated with these photoluminescence and the excitation spectra was observed, which confirmed that these Pl could be due to trap states only. The broadening of Pl spectra indicated that it is composed of both shallow as well as deep trap states. The Pl life time was found to be maximum in the case of QDs synthesized with 0.5:0.5, followed by 1.0:0.5 and 0.5:1.0 mM of Cd:Se. The XRD study revealed that the CdSe QDs are in zinc blende phase with crystallite size ~2.0 nm. From the TEM image, the size of the QDs were found to be ~3.0 nm with very good monodispersity. The SEM images revealed the rod shaped morphology of the QDs synthesized with 1.0:0.5 and 0.5:1.0 mM of Cd:Se while a mixed spherical and rod shaped morphology was obtained for the QDs synthesized with 0.5:0.5 mM of Cd:Se. From the FTIR study we found that the QDs are attached with 1-thioglycerol *via* the S atom which was in agreement with the HSAB principle.

The reaction mechanism involved in the synthesis was investigated by the cyclic voltammetry (CV). The CV study revealed that the Se atom in Na_2SeO_3 was electro activated by the S atom present in 1-thioglycerol. Also the S atom of 1-thioglycerol form a complex with the Cd atom which subsequently gives the CdSe QDs.

In the BSA assisted synthesis of CdSe QDs we have performed a systematic in-depth study on the growth of the CdSe QDs by monitoring the time dependent absorption and Pl properties. The fluorescence of BSA was found to quench in the presence of $SeSO_3^{2-}$ immediately after adding $SeSO_3^{2-}$ with no further time dependent quenching. However, in presence of both the Cd^{2+} and $SeSO_3^{2-}$ after initial quenching of BSA fluorescence, we observed a time dependent quenching of BSA fluorescence along with simultaneous growth in the Pl of CdSe QDs with isoemissive point. The growth rate constant of CdSe QDs synthesized with different stoichiometric ratio of Cd:Se obtained from the absorption spectra was found to be of the order 10^{-4} s^{-1}. The growth rate constant of CdSe QDs obtained from the Pl was found to be of the order 10^{-3} s^{-1}. This discrepancy in the growth rate constant obtained from the absorption and Pl spectra indicated the involvement of FRET process in which BSA acted as donor and CdSe QDs as acceptor. We have determined the fluorescence life time of the BSA at various time interval and found that the life time has two components which could be attributed to the two tryptophan units present in the BSA (Trp-134 and Trp-213). The fluorescence life time corresponding to these two tryptophan units also decreased with time showing the close proximity of these units with the growing QDs inside the BSA matrix. We have determined various FRET parameters at different time of the reaction. Our study could be able to demonstrate clearly that the CdSe QDs are formed in the close proximity to the BSA molecules so that FRET could occur and the tertiary structure of BSA provides a suitable environment so that these QDs do not undergo agglomeration.

6.2. Future perspectives

Development of sustainable protocol for synthesis of good quality nanoparticles which involve ambient experimental conditions like- normal temperature, pressure and minimal energy consumption, no involvement of toxic reducing and capping agents and time efficient is still a challenge for researchers and scientists. The synthesis methodologies used here are highly facile, one step and time efficient. The radiation and photochemical method of synthesis of nanoparticles can be potentially used for the synthesis of various nanoparticles to achieve the above mentioned goals. Based on our study accomplished in the present thesis work, the radiation chemical and photochemical methods can be used as effective tools to synthesize semiconductor QDs and metal nanoparticles of extremely small size. Various biomolecules and biocompatible molecules can be used effectively for the surface passivation/capping of the nanoparticles. Capping of nanoparticles with molecules like- saccharides and L-cysteine could substantially reduce the cytotoxicity of the nanoparticles. Various other biomolecules having same functional group can also be used as capping agents to reduce the cytotoxicity of the nanoparticles.

The photochemical method of synthesis could be potentially used in large scale synthesis with the provision of photoirradiation on wider area. We have demonstrated the extraction of starch capped CdSe QDs from the colloidal solution using the sedimentation properties of starch molecules. Employing this method, starch capped nanoparticles could be easily extracted from the colloidal solution in the powder form. The powder form of the nanoparticles can be further functionalized with different molecules to improve their optical properties. The as functionalized nanoparticles with improved optical properties can be used in various applications like- metal ion sensing, bio imaging etc. Utilizing the knowledge of Pl quenching mechanism, one can specifically various synthesize nanoparticles for the fluorimetric detection of a specific metal ion. Using radiation chemical method choosing suitable solvent system, the

particle size and hence the optical properties of various nanoparticles can be successfully tuned. The radiation chemical, photochemical and the green chemical methods used in the synthesis of CdSe QDs can be further successfully employed to synthesize other QDs/nanoparticles like- CdTe, PbSe, CuSe, SnSe, etc. The study of FRET involved in the BSA mediated synthesis provide the insights of the optical properties of the QDs and its growth kinetics. This aspect can be utilized for better understanding of various prospects such as crystal growth, defect formation and the energy transfer process in different systems.

References

1. J. Zhou, J. Ralston, R. Sedev, D.A. Beattie, *J. Coll. Inter. Sci.* 331 (2009) 251-262.

2. I. Freestone, N. Meeks, M. Sax, C. Higgitt, *Gold Bulletin*, 40 (2007) 270-277.

3. R.P. Feynman, *J. Microelectromech S*, 1 (1992) 60.

4. E. Drexler, *Engines of Creation: The Coming Era of Nanotechnology,* (1986).

5. M. Rakesh, T.N. Divya, T. Vishal, K. Shalini, J *Nanomedicine Bio therapeutic Discov.* 5 (2015) 1000131.

6. U. Resch-Genger, M. Grabolle, S. Cavaliere-Jaricot, R. Nitschke, T. Nann, *Nat. Methods,* 5 (2008) 763-775.

7. S.W. Koch, M. Kira, G. Khitrova, A.M. Gibbs, *Nat. Mater.,* 5 (2006), 523-531.

8.Nanotechnology timeline. National Nanotechnology Initiative, http://www.nano.gov/timeline.

9. R. Rossetti, S. Nakahara, L.E. Brus, *J. Chem. Phys.* 79 (1983) 1086-1088.

10. L. Brus, *J. Phys. Chem*. 90(1986) 2555-2560.

11. M.A. Reed, J.N. Randall, R.J. Aggarwal, R.J. Matyi, T.M. Moore, A.E. Wetsel, *Phys. Rev. Lett.* 60 (1988) 535-539.

12. C.B. Murray, D.J. Norris, M.G. Bawendi, *J. Am. Chem. Soc.* 115 (1993) 8706-8715.

13. N. Chestnoy, T.D. Harris, R. Hull, L.E. Brus, *J. Phys. Chem.* 90 (1986) 3399-3406.

14. L. Li, J. Hu, W. Yang, A.P. Alivisatos, *Nano Lett.* 1 (2001) 349-351.

15. M.A. El-Sayed, *Acc. Chem. Res.* 37 (2004) 326-333.

16. A.M. Smith, S. Nie, *Acc. Chem. Res.* 43 (2010) 190-200.

17. M. Aresti, M. Saba, R. Piras, D. Marongiu, G. Mula, F. Quochi, A. Mura, C. Cannas, M. Mureddu, A. Ardu, G. Ennas, V. Calzia, A. Mattoni, A. Musinu, G. Bongiovanni, *Adv. Funct. Mater*. (2014) 1-10.

18. R.K. Ratnesh, M.S. Mehata, *AIP Advances,* 5 (2015) 097114-23.

19. (a) A.P. Alivisatos, *J. Phys. Chem*. 100 (1996) 13226-13239, (b) A. Guleria, A.K. Singh, M. C. Rath, S. Adhikari, *Mater. Res. Express,* 2 (2015) 04500, (c) W.W. Yu, L. Qu, W. Guo, X. Peng, *Chem. Mater*. 15 (2003) 2854-2860.

20. F. Chandezon, P. Reiss, *Techniques de l'Ingenieur*, RE, 22 (2004) 1-15.

21. A.P. Alivisatos, *Science,* 271 (1996) 933-937.

22. F. Wang, A. Dong, W.E. Buhro, *Chem. Rev.* 116 (2016), 10888−10933.

23. M.G. Bawendi, P.J. Carroll, W.L. Wilson, L.E. Brus, *J. Chem. Phys.* 96 (1992) 946-954.

24. X. Wang, L. Qu, J. Zhang, X. Peng, M. Xiao, *Nano Lett.*, 3 (2003) 1103-1106.

25. M. Kuno, J.K. Lee, B.O. Dabbousi, F.V. Mikulec, M.G. Bawendi, *J. Chem. Phys.* 106 (1997) 9869-9882.

26. F. Wu, J.Z. Zhang, R. Kho, R.K. Mehra, *Chem. Phys. Lett.* 330 (2000) 237-242.

27. M. Abdellah, K.J. Karki, N. Lenngren, K. Zheng, T. Pascher, A. Yartsev, T. Pullerits, *J. Phys. Chem. C,* 118 (2014) 21682-21686.

28. M. O'Neil, J. Marohn, G. McLendon, *J. Phys. Chem.* 94 (1990) 4356-4363.

29. B. Kang, J. Lee, S. Lee, S. Kim, J. Lee, S. Gopalan, J. Park, D. Kwon, J. Bae, H. Kim, S. Kang, *Nat. Sci. Rep.* 6 (2016) 34659.

30. S. Pramanik, S. Bhandari, S. Roy, A. Chattopadhyay, *J. Phys. Chem. Lett*. 6 (2015) 1270-1274.

31. F. Zhang, S. Wang, L. Wang, Q. Lin, H. Shen, W. Cao, C. Yang, H. Wang, L. Yu, Z. Du, J. Xue, L.S. Li, *Nanoscale,* 8 (2016) 12182-12188.

32. M.A. Schreuder, K. Xiao, I.N. Ivanov, S.M. Weiss, S.J. Rosenthal, *Nano Lett.* 10 (2010) 573-576.

33. P.V. Kamath, *J. Phys. Chem. Lett.* 4 (2013) 908-918.

34. M.C. Beard, *J. Phys. Chem. Lett.* 2 (2011) 1282-1288.

35. G. Konstantatos, E.H. Sargent, *Infrared Phys. Technol*. 54 (2011) 278–282.

36. P. Martyniuk, A. Rogalski, *Prog Quantum Electronics,* 32 (2008) 89–120.

37. M.F. Frasco, N. Chaniotakis, *Sensors*, 9 (2009) 7266-7286.

38. H. Liu, M. Li, O. Voznyy, L. Hu, Q. Fu, D. Zhou, Z. Xia, E.H. Sargent, J. Tang, *Adv. Mater.* 26 (2014) 2718–2724.

39. L. Ge, F. Zuo, J. Liu, Q. Ma, C. Wang, D. Sun, L. Bartels, P. Feng, *J. Phys. Chem. C,* 116 (2012) 13708-13714.

40. G. Li, D. Zhang, J.C. Yu, *Environ. Sci. Technol.* 43 (2009) 7079-7085.

41. M. Roushani, M. Mavaei and H.R. Rajabi, *J. Mol. Catal. A: Chem.* 409 (2015) 102-109.

42. I.V. Martynenko, A.P. Litvin, F. Purcell-Milton, A.V. Baranov, A.V. Fedorov, Y.K. Gunko, *J. Mater. Chem. B,* 5 (2017) 6701-6727.

43. W.R. Algar, K. Susumu, J.B. Delehanty, I.L. Medintz, *Anal. Chem.* 83 (2011) 8826-8837.

44. (a) I.L. Medintz, H. Mattoussi, *Phys. Chem. Chem. Phys.* 11 (2009) 17-45. (b) J. Saha, A.D. Roy, D. Dey, D. Bhattacharjee, S.A. Hussain, *Mater. Today: Proc.* 5 (2018) 2306–2313.

45. C.A. Leatherdale, W.K. Woo, F.V. Mikulec, M.G. Bawendi, *J. Phys. Chem. B,* 106 (2002) 7619-7622.

46. C.E. Bradburne, J.B. Delehanty, K.B. Gemmill, B.C. Mei, H. Mattoussi, K. Susumu, J.B. Blanco-Canosa, P.E. Dawson, I.L. Medintz, *Bioconjugate Chem.* 24 (2013) 1570-1583.

47. T. Jamieson, R. Bakhshi, D. Petrova, R. Pocock, M. Imani, A.M. Seifalian, *Biomaterials*, 28 (2007) 4717-4732.

48. R. Hardman, *Environ. Health Perspect*. 114 (2006) 165-172.

49. A.M. Derfus, W.C.W. Chan, S.N. Bhatia, *Nano Lett.* 4 (2004) 11-18.

50. M. Kondoh, S. Araragi, K. Sato, M. Higashimoto, M. Takiguchi, M. Sato, *Toxicology,* 170 (2002) 111-117.

51. H.M. Shen, C.F. Yang, C. N. Ong, *Int. J. Cancer*, 81(1999) 820–828.

52. A. Shiohara, A. Hoshino, K. Hanaki, K. Suzuki, K. Yamamoto, *Microbiol. Immunol.* 48 (2004) 669–675.

53. W.J. Parak, T. Pellegrino, C. Plank, *Nanotechnology*, 16 (2005) R9–R25.

54. C. Dhand, N. Dwivedi, X.J. Loh, A.N.J. Ying, N.K. Verma, R.W. Beuerman, R. Lakshminarayanan, S. Ramakrishna, *RSC Adv.* 5 (2015) 105003-105037.

55. E. Groeneveld, C.M. Donega, *Nanoparticles: Workhorse of Nanoscience,* Springer Publication, Chapter 6, 145.

56. (a) M.A. Malik, P. O'Brien, N. Revaprasadu, *J. Mater. Chem.* 11 (2001) 2382-2386, (b) A.M. Salaheldin, J. Walter, P. Herre, I. Levchuk, Y. Jabbari, J.M. Kolle, C.J. Brabec, W. Peukert, D. Segets, *Chem. Eng. J.* 320 (2017) 232–243, (c) C.M. Donega, P. Liljeroth, D. Vanmaekelbergh, *small*, 1 (2005) 1152 – 1162.

57. (a) H. Hayashi, Y. Hakuta, *Materials*, 3 (2010) 3794-3817, (b) M. Mo, J. Zeng, X. Liu, W. Yu, S. Zhang, Y. Qian, *Adv. Mater.* 14 (2002) 1658-1662, (c) M.S. Akhtar, M.A. Khan, M.S. Jeon, O. Yang, *Electrochimica Acta,* 53 (2008) 7869–7874.

58. (a) M.G. Pinilla, E. Martinez, G.S. Vidaurri, E. Perez-Tijerina, *Nanoscale Res. Lett.* 5 (2010) 180-188, (b) M. Kawakami, A.B. Hartanto, Y. Nakata, T. Okada, *Jpn. J. Appl. Phys.* 42 (2003) 33-35,

(c) D. Amans, C. Malaterre, M. Diouf, C. Mancini, F. Chaput, G. Ledoux, G. Breton, Y. Guillin, C. Dujardin, K. Masenelli-Varlot, P. Perriat, *J. Phys. Chem. C,* 115 (2011) 5131-5139.

59. (a) Y. Chen, C. Yeh, *Colloids Surf. A*, 197 (2002) 133-139, (b) L. Kungumadevi, R. Sathyamoorthy, *Bull. Mater. Sci.* 36 (2013) 771–778, (c) H. Lv, D.D. Sang, H.D. Li, X.B. Du, D.M. Li, G.T. Zou, *Nanoscale Res. Lett.* 5 (2010) 620–624.

60. (a) X. Xu, M. Shao, J. Huang, Q. Zhang, L. Ma, *J. Nanosci. Nanotechnol*. 14 (2014) 2635-2639, (b) Z. Wang, R. Guo, L. Ding, Y. Tong, G. Li, *Sci. Rep.* 3 (2013) 1-8, (c) K.V. Singh, A.A. Martinez-Morales, G.T.S. Andavan, K.N. Bozhilov, M. Ozkan. *Chem. Mater.* 19 (2007) 2446-2454.

61. (a) W.S. Hummers, R.E. Offeman, *J. Am. Chem. Soc.* 80 (1958) 1339, (b) P.G. Prabhash, S.S. Nair, *AIP Adv.* 6 (2016) 055003-055008.

62. (a) M.Y. Han, C.H. Quek, *Langmuir*, 16 (2000) 362-367, (b) C.M. Gonzalez, W. Wu, J.B. Tracy, B. Martin, *Chem. Commun.* 51 (2015) 3087-3090.

63. (a) A. Abedini, A.R. Daud, M.A.A. Hamid, N.K. Othman, E. Saion, *Nanoscale Res. Lett.* 8 (2013) 874-883 (b) X. Jiang, Y. Xie, J. Lu, L. Zhu, W. He, Y. Qian, *Chem. Mater.* 13 (2001) 1213-1218.

64. C.B. Murray, C.R. Kagan, M.G. Bawendi, *Annu. Rev. Mater. Sci.* 30 (2000) 545-610.

65. L.O. Cinteza, *J. Nanophoton.* 4, (2010) 042503.

66. L. Jing, S.V. Kershaw, Y. Li, X. Huang, Y. Li, A.L. Rogach, M. Gao, *Chem. Rev.* 116 (2016) 10623–10730.

67. B. Zhang, R. Hu, Y. Wang, C. Yang, X. Liu, K.T. Yong, *RSC Adv.* 4 (2014) 13805-13816.

68. X. Michalet, F.F. Pinaud, L.A. Bentolila, J.M. Tsay, S. Doose, J.J. Li, G. Sundaresan, A.M. Wu, S.S. Gambhir, *Science*, 307 (2005) 538-544.

69. N. Hildebrandt, C.M. Spillmann, W.R. Algar, T. Pons, M.H. Stewart, E. Oh, K. Susumu, S.A. Díaz, J.B. Delehanty, I.L. Medinitz, *Chem. Rev.* 117 (2017) 536–711.

70. M. Sakamoto, M. Fujistuka, T. Majima, *J. Photochem. Photobiol.C: Photochem. Rev*. 10 (2009) 33-56.

71. H. Park, X. Zhang, Y. Choi, H. Park, R.H. Hill, *J. Nanomaterials,* 2001 (2010*)* 1-7.

72. M.Y. Han, C.H. Quek, *Langmuir,* 16 (2000) 362-367.

73. P.R. Levstein, H.V. Willigen, *J. Chem. Phys.* 95 (1991) 900-908.

74. K. Esumi, M. Wakabayashi, K. Torigoe*, Colloids Surfaces A: Physicochem. Eng. Aspects*. 109 (1996) 55-62.

75. C.Y. Wang, X. Mo, Y. Zhou, Y.R. Zhu, H.T. Liu, Z.Y. Chen, *J. Mater. Chem.* 10 (2000) 607-608.

76. Y. Shiraishi, M. Ikeda, D. Tsukamoto, S. Tanakab, T. Hirai, *Chem. Commun.* 47 (2011) 4811-4813.

77. M. Zaarour, M.El Roz, B. Dong, R. Retoux, R. Aad, J. Cardin, C. Dufour, F. Gourbilleau, J.P. Gilson, S. Mintova, *Langmuir*, 30 (2014) 6250-6256.

78. C.M. Gonzalez, W. Wu, J.B. Tracyb, B. Martin, *Chem. Commun.* 51 (2015) 3087-3090.

79. C. Dispenza, N. Grimaldi, M. A. Sabatino, I.L. Soroka, M. Jonsson, *J. Nanosci. Nanotechnol.* 15 (2015) 3445-3467.

80. G.V. Buxton, C.L. Greenstock, W.P. Helman, A.B. Ross, *J. Phys. Chem. Ref. Data,* 17 (1988) 513-886.

81. M. Piechowski, M. Thelen, J. Hoign, R.E**.** Buhler, *Ber. Bunsenges. Phys. Chem*. 96 (1992) 1448-1454.

82. E. Janata, M. Kelm, B.G. Ershov, *Radiat. Phys. Chem.* 63 (2002), 157-160.

83. S. Singh, A. Guleria, M.C. Rath, A.K. Singh, S. Adhikari, S.K. Sarkar, *Mater. Lett.* 65 (2011) 1815-1818.

84. W. Wang, Y. Geng, P. Yan, F. Liu, Y. Xie, Y. Qian, *J. Am. Chem. Soc.* (2011) 121, 4062-4063.

85. (a) W. Wang, I. Germanenko, M.S. El-Shall, *Chem. Mater.* (2002) 14, 3028-3033. (b) X. He, L. Gao, N. Ma, *Sci. Rep.* (2013) 3 2825.

86. N.H. Chou, X. Ke, P. Schiffer, R.E. Schaak, *J. Am. Chem. Soc.* (2008) 130, 8140–8141.

87. https://en.wikipedia.org/wiki/Classical_nucleation_theory.

88. J.W. Mullin, *Crystallization*, 4th ed., (1997) Butterworth-Heinemann: Boston.

89. N.T.K. Thanh, N. Maclean, S. Mahiddine, *Chem. Rev.* 114 (2014) 7610−7630.

90. https://en.wikipedia.org/wiki/Critical_radius.

91. Z.A. Peng, X. Peng, *J. Am. Chem. Soc*. 124 (2002) 3343-3353.

92. V.K. LaMer, R.H. Dinegar, *J. Am. Chem. Soc*. 72 (1950) 4847-4854.

93. A.T. Hubbard, *Encyclopedia of Surface and Colloid Science,* CRC Press 2004, 4230.

94. (a) Y. Yoshida, S. Tagawa, Y. Tabata, *Pulse Radiolysis*, CRC Press, (1990) (b) J.H. Baxendale, F. Busi, Eds., *The Study of Fast Processes and Transient Species by Electron Pulse Radiolysis,* Springer Netherlands, Dordrecht, Holland (1982), (c) A. Hummel, *Adv. Radiat. Chem*. 4 (1974) 1-102; (d) Y. Yoshida, S. Tagawa, Y. Tabata, *Radiat. Phys. Chem*. 23 (1984) 279-285.

95. B. Smaller, J.R. Remko, E.C. Avery, *J. Chem. Phys.* 48 (1968) 5174-5181.

96. K.H. Schmidt, W. L. Buck, *Science,* 151 (1966) 70-71.

97. Y. Tabata, *Pulse Radiolysis of Irradiated Systems*, CRC Press, (1991).

98. G.V. Buxton, C.R. Stuart, *J. Chem. Soc. Faraday Trans.* 91 (1995) 279-281.

99. K. Shih, K ed., *X-Ray Diffraction: Structure, Principles and Applications*, Nova Science, (2013).

100. A.R. West, *Basic Solid State Chemistry*, John Wiley & Sons, 2nd ed. (1999).

101. U. Holzwarth, N. Gibson, *Nat. Nanotechnol*. 6 (2011) 534-534.

102. B. Fultz, J. Howe, *Transmission Electron Microscopy and Diffractometry of Materials*, Springer, (2007).

103. R. Egerton, *Physical principles of electron microscopy*, Springer, (2005).

104. E. Kirkland, *Advanced computing in Electron Microscopy*, Springer, (1998).

105. D. McMullan, *Scanning*, 17 (2006) 175-185.

106. P. Echlin, D. C. Joy, C. Fiori, E. Lifshin, G.I. Goldstein, D.E. Newbury, *Scanning electron microscopy and x-ray microanalysis*, Plenum Press, New York (1981).

107. K.K. Rohatgi-Mukherjee, *Fundamentals of Photochemistry*, Wiley Eastern Ltd: India (1986).

108. D.A. Skoog, F.J. Holler, S. R. Crouch, C.A. Belmont, T. Brooks/Cole, *Principles of Instrumental Analysis*, 6th ed. (2007).

109. J.R. Lakowicz, *Principles of Fluorescence Spectroscopy*, Springer Science, New York, 3rd ed., (2006).

110. M. Y. Berezin, S. Achilefu, *Chem. Rev*. 110 (2010) 2641–2684.

111. D.V. O'Connor, D. Phillips, *Time-Correlated Single-Photon Counting*, Academic Press, London, (1984).

112. B.C. Smith, *Fundamentals of Fourier Transform Infrared Spectroscopy*, CRC Press, 2nd ed. (2011).

113. B.H. Stuart, *Infrared Spectroscopy: Fundamentals and Applications*, Wiley (2004).

114. R. White, *Chromatography/Fourier Transform Infrared Spectroscopy and its Applications*, CRC Press, Ist ed. (1989).

115. F.M. Mirabella, *Practical Spectroscopy Series; Internal reflection spectroscopy: Theory and applications*, CRC Press (1992).

116. Technical note on FTIR spectroscopy, PerkinElmer.

117. J.R. Ferraro, *Introductory Raman Spectroscopy*, Academic Press Inc, 2nd ed. 4 (2002).

118. B. Schrader, *Infrared and Raman Spectroscopy*, VCH Publishers Inc., New York, (1995).

119. A.B. Myers, R.A. Mathies, *Biological Applications of Raman Spectroscopy: Resonance Raman Spectra of Polyenes and Aromatics*, John Wiley and Sons, New York, (1987).

120. P. Larkin, *Infrared and Raman Spectroscopy; Principles and Spectral Interpretation*, Elsevier Science Publishing Co Inc. (2011).

121. M. Sakamoto, M. Fujistuka, T. Majima, *J. Photochem. Photobiol. C: Photochem. Rev.* 10 (2009) 33–56.

122. F. Shaik, W. Zhang, W. Niu, *J. Phys. Chem. C*, 121 (2017) 9572−9578.

123. K. Mallick, Z.L. Wang, T. Pal, *J. Photochem. Photobiol. A: Chem.* 140 (2001) 75–80.

124. A.L. Stroyuk, V.V. Shvalagin, S.Y. Kuchmii, *J. Photochem. Photobiol. A: Chem.* 173 (2005) 185–194.

125. B. Pietrobon, V. Kitaev, *Chem. Mater.* 20 (2008) 5186–5190.

126. K.L. McGilvray, M.R. Decan, D. Wang, J.C. Scaiano, *J. Am. Chem. Soc.* 128 (2006), 15980-15981.

127. J. Zhu, X. Liao, J. Wang, H. Chen, *Mater. Res. Bul.* 36 (2001) 1169 –1176.

128. K.M. Tsoi, Q. Dai, B.A. Alman, W.C.W. Chan, *Acc. Chem. Res*. 46 (2013) 662-671.

129. F.M. Winnik, D. Maysinger, *Acc. Chem. Res.* 46 (2013) 672-680.

130. I.L. Medinitz, H.T. Uyeda, E.R. Goldman, H. Mattoussi, *Nat. Mat.* 4 (2005) 435-446.

131. T. Jamieson, R. Bakhshi, D. Petrova, R. Pocock, M. Imani, A.M. Seifalian, *Biomaterials,* 28 (2007) 4717–4732.

132. A.M. Derfus, W.C.W. Chan, S.N. Bhatia, *Nano Lett.* 4 (2004) 11-18.

133. S. Singh, M.C. Rath, A.K. Singh, T. Mukherjee, O.D. Jayakumar, A.K. Tyagi, S.K. Sarkar, *Radiat. Phys. Chem.* 80 (2011) 736-741.

134. S. Singh, M.C. Rath, S.K. Sarkar, *J. Phys. Chem. A,* 115 (2011) 13251–13258.

135. P.J. Jenkins, A.M. Donald, *Carbohydr. Res.* 308 (1998) 133-147.

136. P. Wardman, *J. Phys. Chem. Ref. Data,* 18 (1989) 1637-1755.

137. M.C. Rath, J.A. Mondal, D.K. Palit, T. Mukherjee, H.N. Ghosh, *J. Nanomaterials*, 1 (2007) (Art ID 36271).

138. A.L. Rogach, A. Kornowski, M. Gao, A. Eychmuller, H. Weller, *J. Phys. Chem. B*, 103 (1999) 3065-3069.

139. A. Monshi, M.R. Foroughi, M.R. Monshi, *World J. Nano Sci. Eng*. 2(2002) 154-

140. A. Tanaka, S. Onari, T. Arai, *Phys. Rev. B*, 45(1992) 6587-6592.

141. F. Jalilehvand, V. Mah, B.O. Leung, J. Mink, G.M. Bernard, L. Hajba, *Inorg. Chem.* 48 (2009) 4219-4230.

142. D.L. Pavia, G.M. Lampman, G.S. Kriz, *Introduction to spectroscopy 3rd Ed.*, USA, (2001).

143. A. Pawlukojc, I. Padureanu, D. Aranghel, *Report Wp13 IDRANA*, 67 (2004).

144. S. Aryal, B.K.C. Remant, N. Dharmaraj, N. Bhattarai, C.H. Kim, H.Y. Kim, *Spectrochimica Acta Part A*, 63 (2006) 160-163.

145. W.W. Yu, L. Qu, W. Guo, X. Peng, *Chem. Mater*. 15 (2003) 2854-2860.

146. A. Javier, D. Magana, T. Jennings, G.F. Strouse, *Appl. Phys. Lett.* 83 (2003) 1423-1425.

147. H.A. Spoehr, H.W. Milner *J. Biol. Chem.* 116 (1936) 493-502.

148. R. Kizil, J. Irudayaraj, K. Seetharaman, *J. Agric. Food Chem.* 50 (2002) 3912-3918.

149. J.E. Stewart, *J. Chem. Phy.* 26 (1957) 248-254.

150. W.N. Wenger, F.S. Bates, E.S. Aydil, *Langmuir*, 33 (2017) 8239−8245.

151. D. Valerini, A. Creti, M. Lomascolo, *Phy. Rev. B,* 71 (2005) 235409-235414.

152. Y. Zhao, C. Riemersma, F. Pietra, R. Koole, C.M. Donega, A. Meijerink, *ACS Nano*, 6 (2012) 9058-9067.

153. N.B.H. Mohamed, M. Haouari, Z. Zaaboub, M. Nafoutti, F. Hassen, H. Maaref, H.B. Ouada, *J. Nanopart. Res.* 16 (2014)2242-2258.

154. A.H. Gore, U.S. Mote, S.S. Tele, P.V. Anbhule, M.C. Rath, S.R. Patila, G.B. Kolekar, *Analyst,* 136 (2011) 2606-2612.

155. International conference on harmonization (ich) of technical requirements for registration of pharmaceuticals for human use, topic q2 (r1): validation of analytical procedures: text and methodology, 2005, http://www.ich.org.

156. W. Du, L. Liao, Li Yang, A. Qin, A. Liang, *Nature Sci. Rep.* 7 (2017) 11451-11462.

157. X. Ding, L. Qu, R. Yang, Y. Zhoua, J. Li, *Lumin.* 30 (2015) 465–471.

158. Y. Yu, R. Zhang, K. Zhang, S. Sun, *J. Nanosci. Nanotech.* 12 (2012) 2783–2790.

159. H.M. Wu, J.G. Liang, and H.Y. Han, *Microchim. Acta*, 161 (2008) 81-86.

160. C. Dispenza, N. Grimaldi, M.A. Sabatino, I.L. Soroka, M. Jonsson, *J. Nanosci. Nanotechnol.* 15 (2015) 3445-3467.

161. D. Wu, X. Ge, Z. Zhang, M. Wang, S. Zhang, *Langmuir,* 20 (2004) 20, 5192-5195.

162. A. Abedini, A.R. Daud, M.A.A. Hamid, N.K. Othman, E. Saion, *Nanoscale Res. Lett.* 8 (2013) 474-483.

163. S.N. Guha, P.N. Moorthy, K. Kishore, D.B. Naik, K.N. Rao, *Proc. Ind. Acad. Sci (Chem. Sci.),* 99 (1987) 261–268.

164. M.L. Wolfrom, W.W. Binkley, L. Mccabe, *J. Am. Chem. Soc.* 81 (1959) 1442-1446.

165. R. Kizil, J. Irudayaraj, K. Seetharaman, *J. Agric. Food Chem.* 50 (2002) 3912-3918.

166. M. Ibrahim, M. Alaam, H. El-Haes, A.F. Jalbout, A. de Leon, *Ecl. Quim*. 31 (2006) 15-21.

167. A.B. Brizuela, L.C. Bichara, E. Romano, A. Yurquina, S. Locatelli, S.A. Brandan, *Carbohydr. Res.* 361 (2012) 212-218.

168. A. Guleria, M.C. Rath, A.K. Singh, S. Adhikari, *J. Nanosci. Nanotechnol.* 15 (2015) 9341-9357.

169. O. Lee, W.R. Bruce, Q. Dong, J. Bruce, R. Mehta, P.J. O'Brien, *Chem.-Biol. Interact*. 178 (2009) 332-339.

170. T. Bose, A.S. Chakraborti, *Biochim. Biophys. Acta,* 1780 (2008) 800-808.

171. P. Pramanick, R.N. Bhattacharya, *J. Solid State Chem.* 44 (1982) 425–425.

172. E. Janata, *Proc. Indian Acad. Sci. (Chem. Sci.)*, 114 (2002) 731-737.

173. J.W.T. Spinks, R. J. Woods, *An Introduction Radiation Chemistry*, 3rd ed., John Wiley & Sons Inc. New York (1976).

174. G.E. Adams, R.L. Willson, *Trans. Faraday Soc.* 65 (1969) 2981-2987.

175. K. Parveen, V. Banse, L. Ledwani, *AIP Conf. Proc.* 1724 (2016) 020048-020053.

176. C. Jiang, S. Xu, D. Yang, F. Zhang, W. Wang, *Luminescence,* 22 (2007) 430-437.

177. J. Yuan, W. Guo, J. Yin, E. Wang, *Talanta*, 77 (2009) 1858–1863.

178. M. Geszke-Moritz, H. Piotrowska, M. Murias, L. Balan, M. Moritz, J. Lulek, R. Schneider, *J. Mater. Chem. B*, 1 (2013) 698-706.

179. W. Na, X. Liu, T. Hu, X. Su, *New J. Chem.* 40 (2016) 1872-1877.

180. F. Shi, S. Liu, X. Su, *New J. Chem.* 41 (2017) 4138-4144.

181. M. Zhao, E. Zeng, *Nanoscale Res. Lett.* (2015) 10:171.

182. Y. Zheng, S. Gao, J.Y. Ying, *Adv. Mater.* 19 (2007) 376–380.

183. H. Sahoo, *J. Photochem. Photobiol. C*, 12 (2011) 20-30.

184. A.R. Clapp, I.L. Medintz, J.M. Mauro, B.R. Fisher, M.G. Bawendi, H. Mattoussi, *J. Am. Chem. Soc.* 126 (2004) 301-310.

185. D.M. Willard, L.L. Carillo, J. Jung, A.V. Orden, *Nano Lett.* 1 (2001) 469-474.

186. C.Y. Zhang, L.W. Johnson, *Angew. Chem. Int. Ed.* 46 (2007) 3482-3485.

187. S.H. Moh, B.H. San, A. Kulkarni, T. Kimac, K.K. Kim, *J. Mater. Chem. C*, 1 (2013) 2412-2415.

188. W.H. Yu, J. Lee, S. Kim, S.J. Kim, I.S. Kim, *Nanotechnology,* 21 (2010) 425501-425510.

189. L. Qu, Z.A. Peng, X. Peng, *Nano Lett.* 1 (2001) 333-337.

190. M. Epifani, E. Pellicer, J. Arbiol, N. Sergent, T. Pagnier, J.R. Morante, *Langmuir,* 24 (2008) 11182-11188.

191. A. Tanaka, S. Onari, T. Arai, *Phys. Rev. B*, 45 (1992) 6587-6592.

192. B.K. Rai, H.D. Bist, R.S. Katiyar, M.T.S. Nair, P.K. Nair, A. Mannivannan, *J. Appl. Phys.* 82 (1997) 1310-1319.

193. N.B. Brahim, M. Poggi, N.B.H. Mohamed, R.B. Chaabane, M. Haouari, M. Negrerie, H.B. Ouada, *J. Lumin.* 177 (2016) 402-408.

194. J. Tauc, R. Grigorovici, A. Vancu, *Phys. Status Solidi B*, 15 (1966) 627-637.

195. D.J. Norris, M.G. Bawendi, *Phys. Rev. B*, 53 (1996) 16338-16346.

196. A.I. Ekimov, F. Hache, M.C. Schanne-Klein, D. Ricard, C. Flytzanis, *J. Opt. Soc. Am. B,* 10 (1993) 100-107.

197. M. Grabolle, M. Spieles, V. Lesnyak, N. Gaponik, A. Eychmuller, U. Resch-Genger, *Anal. Chem.* 81 (2009) 6285-6294.

198. J.P. Danehy, K.N. Parameswaran, *J. Chem. Eng. Data*, 13 (1968) 386-389.

199. M.C. Rath, V.B. Gawandi, T.K. Ghanty, H. Mohan, T. Mukherjee, *Res. Chem. Intermed.* 30 (2004) 579-593.

200. M.R. De Felippis, M. Faraggi, M.H. Klappe, *J. Phys. Chem.* 94 (1990) 2420-2424.

201. A. Durairajan, B.R. Haran, R.E. White, B.N. Popov, *J. Electrochem. Soc.* 147 (2000) 4507-4511.

202. P.S. Rao, E. Hayon, *J. Phys. Chem.* 79 (1975) 865-868.

203. R.B. Kale, C.D. Lokhande, *Semicond. Sci. Technol.* 20 (2005) 1-9.

204. M. Ahmed, A. Guleria, M.C. Rath, A.K. Singh, S. Adhikari, S.K. Sarkar, *J. Nanosci. Nanotechnol.* 14 (2014) 5730-5742.

205. R. de la Rica, H. Matsui, *Chem. Soc. Rev.* 39 (2010) 3499-3509.

206. L. Au, B. Lim, P. Colletti, Y.S. Jun, Y. Xia, *Chem. Asian J.* 5 (2010) 123-129.

207. M. Ahmed, A. Guleria, A.K. Singh, T. Bandyopadhyay, S.K. Sarkar, *Ind. J. Biochem. Biophys.* 51 (2014) 175-187.

208. S. Dasmandal, A. Kundu, S. Rudra, A. Mahapatra, *RSC Adv.* 5 (2015) 79107-79118.

209. S. Ghosh, B.K. Paul, N. Chattopadhyay, *J. Chem. Sci.* 126 (2014) 931-944.

210. A.R. Clapp, I.L. Medintz, B.R. Fisher, G.P. Anderson, H. Mattoussi, *J. Am. Chem. Soc.* 127 (2005) 1242-1250.

211. A.C. Vinayaka, M.S. Thakur, *Bioconjugate Chem.* 22 (2011) 968-975.

212. X. Huang, L. Li, H. Qian, C.R. Dong, *J. Angew. Chem. Int. Ed.* 45 (2006) 5140-5143.